JLU
NEUE WEGE. SEIT 1607.

JUSTUS-LIEBIG-
UNIVERSITÄT
GIESSEN

Meson transition form factors and electromagnetic decays in the Dyson-Schwinger-approach

Autor:
Esther-Danielle Weil

Dissertation zur Erlangung des Doktorgrades der Naturwissenschaften
verfasst am Institut für theoretische Physik,
Justus-Liebig Universität Giessen
Feb. 2020

Erstprüfer: Prof. Dr. Christian S. Fischer
Zweitprüfer: Prof. Dr. Lorenz von Smekal

Table of content

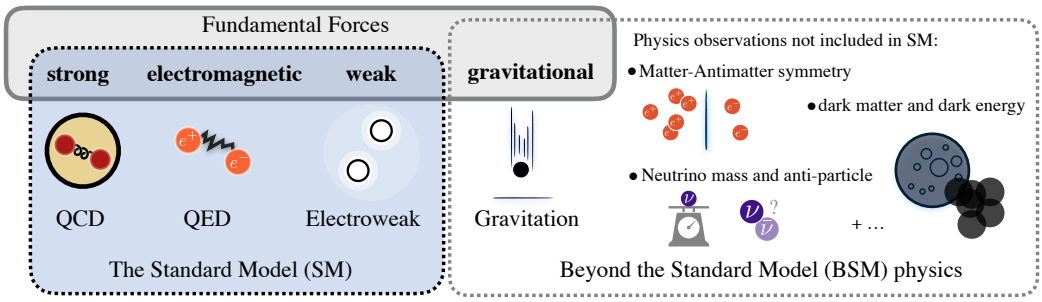

Figure 1: The Standard Model describes the strong, electromagnetic and weak interactions. The right side shows phenomena that are not described by the Standard Model.

1 Introduction

The Standard Model of particle physics and beyond. The Standard Model (SM) of particle physics is a mathematical description of all known particles and their interactions. It includes the effects of the strong, electromagnetic and weak forces as summarized in Fig. 1. With the discovery of the Higgs boson in 2012, by the ATLAS and CMS collaborations using the Large Hadron Collider at CERN, the final piece of the SM has been experimentally verified. This represents a remarkable scientific achievement, as the SM not only describes a wide variety of particle experiments but is also, in its prediction of certain quantities, the most accurate description of nature ever constructed. One striking example is the magnetic moment of the electron, which is theoretically predicted to 10 significant digits and shows excellent agreement with the experimentally determined value.

At the same time, the SM is known to be incomplete and the particle physics community is facing many unanswered questions that require further investigation and will ultimately require an extension or complete modification of the currently accepted paradigm. In order to guide advances in this direction, one of the goals of modern physics is to identify concrete observables that not only give clear evidence of new physics but also provide specific predictions about the nature of the new particles and forces beyond the SM (BSM).

It should be emphasized that, although we do not understand the detailed nature of BSM physics, the evidence that the SM is incomplete is overwhelming. In particular, the following observed phenomena cannot be explained by the fundamental theory in its present formulation:

- **gravity:** This force is not included in the SM and efforts to include it, by introducing the graviton as the force-carrying particle, have so far failed. The problem is that, in many implementations, the theory becomes mathematically ill-defined when the graviton is included. An exception to this is string theory, which does provide a rigorous definition of quantum gravity. But so far this framework has not allowed an inclusion of the remaining particles and forces of the SM.

- **dark matter:** Observations of galaxy rotation and other astronomical processes provide clear evidence that $\sim 26\%$ of the energy present in our universe is so-called "dark matter", which feels the gravitational force but otherwise interacts very weakly. The SM does not contain any fundamental particles that have the properties of dark matter, and the matter that it does describe makes up only 5% of the observed energy budget.

- **dark energy:** The remaining $\sim 69\%$ of the total energy contained in our universe is the so-called "dark energy", which is a constant energy density of the vacuum. Attempts to describe this within the SM disagree with the measured value by many orders of magnitude.

- **matter-antimatter symmetry:** The SM includes a description for anti-matter and suggests that, in the early universe, it was created in equal amounts to normal matter. However, we observe that our universe today is matter dominated. So far there is no mechanism in the SM that can fully account for this imbalance.

- **the strong CP-problem:** This refers to the fact that no experiment involving the strong-interaction has shown a violation of CP-symmetry, i.e. the combination of charge conjugation and parity symmetry. However, the mathematical description of the strong force (Quantum Chromodynamics) predicts that a violation of this symmetry should occur. Particle theorists therefore expect that some mechanism must be forcing it to take on the very small value observed in nature.

- **neutrino masses:** Within the description of the SM, neutrinos are massless particles. However, neutrino oscillation experiments have shown that these particles do in fact carry a non-zero mass. In fact, there are multiple known ways to modify the SM and include neutrino masses, but so far it is not known which approach correctly describes our universe. An issue closely related to this is that it is unknown whether the neutrino is its own anti-particle.

All of these open questions make it an interesting and exciting time for particle physics research. The discrepancy between an experimental measurement and a theoretical prediction based on SM physics is what ultimately could lead to an indication of how to modify the SM. For this reason, it is very important that we continue to refine our mathematical tools, in order to properly extract SM predictions. More specifically, scientists quantify the discrepancies between experiment and theory by some number of standard deviations (σ). Currently, many examples of 2 to 3 σ disagreements exist and have motivated the community to pursue improvements on both the theoretical and experimental side. If such tensions can reach the level of 5 σ, then this is generally accepted as a discovery of BSM effects.

To gain further understanding, new experimental data are needed. Present and future experiments can be roughly divided into two categories: high energy and high precision. The main example of the first type is the Large Hadron Collider (LHC) at CERN. The LHC is currently in its second long shutdown and is being upgraded for a high-luminosity phase, with the first beam expected in the Spring of 2021. As the generation of new data continues, together with the analysis of existing data sets, the coming years offer great potential for new-physics discoveries.

On the other hand as the difficulty and cost of high-energy experiments increases, high precision experiments become increasingly important. A current example in this category is the $g-2$ experiment at Fermilab. This experiment aims to obtain information about BSM physics by measuring the muon's magnetic moment to unprecedented precision and is expected to release new data this year. The experiment is well motivated since muonic $g-2$ is an example of the quantities mentioned above, that currently exhibit a few σ tension. For this reason, the theory community is also working towards lowering the uncertainty on the SM prediction, where non-perturbative effects from QCD currently dominate. Another example of an observable that shows tension is the decay rate for $\pi^0 \to e^+e^-$, which is one of the less frequent decay channels and has shown discrepancies between measurements at KTeV and theoretical predictions.

In order to calculate these kinds of physical observables from the mathematical framework of the SM, one must apply a non-perturbative method. Four types of methods are currently being pursued: effective theories, Lattice QCD, data-driven dispersive methods and functional methods. All of these carry their own advantages and disadvantages, and the choice of approach depends on the observable being considered. In addition, it is beneficial to pursue several paths, in order to get independent theoretical confirmation. The work presented in this thesis is based on the functional approach of the Bethe-Salpeter and Dyson-Schwinger

equations. Working in this framework, results are presented for important inputs in the theory calculation of muonic $g-2$. In addition the rare decay of the neutral pion, $\pi^0 \to e^+e^-$, is determined and compared with experiment.

Structure. This thesis is structured as follows: We begin, in Sec. 2, by laying out the mathematical description of the SM and discussing how to generally calculate the observables relevant in this thesis. The next chapter, Sec. 3, contains a brief historical motivation and general background for a particular observable, the pion transition form factor, relevant for the muonic $g-2$. After this, we dive into the heart of this thesis in Sec. 4, by describing how transition form factors are generally calculated within the DSE-BSE framework. This leads to the main chapter, the numerical results in Sec. 5. This section is divided into the following subsections: results for the pion transition form factor, other electromagnetic decays of the pion as an application of the latter, the η and η' transition form factors, an outlook for the calculation of scalar transition form factors and, finally, the contribution of transition form factors to the hadronic-light-by-light contribution of the muon's anomalous magnetic moment. We conclude with a summary and an outlook in Sec. 6.

2 Formalism

2.1 Basic concepts in QCD

Lagrangian. Many quantum field theories are defined by first introducing the Lagrangian.[1] This contains all fundamental particles of the theory and establishes if and how the particles interact. The Lagrangian of the Standard Model (SM) of particle physics includes interactions for the weak, electromagnetic and the strong forces. Historically, many different models, with their corresponding Lagrangians, have been used to study various field theories and their behavior compared to what we see in nature. For example, chiral-perturbation-theory (χPT) is based on a Lagrangian using composite particles as effective degrees of freedom rather than the known fundamental particles, quarks and gluons. By exploring different forms of theories we obtain a better understanding of how to describe the phenomena we observe in nature.

Let us start by considering the strong force in isolation. Here the relevant theory is quantum chromodynamics (QCD). In QCD the fundamental degrees of freedom are quarks and gluons, which are the only fields present in the Lagrangian density:

$$\mathcal{L}_{\text{QCD}}\left[A,\bar{\psi},\psi\right] = \bar{\psi}\left(\not{D} + \mathsf{m}\right)\psi + \frac{1}{2}\,\text{Tr}[F_{\mu\nu}F_{\mu\nu}]\,. \tag{2.1}$$

Here ψ and $\bar{\psi}$ are the quark and anti-quark fields, respectively, the gluons are represented by the field-strength tensor $F_{\mu\nu}$ and $\mathsf{m} = \text{diag}(m_u, m_d, m_s, \dots)$ is the quark mass matrix for N_f flavors. The covariant derivative is denoted by $D_\mu = \partial_\mu + igA_\mu$ where A_μ is the vector gauge field of the gluon, related to $F_{\mu\nu}$ by $F_{\mu\nu} = \partial_\mu A_\nu - \partial_\nu A_\mu + ig\,[A_\mu, A_\nu]$. The second term in the covariant derivative, D_μ, represents the interaction between quarks and gluons with the coupling constant g.

All of the objects appearing on the right-hand side of Eq. (2.1) carry implicit indices associated with the color charge defining QCD. In particular, the vector fields are 3×3 matrices in this space and are related to eight individual fields by $A_\mu = A^a_\mu\, t^a$ where the t^a are the Gell-Mann matrices, the generators of the QCD gauge group, $SU(3)$. Similarly, the field strength tensor satisfies $F_{\mu\nu} = F^a_{\mu\nu}\, t^a$. This implies that both A^a_μ and $F^a_{\mu\nu}$ are in the adjoint representation of the group. The Gell-Mann matrices satisfy the commutation relation $[t_a, t_b] = i f_{abc}\; t_c$, where f_{abc} are called structure constants. The dimension of the representation used for $SU(3)$ generators can vary and the fact that the Gell-Mann matrices are three dimensional comes from the requirement that quarks transform in the fundamental representation. This means, for example, that an infinitesimal transformation takes the form $\psi_i \to \psi_i + i\alpha^a t^a_{ij}\psi_j$.

The action is obtained by integrating the Lagrangian density over all of spacetime

$$S_{\text{QCD}} = \int d^4x\; \mathcal{L}_{\text{QCD}}\left[A,\bar{\psi},\psi\right]. \tag{2.2}$$

QCD is an $SU(3)$ gauge theory, meaning that action is invariant under the local transformation

$$\begin{aligned}\psi'(x) =& U(x)\psi(x)\,, \quad A'_\mu(x) = U(x)A_\mu(x)U^\dagger(x) - \frac{i}{g}U(x)(\partial_\mu U^\dagger(x))\,, \\ & F^{\mu\nu\prime}(x) = U(x)F^{\mu\nu}(x)U^\dagger(x)\,,\end{aligned} \tag{2.3}$$

where $U(x) \in SU(3)$. The physical interpretation of this is that the quark fields carry a color charge in analogy to the electric charge of protons and electrons. Just as every positron or

[1] Strictly speaking theories exist without a Lagrangian but this is a highly mathematical topic not relevant for this work.

electron has a charge of plus or minus one, every quark has a color charge of red, green or blue.[1]

Renormalization. In QFT, one encounters short-distance fluctuations that complicate the calculations of observables by introducing infinities. However as physics at short and long distances decouples, we can solve this problem by modifying the theory at short distances to get a finite answer. This is called regularization. To be certain that this does not affect the final results we need a way to vary the regularization without changing the observables. This is called renormalization.

The Lagrangian and the action were defined above in terms of bare fields. Their renormalized counterparts are related through renormalization constants for the fields, the masses, and the coupling constant,

$$\psi = Z_2^{1/2}\psi_r\,, \quad A = Z_3^{1/2}A_r\,, \quad \mathsf{m} = Z_m\mathsf{m}_r\,, \quad g = Z_g g_r\,. \tag{2.4}$$

The renormalized fields will be used in all calculations throughout this thesis, but the subscript will be suppressed from Sec. 4 on.

To give some insight into these ideas, we consider the scenario of two theorists independently calculating the proton mass in $N_f = 2$ QCD. Suppose each theorist has a non-perturbative method but they make different choices in the regularization, e.g. different values for the ultraviolet cutoff on divergent integrals. Each theorist renormalizes (chooses the values of the Z factors) to get the correct results for the pion mass and decay constant. This fixes all inputs so that a prediction for the proton mass can be made. Even though different choices were made for *regularization* the differences are compensated by the *renormalization* so that the same value is predicted. The fact that such predictions must agree is a highly non-trivial property of QCD and the Standard Model called *renormalizability*. The general criteria for a renormalizable QFT is explained in [1–3].

Green functions and generating functionals. To calculate physical observables like bound-state masses or decay-rates, we need to consider the most fundamental mathematical tool that provides us access to these quantities: the Green functions of the theory. These encode all possible interactions between n incoming and m outgoing particles. One naturally forms the position-space Green functions (this follows more directly from the position space Lagrangian density) and by applying a Fourier transform to momentum space and taking the limit to put the particles on their mass-shell, one can calculate physical observables such as scattering amplitudes.

Green functions can be defined in two different ways. One approach is to express the functions in terms of time ordered products of the field operators. This is the canonical formalism, in which the fields are treated as operators in the Fock space and obey canonical (anti-)commutator relations. In the second approach, the Green function is defined through a path-integral which runs over all possible field values at every point in spacetime. In this approach, the fields are commuting functions of space-time coordinates, not operators. Let $\varphi(x)$ abbreviate the general fields. The Green function, $G[\varphi(x)]$, is defined as

$$\langle G[\varphi(x)]\rangle := \langle 0|\mathsf{T}\, G[\varphi(x)]|0\rangle = \frac{\int \mathcal{D}\varphi\, e^{-S[\varphi]}\, G[\varphi(x)]}{\int \mathcal{D}\varphi\; e^{-S[\varphi]}}\,, \tag{2.5}$$

where the middle expression refers to the operator formalism and the right-most to the path integral.

[1] The first indication that the number of possible colors is exactly three followed from observing the decay rate of the neutral pion into two photons and its relation to the axial anomaly, as discussed in Sec. 4.

A useful tool to calculate Green functions is the **generating functional** or partition function. This corresponds to the definition of the path-integral with an additional source term introduced into the Lagrangian. It can be understood as a trick to express Eq. (2.5) in yet another way. Each field gets multiplied with a corresponding source and summing this product over all fields in the theory defines a shift to the Lagrangian density. The generating functional reads,

$$Z[J] = \int \mathcal{D}\varphi \; e^{-\left(S[\varphi] - \int_x \varphi(x) J(x)\right)} \,. \tag{2.6}$$

The Green functions are then obtained by taking functional derivatives with respect to the sources J and setting them to zero after differentiation,

$$\langle G[\varphi(x)] \rangle = G\left[\frac{\delta}{\delta J}\right] \frac{Z[J]}{Z[0]}\bigg|_{J=0} \,. \tag{2.7}$$

In general, the functional derivative is defined through,

$$\frac{\delta\varphi(x)}{\delta\varphi(y)} = \delta^4(x-y) \qquad \Leftarrow \qquad \varphi(y) = \int d^4x \, \delta(x-y)\varphi(x) \,. \tag{2.8}$$

To understand the concept, consider for example the correlation function for two fields, one at position x_1 and one at x_2, which is given by

$$G(x_1, x_2) = \langle 0 | \mathsf{T}\, \varphi(x_1)\varphi(x_2) | 0 \rangle = \frac{\int \mathcal{D}\varphi \; e^{-S[\varphi]} \; \varphi(x_1)\varphi(x_2)}{\int \mathcal{D}\varphi \; e^{-S[\varphi]}} = \frac{1}{Z[0]} \; \frac{\delta}{\delta J(x_1)} \frac{\delta}{\delta J(x_2)} \; Z[J]\bigg|_{J=0} \,. \tag{2.9}$$

The generating functional introduced above, Eq. (2.6), generates full Green functions. These contain all possible interactions. In a diagrammatic sense these are represented by all possible diagrams that one can draw based on the interaction specified in the Lagrangian and the involved incoming and outgoing particles, specified by the Green function. The diagrammatic representation is an intuitive way to visualize and order the contributions for chosen physical process. Each *Feynman diagram* stands for a particular number, or a function of external parameters, and can be calculated using *Feynman rules*.

Besides the full Green functions, it can be useful to define alternative Green functions built using only a subset of the Feynman diagrams. For example, if one keeps only the set of fully connected diagrams, this defines the connected Green function which is directly related to the scattering amplitude. Similarly, one can define a new function by including all Feynman diagrams that stay connected even after a single line is cut. These are called one-particle irreducible (1-PI) diagrams.

Studying the mathematical relations between these different types of functions can teach us a great deal about the theory. Remarkably, it is possible to define a new generating functional, called $W[J]$, that directly provides connected Green functions. This satisfies a simple relation to the original functional, related through $W[J] := \ln(Z[J])$. The so called effective action $\Gamma(\tilde{\varphi})$, is the functional for the (1-PI) Green functions and is related to $W[J]$ through a Legendre transformation,

$$Z[J] = e^{W[J]} = e^{(\Gamma[\tilde{\varphi}] + \int_x \tilde{\varphi}(x) J(x))} \,, \quad \Gamma(\tilde{\varphi}) = -\ln\left(Z[J]\right) - J\tilde{\varphi} \,. \tag{2.10}$$

The effective action depends on the averaged field $\tilde{\varphi}$, which is the expectation value of φ in presence of an external source J,

$$\tilde{\varphi}(x) := \langle \varphi(x) \rangle_J = -\frac{\delta W[J]}{\delta J(x)} = \frac{\int \mathcal{D}\,\varphi \, e^{-S[\varphi] + \int_x \varphi(x) J(x)} \, \varphi(x)}{\int \mathcal{D}\,\varphi \, e^{-S[\varphi] + \int_x \varphi(x) J(x)}} \,. \tag{2.11}$$

This idea generalizes to n-PI Green functions, which are composed of diagrams that stay connected when any n lines are cut.

The Dyson-Schwinger equations (DSE) are derived directly from the effective action introduced above and are a key ingredient to calculating QCD observables in the functional approach. They provide a relation between n- and $n+1$-point Green functions, which can be interpreted diagrammatically as regrouping the information into different sub-sets of the original correlation functions/Feynman diagrams. They form an infinite coupled set of iterative integral equations and, in order to numerically solve them, approximations at the level of the $n+1$ Green functions are necessary. A thorough discussion will follow in Sec. 2.4.1.

Flavor symmetries. By understanding symmetry structures of the underlying theory, we can learn a great deal about its phenomenology. In particular, by examining the approximate global flavor symmetries of the QCD Lagrangian, we can understand various properties of the hadrons seen in nature. In the case of QCD with massless quarks, the global symmetry group is $U(1)_V \otimes U(1)_A \otimes SU(N_f)_V \otimes SU(N_f)_A$ and in the full quantum theory the various subgroups have very different consequences. For example, the $SU(N_f)_V$ symmetry leads to the multiplet structures of the hadrons. By analogy one would expect the $SU(N_f)_A$ symmetry to lead to similar patterns, relating the positive and negative parity states. This, however, is not observed. The reason is that the symmetry is spontaneously broken, meaning that the vacuum is not invariant. The $U(1)_A$ symmetry is also violated, not due to spontaneous breaking, but another effect referred to as the anomaly. This explains the large mass difference between the π and the η, which would otherwise be nearly degenerate. In fact, in the presence of electromagnetism, the $SU(N_f)_A$ is also anomalously broken. This is of particular interest for the neutral pion decay ($\pi^0 \to \gamma\gamma$), as we will explore in more detail in Sec. 3.1. As is clear from this short summary, the consequences of symmetries and symmetry breaking are complicated. The purpose of this subsection is to explore this in some detail.

Noethers theorem states the following: Any continuous (global or local) symmetry transformation, which leaves the action invariant, implies the existence of a conserved current when the equations of motion are satisfied.

Let us consider a continuous global transformation defined as $U = e^{i\theta_a t_a}$ where the t_a are matrices, referred to as generators of the symmetry group. Without loss of generality we can take the θ_a to be infinitesimal, implying $U = 1 + i\theta_a t_a$. Then the fields transform as $\psi' := U\psi = \psi + i\theta_a t_a \psi := \psi + \delta\psi$. We consider a Lagrangian $\mathcal{L}$ which is invariant under the transformation U. This implies $\delta\mathcal{L} = 0$, where we have defined

$$\delta\mathcal{L} := \mathcal{L}(\psi', \partial_\mu\psi') - \mathcal{L}(\psi, \partial_\mu\psi) = \frac{\partial\mathcal{L}}{\partial\psi}\delta\psi + \frac{\partial\mathcal{L}}{\partial(\partial_\mu\psi)}(\partial_\mu\delta\psi)\,. \tag{2.12}$$

We now use the product rule to rewrite $\delta\mathcal{L}$ as

$$\delta\mathcal{L} = \partial_\mu \underbrace{\left(\frac{\partial\mathcal{L}}{\partial(\partial_\mu\psi)} i t_a \psi\right)}_{=:\, j_a^\mu} \theta_a + \left(\frac{\partial\mathcal{L}}{\partial\psi} - \partial_\mu \frac{\partial\mathcal{L}}{\partial(\partial_\mu\psi)}\right)\delta\psi\,. \tag{2.13}$$

As we have indicated, the first term defines the current j_a^μ and the second term is the Euler-Lagrange term, which vanishes when the equations of motion are fulfilled. This result tells us that when $\delta\mathcal{L} = 0$ (due to the symmetry) and the Euler-Lagrange term also vanishes (due to the equations of motion), then

$$\partial_\mu\, j_a^\mu = 0\,. \tag{2.14}$$

In this case, j_a^μ is a **conserved current**. Note that a current can also be considered approximately conserved if the change in the Lagrangian is small. If we integrate Eq. (2.14) over

$\int d^3x$ and apply Gauss' law we can write

$$\int d^3x \left[\partial_t j_a^0(x) - \partial_i j^i(x)\right] = \int d^3x \left[\partial_t j_a^0(x)\right] - \int d\vec{\sigma} \cdot \vec{j}(x) = 0\,. \tag{2.15}$$

If we then assume that $\vec{j}$ vanishes at the boundary, then we find

$$\partial_t \int d^3x j_a^0(x) = 0 \quad \Longrightarrow \quad Q_a(t) = \int d^3x \; j_a^0(x) = \text{const}\,. \tag{2.16}$$

In words, we have found that the charge, Q_a, is conserved. On the quantum level the charge is an operator, due to the fields being operators too. The charge satisfies the same commutator relation as the group generators, t_a, which reads $\left[Q^a, Q^b\right] = f_{abc}\, Q^c$. This forms a representation of the Lie algebra on the Hilbert space, referred to as the charge algebra. Historically it was one of the first tools to encode symmetry structures of the theory, followed by the effective action, as will be discussed in sec. 2.4.3.

As already summarized at the beginning of this subsection, a symmetry can be broken due to different reasons. We differentiate between **explicit** or classical, **anomalous** and **spontaneous** breaking.

Explicit breaking of the symmetry happens when the action is not invariant. In this case, we can still define a current and the corresponding charge, they just will not be conserved. In general, the concept of non-conserved currents is a helpful tool for both classical and quantum field theories. For example, isospin symmetry is explicitly broken by the difference in the up and down mass. However, it still serves as a useful label both for describing transitions where isospin is conserved and those where it is violated. The example of isospin is also a case of interest because the breaking is small, and thus the charge is approximately conserved. The small difference between the up and down quark masses, and the small value of the electromagnetic coupling, leads to the approximate conservation of the isospin current.

Anomalous breaking happens on the quantum level. When the theory is quantized, ultraviolet diverges arise and a scheme, referred to as regularization, must be used to remove these and give finite answers. In certain circumstances, it is impossible to find a regularization that preserves the symmetries of the classical theory. The interpretation here is that quantum fluctuations actually break the symmetry. In other words, a symmetry leaving the action invariant might still be broken at the level of the path-integral, through the non-invariant integration measure. As with explicit breaking, when anomalous breaking occurs the current is no longer conserved.

Anomalies of local symmetries are called gauge anomalies. These violate unitary, as they introduce unphysical longitudinal polarizations. As a result, a theory with such an anomaly is not well defined and cannot be a useful description of nature. On the other hand, anomalies in global symmetries do not lead to inconsistencies. In fact, this kind of symmetry breaking is realized in the Standard Model and understanding this was crucial to solving historical puzzles about the properties of hadrons.

Two cases of anomalous breaking are the $U(1)_A$ and the $SU(N_f)_A$ anomalies. The latter plays an important role for the decay of the neutral pion ($\pi^0 \to \gamma\gamma$). The $U(1)_A$ anomaly is the reason why the η' meson is so heavy. This anomaly is a pure QCD phenomenon, whereas the $SU(N_f)_A$ anomaly is introduced by the QED part of the Lagrangian.

If a symmetry is classically realized, the action is invariant. If a symmetry leaves the vacuum invariant, then all group generators t_a must annihilate the vacuum, such that $Q_a|\Omega\rangle = 0$. **Spontaneous** breaking occurs when the vacuum carries the charge corresponding to a symmetry and is not invariant, $Q_a|\Omega\rangle \neq 0$. In this case, the ground-state and Green functions

no longer share the global symmetry of the action. In contrast to anomalous breaking, with spontaneous breaking, the current is still conserved.

Goldstone's theorems states that spontaneous breaking of continuous global symmetries implies the existence of massless particles. Each generator that does not leave the vacuum invariant corresponds to a massless Goldstone Boson.

The QCD example for spontaneous breaking is **chiral symmetry**. To understand this, consider the quark-field dependent part of the Lagrangian in the chiral limit, meaning all quark masses are set to zero ($\mathsf{m} = 0$)

$$\mathcal{L} \supset \bar{\psi}_i \not{D} \delta_{ij} \psi_j \,, \tag{2.17}$$

where we have shown the flavor indices. Because the matrix between $\bar{\psi}_i$ and ψ_j is the identity in flavor, the Lagrangian does not change if we replace $\psi \longrightarrow U\psi$ and $\bar{\psi}_i \to \bar{\psi}_i U^\dagger$, where $U \in SU(N_f)_V$.

It is useful to reformulate the Lagrangian using left- and right-handed spinors, $\psi_{R/L} = \frac{1}{2}(1 \pm \gamma_5)\psi$

$$\mathcal{L} \supset \bar{\psi}_{R,i} \not{D} \delta_{ij} \psi_{R,j} + \bar{\psi}_{L,i} \not{D} \delta_{ij} \psi_{L,j} \,. \tag{2.18}$$

We see that $\mathcal{L}$ has a larger symmetry, called chiral symmetry, and denoted $SU(N_f)_R \times SU(N_f)_L$. The vector part is the diagonal subgroup of this product, which rotates left- and right-handed fields in the same way. On the contrary the axial part corresponds to rotating right and left in opposite directions. We thus have $SU(N_f)_R \times SU(N_f)_L = SU(N_f)_V \times SU(N_f)_A$. The axial part of the symmetry, $SU(N_f)_A$, is spontaneously broken.

In the case of $N_f = 3$, $SU(N_f)_A$, has eight generators. These correspond to eight Goldstone bosons, which are the eight lightest pseudoscalar mesons (the pions, kaons and the eta). In the case of $N_f = 2$ this reduces to the three pions, corresponding to the three generators of $SU(2)_A$ usually chosen to be the Pauli-matrices. Even though chiral symmetry is only an approximate symmetry, it helps to explain the unnaturally light mass of the pion due to its Goldstone-boson nature.

Tab. 2 shows an overview of the global flavor symmetries. For low-energy processes such as those considered in this thesis, one typically takes $N_f = 3$ (for the up, down and strange quarks). Furthermore, we work in the so-called isospin limit, where the up and down quark masses are degenerate. For each symmetry, the table contains information about the corresponding transformations U, if and when the transformation leaves the Lagrangian invariant ($\Delta\mathcal{L}$), as well as a statement of current conservation ($\partial_\mu J_\mu$) and the (conserved) charge Q_a. Here ψ is the quark field, A^a_μ the gluon field, as introduced in the Lagrangian, M is the quark mass matrix and $F^a_{\alpha\beta}$ is the field strength tensor of the gluon. Similarly, we denote by $F_{\alpha\beta}$ the field strength tensor of the photon, which enters when we consider the combined QED and QCD Lagrangian. We also define g as the strong coupling constant, e as the electromagnetic coupling constant and γ_μ for the gamma (Dirac) matrices. These are a set of conventional matrices defined with specific anti-commutation relations. The gamma matrices (γ^μ, $\mu \in \{0, 1, 2, 3, 5\}$) allow us to combine quark fields into Lorentz vectors. This is an important tool, as vector-like objects are observed in nature, but in the context of constructing the Lagrangian we can combine γ^μ with ∂_μ to form a Lorentz invariant.

Starting at the top of Tab. 2, we have:

- $U(1)_V$

  This is the only exact symmetry of the theory and we can define a conserved vector current, $V_\mu = \bar{\psi}\gamma_\mu\psi$, as well as a conserved charge, B, which reflects the baryon-number conservation. This counts the difference between the number of quarks and anti-quarks,

sym.	U	$\Delta\mathcal{L}$	(conserved) current j^μ_a	(conserved) charge Q_a
$U(1)_V$	$e^{i\theta}$	$=0$	$\partial^\mu J_\mu = 0 \qquad J_\mu = \bar{\psi}\gamma_\mu\psi$	• Baryon number $B = \frac{1}{3}\int d^3x\ \psi^\dagger\psi$
$U(1)_A$	$e^{i\gamma_5\theta}$	$\neq 0$ explicit if $M\neq 0$ + anomalous	$\partial^\mu J^5_\mu = 2i\bar{\psi}M\gamma_5\psi - \frac{g^2 N_f}{32\pi^2}\varepsilon^{\alpha\beta\mu\nu}F^a_{\alpha\beta}F^a_{\mu\nu}$	• No conserved charge!
$SU(N_f)_V$	$e^{i\theta^a t^a}$	$=0$ if a = 3,8 or $M = m\mathbb{1}$	$\partial^\mu J^a_\mu = i\bar{\psi}\,[t_a, M]\,\psi$	• Isospin: a=3 and Hypercharge: a=8 $Q^V_a = \int d^3x\ \psi^\dagger t_a\psi$
$SU(N_f)_A$ QED+ QCD	$e^{i\theta^a t^a\gamma_5}$	$\neq 0$ explicit if $M\neq 0$ + spontaneous + anomalous	$\partial^\mu J^{a5}_\mu = i\bar{\psi}\gamma_5\{t_a, M\}\psi$ $-t_a Q^2\frac{e^2}{16\pi^2}\varepsilon^{\alpha\beta\mu\nu}F_{\alpha\beta}F_{\mu\nu}$	• Axial charges in chiral limit $Q^A_a = \int d^3x\ \psi^\dagger\gamma_5 t_a\psi$

QCD QED = axial anomalies

Figure 2: Overview of QCD flavor symmetries: $U(1)_V \otimes U(1)_A \otimes SU(N_f)_V \otimes SU(N_f)_A$, where N_f is the number of flavors. The table shows their associated transformations, currents and conversations.

divided by three, and is zero for mesons, one for baryons, and takes on higher values for multi-baryon systems.[1]

- $U(1)_A$

  The mass matrix term in the Lagrangian breaks this symmetry explicitly. However, in the chiral limit ($M = 0$) it is classically conserved. More interestingly, it is anomalously broken due to the non-invariance of the integration measure. In Tab. 2, the anomaly term is indicated in light orange. The $U(1)_A$ anomaly has consequences for the masses of the η and η' mesons.

- $SU(N_f)_V$

  In QCD with $N_f = 3$ flavors, the generators, t_a, of $SU(3)_V$ are the eight Gell-Mann matrices ($a \in \{1, \cdots, 8\}$). The flavor vector symmetry is explicitly broken by unequal quark masses in the mass matrix ($M \neq m\mathbb{1}$), but conserved in the degenerate limit. Furthermore, the transformation with the third and the eighth generators leave the action invariant and define a true symmetry for two $U(1)$ subgroups of $SU(3)_V$. In these cases, one can define conserved charges. For $a = 3$ this corresponds to the isospin charge ($Q^V_3 =: I_3$), for $a = 8$ the hyper-charge ($Q^V_8 =: Y$). These are useful quantum numbers for characterizing hadrons, eg. the meson multiplet is a hexagon in the $(I_3 - Y)$-plane.

- $SU(N_f)_A$

  The axial vector symmetry is broken explicitly, spontaneously and anomalously. Explicit breaking occurs once more due to the mass term in the Lagrangian ($M \neq 0$). Away from the chiral limit the corresponding axial-vector current and the divergence, given

[1] In the complete Standard Model, including weak iterations, baryon number is anonymously by quantum effects from the weak part of the path-integral measure.

in the table, read

$$j^{\mu}_{a\,5}(x) := \bar{\psi}(x)\,\gamma_5\gamma^{\mu}t_a\,\psi(x)\,, \quad \partial^{\mu}\,j^{\mu}_{5\,a} = i\bar{\psi}\,\gamma_5\{t_a, M\}\psi \xrightarrow{M=m\mathbb{1}} 2im\,\bar{\psi}\gamma_5 t_a\psi\,, \tag{2.19}$$

where here we are suppressing the anomaly term in the divergence. For equal quark masses and solely considering QCD effects, the divergence simplifies into the so-called **partially conserved axial-vector current** (PCAC) relation. Partially, as the current would be conserved in the chiral limit when $m = 0$. The expression on the right can be identified as a pseudo-scalar density ($j_{5\,a}(x) := \bar{\psi}(x)i\gamma_5 t_a\psi(x)$). Thus, the PCAC relation tells us that the divergence of the axial-vector is related to a pseudo-scalar density. The relation carries multiple consequences which will be explored in later sections (4.1-4.2).

Anomalous breaking enters when considering QED + QCD and comes from an invariance of the measure, similar to the $U(1)_A$ case, but from the QED part. In Tab. 2, the QED axial anomaly is highlighted in light red. This anomaly plays an important role in the calculation of the neutral pion decay rate ($\pi^0 \to \gamma\gamma$), as the result is dominated by anomaly effects. (A detailed discussion follows in section 3.1.) In comparison to the $U(1)_A$ gluon anomaly, the QED anomaly effects are numerically much smaller due to the difference in the coupling strength ($e \ll g$) but are not less important.

Finally, spontaneous breaking of $SU(3)_A$ is a dynamical and non-perturbative effect based on the strong interactions between quarks and gluons. It is visible through Green functions containing external quark and anti-quark legs, as these do not share the symmetry of QCDs action, due to non-perturbatively generated tensor structures. The topic will be further explored in the context of the quark propagator in Sec. 4.1.

2.2 Multi-hadron processes

Form factors are an essential set of quantities in the broad landscape of particle physics observables. Describing the coupling of photons, and other electroweak currents, to all possible hadrons, they contain valuable information about the underlying structure of QCD bound states. The coupling of a non-composite particle to a current is given by a simple coupling constant (e.g. the electron-photon coupling e is related to the fine-structure constant $\alpha_e = e^2/(4\pi) \sim 1/137$). In the case of a hadron, however, this constant becomes a momentum-dependent function, carrying information about the charge distribution of the probed hadron.

One of the main goals in theoretical particle physics today is to calculate physical observables that are measured in experiment and test whether the theory correctly describes the measured results. Going beyond this, theoretical physicists aim to provide predictions for ongoing and future experiments and to guide their interpretation. Interesting discrepancies have been discovered over the years, such as in the anomalous magnetic moment of the muon, as discussed in detail in section 3.2. In the following, the aim is to give a brief overview of physical observables, involving both single- and multi-particle states, possibly coupled to external currents. In doing so I will also make some general comments about the current theoretical situation and how the objectives of this thesis fit within the broader picture.

To gain an overview, it is useful to classify physical observables by the number of particles involved, as well as the number (and the nature) of the external currents. This organization is summarized in Fig 3. Here the horizontal axis represents the number of currents, whereas the vertical axis classifies the types of external states. For the latter we distinguish between three choices: (1) at least one of the states is the QCD vacuum, denoted $|\Omega\rangle$, (2) initial and final state are the same one-particle state and (3) the initial and final states may or may not match, but at least one is a multi-particle state. We now go through the three columns

in turns, to examine how the external currents couple to the states define the extracted observable.

In case of no currents (first column), we are dealing with an observable that is solely described by interactions through the strong force (QCD). This can only provide non-trivial information if the states are different (otherwise we only accesses a normalization factor) and have a nonzero overlap (e.g. $\langle\Omega|\pi\rangle = 0$). It turns out that this is only possible for multi-particle states, so that only the bottom row of the first column offers a non-trivial entry. This leads us to define the **scattering amplitude**, denoted $\mathcal{M}_{n\to m}$, which describes interactions between n incoming and m outgoing particles, in the presence of only QCD. The definition reads

$$i\mathcal{M}_{n\to m}(p_1,\cdots,p_n|p'_1,\cdots,p'_m)\times(2\pi)^4\delta^4\Big(\sum_i p_i-\sum_j p'_j\Big)=\langle m,\text{out}|n,\text{in}\rangle_{\text{connected}}\,, \quad (2.20)$$

where the label "connected" means that we only keep contributions with all particles involved in the scattering event. In short, the scattering amplitude is a pure QCD quantity, describing the interaction through the strong force in isolation.

Various tools are available to predict scattering amplitudes theoretically. For example, effective field theories, such as chiral perturbation theory, provide a low-energy description based on approximate symmetries of the underlying theory. This gives important basic knowledge, e.g. about the low-energy scattering of pions, but the approach generally breaks down as the scattering energy is increased. Numerical lattice QCD is also a powerful tool, somewhat surprisingly given that calculations are restricted to a finite volume and to Euclidean time. However, these challenges have been at least partially overcome leading to a variety of amplitude predictions, see Ref. [4]. The DSE and BSE framework has been able to provide results on various observables in this context, ranging from simple bound states, such as mesons and baryons, see Refs. [5–7], to more complex structures, like tetra-quarks (a four-quark bound-state) [8], Hybrids (bound-state with external gluon) [9], or glueballs (pure gluon bound-sates) [10, 11].

Returning again to Fig 3, we now focus on the second and third columns, describing cases in which external currents are involved. This allows us to further take electromagnetic (QED) and weak forces into account.[1] The simplest example, appearing at the top of the second column, is the **decay constant**. This describes the decay amplitude of a particle going into a non-QCD final state. It is given by a one-particle initial state, coupling via a single current to the vacuum. For example the pion decay constant, f_π, is given by

$$\langle 0|\Gamma^\mu_{0\,5}|\pi,p\rangle = i f_\pi p_\mu\,, \quad (2.21)$$

with the axial current defined as $\Gamma^\mu_{0\,5} = \bar{q}\gamma^\mu\gamma_5 q$.

Moving down the second column brings us to form factors. As shown in the figure, a **form factor** describes the coupling of a hadron to a single current. For electromagnetic currents the initial and final states must be the same single-particle state, as the quark flavors cannot be changed by the intermediate photon. Here the simplest example is the pion form factor, denoted F_π and defined via

$$\langle\pi,p'|j_\mu|\pi,p\rangle = (p+p')_\mu\; F_\pi(-(p+p')^2)\,. \quad (2.22)$$

The form factor describes the underlying charge structure of the particle. As mentioned above, if it were elementary and had no substructure, the corresponding form factor would be

[1] At high energy scales the electromagnetic and weak forces are unified into the electroweak. However, in the case of QCD matrix elements, one is necessarily looking at low energy scales where the forces act independently and are described by independent currents.

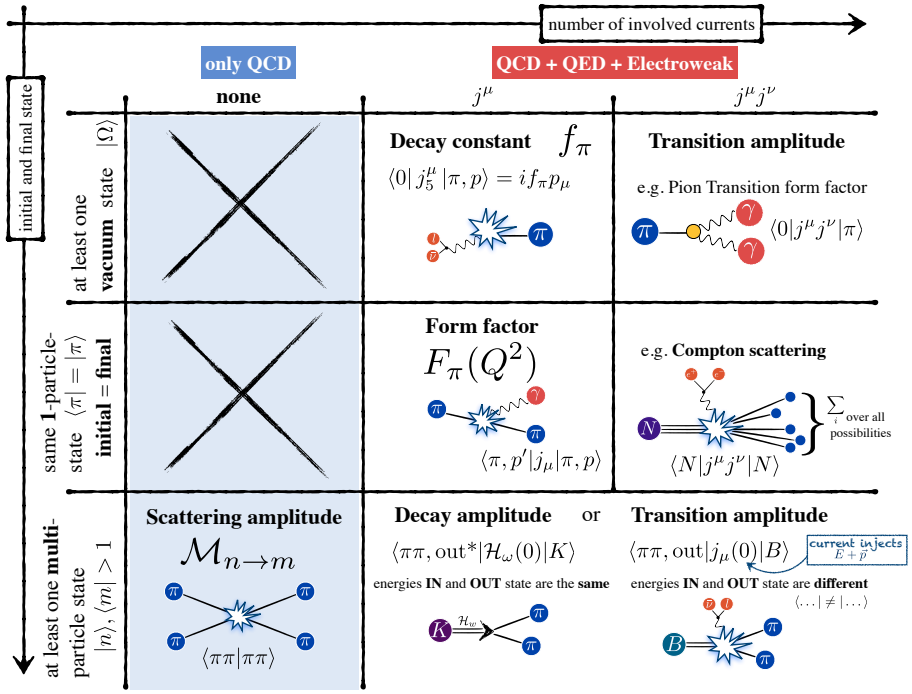

Figure 3: Comparison of different multi-state observables. The x-axis represents the number of involved currents and in case of none we consider pure QCD observables. The y-axis corresponds to different choices for initial and final state in the matrix element.

constant. The decomposition on the right-hand side in Eq. 2.22 follows from the fact that the matrix element must fulfill the transversality criteria $[(p-p')_\mu \langle j^\mu\rangle = 0]$ demanded by vector current conservation ($\partial^\mu j_\mu = 0$).

We will discuss the transition and decay amplitudes, appearing in the bottom right of Fig. 3, in the following paragraph. Before doing so, we now briefly move to the third and final column to explore the role of multiple external currents in matrix elements. Following the established pattern, we first consider the transition from hadron to vacuum, indicated in the upper right corner. In the two-current case, this describes multi-photon decays of hadrons, e.g. $\pi^0 \to \gamma\gamma$, defined by

$$\langle 0|j^\mu j^\nu|\pi\rangle = \varepsilon^{\mu\nu\alpha\beta}\; Q^\alpha Q'^\beta F_\pi(Q^2, Q'^2)\,. \tag{2.23}$$

This class of processes (**transition matrix elements**) is the main focus of this work and will be discussed in great detail in the following sections (3, 4, 5.1). For completeness, we also mention the case of incoming and outgoing hadrons coupled to two external currents. This describes **Compton scattering** and is crucial for unlocking richer hadronic structural information, generally referred to as distribution functions. This goes well beyond the scope of this work and we point the reader to Refs. [12, 13] for more information.

We close our tour of Fig. 3 by considering **decay** and **transition amplitudes**, both characterized by the coupling of an incoming hadron to a multi-particle final state and to at least one external current. The distinction in the term "decay" and "transition" arises from the intermediate current. In case of the decay amplitude, the current does not inject energy or momentum into the system. An example is the weak decay of the kaon: $K \to \pi\pi$, described by the matrix element $\langle \pi\pi, \text{out}|\mathcal{H}_W(0)|K\rangle$. By contrast, in a transition amplitude, the current does inject energy-momentum, corresponding to non-QCD particles adding energy or removing it from the system. An example here is the process $B \to \pi\pi\bar{\nu}l$, encoded in the matrix element $\langle \pi\pi, \text{out}|j_\mu(0)|B\rangle$.

2.3 Non-perturbative physics

So far we have established that the Green functions of our quantum field theory (QFT) encode the physical observables. We have furthermore indicated that Feynman rules are a useful tool to calculate a chosen Green function, by representing mathematical expressions intuitively using diagrams. The allowed propagators and vertices are based on the interactions specified in the Lagrangian.

In a theory with only one type of interaction vertex, such as QED, a natural way to order these diagrams, based on an underlying hierarchy, is to count the number of vertices. This corresponds to a series in powers of the coupling constant. Perturbation theory is based on this expansion and is applicable when the coupling constant is small. Consider the QED Lagrangian with the electromagnetic coupling constant e,

$$\mathcal{L}_{\mathrm{QED}} = \bar{\psi}\left(\not{\partial} + m\right)\psi + ie\bar{\psi}\not{A}\psi + \frac{1}{4}F_{\mu\nu}F_{\mu\nu}\,, \tag{2.24}$$

where A^μ is the $U(1)$-gauge field for the photon, $F^{\mu\nu}$ is the field strength tensor of the photon and $e = \sqrt{4\pi\alpha}$ is related to the fine-structure constant $\alpha^{-1} \approx 137$. Thus, $e \approx 0.3$ has a value smaller than one, making it the perfect expansion parameter.

To explore subtle details about this type of expansion, consider the simple function $f(x) = 1/(1-x)$. We can expand it into a series for small values of x, which leads to $1/(1-x) = (1 + x + x^2 + x^3 + \cdots)$. The series is convergent for $x < 1$ and divergent if $x > 1$. In comparison, the series one obtains for the expansion of a QFT Green function is not *convergent* but instead *asymptotically divergent*. Unlike the series of $f(x)$ the expansion carries growing coefficients (eg. $G(e) \approx 1 + 2!(e) + 3!(e)^2 + 4!(e)^3 + \cdots$), corresponding to the numbers of diagrams that one can draw for each powers in e. The amount of possible diagrams grows with each extra power of the coupling constant and thus the coefficients multiplying the powers grow factorially.

The consequence of this is that, if the coupling is small, one can calculate up to some finite order to get an estimate for the Green function. But no matter what, at some higher order the terms get bigger and the calculation must stop. As the QED coupling constant is small ($e < 1$), the series can be calculated up to a very high order ($\sim \mathcal{O}(\alpha^{137})$). After this point, higher order terms are bigger than previous terms. However since one is able to calculate up to such high orders, the QED expansion could in principle give predictions that are precise to the $\sim$ 300th digit.

What happens for Green functions in QCD? In the context of the QCD Lagrangian, Eq. (2.1), we introduced the strong coupling constant g, which quantifies the interaction between quarks and gluons. When considering QCD at all scales, this coupling "constant" is in fact not constant but an energy-dependent function refereed to as QCD's *running coupling*. The coupling decreases as energy is increased, such that it is small for high-energy processes but very large for low energies. This phenomenon is known as asymptotic freedom. At the scale of hadrons the coupling constant is large, and thus principles of perturbation theory do not work.

As the perturbative evaluation fails, one needs to calculate the correlation functions non-perturbatively. This is a highly non-trivial task and a wide landscape of methods trying to deal with the associated difficulties has been developed over the last few decades. Over time, the most prominent methods have shown great success in reproducing experimental data for a wide range of physical observables. In the context of this thesis, I will discuss three of these methods. I will mainly focus on the Dyson-Schwinger equations, presenting results of my own work using this functional method. I will compare the results to those from two other techniques, lattice QCD and the data-driven dispersion relation.

Dyson-Schwinger framework is considered a functional method to calculate QCD observables. The basic concept of the Dyson-Schwinger equation (DSE) and Bethe-Salpeter equation (BSE) approach is to calculate n-point Green functions by solving coupled integral equations. These equations connect different orders of Green functions in a hierarchical way and are derived by taking functional derivatives of generating functionals, such as $Z[J]$ defined in Eq. (2.10). The equations are exact, as they are non-perturbative by construction. In practice, however, as they form an infinite tower of coupled integral equations, they need to be truncated to enable numerical evaluations. The demand for truncation introduces a modeling component to the approach. Nonetheless, it has been shown over the last twenty-five years, that even with the uncertainties due to the truncation, the approach has been able to confirm and explain experimental measurements (See e.g. Ref. [5] for detailed review) and therefore provides a powerful tool for obtaining *ab initio* results for QCD observables with relatively moderate computational effort. It will be introduced in detail in the following section 2.4.

Functional renormalization group is another approach in the functional methods category. The idea here is to introduce an infrared momentum cutoff (regulator) into the effective action and study the changes when varying the cutoff scale. Ultimately the cutoff is sent to infinity recovering the true physical situation. The regulator suppresses the IR modes and makes the generating functional a scale-dependent function. Similar to the DSE approach, one then derives a coupled set of equations by taking further derivatives of the effective action with respect to fields. For the FRG approach, those turn out to be differential equations rather than integral equations used in the DSE framework. This also leads to a set of coupled equations relating various Green functions to another. Facing similar difficulties as in the DSE approach (such as the infinite tower of coupled equations), the FRG directly approximates the effective action with an ansatz motivated by the quark-meson model. Despite many similarities, the methods are quite different in their detailed construction. A full explanation of the functional renormalization group goes beyond the scope of this thesis. An introduction and overview on the topic can be found in Refs. [14–18]. Ref. [17] is a short introduction based on lecture notes in contrast Ref. [16] is a broad overview of all FRG related topics and even offers a direct comparison to the DSE approach in Chap. IV. The FRG is often applied to compute thermodynamic and spectral properties of QCD, such as spectral functions, which ultimately lead to propagators and transport coefficients. Advances on observables explored in this thesis, such as bound-states and form factors, have recently started, see Ref. [19].

Lattice QCD is a numerical approach in which the QCD path-integral, see e.g. Eq. (2.5), is solved by discretizing spacetime on a grid. The value of the integral can then be estimated numerically using Monte Carlo importance sampling. The calculations require using not only the discrete lattice but also a finite box size in all four dimensions. This is necessary to make the path integral finite-dimensional

$$\int \mathcal{D}\varphi \longrightarrow \prod_{i=1}^{N} \int d\varphi_i \,, \tag{2.25}$$

where N is the total number of points. Modern-day lattices range from 48 to 96 points in each direction for a total of up ~ 90 million points. But even with these massive grids, it can be challenging to fit all the scales into the system. For example a calculation using charm quarks requires $m_c \ll 1/a$ but still $1/L \ll m_\pi$, where a and L are the lattice spacing and box size respectively, and thus L/a is the number of points in each direction.

Because very large grids are required, lattice QCD calculations become very expensive and require state-of-the-art computing resources. The cost of the calculation scales as a power

of (L/a) and, as a result, many calculations use values of a (L) that are large enough (small enough) to still have significant effects on the observables. In addition, many calculations work at heavier than physical pion masses, which speeds up the calculation and makes it easier to achieve $1/L \ll m_\pi$. To summarize, the calculation gives a modified version of the observable depending on the lattice spacing, box size and pion mass, $\mathcal{O}(a, L, m_\pi)$, and one must try to extrapolate to $\mathcal{O}(0, \infty, 135\,\mathrm{MeV})$. Of the three parameters, only the effects of unphysical m_π can be completely circumvented, by working directly at the physical mass. Indeed this is becoming increasingly common and by now multiple groups are working with directly physical parameters. Whatever extrapolation is required, e.g. that in a and L is unavoidable, will often introduce systematic errors that must be estimated, for example by using different fit functions to the a, L and m_π dependence. A final potential issue is that lattice calculations are only possible in Euclidean signature, similar to the Dyson-Schwinger approach. This means that some observables cannot be accessed, or require creative techniques. (See Refs. [4, 20–22])

For the discussion of lattice results below it will be useful to briefly describe the workflow of a typical modern lattice QCD calculation. To estimate the finite-dimensional path integral stochastically, one typically requires a few hundred samples of representative gauge field configurations. Here only the gluons must be sampled numerically as the quark part of the integral can be evaluated analytically. The generation of gauge fields is often the most expensive part of the calculation and is typically done in large collaborations that share computing resources. For example, the CLS collaboration brings together groups from over five institutions for this first step. (See, e.g., Refs. [23, 24].) Once the fields have been calculated, specific observables can be determined in a second step. This is often less expensive and can be done in smaller groups. In this work, for example, I compare to CLS based calculations in which the final observables were determined by the Mainz group [25].

For a general introduction to lattice QCD many text books are available including Refs. [26–28].

Dispersion relations are universally applicable equations, that follow from fundamental principles of analyticity and unitarity in our QFT. Historically these equations stem from the more general mathematical relations, derived by Kramers and Kronig in the 1920s, which connect the real and imaginary parts of a complex function that is analytic in the upper half-plane. In QCD, this function is identified with the scattering amplitude and we can apply the relation based on the unitary requirement of the S-matrix [1]. This unitary requirement leads to the optical theorem, which furthermore relates the imaginary part of a scattering amplitude to experimentally measurable cross-sections. Thus, the dispersion relation can use data from cross-sections and decay processes of intermediate states to combine into new information about a physical observable of interest, such as form factors or other transition matrix elements.

The dispersion relations are mathematically exact relations. Approximations enter this approach only at the level of the data needed for new predictions. Given that this is a data-driven approach, high-precision measurements of cross sections are required. This is what ultimately limits the approach, as it is strongly dependent on available data-sets. However, as experimental measurements continue delivering new and more precise data, the dispersive approach has become more successful in providing results for different physical observables. On the other hand, its data-driven nature is one of the biggest advantages, as this enables a reliable error estimate through error propagation from the error associated with

[1] The scattering matrix is included in the full Green function and represents the overlap between two particle states and contains the physical information (e.g poles masses and widths), that we want to extract. The LSZ reduction formula is one way to extract the S-matrix from a Green function. In the DSE approach will use a similar principle, by evaluating the residues at particle poles.

the experimental analysis. This allows the approach to provide a systematic error estimate and thus can have a high impact in areas of high-precision physics, such as the anomalous magnetic moment of the muon a_μ, Sec. 3.2.

For multiple references on the topic, see Refs. [29–34], where the older ones are a more general introduction and the more recent apply the dispersive technique to a particular physical observable. A brief introduction about the background of the relation is given in App. C and the application in the particular case of the pion transition form factor is discussed in Sec. 5.1.

2.4 The Dyson-Schwinger and Bethe-Salpeter approach

In this section we introduce the underlying equations of the Dyson-Schwinger approach. We show how these are used to calculate QCD propagators and vertices, explaining their origin and setting up the framework for explicit application later on.

2.4.1 Equations and implications

Key ingredients to the functional approach used in this work are the Dyson-Schwinger and Bethe-Salpeter equations (referred to as DSEs and BSEs respectively). These enable us to calculate gauge-fixed correlation functions including the quark and gluon propagators, as well as higher-order Green functions. They are used to calculate physical observables, such as bound-state masses, form factors, and other scattering and transition amplitudes. All physical observables are, by definition, gauge independent. This means that gauge-fixed correlation functions must always be combined into gauge-invariant objects to extract meaningful observables.

Gauge fixing is done at the level of the path integral. The path integral as it stands has gauge redundancies meaning that it is ill-defined. The problem is that the integration runs over both physically distinct fields and also gauge-equivalent fields. The integration over the latter leads to an infinity since the integrand (e^{-S}) is gauge invariant.[1] To resolve this problem gauge fixing is required. This can be represented by an additional term in the action

$$S_{\mathrm{GF}}[A, c, \bar{c}] = \bar{c}\,\partial^2\, c + g f^{abc}\,\bar{c}^a\,\partial_\mu (A^c_\mu c^b)\,, \tag{2.26}$$

where $\bar{c}$ and c are the Fadeev-Popov ghosts fields.

The most common choice in the context of the DSE approach is Landau gauge, which is preferred because it leads to a simple form for most of the propagators. The gauge-fixed generating functional of QCD is given by,

$$Z[J, \eta, \bar{\eta}, \sigma, \bar{\sigma}] = \int \mathcal{D}\left[A, \psi, \bar{\psi}, c, \bar{c}\right]\; e^{-S_{\mathrm{QCD}}[A,\psi,\bar{\psi}] - S_{\mathrm{GF}}[A,c,\bar{c}] - S_J}\,, \tag{2.27}$$

where the source term is

$$S_J = \int d^4x\; \left[A^a_\mu J^a_\mu + \bar{\eta}\psi + \eta\bar{\psi} + \bar{\sigma}c + \sigma\bar{c}\right]\,, \tag{2.28}$$

represented as $\int_x \varphi(x) J(x)$ in Eq. (2.6) above.

[1] This is analogous to

$$\int_{-\infty}^{\infty} dx \int_{-\infty}^{\infty} dy f(x) = \infty\,,$$

where x represents the physically distinct fields and y represents the gauge redundancy.

Dyson-Schwinger-equations (DSE). The DSEs follow from the translation invariance of the generating functional $Z[J]$, Eq. (2.6). To explain this we return to the compact notation used above with quark (ψ), ghost (c) and gluon (A^μ) fields indicated through $\varphi = \{\psi, \bar{\psi}, c, \bar{c}, A\}$. Shifting the fields by $\varphi(x) \to \varphi(x) + \epsilon(x)$ and assuming that the integral measure stays invariant we deduce $Z[J] = Z'[J]$. From this one arrives at the relation,

$$\left\langle \frac{\delta S[\varphi]}{\delta\varphi(x)} \right\rangle_J = Z[J]^{-1} \frac{\delta S}{\delta\varphi} \left[\frac{\delta}{\delta J(x)}\right] Z[J] = J(x)\,, \tag{2.29}$$

where the derivative in square brackets is meant to be used as an argument of the function surrounding it. To avoid double counting and to relate to observables, we are interested in amputated and connected correlation functions. For this reason we start from the effective action $\Gamma[\tilde{\varphi}]$, Eq.(2.10), rather then from the basic generating function $Z[J]$. We can use the transformation between functionals, Eq.(2.10), to transform Eq. (2.29) into the **generating DSE** for all (1-PI) Green functions,

$$\Gamma'[\tilde{\varphi}]_x = \frac{\delta S}{\delta\varphi}\left[\tilde{\varphi}(x) + \int_y \Gamma''\,[\tilde{\varphi}]^{-1}_{xy}\,\frac{\delta}{\delta\tilde{\varphi}(y)}\right] \mathbb{1} = J(x). \tag{2.30}$$

Here we define the short-hand, $\Gamma'[\tilde{\varphi}]_x := (\delta\,\Gamma[\tilde{\varphi}]/\delta\,\varphi(x))|_{\tilde{\varphi}=0}$, which is applied twice for the second term in the bracket on the right-hand side. If we were to set the second term to zero we would recover that the effective action $\Gamma[\tilde{\varphi}]$ becomes identical to the classical action $S[\tilde{\varphi}]$. Thus we interpret the second term as the quantum corrections to the classical theory. Note that for the derivatives $\delta/\delta\varphi$ we can choose φ to be any specific field (e.g. a fermion or a gluon), depending on the relation we are interested in. However, even after making an explicit choice for the outside derivative, for the φ inside the square brackets we will have to consider all fields of theory.

By taking further derivatives with respect to the fields and setting the averaged field to zero ($\tilde{\varphi} = 0$), one arrives at the individual DSEs for the quarks, ghosts and gluons. Each equation relates the propagators of the field (equivalently the two-point correlation function), to higher-order Green functions (three- and higher-point functions). In a last step one usually performs a Fourier transformation to momentum space, which results in the equations most commonly referred to as DSE or Schwinger-Dyson equations ([1], Ch. (14.7)).

As a specific example, we first consider the quark DSE (see also the left panel of Fig. 13 in Sec. 4 below). Begin by noting that $\Gamma''\,[\tilde{\varphi}]$, appearing in the second term in brackets, is equal to the propagators of the various fields represented by φ. For example, when φ is a quark field one has

$$\mathbf{S}(x-y) = \langle 0|\,\mathsf{T}\,\psi(x)\,\bar{\psi}(y)\,|0\rangle := \left(\frac{\delta^2\Gamma[\tilde{\varphi}]}{\delta\bar{\psi}(x)\delta\psi(y)}\right)^{-1} = \Gamma''\,[\tilde{\varphi}]^{-1}_{xy}\ . \tag{2.31}$$

In the middle equality the inverse is understood as a matrix inverse on the x, y coordinates. To see why this holds note that the derivatives with respect to the classical action given the bare propagator (in momentum space $\widetilde{\mathbf{S}}_0(p) = [i\not{p} + m]^{-1}$). Adding in the quantum fluctuations, the second term in the brackets of Eq. (2.30), then adds in the self energy (sum of all 1PI diagrams) to reach the full propagator (in momentum space $\widetilde{\mathbf{S}}(p) = [i\not{p} + m + \mathbf{\Sigma}(p)]^{-1}$).

We now aim to use this result together with Eq. (2.30) to derive an expression for $\widetilde{\mathbf{S}}(p)$ in terms of other n-point functions. To get the inverse quark propagator on the left-hand side of Eq. (2.30) we need to take yet another derivative of the generating DSE with respect to the conjugated quark field. This gives

$$\Gamma''\,[\tilde{\varphi}]_{zy} = \mathbf{S}(z-y)^{-1} = \frac{\delta}{\delta\bar{\psi}(z)}\left(\bar{\psi}(y) + \int_{y'} \mathbf{S}(y-y')\frac{\delta}{\delta\psi(y')}\right)\left(\not{\partial} + ig\not{A}(y) + \mathsf{m}\right)\,, \tag{2.32}$$

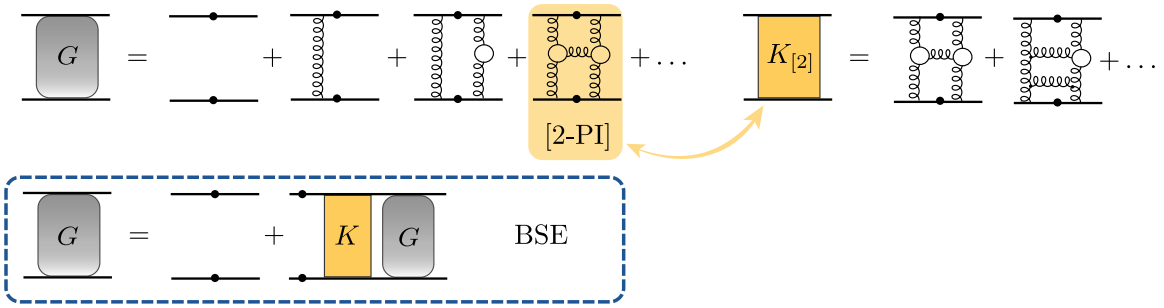

Figure 4: The quark four-point function G contains all diagrams. The (2-PI) scattering kernel $K_{[2]}$ is a subset of this and the two can be related by equation in the last line, Eq. (2.37). This is the **Bethe-Salpeter equation** for $n = 4$ (quark-antiquark bound-state = mesons). It generally holds for all n.

where we have plugged in $\delta S/\delta\psi$ derived from the QCD action given in Eq. (2.1) and furthermore replaced all fields by the expression in rectangular brackets in Eq. (2.30).[1]

Now the final step is to apply the $\bar{\psi}(z)$ derivative. This acts in two places, once on $\bar{\psi}(y)$ and once on $\not{A}(y)$. Doing so and switching to momentum space we find

$$\widetilde{\mathbf{S}}(p)^{-1} = \widetilde{\mathbf{S}}_0^{-1}(p) + \int \frac{d^4q}{(2\pi)^4} (ig\gamma_\mu)\, \widetilde{\mathbf{S}}(q) \left[\frac{\delta}{\delta\psi(q)} \frac{\delta}{\delta\bar{\psi}(p)} A_\mu(p-q) \right] . \tag{2.33}$$

Evaluating the final derivatives leads to the **Dyson-Schwinger equation** for the quark propagator

$$\widetilde{\mathbf{S}}^{-1}(p) := \widetilde{\mathbf{S}}_0^{-1}(p) + \Sigma(p) = \widetilde{\mathbf{S}}_0^{-1}(p) + \int \frac{d^4q}{(2\pi)^4} (ig\gamma_\mu)\, \widetilde{\mathbf{S}}(q)\, \Gamma_\nu(q,p)\, D_{\mu\nu}(q-p) . \tag{2.34}$$

The second term contains the fully dressed quark ($\widetilde{\mathbf{S}}$) and gluon ($D^{\mu\nu}$) propagators, and the bare (γ^μ) and dressed (Γ^ν) quark-gluon vertices. The vertex is a higher-order Green function, which describes the interaction between quarks and gluons. It fulfills its own DSE, which can be derived by taking the derivative of the effective action with respect to the vertex Green function. The same can be said for the gluon propagator. Taking a derivative of the generating DSE, Eq.(2.30), with respect to the gluon field A_μ leads to the gluon DSE, which once more depends on higher-order Green functions. In short, the quark DSE in Eq. (2.35) leads to an infinite tower of coupled equations relating Green functions that need to be truncated to allow numerical evaluation. A more detailed derivation of the DSEs can be found in [1, 35–37].

The quark self-energy term can be related to a new effective action, denoted $\tilde{\Gamma}_{[2]}$, by a functional derivative

$$\frac{\delta\, \tilde{\Gamma}_{[2]}[\mathbf{S}]}{\delta\mathbf{S}} = \int \frac{d^4q}{(2\pi)^4} (i\gamma^\mu)\, \widetilde{\mathbf{S}}(q)\, \Gamma^\nu(q,p)\, D^{\mu\nu}(q-p) . \tag{2.35}$$

This generating functional is the interacting (2-PI) effective action with respect to the quark propagators. It contains all diagrams that stay connected when any two quark lines are cut. This relation will become relevant once we need to start to truncate our coupled system and require consistency between quark DSE and meson BSE. The next section will introduce the BSE.

[1] In principle we obtain the second term in the rectangular bracket of Eq. (2.30) for the gluon field as well, however as this acts on a constant to the right, the derivative vanishes.

Bethe-Salpeter equations (BSE). The fundamental particles of QCD, quarks and gluons, are not directly observed in nature due to confinement. Instead, experimentalists detect a combination of these elementary building blocks, called hadrons. A hadron can be every combination of quarks and gluons that is color neutral, meaning that the colors of the composite quarks have to either combine to be neutral by including one of each color ($rgb \to$ baryons), or through a combination of quarks and anti-quarks ($\bar{r}r, \bar{b}b, \bar{g}g \to$ mesons). The bound-state equation will ultimately help us to obtain physical observables, like bound-state masses and decay widths. Bound states appear as poles in n-point ($n > 4$) correlation functions and we will explain how this information is extracted from them in the next section. To familiarize the reader with the BSE we will start with a diagrammatic representation. The derivation relies upon the classification of diagrams according to basic properties such as (ir)reducibility. Similar to the DSE, the BSE can be thought of as a rearrangement of diagrams into various subsets of all possible Feynman diagrams needed to describe bound states.

Consider the quark four-point Green function, $\mathbf{G}$, which contains poles corresponding to mesons

$$\mathbf{G}(x_1, x_2, x_3, x_4) = \langle 0|\mathsf{T}\psi(x_1)\bar{\psi}(x_2)\psi(x_3)\bar{\psi}(x_4)|0\rangle\,. \tag{2.36}$$

For simplicity, all Dirac, color and flavor indices are suppressed for now. This function contains all possible interactions between a quark anti-quark pair and is sketched in Fig. 4. The graphs are obtained by following the Feynman rules based on the interactions and fields specified in the Lagrangian, Eq. (2.1). The four-quark scattering kernel, $K_{[2]}$, forms a subset of the diagrams in $\mathbf{G}$, see second row in Fig. 4. The kernel is a two-particle irreducible (2-PI) Green function with respect to the quark propagators. The scattering kernel includes all diagrams of $\mathbf{G}$ that do not fall apart when cutting two quark lines (one quark and one anti-quark in this case). With this definition one can rewrite the full Green function and obtain the well-known Bethe-Salpeter, or hadronic bound-state equation,

$$\mathbf{G} = G_0 + G_0\,\mathbf{K}\,\mathbf{G}\,, \tag{2.37}$$

where G_0 denotes the disconnected product of two quarks propagators, i.e. $G_0 = SS$. The BSE thus separates interacting and non-interacting parts of the $\mathbf{G}$ matrix. Besides the full Green function, one also frequently uses the amputated and connected part of $\mathbf{G}$, denoted by T and referred to as the T matrix. This is related by $\mathbf{G} = G_0 + G_0\,T\,G_0$. For later usage it will be convenient to also define the inverse version of the above equation

$$(\mathbf{G})^{-1} = (G_0)^{-1} - \mathbf{K}\,. \tag{2.38}$$

Besides the more intuitive graphical derivation (Fig. 5), Eq. (2.37) can be solely derived by considering the different functionals (n-PI effective actions) and relating them to one another using functional derivatives. I do not present the derivation of this approach here, but instead refer the reader to Ref. [5]. Nevertheless I would like to give one relation that arises in the functional-based derivation. One can show that the interaction kernel satisfies

$$K_{[2]} = -\frac{\delta}{\delta\mathbf{S}}\frac{\delta\,\tilde{\Gamma}_{[2]}[S]}{\delta\mathbf{S}} = -\frac{\delta}{\delta\mathbf{S}}\mathbf{\Sigma}\,. \tag{2.39}$$

In particular, the second equality, which relates the interaction kernel to the quark self-energy, is useful in defining self-consistent truncations, as discussed in Sec. 4.4.

2.4.2 Extracting hadronic spectra

So far we have established multiple ways to represent QCD's Green functions and explored useful relations between different quantities. However, ultimately we are interested in the

Figure 5: Bethe-Salpeter equation close to bound-state pole ($P^2 = -m_\lambda^2$). The Bethe-Salpeter wavefunction Ψ is the residue at the pole. In the proximity of the pole Eq.(2.37) reduces to Eq. (2.44).

hadron properties encoded in these field-theoretic functions, and this leads to an important question: How exactly can we extract properties like bound-state masses from our Green functions?

All hadrons are contained in the Hilbert space of QCD as eigenstates of the QCD Hamiltonian. A self-adjoint Hamiltonian has a complete set of orthogonal eigenstates denoted $|\lambda\rangle$. Because the Hamiltonian commutes with the momentum operator, we can choose the $|\lambda\rangle$ to be eigenstates of both and write $|\lambda, \mathbf{p}\rangle$. Then, due to Lorentz invariance, if the eigenvalue of $|\lambda, \mathbf{0}\rangle$ is denoted M_λ, the corresponding eigenvalue of $|\lambda, \mathbf{p}\rangle$ is $\omega_{\lambda,p} = \sqrt{\mathbf{p}^2 + M_\lambda^2}$. This leads to the following completeness relation

$$1 = \sum_\lambda \frac{1}{(2\pi)^3} \int \frac{d^3p}{2\omega_{\lambda,p}} |\lambda, \mathbf{p}\rangle\langle\lambda, \mathbf{p}| = \sum_\lambda \frac{1}{(2\pi)^3} \int d^4p\, \theta(p^0)\, \delta(p^2 + M_\lambda^2) |\lambda, \mathbf{p}\rangle\langle\lambda, \mathbf{p}| \,, \quad (2.40)$$

where the factor of $2\omega_{\lambda,p}$ arises from the normalization convention of the state. This is convenient as it leads to a Lorentz invariant measure, as can be seen from the second form of the integral. The eigenstate space is enormous and contains all possible QCD states. How can we make sure to obtain the bound-state property of interest, in this infinite-dimensional space?

It is well established that bound states and resonances appear as poles in higher-order n-point functions. We can insert the completeness relation, Eq. (2.40), in any correlation function. The overlap of the eigenstates and the fields then produce the poles. If the correlator is evaluated at energies in the proximity of the bound-state pole, the pole contribution will dominate and enable us to separate out the amplitude from the sub-leading contributions of the other states in the Hilbert space.

Consider once more the four-point Green function, Eq. (2.36)

$$\mathbf{G}_{\alpha\beta\gamma\delta}(x_1, x_2, x_3, x_4) = \langle 0|\mathsf{T}\psi_\alpha(x_1)\bar{\psi}_\beta(x_2)\psi_\gamma(x_3)\bar{\psi}_\delta(x_4)|0\rangle \,. \quad (2.41)$$

The greek letters represent the combination of Dirac, color and flavor indices, and the choice determines the quantum number of the field combinations and ultimately the quantum numbers of the bound state. Inserting Eq. (2.40) into (2.41) and Fourier transforming to momentum space, the Green function can be expressed in terms of a sum of poles together with regular terms,

$$\mathbf{G}_{\alpha\beta\gamma\delta}(p, q, P) = \sum_\lambda \frac{\mathbf{\Psi}^\lambda_{\alpha\beta}(p, P_\lambda)\, \bar{\mathbf{\Psi}}^\lambda_{\gamma\delta}(q, -P_\lambda)}{P^2 - P_\lambda^2} + R(q, p, P) \,, \quad (2.42)$$

where Ψ is the Bethe-Salpeter wave-function, (q, p) are relative momenta and P the total momentum. This is referred to as the spectral decomposition of the Green function in momentum space. At the pole the bound-state is on-shell, meaning $P_\lambda^2 = -M_\lambda^2$. The wave-function is defined as the residue at the pole and is given in coordinate space by

$$\mathbf{\Psi}^{\lambda\,(4)}_{\alpha\beta}(x_1, x_2, P_\lambda) = \langle 0|\mathsf{T}\,\psi_\alpha(x_1)\bar{\psi}_\beta(x_2)|\lambda(P_\lambda)\rangle \,, \quad (2.43)$$

which identifies it as the transition element between the vacuum and a bound-state $|\lambda\rangle$, in this case a meson, with momentum P_λ.

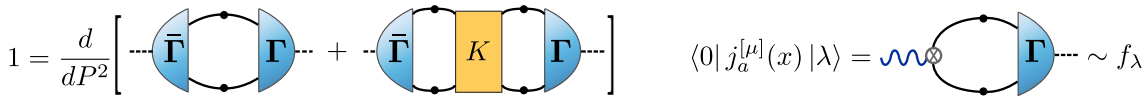

Figure 6: *Left*, normalization condition for a meson, Eq (2.50). *Right*, the lepton decay constant f_λ is proportional to correlation function between the Bethe-Salpeter meson amplitude and a current-vertex $j_a^{[\mu]}$, eg. for the vector current Eq. (2.62).

Evaluating the BSE, Eq. (2.37), in the proximity of the bound-state poles leads to the **homogeneous Bethe-Salpeter equation**, as shown in Fig. 5:

$$\mathbf{G} \xrightarrow{P_\lambda^2 \to -M_\lambda^2} \frac{\mathbf{\Psi}\,\bar{\mathbf{\Psi}}}{P^2 + M_\lambda^2} \quad \Longrightarrow \quad \mathbf{\Psi} = G_0\,\mathbf{K}\mathbf{\Psi}\,. \tag{2.44}$$

The pole part of the spectral representation, Eq. (2.42), dominates the regular terms as well as the inhomogeneous term G_0 in the full BSE, Eg. (2.37), and we obtain the reduced homogeneous BSE, an iterative equation that can be used to determine the Bethe-Salpeter wave-function. We define the amputated version of the Bethe-Salpeter wave-function Ψ as the Bethe-Salpeter amplitude, Γ, which leads to the relation

$$\mathbf{\Psi} = G_0\,\mathbf{\Gamma} \quad \Longrightarrow \quad \mathbf{\Gamma} = \mathbf{K}\,G_0\,\mathbf{\Gamma}\,. \tag{2.45}$$

Normalization. Evaluated at the bound-state pole, the BSE (Eq. (2.44)) is a homogeneous equation, which constrains $\mathbf{\Psi}$ up to an arbitrary multiplicative constant. An additional normalization is needed to fix this coefficient and ultimately ensure the correct determination of physical observables. The canonical quantization condition demands that the residue at the bound-state pole is one, such that the decomposition in Eq. (2.42) holds exactly.

To see how this works out, consider $\mathbf{G}$ evaulated arbitrarily close to the pole at $P^2 = -M_\lambda^2$ and take a derivative with respect to P^2

$$\frac{d\mathbf{G}}{dP^2} = -\frac{\mathbf{\Psi}\,\bar{\mathbf{\Psi}}}{(P^2 + M_\lambda^2)^2}\,, \tag{2.46}$$

where we drop sub-leading terms at the pole. Note that the derivative does not act on $\mathbf{\Psi}$ and $\bar{\mathbf{\Psi}}$ as they are evaluated at fixed P^2, on the mass shell. Next we multiply by $\bar{\mathbf{\Psi}}\mathbf{G}^{-1}$ on the left and $\mathbf{G}^{-1}\mathbf{\Psi}$ on the right to reach

$$\bar{\mathbf{\Psi}}\mathbf{G}^{-1}\frac{d\mathbf{G}}{dP^2}\mathbf{G}^{-1}\mathbf{\Psi} = -\bar{\mathbf{\Psi}}\left[\frac{\mathbf{\Psi}\,\bar{\mathbf{\Psi}}}{(P^2 + M_\lambda^2)}\right]^{-1}\frac{\mathbf{\Psi}\,\bar{\mathbf{\Psi}}}{(P^2 + M_\lambda^2)^2}\left[\frac{\mathbf{\Psi}\,\bar{\mathbf{\Psi}}}{(P^2 + M_\lambda^2)}\right]^{-1}\mathbf{\Psi} = -1\,. \tag{2.47}$$

The next step is to use the matrix identity $d\mathbf{M}/dx = -\mathbf{M}\,[d\mathbf{M}^{-1}/dx]\,\mathbf{M}$ to reach

$$\bar{\mathbf{\Psi}}\,\frac{d\mathbf{G}^{-1}}{dP^2}\,\mathbf{\Psi}\Big|_{P^2=-M_\lambda^2} = 1\,. \tag{2.48}$$

Combining this with Eqs. (2.38) and (2.45), we reach

$$\bar{\mathbf{\Gamma}}\left(\frac{dG_0}{dP^2} + G_0\frac{d\mathbf{K}}{dP^2}G_0\right)\mathbf{\Gamma}\Big|_{P^2=-M_\lambda^2} = -1\,. \tag{2.49}$$

We stress that this is just the normalization condition, rewritten in a more convenient form.

In the case of the four-point Green function we can furthermore identify $G_0 = \mathbf{S}\,\mathbf{S}$ and obtain,

$$-1 = \left[\int_q \bar{\mathbf{\Gamma}}(q,-P_\lambda)\ \frac{d}{dP^2}\left(\widetilde{\mathbf{S}}(q,P)\,\widetilde{\mathbf{S}}(q,P)\right)\mathbf{\Gamma}(q,P_\lambda)\Big|_{P_\lambda^2=-M_\lambda^2}\right. \tag{2.50}$$
$$\left. + \int_q\int_p \bar{\mathbf{\Psi}}(q,-P_\lambda)\,\frac{d}{dP^2}\mathbf{K}(q,p,P)\,\mathbf{\Psi}(q,P_\lambda)\right]\Big|_{P_\lambda^2=-M_\lambda^2}.$$

Note that all these objects are defined in Dirac, flavor and color space and that all indices are contracted to give a simple number. The contraction pattern follows from the definitions above, for example

$$\bar{\mathbf{\Gamma}}G_0\mathbf{\Gamma} = \bar{\mathbf{\Gamma}}_{\alpha\beta}\ G_{0;\alpha\beta\gamma\delta}\ \mathbf{\Gamma}_{\gamma\delta} = \bar{\mathbf{\Gamma}}_{\alpha\beta}\ \mathbf{S}_{\alpha\gamma}\mathbf{S}_{\beta\delta}\ \mathbf{\Gamma}_{\gamma\delta}\,. \tag{2.51}$$

Equation (2.50) is displayed in the left panel of Fig. 6. To enforce the demand that the residue equals one, we introduce a normalization constant which relates normalized and unnormalized Bethe-Salpeter amplitudes through $\Gamma = \mathcal{N}\,\Gamma_{[\text{unnormalized}]}$.

2.4.3 Current-$\bar{q}q$-vertices and their implications

In the previous section, we mainly worked with Green functions describing the correlations between fields. Current vertices, which are the Green functions between a quark and an anti-quark field and a current (eq. vector, axial-vector or pseudo-scalar), lead to several model-independent consequences ranging from relations between singularity structures to physical observables to symmetry relations between Green functions obtained through the PCAC. This makes them highly interesting quantities and preserving their known properties guide our choice for the truncations of the DSEs and BSEs. Furthermore, current vertices give access to observables such as decay constants. This section connects back with the flavor symmetry overview in Tab. 2 as the relevant currents are associated with the underlying flavor symmetries.

The **vector**, **axial-vector** and **pseudo-scalar quark-antiquark vertices** are obtained by inserting a current, $j_a^{[\mu]}$, into the quark propagator, $\mathbf{S}$, Eq. (2.31). The vertices are defined as

$$\mathrm{S}_a^{[\mu]} \in \{\mathrm{S}_a^\mu, \mathrm{S}_{a\,5}^\mu, \mathrm{S}_{a\,5}\}\,, \quad \Rightarrow \quad \mathrm{S}_{a\,\alpha\beta}^{[\mu]}(x,y,z) = \langle 0|\mathsf{T}\ \psi_\alpha(x)\ \bar{\psi}_\beta(y)\ j_a^{[\mu]}(z)\ |0\rangle\,. \tag{2.52}$$

The current is abbreviated with $j_a^{[\mu]}$ and a is the flavor index, indicating that both $\mathrm{S}_a^{[\mu]}$ and $j_a^{[\mu]}$ are vectors in flavor space. The generic label $[\mu]$ runs through the different choices for the currents, which are abbreviated by

$$j_a^{[\mu]} \in \{j_a^\mu,\, j_{5\,a}^\mu,\, j_{5\,a}\} \quad \Rightarrow \quad j_a^{[\mu]}(x) := \bar{\psi}(x)\ \Gamma_{0\,a}^{[\mu]}\ \psi(x)\,, \tag{2.53}$$

with yet another abbreviation for the renormalized Dirac-flavor structures, $\Gamma_{0\,a}^{[\mu]}$, which encode the various current properties. For vector, axial-vector and pseudo-scalar currents these are given by,

$$\Gamma_{0\,a}^{[\mu]} \in \{\Gamma_{0\,a}^\mu = Z_2 i\gamma^\mu t_a,\ \Gamma_{0\,5a}^\mu = Z_2\gamma_5\gamma^\mu t_a,\ \Gamma_{0\,5a} = Z_4 i\gamma_5 t_a\}\,, \tag{2.54}$$

respectively. Here we include the renormalization constants introduced in Eq. (2.4). We have also introduced t_a as the generator of the $SU(N_f)$ group, with normalization convention $\mathrm{Tr}[t_a^2] = 1/2$.

We next introduce $\Gamma^{[\mu]}$, without the 0 subscript, as the amputated version of the current vertex $\mathrm{S}^{[\mu]}$, Eq. (2.52). It is easily obtained by removing the external quark propagators and

Figure 7: *Left*, inhomogeneous Bethe-Salpeter equation for a vector current vertex. *Right*, vector-vector current correlation, which describes the hadronic vacuum polarization.

has a similar definition to the relation between Bethe-Salpeter wave-function and amplitude,

$$-\mathrm{S}^{[\mu]}(p,P) = \widetilde{\mathbf{S}}(p_+)\,\Gamma^{[\mu]}(p,P)\,\widetilde{\mathbf{S}}(p_-) = G_0(p,P)\,\Gamma^{[\mu]}(p,P) = \mathbf{G}(p,P)\,\Gamma^{[\mu]}_{0\,a}(p,P)\,, \tag{2.55}$$

where once more $\mathbf{G}$ and G_0 denote the full and disconnected four-point functions and $\widetilde{\mathbf{S}}(p)$ the quark propagator evaluated at the momentum p. Note that the the vertex with quark legs attached, $\mathbf{S}^{[\mu]}$, as well as the amputated version, $\Gamma^{[\mu]}$, are general matrix elements which still contain singularities when evaluated at bound-state poles. By contrast, the Bethe-Salpeter wave-function $\mathbf{\Psi}^\lambda$ and amplitude $\mathbf{\Gamma}^\lambda$ are the residues of the bound-state correlation functions at the meson poles.

Vertex BSE. In analogy to the Bethe-Salpeter wave-function, the current vertices obey Bethe-Salpeter equations. Using the fact that the Green functions satisfy, $\mathbf{G} = G_0 + G_0\,\mathbf{K}\,\mathbf{G}$ we can insert this into Eq. (2.55) above and obtain,

$$-\mathrm{S}^{[\mu]} = G_0\,\Gamma^{[\mu]}_0 - G_0\,\mathbf{K}\,\mathrm{S}^{[\mu]} \quad \Rightarrow \quad \Gamma^{[\mu]} = \Gamma^{[\mu]}_0 + \mathbf{K}\,\Gamma^{[\mu]}\,. \tag{2.56}$$

The equation on the right-hand side follows from multiplying both sides of the preceding equation with G_0^{-1}. This result represents an inhomogeneous Bethe-Salpeter equations which we can solve iteratively to determine the vertex $\Gamma^{[\mu]}$, see Fig. 7 left. The inhomogeneous terms are the Dirac-flavor matrices, $\Gamma^{[\mu]}_{0\,a}$, and depend on the choice of current. Calculating electromagnetic transition matrix elements, such as form factors, requires knowledge of these quark antiquark current vertices. In particular the vertex associated with the vector current (j^μ_a) corresponds to the **quark-photon vertex**, which describes the non-perturbative effects between quarks and photons. This vertex contains vector-meson poles, and the existence of the poles will determine the scaling behavior of the form factor. For this reason, the vector-meson dominance model (VMD) is a popular model to fit or describe transition form factor data.

Singularities and decay constants. To understand the underlying singularity structures, we take a closer look at the poles in the current vertices. While the four-point Green function, $\mathbf{G}$, contains all existing meson poles, Eq. (2.42), the current vertices only contain a subset. These poles correspond to particles with the quantum numbers matching the structure of the current. In other words, poles appear if we have a non-zero overlap between the current on the vacuum $\langle 0|j^{[\mu]}_a$ and the meson state of interest $|\lambda\rangle$. This is represented by the vacuum-to-hadron matrix element of the current and is given by the following expression,

$$\begin{aligned}\langle 0|\,\bar\psi(x)\,\Gamma^{[\mu]}_{0\,a}\,\psi(x)\,|\lambda\rangle\,e^{-ix\cdot p} = \langle 0|\,j^{[\mu]}_a(x)\,|\lambda\rangle e^{-ix\cdot p} =: \mathcal{J}^{[\mu]}_{\Omega\lambda}\,,\\ \mathcal{J}^{[\mu]}_{\lambda\lambda'}(p_f,p_i) = \langle\lambda(p_i)\,|\,j^{[\mu]}(0)\,|\lambda'(p_f)\rangle\,.\end{aligned} \tag{2.57}$$

In a second step we have introduced yet another definition, namely the matrix elements $\mathcal{J}^{[\mu]}_{\lambda\lambda'}$. This generally describes the transition between a incoming state, λ, and an outgoing

meson, λ', with an external current, $j^{[\mu]}$. The special case of one state being the vacuum then corresponds to the previously defined correlation function. Current matrix elements are interesting, as they encode the electromagnetic form factors of a bound-sate (such as introduced in Fig. 3 in the second row, in the frame labeled Compton scattering).

To familiarize ourselves with this concept let us look at a specific example of a vacuum-to-hadron transition element for the pseudo-scalar mesons. In this case we have a non-zero overlap with the axial-vector and the pseudo-scalar currents, which leads to,

$$\begin{aligned} \langle 0|\, j^{\mu}_{5\,a}(x)\,|\lambda_b\rangle &= \langle 0|\,\bar\psi(x)\,\Gamma^{\mu}_{0\,5a}\,\psi(x)\,|\lambda_b\rangle = -i\delta^{ab}\,P^{\mu} f_\lambda e^{-ix\cdot P}\,, \\ \langle 0|\, j_{5\,a}(x)\,|\lambda_b\rangle &= -i\delta^{ab}\, r_\lambda\, e^{-ix\cdot P}\,. \end{aligned} \tag{2.58}$$

The transition between an axial-current and a pseudo-scalar meson is proportional to the decay constant f_λ. Similarly, r_λ is a momentum-independent constant referred to as the pseudo-scalar transition matrix element.

The decay constant is an observable that can be measured in experiment, and the mass and decay constant of the lightest meson (the pion) are important input parameters in many non-perturbative QCD approaches, as they are often used to fix the scale and the quark masses. By contrast, r_π is not directly measurable. However we can use its definition to derive an important relation. Recall the PCAC relation, Eq. (2.19), which is the divergence of the axial-vector current in the limit of equal quark masses ($M = m\mathbb{1}$) and for on-shell momenta ($P^2 = -M_\lambda^2$). Combining the information of Eq. (2.58) and the PCAC relation we can show,

$$\text{Eq. (2.58)} \quad \text{and} \quad \partial^\mu j^{\mu}_{a\,5}(x) = 2im\,\bar\psi(x)\,\gamma_5\,t_a\,\psi(x) = 2im\, j_{5\,a} \quad \Rightarrow \quad f_\lambda\, M_\lambda^2 = 2m\, r_\lambda\,. \tag{2.59}$$

This result is an important step towards the Gell-Mann-Oakes Renner (GMOR) relation, but is incomplete because we do not yet know whether f_λ or M_λ (or both) must vanish when $m \to 0$.

Following the same principle as for the G function in Eq. (2.42), we can formally express[1] the vertex as the sum of pole contributions plus remainder terms, denoted $\tilde\Gamma^{[\mu]}$. If we then evaluate the vertex at the meson pole, this leads to,

$$\Gamma^{[\mu]}(p,P) = \sum_\lambda \frac{R_\lambda^{[\mu]}(p,P)}{P^2 + M_\lambda^2} + \tilde\Gamma^{[\mu]} \xrightarrow{P^2 \to -M_{\lambda'}^2} \frac{R_{\lambda'}^{[\mu]}(p,P)}{P^2 + M_{\lambda'}^2}\,. \tag{2.60}$$

If a vertex has a non-zero overlap with a bound-state, λ', the remainder $\tilde\Gamma^{[\mu]}$ is regular and the pole contribution dominates in the limit $P^2 \to -M_{\lambda'}^2$. The residue at the pole is exactly this overlap, which then corresponds to the previously defined transition element. For the axial-vector and the pseudo-scalar vertex, the full structure can be written as


$:= \Gamma_5^\mu = P^\mu \sum_\lambda \frac{2if_\lambda}{P^2 + M_\lambda^2}\mathbf{\Gamma}_\lambda + \tilde\Gamma_5^\mu\,,$

$:= \Gamma_5 = \sum_\lambda \frac{2ir_\lambda}{P^2 + M_\lambda^2}\mathbf{\Gamma}_\lambda + \tilde\Gamma_5\,.$ (2.61)

Similarly, we can define a non-zero overlap between the vector meson (in particular $\lambda = \rho$) and the vector-current vertex,

$$\langle 0|\, j_3^\mu(x)\,|\rho_0\rangle = \mathrm{Tr}\int \frac{d^4k}{(2\pi)^4}\,\Gamma_0^\mu\,\widetilde{\mathbf{S}}(k_+)\,\mathbf{\Gamma}_\rho^\nu(k,P)\,\widetilde{\mathbf{S}}(k_-)\,e^{-ix\cdot P} = i f_\rho m_\rho\, t_P^{\mu\nu}\, e^{-ix\cdot P}\,, \tag{2.62}$$

with the usual definition for momenta of the quark propagator $k_\pm = k \pm P/2$. The rho-pole is contained in the transverse part of the vertex. It is for this reason that the transverse

[1] The expression only holds formally because the definition of the meson amplitudes are only meaningful objects on the mass shell, $P^2 = -M_\lambda^2$.

projector $t_P^{\mu\nu} = (\delta^{\mu\nu} - P^\mu P^\nu / P^2)$ appears on the right-hand side. As the matrix element describes the vector transition between the vacuum and the rho-state, it is also defined to be proportional to the decay constant f_ρ. For a diagrammatic representation of the integral see the right panel of Fig. 6.[1]

Ward-Takahashi identities. The Ward-Takahashi-identities (WTI) (or Slavnov-Taylor identities (STI), which are a special case of the non-Abelian WTIs) are symmetry relations between n and $(n+1)$-point Green functions, which follow from both global and gauge symmetries. They remain valid after renormalization, which implies the highly non-trivial statement that charge quantization, e.g. the equal magnitudes of the proton and electron charges, survives renormalization. Furthermore, they enforce current conservation on the level of Green functions, which makes them the quantum version of Noether's theorem. They furthermore imply the QED Ward-identity, as a special case of the full WTIs, which tells us that the longitudinal components of a vertex with an on-shell photon vanishes. Historically the WTIs were first used in QED to relate the wave-function renormalization of an electron to its vertex renormalization factor [38, 39]. This guaranteed the cancellation of ultraviolet divergences to all orders in perturbation theory.

In the context of the Dyson-Schwinger framework, useful implications are obtained from the vector WTI (VWTI) and axial-vector WTI (AXWTI). These can be derived either directly from the invariance of the generating functional under QCD's flavor symmetries, see Tab. 2, or by considering the divergence of the vector and axial-vector current vertices, as introduced in the previous section.[2] A detailed derivation of the AXWTI from the generating functional can be found in the Appendix B. In this case, one starts by using the invariance of the generating functional under the global $U(N_f)_A = U(1)_A \times SU(N_f)_A$ symmetry. The VWTI and AXWTI in momentum space are given by

$$iP^\mu \Gamma^\mu(p,P) = -\widetilde{\mathbf{S}}^{-1}(p_+) + \widetilde{\mathbf{S}}^{-1}(p_-) \,, \tag{2.63}$$

$$iP^\mu \Gamma_5^\mu(p,P) + 2m\,\Gamma_5(p,P) = \widetilde{\mathbf{S}}^{-1}(p_+)\, i\gamma_5 + i\gamma_5\, \widetilde{\mathbf{S}}^{-1}(p_-) \,. \tag{2.64}$$

These relate the amputated current-$\bar{q}q$-vertices, $\Gamma^{[\mu]}$ in Eq. (2.60), to inverse quark propagators, defined in Eq. (2.31). The WTI's are displayed in Fig. 16. P is the total momentum of the current, $p_+ = p + P/2$ the momentum of the out-going and $p_- = p - P/2$ of the in-coming quark.

The **VWTI** (Eq. (2.63)) relates the longitudinal[3] part of the vector vertex, Γ^μ, with the inverse quark propagator. In general we can decompose every Green function into its individual tensor elements, $\tau_i^{[\mu]}$, multiplied by scalar dressing functions, f_i. In the case of the quark-photon vertex (which corresponds to a vector-current $\bar{q}q$-vertex) there are twelve tensor components, which can furthermore be separated into four longitudinal and eight transverse parts,

$$\Gamma^\mu(p,P) = \sum_{i=1}^{12} f_i \tau_i^\mu(p,P) = i\gamma^\mu \Sigma_A(\mathbf{S}) + 2p^\mu (i\not{p}\Delta_A(\mathbf{S}) + \Delta_B(\mathbf{S})) + \sum_{j=1}^{8} \tilde{f}_j \tilde{\tau}_j^\mu(p,P) \,. \tag{2.65}$$

[1] Note that these definitions only strictly make sense if the rho is treated as a stable particle, leading to a pole on the real axis. Although this is not the case in general, working in the rainbow-ladder truncation does lead to a stable vector meson.

[2] When deriving the WTIs in the second method, i.e. by taking divergences, then it is useful to define a current algebra. This is based on the fact that the charges, Q_a, satisfy the same commutator relation as the generators of the underlying symmetry groups, and thus can be used to formulate a set of commutator relation on the level of operators rather than matrices.

[3] Due to the contraction with P^μ only the longitudinal parts of the three point function on the right-hand side remains.

In the second step we have separated the longitudinal and transverse parts, and used the fact that one of the four longitudinal components vanishes. The functions in the longitudinal part $(\Sigma_A(\mathbf{S}), \Delta_{A/B}(\mathbf{S}))$, are averages and differences of the quark-propagator dressing functions and will be specified in Sec. 4.3. For now note only that the longitudinal part is then completely determined by the quark propagator. To ensure vector-current conservation any choice of approximation for the quark-photon vertex needs to at least obey the VWTI.

The **AXWTI** (Eq.(2.64)) relates the longitudinal part of the axial-vector vertex and the pseudoscalar vertex to inverse quark propagators. This will help to prove Goldstone's theorem, which implies the existence of massless particles, called Goldstone bosons, whenever a symmetry is spontaneously broken. This will be discussed in Sec. 4.1. Note that the relation only holds for flavor non-singlet vertices. This is because, in the singlet channel, the divergence of the axial-vector current in Eq. (2.19) carries an additional term due to the QED axial anomaly.

The AXWTI will furthermore help us to consistently truncate the Green functions used in the quark self-energy, $\mathbf{\Sigma}$, and the Bethe-Salpeter interaction kernel, $\mathbf{K}$. See Sec. 4.4. Any reasonable truncation on our system of coupled integral equations needs to obey the AXWTI to ensure current conservation, and accordingly the implications of the GMOR relation. This will be discussed in Sec. 4.2. Similarly, the relation between the kernel and self-energy as introduced Eq. (2.39) must hold. However, in practice, the WTI is a more useful tool to construct a reasonable truncation.

Hadronic vacuum polarization. Another current vertex element and furthermore the simplest observable that tests the structure of the quark-photon vertex, is the hadronic-vacuum polarization (HVP). So far we have looked at the current vertices and the hadron-to-vacuum transition elements individually. The HVP, by contrast, is defined as the Fourier transform of the vector-vector correlator,

$$\Pi^{\mu\nu}(P) = \int d^4x\, e^{iP\cdot x}\, \langle 0|\mathsf{T}\, j^\mu(x)\, j^\nu(0)\, |0\rangle\,. \tag{2.66}$$

In this sense it describes the vacuum matrix transition element between a current injecting P and a second current carrying P away. This is the loop diagram with one dressed and one bare quark-photon vertex (vector-current vertex) [see the right panel of Fig. 7],

$$\Pi^{\mu\nu}(P) = \mathrm{Tr} \int \frac{d^4k}{(2\pi)^4}\, Z_2 i\gamma^\mu\, S(k_+)\, \Gamma^\nu(k,P)\, S(k_-) = \Pi(P^2) P^2\, t_P^{\mu\nu} + \tilde{\Pi}(Q^2)\delta^{\mu\nu}\,. \tag{2.67}$$

As shown in the final step, we can divide the correlator into a transverse part ($\sim t_P^{\mu\nu}$) and a longitudinal part $\tilde{\Pi}^{\mu\nu}$, which should be zero when gauge-invariance is enforced. The transverse part is thus the contribution that is physically relevant and is completely described by the dressing function of the off-shell quark-photon vertex, Eq. (2.56). This then thus probes the full vertex dynamics.

The HVP is also an interesting Green function, as it is the non-perturbative input in the leading hadronic contribution to the muon's $g-2$, as will be discussed in Sec. 3.2 and has been calculated in the DSE approach in this context in Ref. [40].

3 Transition form factors: Motivation & Application

A transition form factor or transition amplitude (see comparison in Tab.3) describes the interaction between a bound-state and two external currents and is subject to effects of the electromagnetic and strong force. A general transition form factor Green function is given by,

$$\Lambda^{\mu\nu}_{ab}(k,\Delta) = \int d^4x \int d^4y \; \langle 0|\, j^{[\mu]}_a(x)\, j^{[\nu]}_b(y)\, |\lambda(\Delta)\rangle\, e^{-iQ\cdot x}\, e^{-iQ'\cdot y}\,, \tag{3.1}$$

where the current $j^{[\mu]}_a$ indicates the choice for either vector, axial-vector or pseudo-scalar current, Eq. (2.53). Transition elements of such kinds are diagrammatically described by a triangle diagram in Fig. 8 (a.).

In this chapter we give background information about the key observable considered in this thesis, the $\pi^0 \to \gamma\gamma$ transition form factor (TFF), and introduce an observable which is a direct application for the TFF, the anomalous magnetic moment of the muon.

3.1 Axial anomaly and the pion transition form factors

In the low-energy region, the $\pi^0 \to \gamma\gamma$ decay is directly connected to the axial anomaly, also sometimes called the Adler-Bell-Jackiw (ABJ) chiral anomaly [41,42]. As shown in Fig. 8, we denote the incoming pion four-momentum by Δ and the outgoing photon momenta by Q and Q'. For the on-shell point (when the particles are on their mass-shell, $Q^2 = Q'^2 = -m_\gamma^2 = 0$) and in the chiral limit ($P^2 = -m_{\pi_0}^2 = 0$), the pion decay amplitude is given entirely by the anomaly. In this case, the calculation can be performed using only perturbation theory, and the one-loop expression is exact to all orders. This not only provides a strong consistency cross-check for the full non-perturbative calculation, furthermore it was one of the first confirmations for the number of colors in QCD [41].

The way anomalies were first understood was with Feynman diagrams. For the axial anomaly, consider the two one-loop triangle diagrams in Fig. (8 a). The decay rate was originally calculated starting with a QED Lagrangian plus a Yukawa coupling, λ, which encodes the interaction between a pseudo-scalar, π, and a fermion, ψ. The strict calculation using the chiral Lagrangian is somewhat ambiguous as can be seen by comparing different textbooks [1, 2]. Following Chapter 30 of Ref. [1] we start with the Lagrangian density,

$$\mathcal{L} = -\frac{1}{4}F_{\mu\nu}F^{\mu\nu} - \frac{1}{2}\pi(\Box + m_\pi^2)\pi + \bar\psi(i\partial\!\!\!/ - eA\!\!\!/ - m)\psi + i\lambda\pi\bar\psi\gamma^5\psi\,, \tag{3.2}$$

where ψ is a fermion, later to be identified with the proton, and π a pseudo-scalar particle, the pion. The one-loop triangle diagram is the first non-zero order in perturbative expansion. The slashed notation denotes the sum over a Lorenz index, with $A\!\!\!/ := A_\mu\gamma^\mu$. As with QED, the coupling parameter e is much smaller than one and higher-order contributions are suppressed. Furthermore, it turns out that higher-order contributions are proportional to the pion mass, m_π. When considering this calculation in the chiral limit (m_π=0) it is thus first-order exact.

By applying Feynman rules we can translate the pictorial diagrams in Fig. (8 a) into mathematical expressions. In this example, we use Feynman rules following the Minkowski conventions (M), working with the mostly minus metric. The sum of the diagrams is given by

$$i\mathcal{M} = -1(-\lambda)(-ie)^2\epsilon^Q_\mu\,\epsilon^{Q'}_\nu\, M^{\mu\nu}(Q^2, Q'^2)\,, \qquad \mathsf{M} \tag{3.3}$$

with the amplitude (in Minkowski metric - M)

$$M^{\mu\nu} = \int \frac{d^4k}{(2\pi)^4}\mathrm{Tr}\left[\gamma^\mu \frac{i(k\!\!\!/ + m)}{(k^2-m^2)}\gamma^\nu \frac{i(k\!\!\!/ + Q\!\!\!/ + m)}{((k+Q)^2-m^2)}\gamma^5 \frac{i(k\!\!\!/ + Q\!\!\!/' + m)}{((k+Q')^2-m^2)} + \begin{pmatrix}\mu\leftrightarrow\nu\\ Q\leftrightarrow Q'\end{pmatrix}\right], \tag{3.4}$$

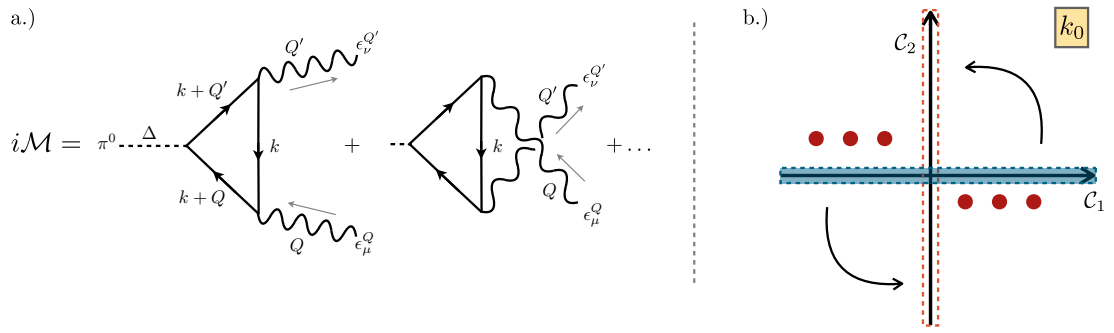

Figure 8: a.) Triangle diagrams for the $\pi^0 \to \gamma\gamma$ decay. The diagrams are one-loop diagrams in perturbative QED. b.) Complex k_0-plane: Minkowski integration path $\mathcal{C}_1$ in light turquoise, Euclidean $\mathcal{C}_2$ in dotted orange, poles of the integrand as red circles.

with the triangle's loop momentum k and the total momentum defined as $\Delta = Q' - Q$. Note that we choose Q' to be outgoing and Q to be incoming so that $Q' - Q$ defines the total outgoing momentum of the two photons. In Eq. (3.3) we have also introduced the helicity vectors ϵ_μ^Q and $\epsilon_\nu^{Q'}$. These project the scattering amplitude to outgoing photons with a definite helicity, either $+$ or $-$ depending on the form of the ϵ_μ chosen.

The trace expression in the numerator evaluates to

$$\mathrm{Tr}\left[\gamma^\mu(\not{k}+m)\gamma^\nu(\not{k}+\not{Q}+m)\gamma^5(\not{k}+\not{Q}'+m)\right] = 4i\,m\,\varepsilon^{\mu\nu\alpha\beta}\,Q_\alpha Q'_\beta\,. \qquad \mathsf{M} \qquad (3.5)$$

Since this is invariant under the simultaneous exchange of $\mu \leftrightarrow \nu$ and $Q \leftrightarrow Q'$, the second term in Eq. (3.4) equals the first and the total gives

$$M^{\mu\nu} = 8m\,\varepsilon^{\mu\nu\alpha\beta} Q_\alpha Q'_\beta \int \frac{d^4k}{(2\pi)^4} \frac{1}{[k^2-m^2]\,[(k+Q)^2-m^2]\,[(k+Q')^2-m^2]}\,. \quad \mathsf{M} \quad (3.6)$$

In the functional approach, we work in Euclidean conventions (see Appendix A). If properly treated the result is independent of whether the integral is evaluated in Minkowski or Euclidean space. The difference between the Minkowski and Euclidean metrics is in the relative sign between the time and space components of the squared four-vectors

$$k_M^2 = (k_0)^2 - \vec{k}^2 \quad , \quad k_E^2 = k_4^2 + \vec{k}^2\,. \qquad (3.7)$$

In order to switch from Minkowski to Euclidean metric we need to perform **two** changes: First we deform the integration path in the complex k_0 plane to run along the imaginary axis, see Fig. 8(b). This is the less trivial step and it is crucial to understand the pole structure of the integrand in order to perform a valid deformation. In the case of our integrand, poles occur in the second and fourth quadrant of the complex k_0 plane, which allows us to rotate the integration contour counter-clockwise (as indicated in the figure). The second step is to do a change of variables, by replacing $k_0 \to ik_4$. In summary the changes for the integration contour in time direction read

$$\int_{\mathcal{C}_1} dk_0 = \int_{-\infty}^{\infty} dk_0 \overset{①}{=} \int_{-i\infty}^{i\infty} dk_0 = \int_{\mathcal{C}_2} dk_0 \overset{②}{=} i\int_{-\infty}^{\infty} dk_4\,, \qquad (3.8)$$

where the integration contours $\mathcal{C}_1$ and $\mathcal{C}_2$ are defined in Fig. (8b). A somewhat related discussion about the implications of poles structure in the complex plane comparing Minkowski and Euclidean with regards to scattering amplitudes can be found in Refs. [43, 44] and will recur in the calculation of the $\pi^0 \to e^+e^-$ decay rate in Sec. 5.3.

Returning to our integral in Eq. (3.4) and switching to the Euclidean metric gives

$$M^{\mu\nu} = -8im\,\varepsilon^{\mu\nu\alpha\beta}Q^{\alpha}Q'^{\beta}\int\frac{d^4k}{(2\pi)^4}\frac{1}{[k^2+m^2]\,[(k+Q)^2+m^2]\,[(k+Q')^2+m^2]}\,. \tag{3.9}$$

This can be further evaluated using Feynman (Eq. (A.15)) and Schwinger parameters (Eq. (A.16)):

$$\begin{aligned} M^{\mu\nu} &= 8im\,\varepsilon^{\mu\nu\alpha\beta}Q^{\alpha}Q'^{\beta}\left(\frac{1}{16\pi^2}\right) \\ &\quad\times\int_0^1 dx\int_0^{1-x}dy\,\frac{1}{m^2+Q^2x(1-x)+Q'^2y(1-y)+xy(\Delta-Q^2-Q'^2)}\,. \end{aligned} \tag{3.10}$$

Finally setting the momenta to their on-shell values ($Q^2 = Q'^2 = 0$ and $\Delta^2 = -m_\pi^2$), Eq. (3.10) simplifies to

$$\begin{aligned} M^{\mu\nu} &= \left(\frac{im}{2\pi^2}\right)\varepsilon^{\mu\nu\alpha\beta}Q^{\alpha}Q'^{\beta}\int_0^1 dx\int_0^{1-x}dy\,\frac{1}{(m^2-xy\,m_\pi^2)} \\ &= 8m\,\varepsilon^{\mu\nu\alpha\beta}Q^{\alpha}Q'^{\beta}\left(\frac{-i}{16\pi^2}\right)\frac{1}{m^2}\left[\frac{1}{2}+\frac{(m_\pi/m)^2}{24}+\frac{(m_\pi/m)^4}{180}+\mathcal{O}\left((m_\pi/m)^6\right)\right], \end{aligned} \tag{3.11}$$

where in the second step we have expanded about $m_\pi/m = 0$. The integral evaluates to a real number, only if $m > m_\pi/2$. In this case, the loop particles cannot go on-shell and no singularities arise in the integral. The general integral evaluates to a poly-logarithmic function. Using the expansion we can easily see that the series converges quickly and we consider the leading order term in Eq. (3.11) as the final result.

Inserting the result for $M^{\mu\nu}$ back into Eq. (3.3) gives the result for the decay amplitude, $\mathcal{M}$. Taking the magnitude squared, summing over photon polarizations and multiplying by the phase-space, gives the total rate,

$$\Gamma(\pi^0\to\gamma\gamma) = \frac{\alpha_e^2}{64\pi^3}\lambda^2\frac{m_\pi^3}{m^2}\,. \tag{3.12}$$

In a last step we need to assign values for the Yukawa coupling λ and the mass m of the fermion running in the loop, which can be done by matching to the chiral Lagrangian. We find $\lambda = \frac{m}{f_\pi}$, so that the parameter m cancels and the final result becomes

$$\Gamma(\pi^0\to\gamma\gamma) = \frac{\alpha_e^2}{64\pi^3}\frac{m_\pi^3}{f_\pi^2} = 7.77\text{eV}\,, \tag{3.13}$$

with the pion decay constant $f_\pi = 0.092\,\text{GeV}$. The experimental value is (7.8 ± 0.9) eV. This shows that, to the current experimental precision, the decay rate for the neutral pion is completely governed by the anomaly.

Although we mentioned at the beginning that this decay comes from the anomaly, so far we have not directly used this in the calculation. But we have used it indirectly, because if the axial symmetry would not be anomalously broken, the triangle diagrams would evaluate to zero. To see this, recall the equation for the anomaly as introduced in Sec. 2.1 in Tab. 2,

$$\partial_\mu J_\mu^{a5} = \frac{e^2}{16\pi^2}\,\varepsilon^{\alpha\beta\mu\nu}F_{\alpha\beta}F_{\mu\nu}\,\text{Tr}_F\left[t_aQ^2\right]\,\text{Tr}_C\left[1\right]\quad,\quad Q = \frac{1}{3}\begin{pmatrix}2&0&0\\0&-1&0\\0&0&-1\end{pmatrix}, \tag{3.14}$$

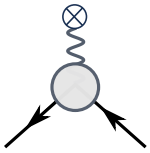

a_μ : Theory contribution	Value $\times 10^{-11}$	Uncertainties $\times 10^{-11}$
QED	116 584 718.931	0.09
Weak	153.6	1
HVP	6931	40
HLbL	**91**	**18**
(HVP+HLbL) NLO	2	1
Total	116 591 896.531	60
Experiment BNL E821 [45]	116 592 080	63

Table 1: Comparison between uncertainties on a_μ for the individual theory contributions and the current most precise measurement from Brookhaven, where the number is based on Ref. [46]. Theoretical numbers are updated based latest results present at the $g-2$ initative meeting (Sep. 2019) [47].

where Q is the quark charge matrix, t_a the generators of the $SU(N_f)_A$ symmetry group and $F_{\alpha\beta}$ the dual photon tensor. In principle, a similar term would appear from QCD with gluon instead of photon tensors. However this vanishes because all quarks have the same color charge, so that Q is replaced with the identity matrix.

As mentioned previously, anomalous breaking occurs when the classical theory does not share the symmetry of the quantum theory. The classical $SU(N_f)_A$ symmetry would tell us that the triangle integral should evaluate to zero. When performing the quantum field version, we need to regularize our integral due to divergences, and there are different choices for the regulator [1]. In fact the author in Ref. [2]-Ch.(75) shows that one can find a regulator such that the integral would evaluate to zero. However, in this case, gauge symmetry would be broken and this is not allowed for a consistent quantum theory.[2] One would rather choose a regulator that preserves the gauge and evaluates a non-zero value for the triangle diagram. Doing so, the regulator chosen changes the measure, this creates the invariant term quoted in Eq (3.14), which breaks $SU(N_f)_A$ and makes the triangle diagram Fig. (8 a) evaluate to a non-zero value, the so-called **anomaly value**.

The anomaly prediction is a powerful cross-check that any meaningful non-perturbative calculation needs to reproduce. To calculate the pion TFF in the full kinematic range, with virtual photon ($\{Q^2, Q'^2\} \neq 0$), one needs to perform a non-pertubative calculation using approaches such as lattice QCD or functional methods like DSEs (Sec. 2.3). Following the same pattern as the calculation of the anomaly prediction, the DSE calculation starts by evaluating the Feynman triangle diagram. Only in this case, the loop particles are quarks and not protons. The quarks are represented by their fully dressed propagator, including all loop corrections of the strong interaction. The quark propagator is obtained by iteratively solving the quark DSE Eq. (2.35). Additionally, the vertices appearing in the corners of the diagrams are dressed (previously bare), describing the interaction between meson and quarks (meson amplitudes) or quarks and photons (quark-photon vertices). The details of the DSE calculation for the ($\pi \to \gamma\gamma$) TFF will be shown in detail Sec. 4.

[1] In Ref. [2]-Ch.(75), the author begins the calculation using Weyl-Fermions, in which case the integral is indeed divergent and directly needs a regularization. The integral presented here is in fact finite, but a consistent regulator needs to be applied to the entire theory and, as is argued in Ref. [2], this leads to the anomalous contribution

[2] Gauge symmetries in QCD are the two vector symmetries $(U(1)_V, SU(N_f)_V)$. If they were broken we would lose properties like charge conservation and due to the broken gauge invariance the theory wouldn't be renormalizable anymore.

3.2 The muon's g-2

Like all charged particles with non-zero spin, leptons (electrons, muons, taus) carry a magnetic moment, which is aligned with the spin axis and is given by

$$\vec{\mu}_\ell = g_\ell \frac{Qe}{2m_\ell}\,\vec{s}, \qquad g_\ell = 2(1+a_\ell)\,, \qquad a_\ell = \frac{g_\ell - 2}{2}\,, \tag{3.15}$$

where the charge of the lepton can either be $Q = \pm 1$, m_ℓ is the mass, e the electronic charge, $\vec{s}$ the spin and g_ℓ the gyromagentic ratio. Dirac theory predicts that for a particle with spin $\frac{1}{2}$, the gyromagentic ratio is $g = 2$. However, the modern theoretical understanding, as well as experimental measurement, confirm that the value for g_ℓ is in fact greater then two. This deviation from the reference value is referred to as the anomaly and denoted by a_ℓ.

The deviation from 2 quantify the effects that arise due to quantum fluctuations. This makes it an excellent observable to probe all three interactions of the Standard Model(SM) and a possible indicator for new physics. In the SM, a_ℓ gets measurable contributions from QED, the strong interaction (QCD) and electroweak interactions:

$$a_\ell^{\mathrm{SM}} = a_\ell^{\mathrm{QED}} + a_\ell^{\mathrm{Had}} + a_\ell^{\mathrm{Weak}}\,. \tag{3.16}$$

The electron's anomalous magnetic moment, a_e, provides one of the most precise determinations for the fine-structure constant, α, and can be seen as an incredible achievement confirming experimental findings using QED and the SM. It is almost entirely explained by QED interactions between electron and photons. The best measurement of the electron's magnetic moment is currently achieved by the Harvard group [48]. On the theory side, as it is dominated by the QED contributions, the calculation is performed using perturbation theory. The current most precise value has evaluated Feynman diagrams up to the 8th order in α [49]. This leads to the current tension between the experimental and theoretic value of 2.5 standard deviations.

The muon's anomalous magnetic moment a_μ (or likewise called the muon's $(g-2)$, Eq. (3.15)) poses a somewhat more interesting case as there is a persistent tension between theory and experimental values of between $3-4\,\sigma$. (For a comparison of these values see last line of Tab.1.) Thus, the tension is higher than in the case of the electron. In addition, due to the muon's larger mass, it is expected to be more sensitive to new physics effects, which scale as $m_\ell^2/\Lambda^2_{\mathrm{BSM}}$. Similar to the electron, a_μ, is dominated by the QED contribution, which has been calculated up to fifth-order $\mathcal{O}(\alpha^5)$. This is considered sufficiently accurate in comparison to the uncertainties achieved in experiments. The same can be said for the weak contribution, which is at the level of two- to three-loop effects.

The main uncertainties of the theoretical prediction are due to strong-interaction effects, see comparison in Tab. 1. These come from the hadronic contribution, representing the strong-interaction dominated by the low-energy, non-perturbative regime of QCD. This has lead to great interest from both the experimental and the theoretical side to improve the QCD calculations to either confirm or resolve the discrepancy. The current precision on the experimental side lies around 0.54 part per million level from the E821 experiment at Brookhaven [45, 50]. Two new experiments at Fermilab [51] and J-PARC [52] are underway, aiming to reduce the experimental error by a factor of four. The final data analysis has been performed, and with this, new results from the Fermilab collaboration are expected this year. A combined effort from the theoretical side aims to publish a white paper around the same time as release of the updated experimental number. This paper summarizes the status of the leading theoretical calculation and concludes with the current theoretical prediction for a_μ, from analytic approaches (such as the dispersive calculation) and lattice calculations. With improved precision from both sides, it remains to be seen if the current tension will be resolved/reduced or increased, i.e. if a_μ will be a strong indicator for physics beyond the Standard Model [53, 54].

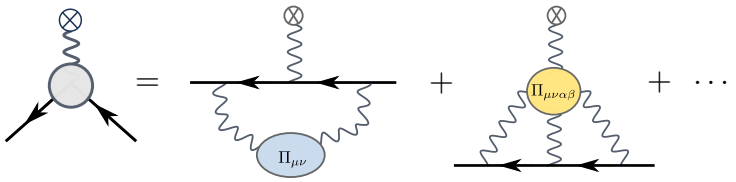

Figure 9: Shows the muon-photon-vertex, which includes the anomalous momentum of of the muon a_μ. The leading hadronic contributions for this vertex are the hadronic-vacuum-polarization (HVP)(middle diagram) and the hadronic Light-by-Light (HLbL) contribution (rightmost diagram).

Muon-photon-vertex. The magnetic moment of the muon is part of the photon-muon-vertex, Γ^α, which at the mass-shell of the muon can be decomposed as

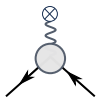

$$= \bar{u}(p')\,\Gamma^\alpha\,u(p) = \bar{u}(p')\left[F_1(Q^2)\gamma^\alpha - F_2(Q^2)\,\frac{\sigma^{\alpha\beta}Q^\beta}{2m_\mu}\right]u(p)\,. \tag{3.17}$$

Here p and p' define the lepton momenta, with corresponding spinors for incoming and outgoing muons. We have also introduced m_μ as the muon mass, Q as the photon momentum and $\sigma^{\alpha\beta} = \frac{-i}{2}\left[\gamma^\alpha, \gamma^\beta\right]$. The anomalous magnetic moment, a_μ, is proportional to the second tensor component, $F_2(Q^2)$, also called the Pauli form factor.

To calculate the hadronic contribution we thus need to write down the corresponding Feynman diagrams, project onto the second scalar amplitude and take the limit for $Q^2 \to 0$. The corresponding projector is given by the expression in the rectangular brackets in the following equation and a_μ is given by the product of projector and the muon-photon-vertex $\Gamma^{\rho\sigma}$, such that

$$a_\mu = F_2(0) = \frac{im_\mu}{12}\lim_{Q\to 0}\mathrm{Tr}\Big[\left[\gamma^\rho, \gamma^\sigma\right]\,\Gamma^{\rho\sigma}(q_q, q_2, q_2, q_3, Q)\Big]\,. \tag{3.18}$$

The diagrams at leading order of the hadronic contributions can be seen in Fig. 9. Historically, the largest error arose from the leading contribution, the **hadronic-vacuum-polarization** (HVP), which corresponds to first diagram in the series representing the muon-photon vertex in Fig. 9. However, due to the forthcoming data from e^+e^- experiments, data-driven dispersive calculations have been able to reduce the error, such that a proper error estimate on the sub-leading contribution (second diagram) is getting more and more relevant. The dispersive approach currently poses as the best result from the theoretical side, as it provides an error estimate that is systematic and smaller than current lattice calculations, compare Refs. [55–62]. The HVP is an interesting quantity as it probes the behavior of the quark-photon vertex, as introduced in Sec. 2.4.3, Eq. (2.67), and has been calculated in the context of the DSE approach in Refs. [63, 64].

The sub-leading diagram is **the Hadronic-Light-by-Light** (HLbL) contribution, shown in the rightmost diagram in Fig. 9. Different than in the HVP case, a systematic error estimate for this contribution is much harder, as it is not as easily related to experimental data, and all present calculations carry some level of model dependence. On the other hand, Lattice QCD is making remarkable progress towards calculating the photon four-point function, $\Pi_{\mu\nu\alpha\beta}$, in the HLbL tensor, from first principles. In addition, the dispersive approach has been able to provide estimates with a systematic error for the leading contribution of this tensor.

However, until such calculations are ready, it is highly encouraged that other non-perturbative approaches take on this challenge, as even an approach with a less systematic error estimate can guide future calculations. In this sense, the functional methods can be

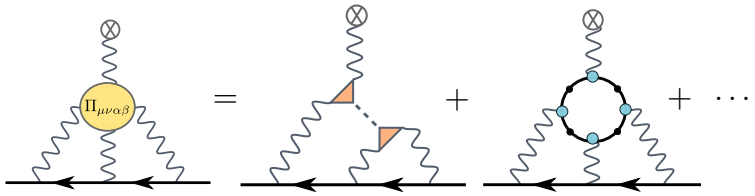

Figure 10: Hadronic-Light-by-Light contribution part to a_μ. The *first* diagram is the meson-exchange contribution. *Second*, the quark-loop contribution.

seen as a complementary tool to lattice QCD and the dispersive calculations. In contrast to the lattice calculation, where one directly evaluates the full four-point function, the dispersive approach decomposes the HLbL tensor into further individual contributions. Our DSE calculations follow along the lines of the dispersive approach, and thus it is natural to compare the intermediate results between the two approaches. This allows for a comparison between a first principles, but model-dependent DSE calculation, and the purely data-driven dispersion relation.

The muon's $g-2$ is, in fact, an **application** for the meson transition form factors, as they appear in the hadronic light-by-light contribution. In the next section, we will see how this part can be furthermore decomposed following the dispersive description, revealing the connection to the form factor.

3.2.1 The hadronic light-by-light contribution

The Hadronic-Light-by-Light (HLbL) part of the photon-muon vertex involved the photon-four-point functions, $\Pi_{\mu\nu\alpha\beta}$, second diagram on the left of Fig. 9. The full photon four-point function is a Green function of four external electromagnetic vector currents (as defined in Eq. (2.53)) and reads,

$$\Pi^{\mu\nu\lambda\sigma}(q_1,q_2,q_3,Q) = -i\int d^4x\, d^4y\, d^4z\, d^4w\, e^{i(q_1\cdot x+q_2\cdot y+q_3\cdot z+Q\cdot w)}\,\langle 0|\mathsf{T}\, j^\mu(x)j^\nu(y)j^\lambda(z)j^\sigma(Q)\,|0\rangle\,. \tag{3.19}$$

Based on Lorenz covariance, the matrix can be generally decomposed into 138 tensor structures times respective scalar amplitude functions, f_i. In Ref. [65], the authors show that only 136 of the elements are truly linear independent and the basis can thus be reduced such that,

$$\Pi^{\mu\nu\lambda\rho}(p,q,k) = \sum_{i=1}^{136} f_i(p,q,k)\,\tau_i^{\mu\nu\lambda\rho}(p,q,k)\,, \tag{3.20}$$

with the momenta in the s-, t- and u-channels given by $p = q_2+q_3 = -q_1-q_4$, $q = q_3+q_1 = -q_2-q_4$ and $k = q_1+q_2 = -q_3-q_4$. The reductions from 138 to 136 elements is a non-trivial task as one has to make sure to avoid the introduction of any singularities in the remaining dressing functions.

Gauge invariance requires the four-point function to satisfy the vector-Ward-Takahashi identity (VWTI), Eq. (2.63),

$$\{q_1^\mu, q_2^\nu, q_3^\lambda, Q^\sigma\}\,\Pi^{\mu\nu\lambda\sigma}(q_1,q_2,q_3,Q) = 0\,, \tag{3.21}$$

where the momentum of the on-shell photon is a linear combination of the others, $Q = q_1+q_2+q_3$. Imposing this constraint will furthermore reduce the number of basis elements. In this step one should again keep in mind that we want to construct a basis where the scalar functions are free of kinematic singularities and zeros and are truly independent. This is especially important as we want to apply a dispersion relation to decompose the photon

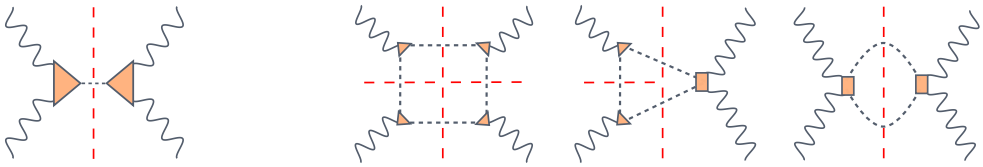

Figure 11: Contribution to a_μ^{HLbL}: Dispersive pion-pole (left) and pion-loop (right) contributions to the photon four-point function $\Pi^{\mu\nu\alpha\beta}(q_1, q_2, q_3, Q)$. The red line indicated that the intermediate propagators are on-shell. The diagrams should be seen as a diagrammatic representation of a unitary relation rather than a usual Feynman diagram. With bare vertices these correspond to the exact set of diagrams in scalar QED.

four-point function into individual contributions later on, and this requires the function to be analytic in the upper-half plane (the general concept of the dispersion relation is summarized in App. C). A scheme to construct an appropriate basis for such a Green function was introduced in the context of Compton scattering in Ref. [66] and Ref. [67]. This leads to a further reduction to 54 tensor structures. The construction in the case of the HLbL tensor is summarized in multiple references, see Refs [65, 68] for more details.

Now let us return to the full Feynman diagram of the Hadronic-Light-by-Light (HLbL) contribution, which is given on the right hand-side of Fig. 10 and can be expressed mathematically by

$$\Gamma^{\rho\sigma} = \int_{q_1}\int_{q_3} \Lambda_+(p')\,\gamma^\mu\,S(k_1)\,\gamma^\nu\,S(k_2)\,\gamma^\lambda\,\Lambda_+(p) D^{\mu\mu'}(q_1)\,D^{\nu\nu'}(q_2)\,D^{\lambda\lambda'}(q_3) \times \frac{\partial}{\partial Q^\rho}\Pi^{\mu'\nu'\lambda'\sigma}(q_1, q_2, q_3, Q)\,, \tag{3.22}$$

and which includes a derivative with respect to the total momentum of the external muon Q. Furthermore, m_μ denotes the muon's mass, S its propagator, Λ_+ its positive-energy projector and $D^{\lambda\lambda'}$ the photon propagator. We abbreviated the momentum integration in four dimensions by $\int_{q_i} := \int d^4q_i/(2\pi)^4$. To extract a_μ^{HLbL} from the full photon-muon vertex $\Gamma^{\rho\sigma}$, we can apply a set of operator projector techniques [55, 69, 70] and expand the vertex around the momentum of the external photon at $Q = 0$, as already indicated in Eq. (3.18), and leads to the following expression,

$$a_\mu^{\mathrm{HLbL}} = \int_{q_1}\int_{q_3} \left[\frac{\partial}{\partial Q^\rho}\Pi^{\mu'\nu'\lambda'\sigma}(q_1, q_2, q_3, Q)\right]_{Q=0} \times \mathrm{Tr}\Big\{ [\gamma^\sigma, \gamma^\rho]\;\Lambda_+(p')\,\gamma^\mu\,S(k_1)\,\gamma^\nu\,S(k_2)\,\gamma^\lambda\,\Lambda_+(p) D^{\mu\mu'}(q_1)\,D^{\nu\nu'}(q_2)\,D^{\lambda\lambda'}(q_3)\Big\}\,, \tag{3.23}$$

where the most complicated object is the photon four-point function.

To calculate the photon four-point function we follow along the lines of the dispersive approach, which offers a unique expansion in terms of diagrams involving one or more intermediate particle states [68, 71–74]. This comes from the unitary relation, which makes it possible to define the contribution to full four-point function from one-hadron, two-hadron, and multi-hadron intermediate states, in direct and crossed channels. Fig. 11 is to be understood as the diagrammatic version of this unitary relation, displaying the diagrams for the one- and two-particle cuts. These individual contributions are then obtained by applying a dispersion relation to relate them to experimentally measurable quantities such as form factors and cross-sections. The complexity of $\Pi^{\mu\nu\rho\sigma}$ makes it hard to sum over all underlying states in the unitarity relation, as done in the case of the HVP. Thus, the aim for the HLbL

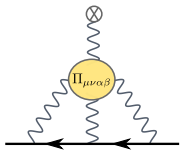

Collaboration	a_μ^{HLbL} $[10^{-11}]$ GeV
Lattice	72(39.8)(16.5)
Analytic approaches	91 ± 18
Glasgow consensus [76]	(105 ± 26)

Table 2: Comparison of the full hadronic-Light-by-Light contribution to a_μ. The most recent numbers are for the lattice and analytic result are taken from the newly released white paper [47] and compared to the previous value at a meeting in Glasgow in 2009 [76].

contribution is to include all possible states to reach up to a desired accuracy, starting with the leading ones.

When we look at the general decomposition of the tensor in terms of basis elements, it can be shown that the mass dimensions of these elements are of dimensions 4, 6 and 8, such that we expect the corresponding scalar dressing functions, f_i, to be strongly suppressed for higher energies. Using this knowledge, one can write down a once-subtracted dispersion relation, see Ref. [75]. To obtain to scalar dressing function through the dispersion relation, one then requires the knowledge of the residues at all poles (in case of single-particle intermediate state) or the discontinuities along the branch cuts (for multi-particle).

This amounts to constraining form factor amplitudes and decay vertices, which can be obtained either directly from experimental data or by dispersively reconstructing the quantities from related experimental data sets. This corresponds to a pure data-driven dispersive evaluation for a_μ^{HLbL}. However, the residues and discontinuities can also be calculated in any other non-perturbative framework, such as Lattice QCD or the functional methods pursued in this thesis, the DSE approach. This opens the possibility for comparison to a data-independent set-up and can furthermore be applied in cases where there is no experimental data available.

The contributions for one- and two-particle exchanges, Fig. 11, are divided into the meson-pole part (right diagram) and the meson-loop diagrams (on the left). The dispersion relation evaluates the intermediate propagator in the diagrams as on-shell quantities, where the single-particle exchange channel (meson-pole contribution) can be identified as the leading part, and the residue at its pole corresponds to the meson transition form factor (indicated as the orange triangle). The full diagram is given by two on-shell meson transition form factor and an intermediate on-shell free meson propagator. As this propagator is proportional to the inverse bound-state mass, the contribution of the lightest meson is considered the leading one, this is the **pion-pole contribution**. This contribution is a direct application of the pion transition form factor and details how to calculate this quantity in the DSE approach will be discussed in the next chapter, Sec. 4.5.

A similar conclusion can be taken for the meson-loop diagrams, as they are partly build of the same Green functions (meson form factors and propagators), making the pion-loop contributions the most relevant (after the pion-pole). One of the contributions of the pion-loop diagrams is the pion-box structure (second diagram of the right panel in Fig. 11). This contains a different form factor which describes the coupling between a pion and one external current, the pion electromagnetic form factor. In Ref. [77] we follow the dispersive set-up for the contribution in HLbL as sketch here, but apply the form factors calculated in the DSE framework. Details on the pseudo-scalar contribution will follow in Sec. 5.6.1, the box topology will not be review in this thesis and the reader is revised to Ref. [77] for details.

We conclude this section by quoting the recently published theory results for a_μ^{HLbL} from the $g-2$ theory-initiative white paper, compared to the previously agreed result from the theory community in 2009, see Tab. 2. The white paper differentiates between the two leading non-perturbative calculations for the hadronic contribution: Lattice QCD and the analytic

Experiment	Uncertain. $\times 10^{-11}$	Measured quantities	Uncertain. $\times 10^{-11}$
		Total ω_a statistics	53
Brookhaven E821	63	Final ω_a systematic	24
Goal Fermilab E89	16	Final $\tilde{\omega}_p$ systematic	20
Goal J-PARC E34	47	CODATA m_μ/m_e	2.6
		CODATA μ_p/μ_e	0.35
		Electrons $g-2$ factor, g_e	0.000035

Table 3: Comparison between uncertainties of $g-2$ experiments. Numbers are taken from Ref. [46] and experimental numbers therein from Ref. [45]. *Left*, experiments. *Right*, quantities measured in the BNL (and JLab) set-up and their associated error.

approach, which refers to a combined effort by data-driven approaches based on the dispersive expansion of the amplitude. Both numbers try to provide an average for multiple comparable results within the same framework, and aim to give a unified number as a benchmark for comparison with the experimental community.

At the current status, the dispersive number provides the most precise result from the theory side and compared to the Glasgow consensus this updated HLbL values reduces the discrepancy to the experimental number. Lattice calculations provide a pure first-principle approach but have not yet achieved a competitive precision. However, as the level of precision is comparable to the current experimental estimate, it serves as an important consistency cross-check and future calculation will continue to reduce the error from this side. Contributions from other non-perturbative methods, such as the DSE approach are contained in the dispersive analysis. As sub-leading channels are hard to obtain from a data-driven approach (due to the lack of data) results in this domain are dominated approaches containing model components.

3.2.2 Experimental status on the muon's g-2.

At the moment, the Brookhaven measurement, performed in 2006, is the most precise experimental analysis for the muonic g-2. The data was taken at the E821 experiment at Brookhaven National Lab [45]. In this measurement, they were able to achieve an uncertainty of 0.54 ppm, which represents a 14-fold improvement to a previous measurement performed at CERN.

The experimental set-up for this measurement is a somewhat unusual particle experiment, as the muons neither collide with another beam nor strike a target. Furthermore, they are "observed from a distance", to infer their spin orientation and their path around the magnet. The muon beam is created as the secondary product of a proton beam hitting a target, which consists of twenty-four 150-mm diameter nickel plates. When the beam hits the target it recoils and produces pions and muons as primary and secondary particles. After a few iterations, the beam line now contains a mix of protons, pions, and muons. This mixture beam is then lead into a delivery ring, where the protons get kicked out and the pions decay away into more muons ($\pi \to \mu\nu$), such that in this phase only muons enter the storage ring. The storage ring is a cyclotron, which accelerates the muons in a magnetic field outwards along a spiral path. The cyclotron keeps the muons in the spiral trajectory with a static magnetic field and accelerates by rapidly varying the electric field of the magnet.

Trapped in the cyclotron, one now measures magnetic properties of the muon. The muon's anomalous moment, a_μ, is related to the anomalous precision frequency of the muon, which can be determined by the difference between spin and cyclotron frequency of a muon moving

in the storage ring. To summarize, the relations are given by,

$$\vec{\boldsymbol{\omega}}_{\boldsymbol{a}} = \vec{\omega}_{\text{Spin}} - \vec{\omega}_{\text{cyclotron}} = -a_\mu \frac{qB}{m_\mu}\,, \quad \Rightarrow \quad a_\mu = \frac{\vec{\boldsymbol{\omega}}_{\boldsymbol{a}}}{\tilde{\boldsymbol{\omega}}_{\boldsymbol{p}}} \left(\frac{\mu_p}{\mu_e}\frac{m_\mu}{m_e}\frac{g_e}{2}\right), \quad \tilde{\boldsymbol{\omega}}_{\boldsymbol{p}} = \omega_p \otimes \rho(r)\,, \tag{3.24}$$

with the masses of muon and electron $m_{\mu,e}$, the average of the magnetic field seen by the muons, $\tilde{\omega}_p$, the gyromagnetic ratio of the electron, g_e, and the muon to proton ratio (μ_p/μ_e), which is determined from muonium hyperfine structure measurements. The quantities in the round bracket are all constants that are determined by other experiments and are taken as external inputs. This leaves the experiment to three quantities that needs to be measured, the averaged magnetic field seen by the muon, which consists of the free proton precision frequency, ω_p, and the distribution of the muons, $\rho(r)$, and finally, the anomalous precession frequency $\vec{\omega}_a$. The latter is derived from a time-histogram of the high-energy e^+-decay events that appear in the cyclotron.

Results from a new and independent measurement following up on the Brookhaven results are expected in early 2020 [46, 78–80]. The E989 experiment at FermiLab follows the same general set-up as the Brookhaven E821 (it even uses the same magnet, transported from Brookhaven) and has already taken all the required data over the past years. The analysis has been performed independently by several groups within the collaboration and the unblinding (removing a blinding factor that was randomly chosen and is kept secret by a few individuals in the collaboration) will be the last step before the final release of the data this year. The new results will show improvements compared to the previous error estimates by a factor of four, delivering a precision up to $\sim 16 \times 10^{-11}$ (recall $a_\mu^{\text{Had}} \sim 700 \times 10^{-10}$). There are four major improvements compared to BNL E821 experiment, which are expected to lead to a better precision in the analysis: (1) Improvements in statistics by storing more muons in the ring, (2) preparation of a more uniform magnetic field, (3) improvements on the instrumentation for measuring the precession frequency, ω_p, and last (4) a better reconstruction of the e^+-decay products, applying a more sophisticated model, which will help to improve ω_a.

There have been proposals for other future experiments to investigate a_μ as well, including J-PARC E34 (see references in Ref. [46]) or a new experiment in Japan. The latter would, for the first time, use a completely different measurement method, determining a_μ by trapping the muon in a cold atom. The results with improved precision from FermiLab E989 will already give some indication of whether the discrepancy between theory and experiment remains, in which case it would be a strong indicator for physics beyond the Standard Model, guiding the way into a new era of particle physics.

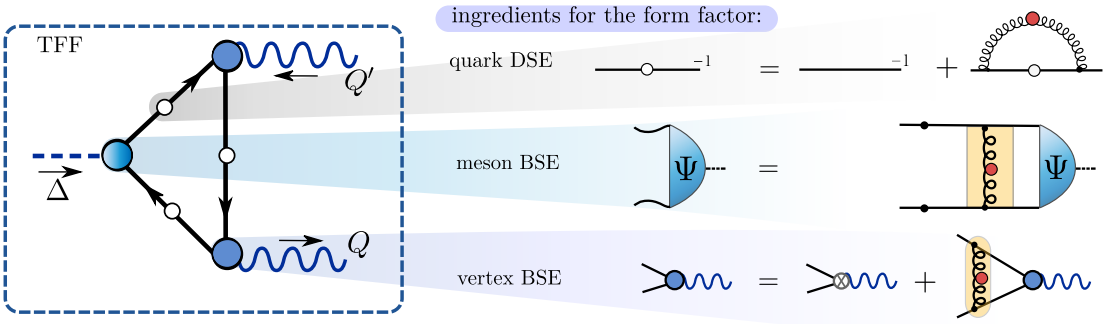

Figure 12: Overview of all transition form factor diagram when considered in the DSE approach and all its ingredients.

4 Transition form factors in the Dyson-Schwinger approach

Greens functions are the key ingredients in the functional Dyson-Schwinger approach. Elementary gauge-dependent correlation functions, such as propagators and vertices, serve as building blocks for more advanced gauge-independent Greens functions, such as bound-states, form factors and other production processes. In this section, we will combine our building blocks to calculate transition form factors in the DSE approach. The corresponding current matrix element is described by the triangle diagram seen in Fig. 12 upper left. It follows that the corresponding ingredients are, the **quark propagator**, the **quark-photon-vertex** and the **meson Bethe-Salpeter amplitude**. Each of those follows a Dyson-Schwinger equation or Bethe-Salpeter equation that is solved numerically and finally combined into the calculation for the transition form factor amplitude.

Transition form factors, in particular, the lightest meson form factor - the pion transition form factor, have been calculated in multiple non-perturbative approaches over the past years. Each of the methods coming its own set of advantages and difficulties, such that a combined effort and comparison between the approaches is strongly encouraged [25, 81–88].

The **DSE approach** is situated between phenomenological modeling and ab-initio non-perturbative calculations, such as lattice QCD. On the one hand, it is derived directly from the QCD Lagrangian and thus provides a first principle calculation, on the other hand, it includes a modeling component due to approximations that need to be taken in order to allow for numerical evaluation.

Advantages of the approach are

- its Standard model nature. As it is derived directly from the QCD Lagrangian, it does not depend on experimental data (besides fixing the scale). Thus it can make independent predictions that are not contaminated by new physics (beyond the Standard Model physics). Hence, a discrepancy between experiment and DSE results can make a strong case for the existence of BSM physics.

- that it deals with the fundamental degree of freedom, quarks and gluons, delivering a unified description of physical phenomena at all scales.

- that (contrary to a NJL model), it takes the full momentum and tensor dependence of the intermediate gauge-fixes objects into account.

- and that the computational effort for solving these iterative integral equations is at a reasonable time-scale. Such that one can guide other approaches by giving insights on phenomenological behavior and possible constraints.

On the other hand, one of the main *challenges* for the functional approach is to provide a reliable error estimate. The generally derived set of Dyson-Schwinger equations poses an infinite tower of the coupled integral equation, which needs to be truncated to allow numerical evaluations. It is extremely hard to quantify the error for the neglected higher-order Green functions. Thus, in particular, for physics requiring high precision, the DSE framework with the current truncation methods is not suited well.

This chapter contains details on how to calculate the individual **ingredients**, Tab. 12, and concludes with the combination of all parts into our main objective, the transition form factor in the DSE approach.

4.1 Quark

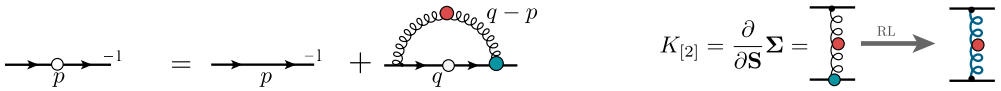

Figure 13: *Left*, Dyson-Schwinger equation for the quark propagator. *Right*, sketched approximation for the self-energy term (or likewise interaction kernel $K^{(4)}_{[2]}$) in the so-called "rainbow-ladder truncation" (RL).

The dressed quark propagator is given by,

$$\mathbf{S}(p) = \frac{-i\not{p}A(p^2) + B(p^2)}{p^2\,A^2(p^2) + B^2(p^2)} = Z_f(p^2)\,\frac{-i\not{p} + M(p^2)}{p^2 + M^2(p^2)} = -i\not{p}\,\sigma_v(p^2) + \sigma_s(p^2)\,, \tag{4.1}$$

where the momentum dependent dressing functions $A(p^2)\,, B(p^2)$ (respectively $Z_f(p^2)\,, M(p^2)$) reflect the scale dependence of the quantum corrections. The general form for the quark propagator follows from Poincaré covariance and includes a vector ($\sigma_v(p^2)$) and a scalar ($\sigma_s(p^2)$) tensor part, which are the only two possible terms. $M(p^2)$ is the quark mass function, which connects current quark mass, as seen in deep inelastic scattering processes at large momenta, to the constituent quark mass for small momenta. In the perturbative limit it reduces to the tree-level mass in the Lagrangian.

The quark propagator is calculated by solving the iterative Dyson-Schwinger equation (DSE), here given as the renormalized version of the previously quoted Eq. (2.35) and graphically represented in the left panel of Fig. 13,

$$\mathbf{S}^{-1}(p) = Z_2\,\mathbf{S}_0^{-1}(p) + \Sigma(p) = Z_2\,\big(i\not{p} + Z_m m\big) - Z_{1\,f}\,g^2\,C_F \int \frac{d^4q}{(2\pi)^4}\, i\gamma^\mu \mathbf{S}(q)\Gamma^\nu_{\rm qg}(q,p)\,D^{\mu\nu}(q-p). \tag{4.2}$$

The inverse quark propagator $\mathbf{S}^{-1}(p)$ equals its tree-level $\mathbf{S}_0^{-1}(p)$ part, where m is the renormalized quark mass from the Lagrangian, plus the self-energy quantum corrections, $\mathbf{\Sigma}(p^2)$. The latter is further specified through the dressed gluon propagator $D^{\mu\nu}(q-p)$ and a higher order Green function, the quark-gluon vertex $\Gamma^\nu_{\rm qg}(q,p)$. Both can be obtained by solving their own DSE, however will be replaced in a later section by an effective model for numerical calculations. The renormalization constants for the quark-gluon vertex is related to the coupling, quark and gluon renormalization constants (as introduced in Eq. 2.4) through ($Z_{1\,f} = Z_g\,Z_2\,Z_3^{1/2}$) and $C_F = (4/3)$ is a constant yielding from the flavor trace in case of $N_f = 3$.

The right panel in Fig. 14 shows a representative result for the quark dressing function calculated by iteratively solving the DSE for light quark masses ($m_{u,d}$) in a realistic truncation (rainbow-ladder, see Sec. 4.4). The effects of dynamical mass generation can be spotted

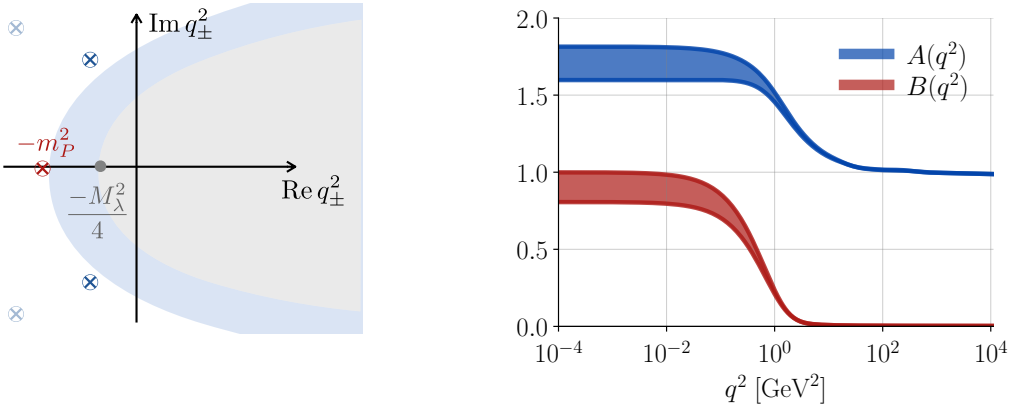

Figure 14: *Left*, sketch of the accessible parabola (shaded blue)) in the complex momentum plane of $q_\pm$. The first set of complex conjugated poles is located at the edged of the defined maxima-parabola with apex at m_P^2. *Right*, results for the quark dressing functions. This is a representative result in a realistic truncation, the rainbow-ladder approximation. The band correspond to a variation in the parameter in the effective interaction, Eq. (4.34), between $\eta \in \{1.85 \pm 0.2\}$.

in the infrared part of the propagators, as the quark mass function $M(p^2) \sim B(p^2)$ carries a non-zero value.

Quark condensate. In the chiral limit (when quark masses are zero, $m = 0$), the QCD action exhibits a chiral symmetry, but the Green functions at the quantum level do not. Precisely, Green functions with external quark anti-quark legs, such as the quark propagator $\langle 0|\bar{\psi}\psi|0\rangle$ do not share the symmetries of the action. The trace over this propagator evaluated in the chiral limit leads to the renormalization point dependent chiral condensate and is given by,

$$-\langle\bar{q}q\rangle = Z_2 Z_m N_C \int \frac{d^4p}{(2\pi^4)} \mathrm{Tr}\,\mathbf{S}(p) = \frac{N_C}{(2\pi)^2} \int dp^2\, Z_f(p^2)\, p^2\, \frac{M(p^2)}{p^2 + M^2(p^2)}\,, \tag{4.3}$$

where N_C is number of colors and $Z_{[i]}$ are the renormalization constants as introduced in Eq. (2.4). A non-zero value of the condensate signals **spontaneous chiral symmetry breaking**(SχSB) and comes from a non-zero value of the quark mass dressing function, $M(p^2)$ in Eq. (4.1). Both quantities can therefore be regarded as order parameters for identifying SχSB, and consequently the mass of the quark propagator is dynamically generated by the refractive effect. The effects of SχSB on the quark mass function can already be explored in a simple model. For a pedagogical introduction, starting with the simplest DSE and proceeding towards the full quark DSE, the reader is referred to references [5, 89].

In principle, we can define any other quantity that depends on the scalar quark condensate ($\langle\bar{q}q\rangle$) or the quark mass function ($M(p^2)$), and vanishes if these functions do, as an indicator for chiral symmetry breaking. The right place to look for such a connection is the axial WTI, Eq. (2.64). The right-hand side of this equation contains two quark propagators and can be easily transformed into the quark condensate. The consequences of spontaneous chiral symmetry breaking will be discussed in context with the pion amplitude in the next section, Sec. 4.2.

Singularities in the quark propagator In the functional DSE approach, all equations are defined in Euclidean space-time. In principle this means we can only access spacelike momenta, as $p_E^2 = p_0^2 + \vec{p}^{\,2} \Rightarrow p^2 > 0$. However, a great deal of interesting physical information (multi-particle observables, such as bound-state masses and form factor amplitudes) are

contained in the timelike region ($p^2 < 0$). These quantities require an analytical continuation from spacelike to timelike momenta. We choose to perform this continuation implicitly, by demanding that our Green functions are evaluated for timelike momenta, directly at their physical on-shell point ($p_E^2 = -m_\lambda^2$). In the Euclidean signature this is only possible by forcing the corresponding four-vector to contain complex values ($p_E^2 < 0 \;\Rightarrow\; \mathrm{Im}\, p_E^0 \neq 0$). However, this choice does not come without a price, as correlation functions contain poles in the timelike region and thus prevent a direct calculation when these singularities arise in the region of integration. One such correlation function is the quark propagator and its singularity structure leads to kinematic restrictions that ultimately limit the accessible momentum domain for most DSE calculations as lots of Green functions involving this fundamental quantity (such as the transition form factor).

The key point is that, when evaluating the quark propagator in the complex plane, one has to be careful to avoid the pole structures or treat them with a strategy, such as path deformation, to properly deal with these infinities. A similar situation will be discussed in Sec. 5.3.1 in context of the ($\pi^0 \to e^+e^-$) decay rate. Carefully analyzing the region where the quark-propagator is analytic will allow us to determine the regions which we are able to access. This ultimately translates into the types of observables and the kinematic regions that are available in the DSE framework with a chosen truncation. In particular, as the composite particle in a bound-state calculation, the quark propagator is evaluated in a parabola centered along the real axis opening into the complex momentum plane. The dressing functions of the quark propagator in Eq. (4.1) develop a certain singularity structure which, depending on the particular truncation, could be in the region of the probed kinematics in the BSE integral.

In a rainbow-ladder truncation the nearest singularities are complex conjugate poles in the timelike momentum region close to the real axis. It is convenient to define a parabola that covers the region where the quark propagator is analytic and in which it can be evaluated. The size and shape of this region depend on the constituent quark mass (see [90, 91] for a detailed investigation). For physical values of the quark mass, a sketch of the parabola is depicted in the left panel of Fig. 14. The figure shows the lowest-lying set of conjugated quark poles in the complex momentum plane and indicates the existence of further pole structures for larger negative momenta. The apex of the parabola is located on the negative real axis and reflects the location of the complex conjugated poles. It is standard to define this as a contour mass (or "pole mass"), which corresponds to the maximum accessible parabola before a calculation would hit the poles. A typical contour mass for the largest accessible parabola in case of light quark is $m_P^{\mathrm{Light}} \sim 0.5$ GeV. A throughout analysis of the analytic structure of quark and gluon propagators can be found in Refs. [90, 92, 93].

Due to the iterative nature of the DSE, solving the equation in the proximity of these poles is a highly non-trivial matter. It would require proper treatment (such as path-deformation) for the self-energy integral, in each step of the iteration. We circumvent this procedure by determining a kinematic "safe region" in which the Euclidean integral can be calculated directly without contour deformation, as we are simply avoiding the pole domains.

To identify a general criteria for such region, we consider a generic Lorentz-invariant integral,

$$\mathcal{I}(p_1, \ldots p_n) = \int d^4k_1 \int d^4k_2 \ldots f(q^2) \ldots \tag{4.4}$$

This integral depends on a collection of external momenta denoted p_i^μ and integrated loop momenta k_j^μ. The integrand is built from products of Lorentz-invariant functions, such as $f(q^2)$, where q^μ stands for a linear combination of external and loop momenta. The loop momenta k_j^μ are always real; however, in case of the on-shell demand for physical observables, the external momentum is time-like ($p_i^2 < 0$) and it will inject imaginary components into

$q^\mu \Rightarrow q \in \mathbb{C}$. Splitting q^μ into its real and imaginary parts, where A, $B \in \mathbb{R}$ and e_μ, e'_μ are Euclidean unit vectors, yields:

$$q_\mu = A\, e_\mu + iB\, e'_\mu \;\Rightarrow\; q^2 = A^2 - B^2 + 2iAB\,(e \cdot e')\,.$$

Because $e \cdot e' \in [-1, 1]$, the Lorentz invariant q^2 is tested inside a parabola $(A \pm iB)^2$ with apex $-B^2$ on the real axis; for $B = 0$ the parabola becomes the positive real axis. In other words, if q^μ has imaginary components then q^2 is sampled inside a complex parabola.

Now, if $f(q^2)$ has singularities in the complex plane, the corresponding parabola passing through the first singularity (e.g., a real pole, complex conjugate poles, or the onset of a cut) defines the "contour mass" $q^2 = -m_P^2$. The kinematically safe region is then defined by the restriction,

$$-B^2 > -m_P^2 \quad \Leftrightarrow \quad [\mathrm{Im}\, q_\mu]^2 = B^2 < m_P^2\,. \tag{4.5}$$

Because the imaginary part of q^μ can only come from the external momenta p_i^μ, this imposes restrictions on the domain of the external Lorentz invariants. The kinematic limitation in the quark propagator have consequences throughout different observables in the DSE approach, and we will explore the kinematic restrictions in the complete calculation of the transition form factor in in Sec. 4.5.

Quark in the complex plane. In the kinetically accessible domain, we can evaluate the quark propagator for complex momenta. Thereby we have the choice of how to distribute the momenta in the quark-self-energy term, which is flexible as long as momentum conservation is maintained. In our expression for the quark DSE, Eq. (4.2), the momentum distribution is chosen such that the complex momentum on the left-hand side of the equation p, is carried completely by the momentum of the gluon propagator $D^{\mu\nu}(q - p)$ on the right side. In this case the quark-propagator in the self-energy term only depends on the real loop momentum $S(q)$. Such that the full complex momentum is passed into the gluon propagator. As the gluon propagator and the quark-gluon vertex will be approximated by an effective interaction (see the section below in particular Eq. (4.33)), the complexity is ultimately running through the modeling component of the approach. This is the somewhat easier choice, as using a complex momentum in the model is trivial. However, it has a slight drawback as the model lacks accuracy for high complex momenta. In the case of heavier mesons, it is thus important to apply another choice, which is routing the complex momenta into the quark-propagator in the self-energy term. This requires a somewhat more advanced solving technique for the complex quark, as now we have to iterate the DSE in the complex plane. In this case one can apply an interpolation using Cauchy's integral theorem. A detailed discussion about different quark propagator calculations can be found in [91]. As this thesis work at the light meson spectra the **"naive method"** (passing the complexity through the gluon effective interaction) is applied throughout.

4.2 Mesons

The meson amplitude is jet another essential quantity in the form factor calculation and describes the transition between the decaying meson into its underlying structures of quark and gluons. To calculate the meson amplitude in the DSE approach we need to iteratively solve a **homogeneous Bethe-Sapeter equation** (BSE), as introduced in Eq. (2.45),

$$\mathbf{\Gamma} = \mathbf{K}\, G_0\, \mathbf{\Gamma}\,, \tag{4.6}$$

where $\mathbf{\Gamma}$ is the bound-state amplitude, $\mathbf{K}$ the 2-PI interaction kernel and G_0 the disconnected product of the full dressed n-point Greens function. When considering a meson (4-point

Greens function), $G_0^{(4)} = \mathbf{S}\,\mathbf{S}$ are two non-interacting quark propagators. In a next step let us specify the momentum dependence of these Green function and indicate the Lorentz, Dirac, color and flavor indices. As quarks are fermions, the according **Bethe-Salpeter amplitude** (BSA) needs to carry Dirac indices. The explicit choice for the underlying structure in these spaces depends on the quantum numbers (J^{PC}) of the considered meson. Dropping the flavor and color indices for now, the meson Bethe-Salpeter amplitude reads,

$$[\mathbf{\Gamma}]^{\mu_1\dots\mu_J}_{\alpha\beta}(p,P) = \int \frac{d^4q}{(2\pi)^4}\,[\mathbf{K}(P,p,q)]_{\alpha\gamma;\delta\beta}\,[S(q_+)\,\mathbf{\Gamma}^{\mu_1\dots\mu_n}\,S(q_-)]_{\gamma\delta}\,, \tag{4.7}$$

where P denotes the total and p the relative momentum of the meson and the quark anti-quark kernel furthermore depends on the loop momentum q. The graphical depiction is shown in the right panel of Fig. 15 . $S(q_\pm)$ represent the dressed quark propagator, as introduced in Eq. (4.2) and is evaluated at

$$q_+ = q + \sigma P\,, \qquad q_- = q - (1-\sigma)P\,, \tag{4.8}$$

with the momentum partitioning parameter $\sigma \in [0,1]$. In Dirac space, a Bethe-Salpeter amplitude corresponds to 4×4 matrices, and states with a non-zero integer spin $J > 0$ carry the corresponding number of Lorentz indices $(\mu_1 \dots \mu_J)$. The BSA can be expanded in terms of its underlying tensor basis and scalar function f_i and is in this case given by

$$[\mathbf{\Gamma}(p,P)]^{\mu_1\dots\mu_J}_{\alpha\beta AB ab} = \sum_i f_i(p^2, p\cdot P, P^2)\;[\tau_i(p,P)]^{\mu_1\dots\mu_J}_{\alpha\beta}\otimes\mathcal{C}^{AB}\otimes\mathcal{F}^{ab}\,, \tag{4.9}$$

where we now indicated the matrix in flavor $\mathcal{F}^{ab}$ and color space $\mathcal{C}^{AB}$ for completion. Once the tensor basis is fixed, the information about the momentum behavior of the bound-state ultimately lies in the Lorentz-invariant-scalar functions f_i, Eq. (4.9), and we can rewrite the BSE into a coupled set of integral equations for each function, by contracting with Dirac structures that individually project out each function. These projectors $P^{\mu_1\dots\mu_J}_{\alpha\beta}(p,P)$ are normalized, such that the following holds,

$$P^{\mu_1\dots\mu_J}_{\alpha\beta}(p,P)\;[\tau_i(p,P)]^{\mu_1\dots\mu_J}_{\alpha\beta} = 1\,,\quad\Rightarrow\quad P^{\mu_1\dots\mu_J}_{\alpha\beta}(p,P)\;[\mathbf{\Gamma}(p,P)]^{\mu_1\dots\mu_J}_{\alpha\beta} = f_i(p,P)\,. \tag{4.10}$$

Recall that Eq. (4.6) comes from an evaluation of the general n-point BSE in the proximity of a bound-state pole. Strictly speaking, it thus only holds for the choice of "on-shell" total momenta, $P^2 = -M_\lambda^2$. The product of complex conjugated time normal BSA was identified as the residue at the pole and it is thus, by definition a singularity free function. On the other hand, this also means that any choice of total momentum $P^2 \in \mathbb{C}$ where Eq. (4.6) holds, corresponds to a bound-state and originally to a pole in the n-point Green function $\mathbf{G}$. As already mentioned, we can distinguish different bound-states by choosing an explicit form of the expansion in Eq. (4.9) motivated by the quantum numbers J^{PC} of interest. However, for a chosen quantum number there is still multiple states that fulfill Eq. (4.6), which correspond to ground-states and radially excited states. Here we identify, that $P^2 \in \mathbb{C}$, where the $P^2 = -M_\lambda^2 \in \mathbb{R}$ corresponds to the ground-state and all complex-valued masses are excited states.

To look for multiple solution of Eq. (4.6) we can reinterpret the equation introducing an artificial momentum dependent eigenvalue $\lambda(P^2)$,

$$\mathbf{\Gamma}\,\lambda(P^2) = \mathbf{K}\,G_0\,\mathbf{\Gamma}\,. \tag{4.11}$$

which turns the BSE into an **eigenvalue equation** corresponding to the original BSE whenever the eigenvalue equals one, $\lambda(P_\lambda^2) = 1$. Any value for P_λ^2 which fulfill this requirement then corresponds to an eigenvector of the equation, which corresponds to a bound-state. We

Figure 15: Bethe-Salpeter equation for a meson ($K = K^{(4)}_{[2]}$). In the rainbow-ladder truncation the kernel is approximated by an effective model, Eq. (4.34)

can thus determine the eigenvalue spectrum $\lambda(P^2)$ for the matrix $\mathbf{K}\,G_0$ and whenever it crosses one, read of the bound-state masses as $P^2_\lambda = -M^2_\lambda$ and calculate the corresponding BSA $\mathbf{\Gamma}_\lambda(p,P) = \mathbf{\Gamma}_\lambda(p^2, p\cdot P, P^2 = -M^2_\lambda)$. Numerically the kernel on the right-hand side of the BSE is in fact a square matrix, where the total size corresponds to the number of grid-point chosen for the discretization of the momentum and Dirac dependence.

To **summarize**, the meson Bethe-Salpeter equation is a homogeneous eigenvalue equation for bound-state amplitudes. The amplitude can be expanded into individual tensor components times scalar functions and the equation can then be rewritten into coupled integral equation for these Lorentz-invariant dressing functions. The eigenvalue spectrum determines the masses for ground and excited states of a bound-state with chosen quantum numbers J^{PC}.

Normalization. As already mentioned in Sec. 2.4.3, by solving Eq. 4.11 for $\lambda(P^2) = 1$, the Bethe-Salpeter amplitude is only determined up to a multiplicative constant, due to the iterative nature of the equation. We need to fix the normalization using the condition introduced in Eq. (2.50). The normalization is performed after solving the eigenvalue equation and completes the determination of a normed BSA. Once the BSA is normalized we can use it to calculate physical observables, such as decay constants. In case of the rainbow-ladder truncation the expression reduces to the first term only, as the interaction kernel does not depend on the total momentum and the derivative in the second term of Eq. (2.50) vanishes. In this case the normalization condition reduces to,

$$-1 = \frac{d}{dP^2}\,\mathrm{Tr}_{\mathrm{DCF}}\left[\int_q \bar{\mathbf{\Gamma}}(q,-P_\lambda)\,S(q_-)\,\mathbf{\Gamma}(q,P_\lambda)\,S(q_+)\right]\Big|_{P^2=-M^2_\lambda}. \tag{4.12}$$

We additionally used the cycling properties of the trace to slightly rewrite the equation compared to Eq. (2.50) and pulled the derivative with respect to P^2 up front. Remember that the objects on the left are matrices in Dirac, color and flavor space. Note, once more, the important distinction between the total momentum P^2, which is the variable we drive with respect to, and the **fixed** bound-state momentum $P^2_\lambda = -M^2_\lambda$. Thus the derivative in Eq. (4.12) only acts on the quark propagators $S(q\pm) = S(q,P)$. The conjugated amplitude is given by applying the charge conjugation matrix $\mathcal{C} = \gamma_0\gamma_2$, such that $\bar{\mathbf{\Gamma}}(p,P) = \mathcal{C}\,\Gamma^{\mathrm{T}}(-p,-P)\,\mathcal{C}^{\mathrm{T}}$. In the case of a meson with a Lorenz index (vector or axial-vector), one needs to additionally average over polarization, by projecting with the transverse tensor and dividing by three. This leads to an additional factor of $(t^{\mu\nu}(P)/3)$ in the integrand of Eq. (4.12). Contracting the indices in color and flavor space leads to factors N_C and N_f, The overall factor from the flavor and color part can vary depending in the particular choice of the normalization in these spaces. However this ultimately channels when the BSA is used in further calculation if one stays consist within a chosen definition.

Decay constant. The normalization of the amplitude is crucial when calculating physical observables. After we have normalized the amplitude we can for example calculate the decay constant of a meson with the relation from the current-matrix element, given by Eq. (2.58) or

Eq. (2.62). Evaluated at the mass-shell, the residues of the vertices correspond to these decay constants. To give a concrete examples, in case of the pion, we start with the pseudo-scalar current-vertex $\Gamma_{0\,5a}$ and evaluate it at on the pion mass-shell, leading to the definition of the pion decay constant as

$$f_\pi\, P^\mu = \mathrm{Tr}_{\mathrm{DCF}} \int \frac{d^4q}{(2\pi)^4}\, [\,\Gamma^\mu_{0\,5a}\, S(q_+)\Gamma(q,P)\, S(q_-)]\,, \tag{4.13}$$

with the Dirac-flavor matrix element $\Gamma^\mu_{0\,5a} = Z_2\,\gamma^5\gamma^\mu$ as defined in Eq. (2.54) and where the color and flavor trace, once more, leads to a factors of N_C and N_f up front (in our set-up this corresponds to $N_f N_C = 6$). The parameters in our truncation applied to the kernel in the BSE, are chosen such that we obtain a physical value for the evaluation of Eq. (4.13) corresponding to a pion decay constant of $f_\pi \approx 0.092\mathrm{GeV}$.

Momentum choice. As long as the on-shell condition is fulfilled Eq. (4.7) holds and is fully Lorentz invariant. If not needed in a particular frame, we usually evaluated the equation in the bound-states rest-frame, due to the simplicity of the involved momenta. In the rest-frame the four-vectors are specified by,

$$P = \begin{pmatrix} 0 \\ 0 \\ 0 \\ iM_\lambda \end{pmatrix}\,,\quad p = \sqrt{p^2}\begin{pmatrix} 0 \\ 0 \\ \sqrt{1-z^2} \\ z \end{pmatrix}\,,\quad p = \sqrt{q^2}\begin{pmatrix} 0 \\ \sqrt{1-z'^2}\,\sqrt{1-y^2} \\ \sqrt{1-z'^2}y \\ z' \end{pmatrix}\,, \tag{4.14}$$

where the total momentum is chosen to be on-shell $P^2 = -M_\lambda^2$ and thus timelike. This is motivated by the fact that one uses spherical coordinates to evaluate the integral on the right hand side of Eq. (4.7), such that the loop integral can be written as

$$\int d^4q = \int_0^\infty dq\, q^2 \int_0^\pi d\theta \sin^2\theta \int_0^\pi d\phi\, \sin\phi \int_0^{2\pi} d\psi = \frac{1}{2}\int_0^\infty dq^2\sigma \int_{-1}^{1} dz'\sqrt{1-z'^2}\int_{-1}^{1} dy \int_0^{2\pi} d\psi\,, \tag{4.15}$$

which contains a set of angles corresponding to the normlaized four-vector products, where the angle between the normalized relative and total momentum is defined as $z := \hat{P}\cdot\hat{p}$. In general the Bethe-Salpeter amplitude depends on three Lorentz invariants, $\{p^2, p\cdot P, P^2\}$, however as the squared total momentum is fixed by the on-shell condition ($P^2 = -M_\lambda^2$), it reduces to two: $\Gamma(p,P) = \Gamma(p^2, p\cdot P) = \Gamma(p^2, z)$.

It turns out that the angular dependence of the BSA scalar functions $f_i(p,P) = f_i(p^2,z)$ is extremely weak (in the case of light mesons). For this reason it is a common procedure to expand the angular dependence in **Chebyshev polynomials**[1], where considering up to a finite order is sufficient to describe the full angular behavior, see Ref. [95]. In principle, any kinda of polynomials that form an orthogonal basis can be used as an expansion, however the particular structure of the Chebyshev is well suited for the expansion in the $\theta = \cos^{-1}(z)$ angle. For $z \in [-1,1]$ the Chebyshev polynomials of the second kind $U_i(z)$ are given by the following recursive definition,

$$U_n(z) = \frac{\sin\left[(n+1)\cos^{-1}(z)\right]}{\sqrt{1-z^2}}\,,\quad U_n(z) = 2\,z\,U_{n-1}(z) - U_{n-2}(z)\,;\quad n = 2,3,\dots\,, \tag{4.16}$$

with $U_0(z) = 1$ and $U_1(z) = 2z$. As they form an orthogonal basis, they fulfill an orthogonality relation,

$$\sum_{k=1}^{N}(1-z^2)\,U_i(z_k)U_i(z_k) = a_{ij}\,,\quad a_{ij} = \begin{cases} (N+1)/2 & i = j \text{ and } i \le N-1 \\ 0 & i \ne j \text{ and } 0 \le i,j \le N-1\,. \end{cases} \tag{4.17}$$

[1]The common use of Chebyshev polynomials is motivated by an approximate $O(4)$ symmetry in bound-state calculation applying the rainbow-ladder truncation for the interaction kernel, see Ref. [94].

An angular dependent function is then expanded through the series by

$$f(z) = \sum_{i=0}^{n} c_i\, U_i(z)\,,\; c_i = \frac{2}{N+2} \sum_{i=1}^{N+1} (1-z_k^2) f(z_k) U_i(z_k) = \frac{2}{\pi} \int_{-1}^{1} \sqrt{1-z^2} U_n(z)^* f(z)\,, \tag{4.18}$$

and with the zeros of the polynomials $U_i(z_k)$ at $z_k = \cos(k\pi/(N+1))$ and both the discrete and the continuum definition for the Chebyshev coefficients c_i. When the bound-state amplitude needs to be evaluated in a boosted frame, z can be complex. However the rest-frame solution is only given for real angles ($z \in [-1,1]$). As the Chebyshev expansion allows for an analytic continuation within the convergence radius of $|z| < 0$, it is a useful tool when needing to change kinematic frames. It can furthermore provide a tremendous efficient gain in numerical evaluations.

Kinematic restrictions. As solving the BSE involves an evaluation of the quark propagator in the complex plane, it also suffers from kinematic restriction, due to the quark poles. In the case of a BSE, this limits the choice for the total momentum P, which corresponds to the accessible bound-states as this is directly connected to the mass. Evaluated at the on-shell point $P^2 = -M_\lambda^2$, and the complex part of the quark momenta is connected to the bound-state mass by,

$$q_\pm^2 = \begin{pmatrix} q+\eta P \\ q-(1-\eta)P \end{pmatrix}^2 = q^2 - \frac{M_\lambda^2}{4} \pm i M_\lambda \sqrt{q^2} z \Big|_{\eta=1/2}\,. \tag{4.19}$$

As the poles of the quark propagator appear at around $q_\pm^2 \approx -m_P^2$, where m_P is the "parabola" mass, defining as the apex of the parabola indicating the accessible region in the complex $q_\pm^2$-plane. If we consider the complex four-vector of the two quark-propagators $p_\pm^\mu$, we can separate it along the lines of Eq. (4.5) and with a choice of $\sigma = 1/2$, we find the following restrictions for the meson mass

$$\left[\mathrm{Im}\, q_\pm^\mu\right]^2 < m_P^2\,, \quad \Rightarrow \quad m_P^2 < -\frac{M_\lambda^2}{4}\,, \quad \Rightarrow \quad M_\lambda < 2 m_P\,. \tag{4.20}$$

The left panel in Fig. 14 sketches the parabola in $q_\pm$-plane probed in case of a BSE calculation (light-grey). In the figure the bound-state mass was chosen to fulfill the condition $M_\lambda < m_P$ (as in case of the pion), positioning the parabola corresponding to the BSE momenta $q_\pm$ inside the accessible domain, indicated by the quark-pole parabola (light blue). In this sense, we can easily access ground-states with small masses and run into restriction for excited states with potentially large masses. The calculation for a heavy-light meson is particularly challenging, as the mass of the light quark dictates the poles mass ($m_P^{\mathrm{Light}} \approx 0.5\mathrm{GeV}$), but the mass of a heavy-light bound-states is larger than a bound-state with only light quark content. In case of light-quark content we are limited to bound-state masses of around $M_\lambda^{\mathrm{Light}} < 1\mathrm{GeV}$.

Spontaneous chiral symmetry breaking and Goldstone's theorem. As explained previously, QCD flavor symmetries can be broken in different manners. Spontaneous breaking occurs if the symmetry of the action is not shared by the Green functions of the theory. An indicator for the spontaneous breaking of chiral symmetry is, e.g. the quark chiral condensate, Eq. (4.3). In the case of spontaneous symmetry breaking, Goldstone's theorem states the existence of massless particles. As an immediate consequence of the PCAC relation, Eq.(2.19) and by identifying the residue structure of the current-quark-antiquark transition matrices, we have obtained a relation between the residues of different matrix elements, Eq (2.59), which is restated here for convenience,

$$f_\lambda\, M_\lambda^2 = 2\, m\, r_\lambda. \tag{4.21}$$

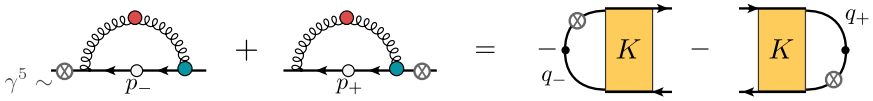

Figure 16: Axial-vector Ward Takahashi identity, Eq. (4.25), relating the interaction kernel **K** with the quark self-energy term Σ.

This relation told us that in the chiral limit ($m = 0$), either the decay constant f_λ or the mass of the bound-state must be zero. Hence if we can show that the decay constant is non-zero in the chiral limit, due to spontaneous symmetry breaking, we proved the existence of a massless particle and consequently Goldstones theorem. A combination of the relation above Eq. (4.21), the definition of the axial-vector and pseudo-scalar $\bar{q}q$-vertex, Eq. (2.60), and the AXWTI, Eq. (2.64) leads to the following relation for the pion decay constant,

$$f_\pi \, \mathbf{\Gamma}_\pi(p, P = 0) = B(p^2) \, \gamma_5 \,, \tag{4.22}$$

with the decay constant f_π, the pion Bethe-Salpeter amplitude $\mathbf{\Gamma}_\pi$ and the quark dressing function $B(p^2)$, Eq. (2.31). The relation has two important implications. On one hand it states that the pion amplitude in the chiral limit is entirely determined by the dressing function of the quark propagator. More importantly it implies that the decay constant is non-vanishing in the chiral limit, as $B(q^2) \neq 0$ due to spontaneous symmetry breaking (recall the value of the function on the right side of Fig. 14) and thus $f_\pi \neq 0$, which ultimately means that due to the connection in Eq. (4.21), $M_\lambda = m_\pi = 0$ in the chiral limit and the pion can be identified as a massless Goldstone Boson. Additionally it serves as a consistency check when solving the pion's Bethe-Salpeter equations, as the normed BSA $\mathbf{\Gamma}_\pi$ has to fulfill the equality. As the pion mass is rather small an approximate version holds even away from the chiral limit. More Details on the derivation can be found in Ref. [5], Eq. (4.33-4.36).

In a last step one can transform Eq. (4.22) to incorporate the quark chiral condensate $\langle\bar{\psi}\psi\rangle$, Eq. (4.3). This is the **Gell-Mann-Oakes-Renner relation** (GMOR) and it is given by

$$f_\pi^2 \, m_\pi^2 = -2m \frac{\langle\bar{\psi}\psi\rangle}{N_f} \,. \tag{4.23}$$

To **summarize**, the theory exhibits a chiral symmetry when considering QCD in the chiral limit ($m = 0$). Due to the occurrence of the spontaneous breaking the mass of the quark propagator is dynamically generated $M(p^2) = (B(p^2)/A/(p^2)) \neq 0$ and respectively the quark condensate $\langle\bar{\psi}\psi\rangle$, and the decay constant carry nonzero values. Therefore the GMOR implies that the bound-state mass needs to be zero ($M_\lambda \to 0$). This corresponds to the massless Goldstone bosons as demanded by Goldstone's theorem. As chiral symmetry is only an approximate symmetry of nature, the Goldstone bosons do carry a non-zero mass, but it is, as expected from the theorem, rather small. Strictly speaking, the GMOR, Eq. (4.2), is only valid in the chiral limit because the condensate is only well-defined in this case. However, Eq. (4.21) can be seen as a generalized GMOR, since all quantities involved are well defined for all quark masses.

Quark anti-quark kernel. The 2-PI interaction kernel $\mathbf{K}^{(4)}_{[2]}(P, p, q)$ contains higher-order Greens functions and similar to the self-energy term $\Sigma(q, P)$ in the quark, it needs to be approximated to enable a numerical evaluation. In fact as shown in Eq.(2.39) and through the AXWTI, Eq. (2.64), the quark self-energy term and the interaction kernel are closely related. The constraints demanded by the AXWTI help us to construct a truncation for these Green functions, ensuring that important symmetries of our theory will be preserved (such as the GMOR). However, as a first guidance and before considering an explicit approximation

on the system of couple equation we can explore the connection given through Eq. (2.39). This relates the self-energy term to the kernel, by a derivative with respect to the quark propagator,

$$\mathbf{K}^{(4)}_{[2]}(P,p,q) = -\frac{\delta}{\delta\,\mathbf{S}}\,\mathbf{\Sigma}(\mathbf{S}) \simeq \Gamma^{\mu}_{\mathrm{qg}}(q,P)\,D^{\mu\nu}(q-p)\,(i\gamma^{\nu})\,, \tag{4.24}$$

where we inserted the definition of the self-energy part in terms of gluon propagator and quark-gluon vertex. Graphically we can interpret the derivative as "cutting the quark lines" in the self-energy diagram. Thus, deducing from the self-energy term, we expect the interaction kernel to be a combination of one bare and one dressed quark-gluon vertex Γ_{qg} and an intermediate gluon propagator $D^{\mu\nu}$, as indicated on the left side of Fig. 15.

However, since the derivative-relation is only valid under multiple assumptions and also does not imply that current conservation is incorporated, the AXWTI should be considered as guidance when constructing a truncation for the kernel. We can transform the general AXWTI, Eq. (2.64) by inserting the quark DSE, Eq. (4.2) and current vertex BSE, Eq. (2.56) into the AXWTI, then use the AXWTI jet another time to obtain the following relation,

$$\{\gamma^5\,\mathbf{\Sigma}(p_+) + \mathbf{\Sigma}(p_-)\,\gamma^5\}_{\alpha\beta} = -\int \mathbf{K}^{(4)}_{[2]\,\alpha\gamma,\delta\beta}(P,p,q)\,\{\gamma^5 S(q_-) + S(q_+)\gamma^5\}_{\gamma\delta}\,, \tag{4.25}$$

where once more $q_\pm = q \pm P/2$ and equally $p_\pm = p \pm P/2$ and where the Greek letters indicate a combination of Dirac, color and flavor indices and can be seen diagrammatically in Fig. 16.

Inserting the assumption,Eq. (4.24), into the relation obtained from the AXWTI, Eq. (4.25), we can see that in fact, the combination of quark-gluon-vertex and gluon propagator fulfills this requirement and can thus be used to describe the interaction kernel in a symmetry preserving manner. In the next step, we need to choose the explicit approximation for the higher-order Green functions in self-energy and kernel. This is done by modeling the quark-gluon interaction through an effective coupling. The simplest model of such a symmetry preserving truncation it the so-called rainbow-ladder truncation with the Maris-Tandy model. This is used throughout this thesis and will be explained in detail in Sec.4.4.

Results for the pion and scalar meson amplitudes will be presented in the corresponding section of the pion and scalar transition form factor Sec. 5.1 and 5.5.

4.3 Quark-photon vertex

We end the ingredients section with the last but most complex component of our triangle diagrams, the quark-photon-vertex (as found in both corner of the diagram Fig. 12). This object connects the non-perturbative QCD effects to QED physics by describing the interaction between quarks and photons. Electromagnetic current matrix elements, such as the transition form factor, strongly depend on the interaction effects contained in such vector vertices, as was already indicated in Sec. 2.4.3.

A numerical solution for the quark-photon vertex is obtained by solving the **inhomogeneous Bethe-Salpeter equation** for the vector $\bar{q}q$-vertex, see Refs. [63, 96–100]. The BSE is displayed in Fig. 17 (a.) and is given by,

$$\Gamma^{\mu}_{a} = \Gamma^{\mu}_{0\,a} + \mathbf{K}\;\Gamma^{\mu}_{a} = Z_2 i\gamma^{\mu} t_a + \mathbf{K}\;\Gamma^{\mu}_{a}\,, \tag{4.26}$$

with the inhomogeneous Dirac-flavor term $\Gamma^{\mu}_{0\,a}$. The kernel $\mathbf{K}$ on the right-hand side of the equation is the same 2-PI interaction kernel appearing in the meson BSE and we chose to truncate it with the same model for the effective quark-gluon interaction (as will be explained in the next section), since only a consistent treatment ensures the current conserving symmetry relations, such as the AXWTI Eq. (4.25).

The vertex carries one open Lorentz index and depends on two independent four vectors, or equally three Lorentz invariant scalar products $\Gamma^{\mu}(q,P) = \Gamma^{\mu}(q^2, q\cdot P, P^2)$. The argument

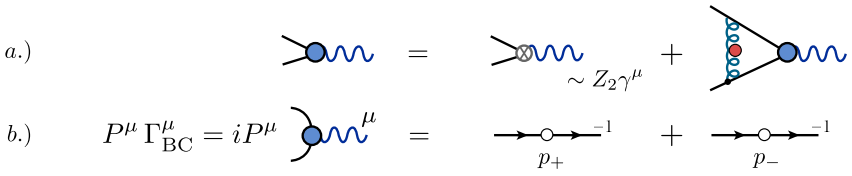

Figure 17: (a.) Inhomogeneous Bethe-Salpeter equation for quark-photon vertex. (b.) vector WTI, as introduced in Eq. (2.63), relating the longitudinal part of the vertex ($\sim P^\mu\Gamma^\mu$) to the dressing function of the quark propagator **S**.

p denotes the average momentum of the two quark legs and P is the incoming photon momentum. Different than in case of the meson BSE, the vertex is mostly evaluated for off-shell total momenta ($P^2 \neq -M_\gamma^2 \neq 0$), making the photon virtual. In this case, the inhomogeneous part of the equation remains. As it is a vector-current-vertex, it carries the quantum numbers $J^{PC} = 1^{--}$. The full vertex is described by twelves basis elements, where eight are purely transverse and the remaining four are the so-called "gauge"-part, as these are constrained by gauge invariance. We can break down the vertex amplitude Γ^μ, in the usual manner, expressing it as a product of basis components τ_i^μ and Lorentz-invariant scalar dressing functions f_i,

$$\mathbf{\Gamma}^\mu(p,P) = \sum_{i=1}^{12} f_i(p^2, p\cdot P, P^2)\,\tau_i^\mu(p,P)\,. \tag{4.27}$$

For a specification of the basis elements see App. B or App. B of Ref. [5]. Due to electromagnetic gauge invariance, the transverse- and gauge-part of the vertex decouple and we can rewrite the vertex as

$$\Gamma^\mu(p,P) = \Gamma^\mu_{\rm BC}(p,P) + \Gamma^\mu_{\mathbf{T}}(p,P)\,, \quad \Gamma^\mu_{\rm BC}(p,P) = i\gamma^\mu\Sigma_A(p,P) + 2p^\mu(i\not{p}\Delta_A(p,P) + \Delta_B(p,P)\,, \tag{4.28}$$

with the dressing functions of the Ball-Chiu vertex (gauge part) denoted as $\{\Sigma_A, \Delta_A, \Delta_B\}$. The Ball-Chiu (BC) vertex generally consists of four tensor components, however one of the associated dressing function is zero, such that the BC term consists of the three tensor structures quoted above. The transverse part is proportional to a basis for a vector meson. When solving the BSE for a vector meson, it is a homogenous equation, as it evaluates Eq. (4.26) in the proximity of the vector-meson pole, where the second summand dominates. The name **Ball-Chiu** vertex, $\Gamma_{\rm BC}$, was first introduced in Ref. [101] and has been explained briefly in the previous chapter, Eq. (2.65). The vector Ward-Takahashi-identity, Fig. 17 (b.), tells us that the BC part is completely determined by the dressing functions of the quark propagator **S**. The dressing function in the BC part are explicitly given by,

$$\Sigma_A = \frac{A(p_+^2) + A(p_-^2)}{2}\,, \quad \Delta_A = \frac{A(p_+^2) - A(p_-^2)}{p_+^2 - p_-^2}\,, \quad \Delta_B = \frac{B(p_+^2) - B(p_-^2)}{p_+^2 - p_-^2}\,, \tag{4.29}$$

with the momentum convention, $p_\pm = p \pm P/2$.

The transverse part vanishes for $P^\mu \to 0$, thus the BC part alone ensures current conservation. It also reproduces the perturbative limit, which ensures that when $Q^2 \to \infty$ the vertex behaves like the inhomogeneous term, $\Gamma^\mu \to Z_2 i\gamma^\mu$. This could lead to the assumption that this part of the quark-photon vertex would be sufficient to describe all electromagnetic effects relevant in calculation of transition current elements, such as the pion TFF. The vertex dependence of the TFF calculation will be investigated in Sec. 5.1 and reveal that it is, in fact, crucial to include the full vertex to reproduces the value of the QED anomaly, Sec. 3.1.

Since transverse and gauge part decouple, the equation can be separately solved for the corresponding dressing functions. in this sense, the vertex BSE can be either solved with the full twelve basis elements, or only for the vector transverse part to obtain the eight dressing functions $\tilde{f}_j$ and apply the BC functions for the remaining gauge functions. More details on the calculation and the full basis structures of the quark-photon vertex can be found in Appendix B.

When working in the rainbow-ladder truncation (see details below around Eq. (4.32)) the transverse part of the vertex contains vector-meson poles in the timelike momentum region. These infinities affect the slope of the vertex in the spacelike domain. When inserted in the TFF calculation, the TFF results inherit the functional form of vertex and it thus correctly implements the vector-meson dominance behavior. It should be stressed, that this structure of the vertex is achieved without the requirement for additional model parameters, and is achieved only, by applying the rainbow-ladder truncation consistently in all BSEs and DSEs to fulfill the symmetry constraints demanded by the AXWTI (Eq. (4.25) and diagrammatically in Fig. 17 (b.)).

Previous studies of the vertex. The quark-photon vertex has been studied intensively within the DSE approach over the past twenty years. In Refs. [5, 96, 102–104] the rainbow-ladder truncation was applied. The authors of Ref. [95, 105] use a more enhanced truncation and discuss its impact on the vertex.

Another recent study Ref. [106], calculates the vector- (quark-photon) and the axial-vector quark anti-quark vertex in lattice QCD and compares the results to the ones obtained in the rainbow-ladder truncation. This serves as an important cross-check for the quality of RL. The calculation of observables in Lattice QCD does not require gauge-fixing. The quark-photon vertex on the other hand, is not an observable but, in fact, a gauge-dependent quantity. To access the vertex and for comparison with the DSE results, the authors needed employ a strategy to gauge-fix on the lattice and in case of this publication the comparison are performed for Landau-gauge. The comparison revealed that the dressing functions of the vertex showed similar momentum dependencies in both approaches, but that there is a clear deviations in the lower momentum regime.

Beyond rainbow-ladder effects on the quark-photon vertex. Although the vector-meson pole is dynamically generated in the quark-photon vertex BSE, working in the rainbow-ladder truncation it is falsely treated as a QCD bound-state rather than its actual physical nature, a resonance. Mathematically this means that the vector-meson pole is located on the real axis and not in the complex plane. A true resonance is represented by a pole on the second Riemann sheet and the distance between pole location and real axis corresponds to its decay width. In terms of diagrammatic representation, the missing resonance is reflected by the fact that the RL truncation does not include any diagrams that represent intermediate resonance states, such as the vector-meson, and thus all mesons are automatically considered as bound-sates.

Refs. [6, 44, 107, 108] summarize the first attempts for a proper treatment of resonances in the DSE approach. In particular, the recent study of the authors in Ref. [107], incorporates pion degrees of freedom into the DSE formalism. This introduces the presence of an intermediate resonance to the Bethe-Salpeter kernel.This then reflects the correct physical picture allowing the rho meson to appear as a pole in the complex plane and implementing its resonance nature. The pion interaction leads to additional pion-exchange diagrams in both the BSE interaction kernel and in the self-energy term of the quark DSE. Within this "beyond-rainbow-ladder truncation" the author's aim was to evaluate the effects of properly treating the vector-meson in the results of the **quark-photon vertex**.

The authors calculated the quark-photon vertex for value in space- and timelike domains

and found that the effects in the spacelike part are negligible. In the timelike region, on the other hand, their more sophisticated truncation leads to differences compared to the rainbow-ladder calculation. Introducing the additional term in the interaction kernel however also carries some perks, as it becomes harder to consistently truncate the set of equations. A straight-forwards implementation of the pion-degrees of freedom in both, the self-energy term of the quark DSE, and the interaction kernel in the BSE lead to a truncation that does not obey the WTIs. However with some tweaks it is possible to define a truncation that it is possible to at least preserving the vector WTI, Eq. (2.63), however on the expense of violating the AXWTI, Eq. (2.64). The vector WTI is more relevant in this context, as it relates to charge conservation in electromagnetic processes. On the other hand this demands for further investigation of an all-symmetry preserving, and physically more rigorous truncation beyond the rainbow-ladder truncation and the particular choice of truncation severs as a useful tool of the advances to include intermediate on-shell bound-state in the evaluation of the quark-photon vertex.

4.4 Effective quark-gluon interaction and truncations

The Dyson-Schwinger, Eq. (2.35), and Bethe-Salpeter equation, Eq. (4.6), include all possible QCD interactions and are in general exact to all orders. However, both equations relate n-point Green functions to $(n+1)$-Green functions and thus require the knowledge of higher-order functions. This ultimately leads to a tower of coupled integral equations, which needs to be truncated to enable numerical evaluation. Truncating in this sense means approximating the $(n+1)$-Green functions.

Furthermore, the truncation has to obey underlying symmetry relations, which demands a consistent treatment when approximating the quark-self energy term ($\mathbf{\Sigma}$) in the quark DSE and the interaction kernel ($\mathbf{K}$) in the meson or likewise vertex BSE. The relation that follows from the AXWTI was laid down in Eq. (4.25), where we revealed the structure of the interaction kernel, based on the choice of the quark self-energy in Eq. (2.35). We identified both structures to depend on the gluon propagator $D^{\mu\nu}(q-p)$ and the quark-gluon vertex $\Gamma^{\mu}_{\mathrm{qg}}(q,P)$. Where the latter is the higher-order Green function that will be approximated.

Before explicitly writing out the truncation, I will make some short comments about the gluon propagator and the quark-gluon vertex to motivate the structure of the truncation.

Gluon propagator. The gluon propagator in Landau gauge is given by,

$$D^{\mu\nu}(k) = \left(\delta^{\mu\nu} - \frac{k^{\mu}k^{\nu}}{k^2}\right)\frac{Z(k^2)}{k^2} = t^{\mu\nu}_{k}\,\frac{Z(k^2)}{k^2}\,, \tag{4.30}$$

with the gluon dressing function $Z(k^2)$. The dressing function is calculated by iteratively solving the gluon DSE (see Ref. [5], Fig. (3.2) on the left), which includes higher-order Green functions such as the three-gluon vertex, see Refs. [109, 110]. The gluon propagator has been studied intensely in different non-perturbative approaches, such as lattice QCD and in functional methods frameworks, as the FRG and the DSE approach have investigates this function, see Refs. [90, 92, 93]. As mentioned previously, propagator and vertices are gauge-fixed objects, and thus it requires the lattice, which usually works without gauge-fixing to impose a gauge procedure in order to compare with the other results on the market. A comparison of gluon propagator calculation can be seen in Ref. [5] Fig. (3.4).

Quark-gluon vertex. The quark-gluon vertex has a similar structure as the quark-photon vertex, Eq.(4.28), and can be expressed in terms of twelve tensor structures. Thereby it contains four elements in the gauge-dependent part and eight purely transverse elements $\Gamma^{\mu}_{\mathrm{T}}$,

$$\Gamma^{\mu}_{\mathrm{qg}}(q,k) = f_1\, i\gamma^{\mu} - f_2\, q^{\mu} + f_3\, iq^{\mu}\not{q} - f_4\, p\cdot k\frac{1}{2}\left[\gamma^{\mu},\not{q}\right] + \Gamma^{\mu}_{\mathrm{T}}(q,k)\,. \tag{4.31}$$

The tensor components of the transverse part are exactly the same as in case of the quark-photon vertex, Eq. (B.2) and the quark-gluon vertex is expressed in terms of the total gluon momentum k and the relative momentum between the two quarks q. In contrast to the quark-photon vertex, constraining the gauge-part of this vertex is a somewhat more difficult, as the Slawnow-Taylor identities (QCD's non-Abelian version of the WTIs, Eq. (2.63)+ (2.64)) are only limited help since they are not exactly solvable. Recall that in the QED version, the gauge part of the quark-photon vertex was entirely determined by the quark propagator and thus we only need to solve for the transverse part. That also leads to the assumption that the momentum dependence of the gauge dressing functions in the case of the quark-gluon vertex, is potentially very different.

Equally to the propagator multiple calculations have been performed, see Refs. [111–115], which show agreement on the quantitative level, see Fig. (3.4) in Ref. [5].

Effective coupling. The simplest choice for a symmetry preserving truncation is the so-called "rainbow-ladder"-truncation (RL). As Eq. (4.25) must hold, we can come up with the easiest tensor element fulfilling this symmetry relation, which is given by a bare vertex structure $\sim \gamma^\mu$. The authors in Ref. [116] show that it can be understood as the first term in a systematic expansion of the Bethe-Salpeter interaction kernel $K^{(4)}_{[2]}$ derived directly from the effective action at two loops order. The connection between kernel and self-energy term, Eq. (4.24), furthermore indicated that the kernel will be a combination of gluon-propagator and quark-gluon-vertex, such that choice of a bare-vertex can be understood to be proportional to the tensor structure of the vertex in Eq. (4.31). Respectively it approximates the quark-gluon vertex by its leading tensor component and is given by,

$$\Gamma^\mu_{\mathrm{qg}}(q,k) = i\gamma^\mu \, \mathcal{G}(k^2)\, t_A \,, \tag{4.32}$$

with the generator of the $SU(N_c)$ color group t_A, which are the Gell-Mann matrices $t_A = \lambda_A/2$ for three-color physics and a scalar dressing function $\mathcal{G}(k^2)$. Besides the truncation in form of omitting further tensor structures, the momentum dependence of the dressing function $\mathcal{G}(k^2)$ was reduced to solely depend on the gluon momentum squared k^2, omitting the dependence on the relative quark momentum q. To include the full dynamics of the coupling between quarks and gluon, we would need to properly couple the DSE for both quark and gluon propagator and solve the coupled set of equations iteratively. This furthermore requires a consistent treatment of the quark-gluon interaction in the kernel of the BSE equation, to provide that the AXWTI remains to be fulfilled. Refs. [113–115] employ studies of such kinda, and in particular when performing calculation for finite-temperature in the DSE approach, it is unavoidable to solve a consistent system of quark and gluon, see recent Refs. [117, 118] for more details on this topic.

In the rainbow-ladder truncation (RL) one does not couple quark and gluon DSE, but simply approximates a combination of gluon dressing function and quark-gluon dressing function into a so-to-say "effective coupling", which is defined by,

$$\alpha(k^2) = \frac{Z_{1f}}{Z_2^2}\frac{g^2}{4\pi}\, Z(k^2)\, \mathcal{G}(k^2) \,, \tag{4.33}$$

as introduced in Eq. (10) of Ref. [119]. The combination of quark-gluon and gluon dressing function together with the renormalization constants Z_i make it a renormalization point independent object and it solely depends on the gluon momentum. We apply a model parametrization for the effective coupling which is the so-called Maris-Tandy interaction, Eq. (10) of Ref. [119], and reads,

$$\alpha(k^2) = \alpha_{\mathrm{IR}}(k^2) + \alpha_{\mathrm{UV}}(k^2) \,, \qquad \alpha_{\mathrm{IR}}(k^2) = \pi\eta^7 \left(\frac{k}{\Lambda}\right)^4 e^{-\eta^2 k^2/\Lambda^2} = \frac{D}{\omega^6} k^4 e^{-k^2/\omega^2} \,. \tag{4.34}$$

It depends on two parameters, which depends on the choice of notation and can either be $\{\eta, \Lambda\}$ or $\{D, \omega\}$. The two version are related via $\omega D = \Lambda^3$ and $\omega = \Lambda/\eta$ and arose due to reformulation by different collaborations of the model over the years. It is composed of the infrared model part and an ultraviolet part, which is specified by,

$$\alpha_{\mathrm{UV}}(k^2) = \frac{2\pi\gamma_m(1 - e^{-k^2/\Lambda_t^2})}{\ln\left[e^2 - 1 + (1 + k^2/\Lambda_{\mathrm{QCD}})^2\right]}\,. \tag{4.35}$$

The parameters in the UV part are $\Lambda_t = 1\mathrm{GeV}$, $\Lambda_{\mathrm{QCD}} = 0.234\mathrm{GeV}$, and $\gamma_m = 12/25$ for four active quark flavors. The UV term ensures the correct behavior in the perturbative limit. However it is not essential, as omitting the term can be done without causing serious damage for observables in the light quark sector, as the important non-perturbative physics happens on the scale of $\sim k^2/\Lambda^2$ and is thus lead by the IR part, see Ref. [120].

The parameters in α_{IR} part are Λ, which represents an IR-scale, and a dimensionless open parameter η. The scale parameter is fixed to experimental input and η is fixed by ensuring the physical values for pion mass and decay constant. Most observables are insensitive to a small change in η and thus a range of η-values, $\eta \in [1.6, 2.0]$, could be identified, which reproduces the same experimental value. See Fig. (3.13) in Ref. [5] for a plot of the full effective coupling $\alpha(k^2)$ for a range of η-parameters.

The variation of the η-parameter will be used throughout this thesis to give an estimate of the theoretical uncertainty due to the truncating taken at the level of the quark-gluon-vertex. The rainbow-ladder truncation can be identified as the leading order in a systematic expansion, however, this is not an expansion in a perturbative sense and thus we can not make a quantitative statement to which level the inclusion of higher-order Green functions or likewise the full tensor structure for the vertex might contribute.

Historically, the rainbow-ladder truncation was introduced as an effective model for both quark-gluon vertex and gluon propagator. After more details on the exact form of the gluon propagator were investigated, the tensor structure of the propagator could be identified to be the expression for the perviously chosen model ($\sim t^{\mu\nu}$) and in modern publications the individual terms are often considered separately. However, this is just a question of the preferred perspective, as it did not change the functional form of truncation but simply the interpretation.

To summarize, the rainbow-ladder approximation with the Maris-Tandy model is replacing the quark-gluon vertex and the gluon propagator by its leading tensor component weighted with an effective coupling $\alpha(k^2)$ with additional simplifying assumptions such that the total replacement reads,

$$g^2 \frac{Z_{1\,f}}{Z_2^2}\, D^{\mu\nu}(k^2)\, \Gamma^{\mu}_{\mathrm{qg}}(q,k) \longrightarrow i\gamma^{\mu}\, \frac{t_k^{\mu\nu}}{k^2}\, 4\pi\, \alpha(k^2)\,. \tag{4.36}$$

The replacement fixed the quark-self energy term and by inspection, the 2-PI interaction kernel in the BSE was constructed accordingly, guided through the AXWTI, Eq.(4.25), demanding a specify relation between self-energy and kernel. Fulfilling the AXWTI, the truncation is consistent with chiral symmetry and consequently preserves the Goldstone nature of the pion.

Beyond rainbow-ladder. Full calculations for the quark-gluon vertex and gluon propagator reveale that rainbow-ladder is still a severe approximation. On one hand, it fulfills important phenomenological properties such as asymptotic freedom and is in agreement with perturbation theory. On the other hand, more realistic calculations for propagator and vertex show, that the expected interaction differs severely from the effective coupling model $\alpha(k^2)$, see Fig. (3.13) in Ref. [5]. Thus the approximation should be seen as a sophisticated phenomenological model leading towards a more systematic truncation scheme. Extensive

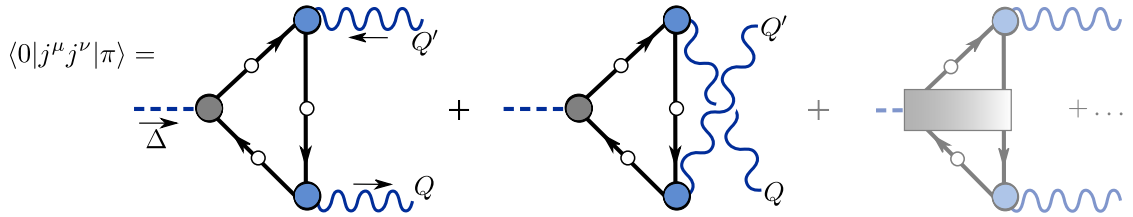

Figure 18: Feynman diagrams for the pion transition form factor (TFF). The gray dot indicates the meson amplitude, the lines along the triangle are dressed quark propagators and the light blue circles are quark-photon vertices. In impulse approximation the first two terms are included and diagrams with higher order vertices are neglected.

studies over the past years have shown that the truncation performs well in the regime of pseudoscalar and vector meson, but underestimates masses of scalar and axial-vector mesons.

The authors in Ref. [114] performed a truncation "beyond rainbow-ladder" by consistently solving the system of coupled DSEs for the quark-, gluon- and ghost-propagators. In this case, the ghost and gluon propagator are obtained from fits of lattice calculations and the infinite set is truncated at the level of four-gluon vertices. This leads to improved masses in for the scalar and axial-vector meson, indicating that a more detailed description of the quark-gluon dynamics is required for these channels. Another calculation along this lines is Ref. [121], which looks at n-point Green functions in the quark and gluon sector (eg. three-gluon vertex) and explores the insights from different gauges such as Coulomb gauge.

As mentioned in the previous section, the authors in Ref. Ref. [107] applied a "beyond rainbow-ladder" truncation, in context of studying the quark-photon vertex, aiming to incorporate the resonance nature of the rho-meson. The study showed that the results for the vertex in the spacelike regime did not change, compared to the calculation in the RL truncation. Reassured by these findings, we are confident to apply the rainbow-ladder truncation in the context of the electromagnetic transition form factor calculation in the DSE approach.

4.5 Transition form factor

Now that we have specified all the ingredients, let us turn to the form factor amplitude, starting by defining the $M \to \gamma\gamma$ transition element as diagrammatically given by the diagrams in Fig. 18,

$$\Lambda^{\mu\nu}(Q,Q') = \langle 0|\, j^{\mu}(x)\, j^{\nu}(y)\, |\lambda\rangle\, e^{-iQ\cdot x}\, e^{-iQ'\cdot y} = \sum_i F_i(Q^2, Q'^2)\, \tau_i^{\mu\nu}(Q,Q')\,, \tag{4.37}$$

where Q and Q' are the photon momenta and the matrix can be decomposed into a tensor part $\tau_i^{\mu\nu}$, which are matrices in Lorentz, Dirac, color and flavor space and the scalar functions $F_i(Q^2, Q'^2)$. The latter contain the momentum depending scale behavior. M indicated the choice for general meson. The number of scalar function ($i \in n$) depends on the decaying meson, as the quantum number will dictate the possible tensor structures and how many dressing functions $F_i(Q^2, Q'^2)$ are required. In case of the neutral pion this involves only one amplitude $F_\pi(Q^2, Q'^2)$.

The transition matrix element is described by the non-perturbative diagrams displayed in Fig. 18, which follows along the derivation of Ref. [103, 122]. This contains two types of diagrams, the simple triangle diagrams on the left and the rightmost diagram, which contains the pseudoscalar coupling to $q\bar{q}$ Bethe-Salpeter kernel and thus to the underlying quark-gluon vertex. When working in the rainbow-ladder truncation, the latter does not contribute, as higher-order vertices, such as the gluon-three-point vertex, are not included. Such that we only consider the two triangle diagrams on the left side of the figure, which correspond

to the different orderings of the same diagram. The diagram contains fully dressed quark propagators as loop particles, two quark-photon vertices, and the Bethe-Salpeter meson amplitude.

Before we specify the underlying Green function further, we begin by defining the involved momenta for the process. The total Δ and relative Σ momentum of the form factor are defined in the usual way,

$$\Sigma = \frac{Q+Q'}{2}\,, \quad \Delta = Q - Q'\,, \quad \Leftrightarrow \quad Q = \Sigma + \frac{\Delta}{2}\,, \quad Q' = \Sigma - \frac{\Delta}{2}\,, \tag{4.38}$$

with the in- and out-going photon momenta (Q, Q') and where $\Delta^2 = -m_M^2$ for on-shell meson. In general the process depends on **three** Lorenz invariant variables $(Q^2, Q'^2, Q\cdot Q')$, if the pion momentum is fixed through the on-shell demand, we are left with **two**. We can define an alternative set of these Lorentz invariant variables which will be a useful tool for plots and deformations later on, consider

$$\eta_+ = \frac{Q^2 + Q'^2}{2} = \Sigma^2 + \frac{\Delta^2}{4}\,, \tag{4.39}$$

$$\eta_- = Q\cdot Q' = \Sigma^2 - \frac{\Delta^2}{4}\,, \tag{4.40}$$

$$\omega = \frac{Q^2 - Q'^2}{2} = \Sigma\cdot\Delta\,, \tag{4.41}$$

and vice versa $\{Q^2, Q'^2; Q\cdot Q'\} = \{\eta_+ \pm \omega; \eta_-\} = \{(\Sigma \pm \Delta/2)^2; \Sigma\cdot\Delta\}$. The angular variable η_- is fixed for on-shell meson the two Lorentz invariant variables are thus either $\{Q^2, Q'^2\}$ or $\{\eta_+, \omega\}$ or $\{\Sigma^2, \Sigma\cdot\Delta\}$. As the TFF is symmetric in Q^2 and Q'^2 it can only depend on ω quadratically. An overview of the kinematic variables in form of a look-up table is given in Appendix B.

Triangle diagram. In the impulse approximation (or likewise rainbow-ladder truncation), the transition form factor for a meson $M \to \gamma^{(*)}\gamma^{(*)}$ is described by the triangle diagram in Fig. 19 and specified by

$$\Lambda^{\mu\nu}(Q^2, Q'^2) = 2e^2\,\mathrm{Tr}\int\frac{d^4k}{(2\pi)^4}\,S^a(k_+)\,\Gamma_\lambda^{a\bar{b}}(k,\Delta)\,S^b(k_-)\,\Gamma^{\mu\ b\bar{c}}(r_-,-Q)\,S^c(k+\Sigma)\,\Gamma^{\nu\ c\bar{a}}(r_+,Q')\,, \tag{4.42}$$

where $S(k_\pm)$ are the dressed quark propagator, Γ_λ is the meson amplitude and $\{\Gamma^\mu, \Gamma^\nu\}$ are the quark-photon-vertices. The trace is summing over flavor, Dirac, and color space, where the roman letters present a combined index. For the color space, the trace trivially evaluates to a multiplicative factor of N_C. Using the definitions for the photons total and relative momentum above, we can additionally define the internal momenta in the triangle diagram with loop momentum k and where

$$k_\pm = k \pm \frac{\Delta}{2}\,, \qquad r_\pm = k + \frac{\Sigma}{2} \pm \frac{\Delta}{4}\,, \tag{4.43}$$

are the internal quark momenta and the relative momenta appearing in the quark-photon vertices, respectively.

The impulse approximation neglects higher vertices contribution (as shown by the third diagram in Fig. 18), but requires that the objects in the triangle diagram are fully dressed and that the electromagnetic quark-photon vertex applied therein, satisfies the AXWTI, Eq. (2.64). This is consistent with the approximations made at the level of quark propagator and meson amplitude, as in the rainbow-ladder truncation higher order vertices (such as the

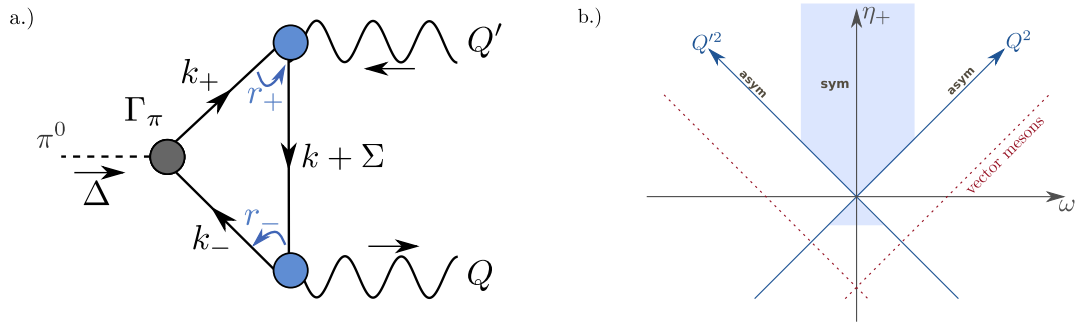

Figure 19: a). Triangle diagrams for athe pion transition form factor (TFF) in impulse approximation with specified momenta. b.) Phase-space sketch for the TFF in the $\{Q^2, Q'^2\}$ or $\{\omega, \eta_+\}$-plane. The blue shaded area indicate region where calculations are accessible. The figure furthermore indicates the location of the vector meson poles in timelike Q^2, Q'^2 region and the symmetric ($Q^2 = Q'^2$) and asymmetric limit ($Q^2 \neq 0, Q'^2 = 0$)

3-gluon vertex) are not included. Exchanging the photon legs on the first triangle diagram leads to another contribution at the level of the applied approximation, see second diagram in Fig. 18. The symmetry factor of 2, in front of Eq. (4.42), stems from considering these two identical diagrams and combining them as they have the same topology. Each quark-photon vertex comes with a factor of the electromagnetic coupling constant e, and the diagrams are evaluated at leading-order in QED. This is sufficient enough, as we have already seen from the anomaly prediction, Sec. 3.1, that the corrections beyond leading order in QED are negligible.

The calculation thus aims to describe the effects coming from the electromagnetic sector as well as the full set of non-perturbative QCD phenomena.

Kinematic restrictions and frames. As already mentioned in the section about the quark propagator, the form factor calculation is subject to kinematic restriction due to the quark poles. To evaluate the accessible domain, let us consider the Lorentz integral for the transition matrix element in Eq. (4.42), where the quark momenta in the loop are given by $k_\pm = k \pm \Delta/2$ and $k + \Sigma$. The loop momentum k is always real, but the meson momentum $\Delta \in \mathbb{C}$ carries complex values. Using Eq. (4.5), one thus arrives at the following condition for the total and relative momentum in the triangle,

$$\left[\mathrm{Im}\,\frac{\Delta}{2}\right]^2 < m_P^2 \quad \text{and} \quad [\mathrm{Im}\,\Sigma]^2 < m_P^2\,, \tag{4.44}$$

with the contour mass of the quark parabola of $m_P^{\mathrm{Ligth}} \sim 0.5\mathrm{GeV}$ for light quarks.

When performing the on-shell calculation, the TFF depends on two independent Lorentz invariants ($\{Q^2, Q'^2\}$ or other linear combinations of these, see Eq. 4.39). To express the kinematic restrictions, Eq. (4.44) in terms of these variables, we need to specify the four-vectors in the triangle diagram. The components of Σ and Δ can be arranged arbitrarily as long as the Lorentz invariants defined in Eqs. (4.39–4.41), ($\{\eta_+, \omega, \eta_-\}$ or equally $\{\Sigma, \Delta^2, \Sigma \cdot \Delta\}$) remain unchanged. For any possible choice, however, one can find a linear combination $\Sigma + \alpha\,\Delta$ that has a four-component only, with an arbitrary parameter $\alpha \in \mathbb{R}$. The general arrangement satisfying these constraints is

$$\Delta = \frac{1}{\mathcal{N}} \begin{bmatrix} 0 \\ 0 \\ -i\sqrt{\Sigma^2 m_\pi^2 + (\Sigma\cdot\Delta)^2} \\ (\Sigma\cdot\Delta) - \alpha m_\pi^2 \end{bmatrix}, \quad \Sigma = \frac{1}{\mathcal{N}} \begin{bmatrix} 0 \\ 0 \\ i\alpha\sqrt{\Sigma^2 m_\pi^2 + (\Sigma\cdot\Delta)^2} \\ \Sigma^2 + \alpha\,(\Sigma\cdot\Delta) \end{bmatrix} \tag{4.45}$$

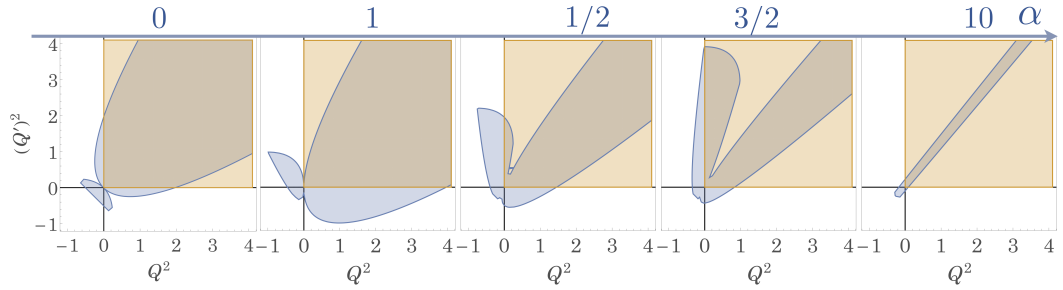

Figure 20: Kinematic accessible region in the $(Q^2 - Q'^2)$-plane in case of the pion TFF ($\pi^0 \to \gamma\gamma$), indicated in light blue. The light orange serves as guidance highlighting spacelike photon momenta ($Q^2 > 0, Q'^2 > 0$). Each plot corresponds to a different value for the frame parameter α, as introduced in Eq. (4.45), taking value from $\alpha = \{0, \frac{1}{2}, 1, \frac{3}{2}, 10\}$. The rightmost, $\alpha = 10$ is sufficiently large to represent the rest-frame ($\alpha \to \infty$).

with $\mathcal{N} = \sqrt{\Sigma^2 + 2\alpha\,(\Sigma \cdot \Delta) - \alpha^2 m_\pi^2} = \sqrt{\sigma + 2\alpha\omega - \alpha^2 m_\pi^2}$ with $\sigma = \Sigma^2$ and ω as defined in Eq. (4.41). In this sense, α represents the parameter for choosing different kinematic frames, which leads to a slightly varied momentum routing through the triangle diagram, but all lead to the required on-shell momentum demand for the total momentum of the meson P.

Take for example the pion's rest frame, which corresponds to $\alpha \to \infty$:

$$\Delta = \begin{bmatrix} 0 \\ 0 \\ 0 \\ im_\pi \end{bmatrix}, \quad \Sigma = \begin{bmatrix} 0 \\ 0 \\ \sqrt{\frac{\omega^2}{m_\pi^2} + \sigma} \\ \frac{\omega}{im_\pi} \end{bmatrix} =: \sqrt{\sigma} \begin{bmatrix} 0 \\ 0 \\ \sqrt{1 - Z^2} \\ Z \end{bmatrix}.$$

Here we define the angle between total and relative momentum as $Z = \hat{\Delta} \cdot \hat{\Sigma}$ and $\sigma = \Sigma^2$. If $\sigma > 0$ and $Z \in [-1, 1]$, Σ is real and the imaginary part comes only from Δ, so the resulting condition $m_\pi < 2m_p$ is always satisfied. However, the situation is different for spacelike photon momenta $\{Q^2, Q'^2\} < 0$ and in the quadrant $|\Sigma \cdot \Delta| < \Sigma^2 - m_\pi^2/4$, as in this case Z is imaginary. Here both Δ and Σ have imaginary four-components and the resulting condition becomes $|\Sigma \cdot \Delta| < m_\lambda m_p$, which defines a narrow strip around the symmetric limit ($\omega = 0$; $Q^2 = Q'^2$).

The arbitrariness of α can be exploited to optimize the frame, i.e. to reach kinematic regions for the form factor that are not accessible in the meson rest frame. The resulting domains are plotted in the $(Q^2 - Q'^2)$-plane in Fig. 20 for different values of α. The leftmost plot shows $\alpha = 0$ and the rightmost plot $\alpha = 10$. For $\alpha \to \infty$, one recovers the meson rest frame, which is already represented by $\alpha = 10$, as the is sufficiently large enough. In case of the frame with parameter $\alpha = 0$ (leftmost plot), the momentum Σ has a four-component only, whereas Δ has an imaginary three-component and, for $\sigma > 0$, this leads kinematic condition between the Lorentz invariants,

$$\omega^2 < (4m_p^2 - m_\lambda^2)\left(\eta_+ + \frac{m_\pi^2}{4}\right). \tag{4.46}$$

For the singly-virtual form factor $F(Q^2, 0)$ the optimal choice is $\alpha = 1/2$ (second plot in Fig. 20). In that case it is the photon momentum $Q = \Sigma + \Delta/2$ that has a four-component (resembling the Breit frame in elastic form factor calculations). The denominator $\mathcal{N} = \sqrt{\eta_+ + \omega}$ is always real if $\eta_+ > 0$ and $|\omega| < \eta_+$, and therefore the three-components of Σ and

Δ are imaginary. The resulting condition is

$$m_M^2\,\eta_+ + \frac{m_M^4}{4} + \omega^2 < 4m_p^2\,(\eta_+ + \omega)\,. \tag{4.47}$$

This region crosses the line $\eta_+ = \omega$ at

$$\eta_+ = \omega = \frac{Q^2}{2} = 4m_p^2\left(1 - \frac{\varepsilon}{2} + \sqrt{1-\varepsilon}\right)\,, \tag{4.48}$$

with $\varepsilon = m_\lambda^2/(4m_p^2)$. For a small meson mass such as the neutral pion $m_\pi = 137$ MeV, ε is small and Eq. (4.48) leads to $\eta_+ \approx 8m_p^2$. Hence, in the asymmetric limit the pion transition form factor can be calculated up to $Q^2_{\max} = (\eta_+ + \omega) \approx 16\,m_p^2 \approx 4$ GeV^2 without crossing any quark singularities.

The complex parts inside the four-vectors of the triangle diagram ultimately come from the on-shell condition ($\Delta^2 = -m_\lambda^2$) and thus, the size of the complex value is proportional to the mass of the decaying particle. Thus larger masses correspond to a larger complex value and a smaller accessible phase-space. This corresponds to the same statement that for heavier mesons, ε will be larger, thus the accessible domain in η_+ smaller. Fig. 21 shows an overview of the kinematically accessible domains for a set of alpha values (x-axis) and different meson masses (y-axis) up to ~ 1 GeV. The considers mesons in this graphics carry light quark content only, in an isospin-symmetric limit ($m_u = m_d$). The pion and the lightest scalar meson ($f_0(500)/\sigma$) masses are chosen exemplary, as they are in particular relevant for the calculation of the corresponding TFFs in this thesis. With increasing value for the bound-state mass, the kinematic accessible regions shrink. For ε greater one, $m_M^2 > 4m_p^2 > 1$, we are completely disabled by the quark poles, and no direct calculation is possible. In this case, a new method is required, which addresses the issue and actively deals with the singularities by performing e.g a path-deformation.

To **summarize**, due to the poles structures in the quark propagator, we can access the TFF for, **spacelike momenta** ($Q^2 > 0, Q'^2 > 0$),

- in the symmetric limit ($Q^2 = Q'^2$)
- a narrow strip around the symmetric limit ($|\Sigma \cdot \Delta| < m_\lambda m_P$)
- in the asymmetric limit ($Q^2 \neq 0, Q'^2 = 0$) up to 4 GeV^2 for light meson (in fact this particular number is associated with the π^0 decay only) and even less for heavier ones (see overview Fig. 21)

and for **timelike momenta**,

- in a small domain in both symmetric and asymmetric limit of restricted by the quark contour mass, $Q^2, Q'^2 \gtrsim -m_P^2$.

Here we consider meson with light quark content such that $m_P^2 \approx 0.25$. For mesons with strange quarks, the domains would be even smaller. The accessible regions are summarized in the sketch, Fig. 19 (b.), showing the region in light-shaded blue and furthermore the asymmetric and symmetric limits and location of the vector-meson poles in the timelike momentum region.

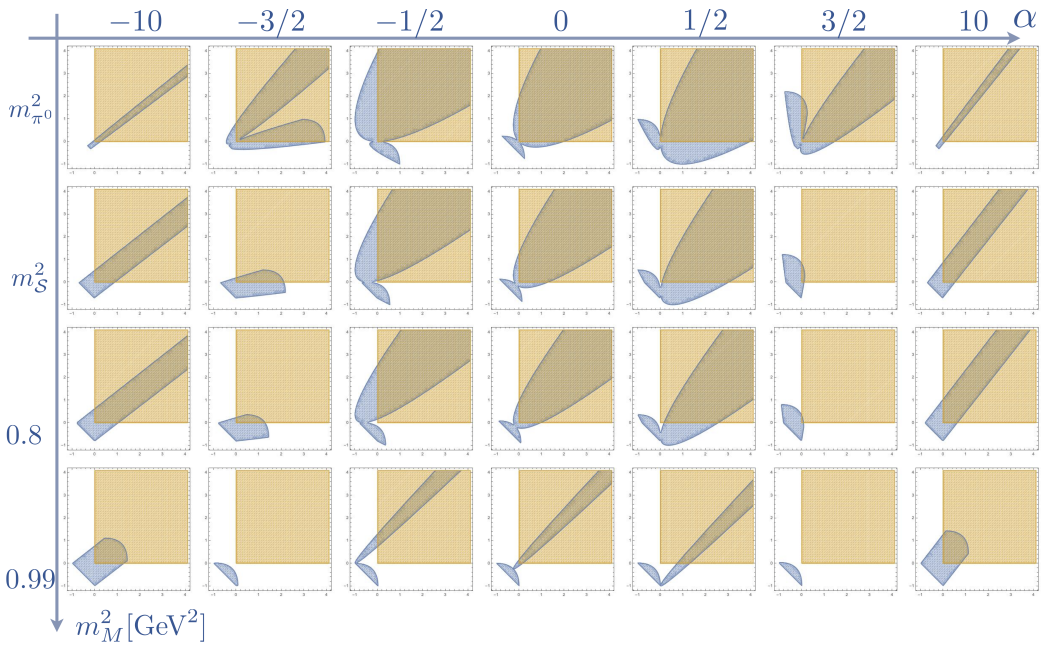

Figure 21: Kinematic accessible regions in the $(Q^2 - Q'^2)$-plane in light blue. The x-axis of plots represent the different frame through varying $\alpha = \{0, \frac{1}{2}, 1, \frac{3}{2}, 10\}$, the y-axis corresponds to the mass of the decaying meson, considering mesons with only light quark content in the isospin-symmetric limit. The Q^2 and Q'^2-plane is shown in the same range as in Fig. 20: $Q^2 \in [-1, 4]$ GeV^2. The meson masses along the y-axis here are based on the DSE rainbow-ladder value, $m_\pi = 135$MeV and $m_\sigma = 675$MeV.

5 Numerical Results

The previous section outlined how to calculate a transition form factor in the DSE framework and specified the approximations in the form of a truncation model, which is applied for all calculations throughout this thesis. This chapter contains a collection of numerical results, mainly focusing on the transition form factor, but also presenting applications in the form of electromagnetic decay processes, Sec. 5.2 and the muon anomalous magnetic moment, Sec. 5.6. The presented results are published in three papers: [81, 82] for the pion transition form factor and [77] for the pseudo-scalar pole contributions to the muon $g - 2$. The last section, about the results corresponding to the latter publication, is concluded with new results for the scalar transition form factor and and outlook for the scalar pole contribution to the hadronic Light-by-Light tensor.

Truncation parameters. Throughout this thesis, the rainbow-ladder truncation and the Maris-Tandy model, Eq. (4.33), are applied. For the form factor calculation we used the parameters $\Lambda = 0.74$ GeV and $\eta = 1.85 \pm 0.2$. The variation in the η-parameter changes the shape of the effective quark-gluon interaction in the infrared, cf. Fig. 3.13 in Ref. [5], and will serve as an estimate of the error associated with the truncation model. The total quoted uncertainty is a combination of model and numerical error estimates, but will also be specified for each quoted result. The two truncation parameters are consistently used in all building blocks used to determine the form factor. This procedure guarantees the preservation of chiral symmetry and satisfied the AXWTI, Eq. (2.64). The rainbow-ladder truncation with this parameter set has shown to produce reliable results in the pseudoscalar and vector-meson sector as well as for nucleon and Δ baryons. Last, we furthermore work in the isospin symmetric limit of equal up and down quark masses with a current light quark

mass of $m_q = 3.57$ MeV at a renormalization point $\mu = 19$ GeV. The choice for the quark mass together with the values in the effective interaction (Λ, η) are fixed to produce physical values for pion mass and decay constant.

5.1 Pion transition form factor

The transition matrix element for the pion transition form factor $\pi^0 \to \gamma\gamma$ is given by,

$$\Lambda_\pi^{\mu\nu}(Q, Q') = e^2 \, \frac{F_\pi(Q^2, Q'^2)}{4\pi^2 f_\pi} \, \varepsilon^{\mu\nu\alpha\beta} Q'^\alpha Q^\beta \,, \tag{5.1}$$

where Q and Q' are the outgoing and incoming photon momenta, $f_\pi \approx 92$ MeV is the pion's electroweak decay constant, and $e^2 = 4\pi\alpha_\mathrm{e}$ the squared electromagnetic charge. This decomposition holds because for pseudoscalar quantum numbers we identify **one** possible tensor structure, the epsilon tensor contracted with two momenta ($\tau_i^{\mu\nu} = \varepsilon^{\mu\nu\alpha\beta} Q'^\alpha Q^\beta$). The corresponding scalar function is the only form factor, $F_\pi(Q^2, Q'^2)$, and the convention of prefactors is chosen such that $F_\pi(0,0) = 1$ in the chiral limit, as follows from the chiral anomaly, Eq. (3.13).

Recall that the form factor was furthermore defined contracting the individual components of the Feynman triangle graph, Fig 19 on the left, and Eq. (4.42), restated here for convenience,

$$\Lambda_\pi^{\mu\nu}(Q, Q') = 2e^2 \frac{N_C}{3} \, \mathrm{Tr} \int \frac{d^4k}{(2\pi)^4} \, S(k_+) \, \mathbf{\Gamma}_\pi(k, \Delta) \, S(k_-) \, \Gamma^\mu(r_-, -Q) \, S(k + \Sigma) \, \Gamma^\nu(r_+, Q') \,. \tag{5.2}$$

We obtain the factor $N_C = 3$ up front from the color trace and a factor $1/3$ from the flavor part, which cancel another. The factor of 2 is a symmetry factor. The remaining trace is understood to sum over the matrices in Dirac space only. The factor from the flavor trace comes due to underlying flavor structure for the TFF matrix element, which for the pion is a combination of the up and the down transition matrices, as the quark field content of the neutral pion is $\overline{\Psi}\mathcal{F}_\pi\Psi = (u\bar{u} - d\bar{d})$. In this sense the pion TFF can be decomposed using the quark charge matrix $\hat{Q}$ for two flavor physics,

$$\Lambda_\pi^{\mu\nu} = \left[(\hat{Q}_u)^2 \Lambda_u^{\mu\nu} - (\hat{Q}_d)^2 \Lambda_d^{\mu\nu} \right] , \quad \hat{Q} = \mathrm{diag}\{+\frac{2}{3}, -\frac{1}{3}\} \,. \tag{5.3}$$

As we are working in the isospin symmetric limit ($m_u = m_d$), $\Lambda_u^{\mu\nu} = \Lambda_d^{\mu\nu}$ and respectively we can combine Eq. (5.3) into the above quoted Eq. (5.2), leading to $\Lambda_{\pi^0}^{\mu\nu} = \Lambda_u^{\mu\nu}/3$. To obtain the scalar form factor amplitude, $F_\pi(Q^2, Q'^2)$, we contract $\Lambda_\pi^{\mu\nu}$ with the following projector $P^{\mu\nu}(Q^2, Q'^2)$,

$$P^{\mu\nu}(Q^2, Q'^2) := \frac{4\pi^2 f_\pi}{e^2} \frac{\varepsilon^{\mu\nu\alpha\beta}}{Q^2 Q'^2} \, Q'^\alpha Q^\beta \quad \Rightarrow \quad F_\pi(Q^2, Q'^2) = P^{\mu\nu}(Q^2, Q'^2) \, \Lambda^{\mu\nu} \,. \tag{5.4}$$

By calculating all ingredients as described in the previous section, we are now able to determine the full $\pi_0 \to \gamma\gamma$ form factor in the spacelike domain $\{Q^2, Q'^2\} > 0$ as well as for small timelike momenta. However as seen and explained around Fig. 20, singularities in the quark propagators restrict the accessible region, making a straightforward calculation only possible in the shaded blue regions in Fig. 20. The different areas correspond to various choices for the frame parameter α, introduced in Eq. (4.45), which allows us to switch the momentum in the triangle based on the optimal choice of $\{Q^2, Q'^2\}$ values.

Pion Bethe-Salpeter amplitude. The pion is a pseudoscalar meson and thus carries quantum numbers $J^{\mathsf{PC}} = 0^{-+}$. These are reflected in the choice of basis for the Bethe-Salpeter meson amplitude. The amplitude is a function of two independent four-vectors, $\Gamma(p, P)$ (a common choice is the total momentum P of the meson and the relative momentum p, between the quark and antiquark legs). The amplitude carries no vector Lorentz index since $J = 0$, but does contain two Dirac indices for the quark-antiquark pair. To construct the basis we start by considering all Dirac structures fulfilling the spin requirements and then saturate the indices with the available four-vectors p and P. To account for negative parity, we include an additional factor of γ_5. The pseudoscalar basis decomposition is then given by

$$\tau_{\pi\,i}(p,P) = \{\mathbb{1},\, i\not{P},\, (p\cdot P)\, i\not{p},\, \left[\not{p},\not{P}\right]\}\,\gamma_5\,, \quad \Rightarrow \quad \mathbf{\Gamma}_\pi^{AB\,ab} = \sum_{i=1}^{4} f_i\,\tau_{\pi\,i}(p,P)\otimes\mathcal{C}_\pi^{AB}\otimes\mathcal{F}_\pi^{ab}\,. \tag{5.5}$$

To obtain the correct properties under charge conjugation symmetry, we first define

$$\bar{\mathbf{\Gamma}}(p,P) = \mathcal{C}\,\Gamma^{\mathrm{T}}(-p,-P)\,\mathcal{C}^{\mathrm{T}}\,, \tag{5.6}$$

where $\mathcal{C} = \gamma_4\gamma_2$ a four-by-four matrix in Dirac space (defined for example in Ref. [2]). Then the requirement is simply $\bar{\mathbf{\Gamma}}(p,P) \stackrel{!}{=} \mathbf{\Gamma}(p,-P)$. It is convenient to let the scalar functions f_i all have the same properties under charge conjugation (in this case even), which is achieved when the charge conjugation property holds for each basis elements separately. This leads to the additional factor of $(p\cdot P)$ in the third basis element. With this, all dressing functions f_i are now symmetric in the angular component $z = \hat{P}\cdot\hat{p}$. Empirically one finds that the dependence on this coordinate is negligible. Returning to Eq. (5.5), note that the amplitude is also a matrix $\mathcal{C}^{AB}$ in color and $\mathcal{F}^{ab}$ flavor space. As the meson is a color-singlet, the underlying matrix in color space is trivial, $\mathcal{C}^{AB} = \delta^{AB}$. The matrix in flavor space depends on the particular pseudo-scalar meson. For a neutral pion and for $N_F = 2$, it is given by the third generator of the $SU(2)_F$ group, proportional to the Pauli matrix σ_3,

$$\mathcal{F}^{ab} = \sigma_3^{ab} \quad \Longrightarrow \quad \overline{\Psi}\mathcal{F}\Psi = \left(\bar{u}u - \bar{d}d\right)\,, \tag{5.7}$$

where the second equation shows the quark field content of the neutral pion. The choice for the normalization of the flavor matrix part is arbitrary but needs to be chosen consistently when when normalizing the full BSE amplitude.[1]

With the choice of Maris-Tandy parameter as introduced at the beginning of this chapter we fixed our parameter to obtain physical values for the pion and this set-up leads to the exact values of $m_\pi = 135.0(2)$ MeV and $f_\pi = 92.4(2)$ MeV. A representative result for a normalized pion Bethe-Salpeter amplitude $\Gamma_\pi(k,\Delta)$ with the Maris-Tandy parameters as specified in the previous paragraph and with $\eta = 1.85$ is given on the left side of Fig. 22. After iteratively solving the Bethe-Salpeter equation, the amplitude was normalized, according to Eq. (4.12) to ensure that subsequent observables are correctly determined.

For the quark-photon vertex we consider the full twelve basis elements, Eq. (4.28). The inhomogeneous equation was solved for the eight transverse tensor components. For the remaining gauge part, the identity in form of the Ball-Chiu vertex is applied. This expresses the function via quark dressing functions using the relation given by the vector Ward-Takahashi identity in Eq. (2.63). Details on the calculation of the vertex can be found in Appendix B. Representative results for the quark-photon vertex in kinematic domain required in the form factor calculation are shown in the right panel of Fig. 22. The quark propagators and the pion

[1] Because the BSE is not directly an observable, different conventions for its normalization may be used. These differences must, of course, cancel for any physical quantity.

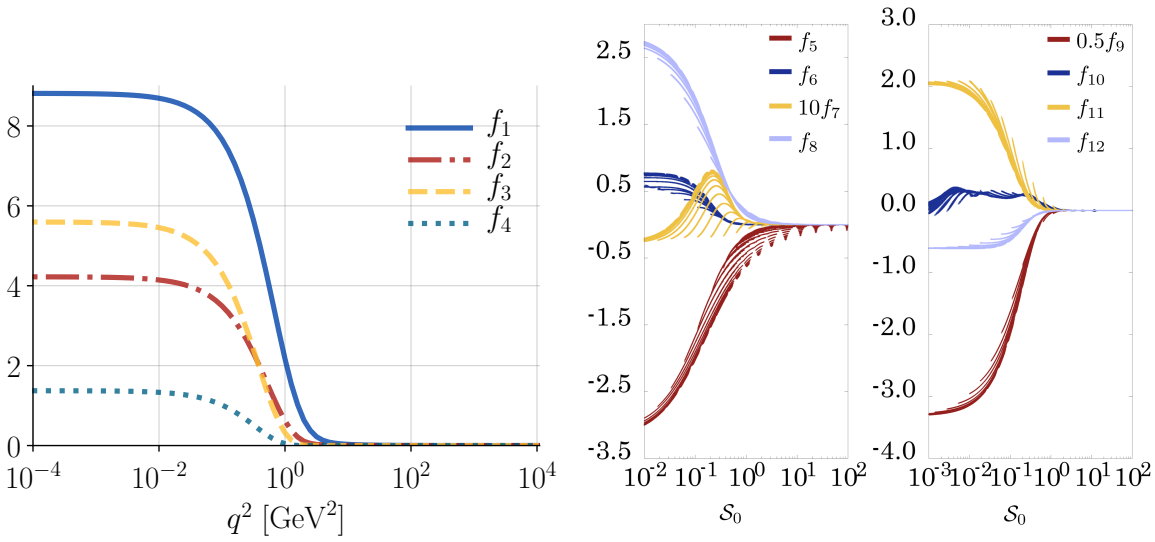

Figure 22: *Left*, dressing functions of the pion Bethe-Salpeter amplitude $\Gamma_\pi(q, P)$. *Right*, representative result of the quark-photon vertex, all eight transverse dressing functions of $\Gamma^\mu(q, p)$, specified in App. B. Following the notation in Ref. [103, 104], with $\mathcal{S}_0 = p^2/3 + Q^2/4$, where the two momenta are the relative and total momentum of the vertex as introduced in Sec. 4.3.

amplitude were calculated directly using the "naive" method, in which complex momenta are routed through the gluon propagator. The different strategies in the case of the quark propagator are briefly mentioned in Sec. 4.1. The combination of the individual ingredients leads to the following results for the pion transition form factor.

Results in symmetric and asymmetric limit. Due to the relatively light pion mass, we are able to access kinematic domains of up to $Q^2 \approx 4\text{GeV}^2$ in the asymmetric limit. In the symmetric limit, we can calculate Q^2 values to all scales in the spacelike domain. Additionally, a small timelike domain is accessible $Q^2, Q'^2 \gtrsim -m_p^2$, which is limited by the poles in the quark propagator, related to a parabola mass of $m_P \sim 0.5\text{GeV}$ (see Fig. 20 for an overview of the kinematic domains). The regions in the Q^2 plane is the same as covered in the previous DSE calculation of Ref. [98]. The authors therein apply the same truncation for their system, using rainbow-ladder with the Maris-Tandy model, and are equally limited by the quark poles.

To determine the TFF in the full spacelike domain we used the interpolation technique applied in Ref. [82]. Hereby the form factor is calculated for off-shell pion momenta, such that the four-vector of the total momentum is real ($\Delta^2 \geq 0 \Rightarrow \Delta \in \mathrm{R}$). In a later step, we then extrapolated to the physical on shell point $\Delta^2 = -m_\pi^2$. This allows us to calculate the TFF for all spacelike momenta and in particular for values in the asymmetric limit larger than $\approx 4\text{GeV}^2$. The procedure is briefly summarized in this section and the reader is referred to Ref. [82] for more details. The technique and evaluation succeed previous studies in the DSE approach (Ref. [98]), as we could, for the first time, access large momenta in the asymmetric momentum regime. The results in the smaller momentum region (up to $Q^2 \sim 5\text{GeV}$ in the asymmetric limit) are in good agreement with the previous DSE determination of Ref. [98].

Results for the form factor in the asymmetric and symmetric limits are shown on the left panel of Fig. 23. The TFF is displayed as a function of $\eta_+ = (Q^2 + Q'^2)/2$, where the symmetric case means $\eta_+ = Q^2$ and the asymmetric case $\eta_+ = Q^2/2$. The plot reveals that the TFF is slightly larger in the asymmetric limit and the evaluation at large momenta will

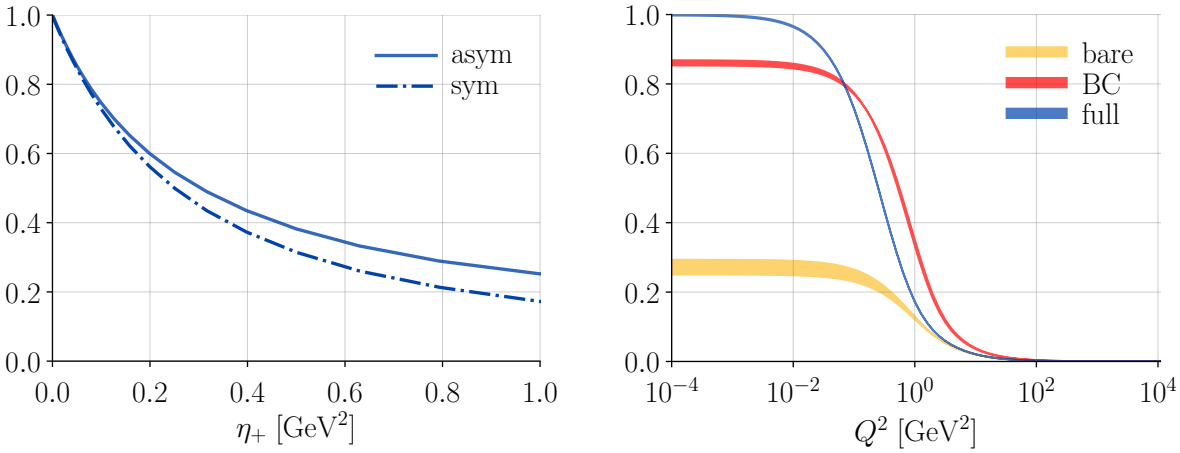

Figure 23: Both panels show the on shell pion transition form factor $F_\pi(Q^2, Q'^2)$. *Left*, in the symmetric ($\eta_+ = Q^2 = Q'^2$) and asymmetric limit ($\eta_+ = Q^2/2\,,\, Q'^2 = 0$), for spacelike momentum up to 1.0 GeV^2 (published in Ref. [81]). *Right*, vertex dependence for the anomaly value for the TFF in the symmetric limit and on a log-scale up to high Q^2 values. The three bands are obtained from using a bare quark-photon vertex, a Ball-Chui vertex or the full quark-photon-vertex. Error-band correponds to variation of the η parameter in Eq. (4.34).

show that this behavior continues up asymptotically to high η_+ [82]. The results were checked for numerical artifacts, such as grid-point and frame independence, and for the dependence of the model in terms of the variation of the η parameter in the interaction, and the variations were found to be negligible.

The TFF was calculated in all directly-accessible domains and a fit function will be provided in the following paragraph. The fit can then be used as input in subsequent calculations, such as leptonic decays of the pion, or for the pion as an intermediate state in the muon anomalous magnetic moment a_μ. But first, we will look at the effects of the quark-photon vertex.

Vertex dependency. As introduced in Sec. 3.1, the QED anomaly in the chiral limit demands that the normalized transition form factor amplitude at the on-shell point $F(0,0)|_{m_\pi=0} = 1$. In our numerical evaluation, we obtain a value of $F(0,0) = 0.996$ at the physical pion mass. This is a powerful consistency cross-check for our method as we obtain the anomaly value directly from our coupled system without any additional model parameters. This means that by applying a consistent truncation, which obeys the underlying symmetry relations (such as the axial-vector Ward-Takahashi identity (AXWTI), Eq. (2.64)) in all ingredients, we ensure the correct physical behavior at the on shell point. In fact, any reasonable non-perturbative method must try to at least fulfill the anomaly prediction, otherwise, the approach would already miss fundamental properties of QCD.

But what exactly incorporates these effects? The TFF calculation revealed that the complete inclusion of the twelve tensor basis elements in the quark-photon vertex is crucial to obtain the value. This means using the gauge Ball-Chiu (BC) part as well as the eight transverse components, calculated by iteratively solving the vertex BSE. In order to explore the effects of the vertex, the TFF was evaluated for different set-ups, which corresponds to the results shown in the right panel of Fig. 23. The calculations are performed in the symmetric limit and for three vertex choices: (1) replacing both vertices in the diagram with bare vertices (γ^μ), (2) only using the BC part or (3) calculating with the full vertex.

The calculation with two bare vertices lead to $F(0,0) \approx 0.29$ and with the BC vertex one obtains a value of $F(0,0) = 0.86$. The latter revelation is somewhat interesting as the BC

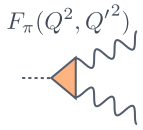

m_v	a_0	a_1	a_2	a_3	b_1	b_2	b_3
0.77 GeV	0.996	0.735	1.214	1.547	0.089	0.133	0.0002

c_1	c_2	d_1	d_2	e_1	e_2
0.384	0.430	2.010	0.024	1.540	0.00005

Table 4: Parameters for the fit function Eq. (5.9) for the **pion transition form factor**.

vertex fulfills the vector WTI and is therefore sufficient to guarantee charge conservation in the electro-magnetic form factor. However, the comparison clearly shows that the transverse components of the vertex are crucial for a quantitative description of the pion TFF.

The transverse part of the vertex contains vector-meson poles (such as ρ-poles) in the timelike region. These are dynamically generated when solving the inhomogeneous BSE and their effects propagate in the calculation of the form factor into the final behavior and slope of the pion TFF. So it seems that these ultimately dictate the anomaly value and thus any reasonable truncation on the vertex must aim to incorporate the effects from the vector poles.

Fit function The Results for the form factor in both the asymmetric and symmetric limit were fitted to construct a parametrization that accurately represents our results in the spacelike domain ($Q^2, Q'^2 > 0$). Abbreviating $w = \eta_+/m_v^2$ and $z = \omega/\eta_+$, the fit for the TFF is described by

$$\mathcal{F}_\pi(Q^2, Q'^2) = \frac{\mathcal{A}(w) + w(1-z^2)\,\mathcal{B}_1(w)\,(1+\mathcal{B}_2(w)z^2)}{(1+w)^2 - w^2 z^2}\,. \tag{5.8}$$

The denominator implements the lowest-lying vector-meson pole (rho-pole) at $wz = \pm(1+w)$, which corresponds to $Q^2 = -m_v^2$ and $Q'^2 = -m_v^2$ with $m_v = 0.77$ GeV. The functions in the numerator ensure that the TFF asymptotically approaches a monopole behavior both in the symmetric ($z = 0$) and asymmetric limit ($z = \pm 1$); they are given by

$$\begin{aligned} \mathcal{A}(w) &= \frac{a_0 + \xi\,(a_1\,b_1\,w + a_2\,b_2\,w^2 + a_3\,b_3\,w^3)}{1 + b_1\,w + b_2\,w^2 + b_3\,w^3}\,, \\ \mathcal{B}_i(w) &= \frac{c_i\,e_i\,w^2}{1 + d_i\,w + e_i\,w^2} \end{aligned}\,. \tag{5.9}$$

The fit parameters for the pion TFF are given in Tab. 4. The parameter $\xi = 1.0 \pm 0.1$ reflects a combined theoretical uncertainty stemming from a variation of the parameter $\eta = 1.85 \pm 0.2$ in the effective interaction, Eq. (4.34), as well as the uncertainty in the determination of the TFF away from the symmetric limit. The latter is due to the kinematic limitations, reviewed in Sec. 4.5, and how we worked around this issue will be discussed at the end of the section. This fit was used in parts as input for the results present in the next sections, where the TFF appears in intermediate stages in the calculation of other π^0 decays, Sec. 5.2, and furthermore in our determination of the pion-pole contribution to the anomalous magnetic moment of the muon a_μ in Sec. 5.6.

The fit is displayed in Fig. 24, where we compare our results to experimental data from the CLEO and CELLO collaborations [123, 124], non-perturbative theoretical calculations from Lattice QCD, Ref. [25], and the data-driven dispersive results, Refs. [125, 126].

Our chosen fit functions, Eq. 5.9, are a set of rational polynomial which resemble a Padé-type fit and the final fit function, Eq. (5.8), combines the individual parts with additional physical constraints, as its denominator contains the vector-meson pole. The combination

of pole structures and polynomials manages to accurately describe our data. A commonly used fit function for the pion TFF in the literature is the vector-dominance-model (VMD), which is parameterized by $F_{\mathrm{VMD}}(Q^2, Q'^2,) = 1/\left[(1+w)^2 - w^2 z^2\right]$. This, however, does not reproduce the monopole behavior observed in the symmetric limit ($z = 0$) (see e.g Fig. 3 in [98], where the authors show a comparison of a monopole and a dipole (VMD) fit with DSE TFF results) and the VMD suggested dipole behavior is only correct in the infrared.

Other non-perturbative approaches such as Lattice QCD rely strongly on choosing an appropriate fit function, as they can only calculate a set of scattered data points; see, e.g., Appendix B of Ref. [127] for a discussion of multiple fit functions. Within this context a more advanced version of the vector-meson-dominance principle was suggested, the LMD+V model [128]. This more refined version reproduces both the symmetric and asymmetric limits and implements two vector-meson poles. Previously this was the preferred fit by the lattice community [129], however the most recent publication Ref. [25] is providing a new fit function, which will be commented on below. The LMD+V and our fit function are indistinguishable in the low Q^2 region. For larger Q^2 the comparison shows agreement in the symmetric and asymmetric limit, yet, in the region between these two limits, the fit functions differ substantially. Whereas the LMD+V develops a sharp peak very close to the asymmetric limit, our fit proceeds with a continuous rise between the symmetric and asymmetric value. Such small and subtle differences could be relevant when the form factor is tested in the whole spacelike doubly virtual domain, such as in the muon's $g-2$.

Results from other non-perturbative approaches and comparison with our result. Over the years, meson transition form factors have been calculated in different non-perturbative methods [25, 125, 130, 131] and in a number of works using the functional approach, see [63, 82, 84, 96, 98, 102, 132, 133] and references therein. In Fig. 24, we choose to compare our result with the two most prominent results on the pion TFF, which are from the lattice QCD collaboration in Mainz and the data-driven dispersive result from Bonn and collaborators.

Direct experimental data for the pion TFF only exist in the singly-virtual case. The first results were obtained from the CELLO and CLEO collaboration, Refs. [123, 124], which can be seen in Fig. 24 on the left. More recent data are available from the Belle and Babar collaboration, Refs. [134, 135], which measured the TFF at larger Q^2 in comparison to the previous measurements and was able to achieve values of up to $Q^2 = 20$ GeV^2.

In the singly-virtual case, the theoretical results show good agreement within error bars and tend to favor the CLEO data. In the doubly virtual and symmetric case, we can see a clear difference between the lattice and our DSE result. Regardless, both results are within the conservative error band of the dispersion approach. The results from the dispersive approach carry a larger error in the doubly-virtual case, as there is no direct data in this limit, such that the TFF is obtained from a set of related cross-section data. In the following, we will give a brief overview of the different non-perturbative approaches to better understand the problems and difficulties that arise.

Other DSE calculations. We start by comparing our results to the ones from other DSE collaborations. Our calculation proceeds along the lines of Ref. [98], where the authors solved the inhomogeneous BSE for the quark-photon vertex to fully incorporate the vertex effects and thus obtained a similar value for the on-shell point close to the anomaly prediction (compare to $g_{\pi\gamma\gamma} = 0.502$ therein, related to the on-shell TFF value by Eq. (18).). As they underlie the same kinematic restriction due to the quark poles, the TFF is evaluated in the same kinematic region and our calculation confirms the previous results.

By contrast, the authors of a more recent DSE study, Ref. [84], used a different tensor basis for the quark-photon vertex. They choose to work directly with the unamputated

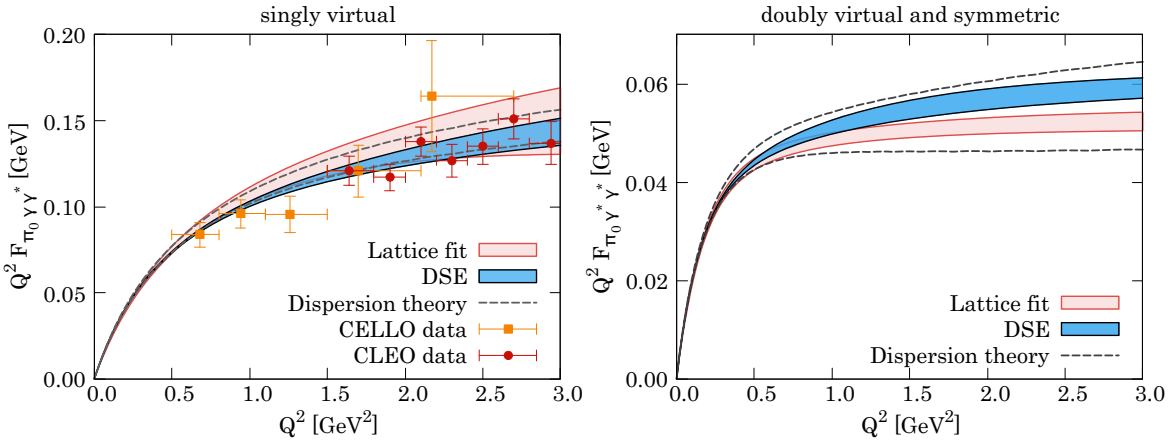

Figure 24: The transition form factor $F_{\pi_0\gamma\gamma}$ in the singly-virtual limit ($Q'^2 = 0$) and the doubly virtual and symmetric limit ($Q'^2 = Q^2$). Compared are the results from the DSE approach [82], lattice gauge theory [25] and dispersion theory [125, 126] together with the experimental results from CELLO [123] and CLEO [124]. The plot is using the most recent lattice data and is updated compared to Fig. 7 in Ref. [77] .

version (vertex with attached quark propagators) and applying Ansätze for it, rather than solving the corresponding BSE. This requires the introduction of additional parameters to the approach in order to reproduce quantities such as the value of the anomaly. In this sense, the vertex is modeled rather than calculated. As the approximations are performed on different levels, it is hard to compare the two studies and draw a conclusion to which extent one or the other truncation scheme seems more justifiable. In our calculation, we decided to pursue the original procedure of Ref. [98], ensuring a consistent treatment of quark-photon vertex and meson amplitude by applying the same truncation in both self-energy and interaction kernel, which requires a total of only three parameters (the quark constituent mass and two parameters in the MT model, of which one to fixes the scale Λ and the other fixes the shape of the quark-gluon interaction, η).

Lattice calculations. The pion transition form factor was calculated in lattice QCD from the collaboration in Mainz [25, 129, 136]. Their first results were published in 2016 [129, 136] and they recently released an updated version in Ref. [25] (early 2019). The most recent calculation was performed with $N_f = 2 + 1$ dynamical flavors and, compared to the earlier $N_f = 2$ work and the recent results were calculated with improved statistics and larger momentum domains. This was achieved by calculating the TFF in two frames (pion rest frame and one moving frame), rather than only the rest frame, which allowed the authors to probe larger photon virtualities, especially in the singly virtual case. With the additional frame, the lattice calculation is now able to access momenta up to $Q^2 \sim 1.5\text{GeV}^2$ in the singly virtual case and can generally probe a wider momentum range also in the doubly virtual case compared to previous calculations. The lattice is able to provide a systematic error estimate including all effects due to the discretization of the theory. The authors performed a thorough analysis including corrections due to finite-size effects, the hyper-cubic lattice and the quark-disconnected contributions into their error estimation. Furthermore, as most of the available ensembles are at unphysical pion mass, they performed an extrapolation to physical values. With this, they are able to reproduce the anomaly value at physical pion mass with a precision of 3.5%.

The lattice calculation carries its own momentum limitations which are completely distinct from those faced by the Dyson-Schwinger calculation described in this work. The lattice limitations come from the periodic boundary conditions of the lattice, which relate the two

photon virtualities and force the accessible domain to be located along parabolas in the real $Q^2 - Q'^2$ plane. The rest-frame calculation is perfectly suited for large momenta in the symmetric double-virtual case but is limited when only one of the photons is virtual. With the additional data from the moving frame, a wider momentum range was probed as the narrow strip of parabolas along the symmetric limit was enlarged. Based on this, the authors of Ref. [25] also concluded that the calculation could proceed to even higher photon virtualities for the singly-virtual case, by calculating in a moving frame with a larger pion momentum. However such calculations are furthermore limited by the signal-to-noise ratio, which gets worse for larger pion momenta. On top of this, a calculation for a new pion momentum (a new frame) requires repeating the numerically most expensive part of the calculation.[1]

To calculate the pion TFF, the authors started by evaluating points on the restricted parabolas in the $Q^2 - Q'^2$-plane at unphysical pion mass. They then perform a fit using a "z expansion" on the unphysical data points and in the last step extrapolate the fit parameters to physical pion mass (Eq. (44) in [25]). In their previous evaluation, the vector-meson-dominance (VMD) model (and more advanced versions) were used to perform the fit. However, the new model is in accord with the asymptotic behavior demanded by Brodsky and Lepage, and is otherwise largely model-independent, making it the preferred choice. The recent lattice results presented in Ref. [25] are compared to the DSE calculation in the singly and doubly-virtual case in Fig. 24. As the lattice calculation was able to further improve their systematic uncertainties for the error estimation, they managed to reduce their error band drastically compared to previous calculations, especially in the doubly virtual case, making their results more competitive to the dispersive calculation.

Dispersion relations. In contrast to the DSE and lattice calculations, the dispersive approach is a data-driven framework that is based on the general principles of analyticity, unitarity and crossing symmetries. With this mathematical tool, it makes use of available experimental data sets to relate them to the observables of interest. This makes the approach to some extent highly dependent on the precision and availability of experimental measurements; on the other hand, the calculations are able to provide a systematic error through error propagation for the experimental uncertainties. The pion transition form factor is in principle directly accessible in experiment, however in practice only in limited regions. A complete measurement covering all kinematic regions is currently not feasible and especially the domains relevant for the hadronic Light-by-Light contribution of the muon's $g-2$ can not be directly measured. Hence the dispersive approach uses the available data on the form factor in the singly-virtual domain and additional data of related processes to obtain results for the TFF in the full space-like domain.

In the dispersive approach, the pion TFF is reconstructed from the most important lowest-lying singularities in the unitarity relation, which can be identified as the exchange of a charged pion pair between the two photons, $\gamma^* \to \pi^+\pi^- \to \gamma^*\pi^0$. The resulting subdiagram includes the pion vector form factor and the $\gamma^* \to 3\pi$ amplitude. These quantities are then constructed from experimental data. For the vector form factor, data from $\pi\pi$-scattering and a direct fit to the form factor as measured in τ decay experiments were used. In the case of the $\gamma^* \to 3\pi$ amplitude, data from the $e^+e^- \to 3\pi$ cross-section can be used, by applying a parametrization and a once-subtracted dispersion relation. Additionally, data from the spacelike singly-virtual process $e^+e^- \to e^+e^-\pi$ were used as well as measurements of the decay width of the $\pi^0 \to \gamma\gamma$. The latter was used to constrain the normalization of the TFF and was taken from data of the PrimEx collaboration. As data taking continues, the error associated with experimental measurements is expected to be reduced, which could

[1] The largest numerical effort in a lattice calculation is the generation of the ensembles. However, Mainz did not generate the ensembles in this work in isolation as they were produced in the collaborative effort of the CLS consortium.

subsequently reduce the error for the dispersive results.

The dispersive results are shown in Fig. 24 together with the calculation from Lattice QCD and our results. The error quoted is of systematic nature, as it follows from error propagation of the errors associated with the experimental data set. As multiple data sets are needed for the evaluation of the TFF in the doubly-virtual limit, the resulting error is larger compared to the singly virtual case.

Canterbury approximants are a generalization of the Padé approximation for bivariate functions. This is yet another data-driven approach and a fit in terms of these approximants is applied to experimental data sets. For a introduction to the approach see Ref. [131], in which the authors apply the method for the pion TFF. A general Canterbury approximant is of the form,

$$C_M^N(Q^2, Q'^2) = \frac{\sum_{n,m=0}^{N} a_{nm}\, Q^{2n}\, Q'^{2m}}{\sum_{n,m=0}^{M} b_{nm}\, Q^{2n}\, Q'^{2m}} \tag{5.10}$$

where by convention $b_{00} = 1$ and where in case of the pion TFF, Bose symmetry of the photons is imposed by requiring $a_{nm} = a_{mn}$ and $b_{nm} = b_{mn}$. This means that the approximants are symmetric with respect to Q^2 and Q'^2. In the singly virtual case ($Q'^2 = 0$) they reduce to Padé approximants. To determine the pion TFF in this approach, one solely constructs a fit of type Eq. (5.10) to available experimental data. In case of the doubly virtual TFF the fits rely on additional constraints from the asymptotic behavior, as available experimental data are limited to singly virtual kinematics.

But even with a limited set of data, the approach is able to reproduce the KTeV measurement for the TFF within 1σ. Equivalently to the dispersive calculation, the approach is highly data-dependent and carries little predictive power. Furthermore, the number of fit parameters is rapidly growing and in the case of the pion TFF there is no proof of convergence. In fact, when using a large value for the number of polynomials in the denominator (M), the denominator can become singular at larger photon momenta.

Large Q^2 behavior. As established around Fig. 20, due to the poles in the quark propagator we can only directly access spacelike momenta up to $Q^2_{\text{max}} \approx 4\text{GeV}^2$ in the asymmetric limit ($Q^2 \neq 0; Q'^2 = 0$). To determine the TFF in the full spacelike domain we need to find a strategy to access larger momenta in the singly-virtual and between the symmetric and asymmetric limits. Our work published in Ref. [82] solves these issues by calculating the form factor for unphysical kinematics and performing an extrapolation to the physical point; the procedure is briefly summarized here. The method allowed us to provide new results on the scaling behavior of the TFF and was used to further improve upon the provided parametrization of the TFF, Eq. (5.9), in the full space-like region.

If Q^2 is taken much larger than the intrinsic scale of the theory, Λ^2_{QCD}, then the form factor factorizes into a perturbative hard scattering piece and a non-perturbative pion distribution amplitude, denoted by $\varphi_\pi(x)$. This is known as the Efremov-Radyushkin-Brodsky-Lepage (ERBL) scaling limit [137, 138] and leads to the result

$$\widetilde{F}(Q^2, Q'^2) = \frac{\eta_+\, F(Q^2, Q'^2)}{4\pi^2 f_\pi^2} \xrightarrow{\eta_+ \to \infty} j(\omega)\,, \tag{5.11}$$

with $\eta_+ = (Q^2 + Q'^2)/2$, $\omega = (Q^2 - Q'^2)/2$ and

$$j(\omega) = \frac{2}{3} \int_0^1 dx\, \frac{\eta_+^2}{\eta_+^2 - \omega^2 (2x-1)^2}\, \varphi_\pi(x)\,. \tag{5.12}$$

In addition, one can show that the pion distribution amplitude $\varphi_\pi(x)$ asymptotically approaches $\varphi_\pi(x) \to 6x(1-x)$. Thus, in the symmetric limit, $Q^2 = Q'^2 \to \omega = 0$, one finds

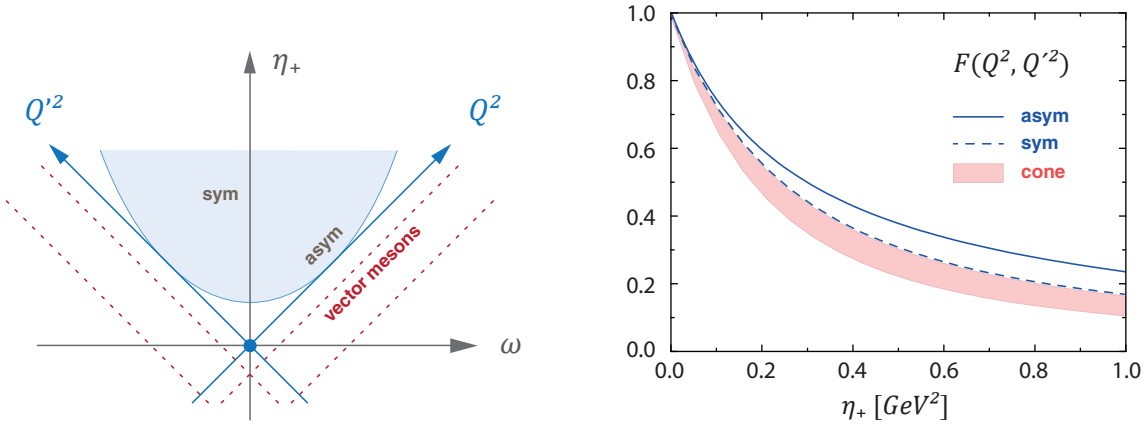

Figure 25: *Left*, kinematic domains in Q^2 and Q'^2 including the symmetric and asymmetric limits. The dotted lines indicate the vector-meson pole locations. The parabola is the spacelike region in the case of constant $t > 0$. *Right*, result for the $\pi^0 \to \gamma\gamma$ TFF, showing the result in the symmetric and asymmetric limits and in the off-shell cone, which is shown in light blue on the left and in Fig. 26.

$$j(0) = \frac{2}{3}\int_0^1 dx\, 6x(1-x) = \frac{2}{3}\,. \tag{5.13}$$

By contrast, in the singly-virtual case $Q^2 = 0$ or $Q'^2 = 0 \to \omega = \pm\eta_+$, the result is

$$j(\pm\eta_+) = \frac{2}{3}\int_0^1 dx\, \frac{6x(1-x)}{1-(2x-1)^2} = 1\,. \tag{5.14}$$

This prediction is rigorous in the symmetric limit, i.e. where both photon momenta are asymptotically large, but has been questioned in the singly-virtual case, where the coupling of the on-shell ($Q^2 = 0$) photon to the pion involves low-energy scales and could well lead to non-perturbative effects. Indeed, experimental data on the transition form factor [123, 124, 134, 135] indicate that the scale for the onset of the asymptotic behavior could be as large as $10 - 100\,\mathrm{GeV}^2$. This is in tension with the usual factorization picture which would predict a scale of order $1\,\mathrm{GeV}^2$. In short, the situation at present is unclear. Whereas the data from the BaBar collaboration [134] indicate that QCD scaling is violated up to $Q^2 \approx 35\,\mathrm{GeV}^2$, the Belle results [135] agree with the asymptotic prediction above $10 - 15\,\mathrm{GeV}^2$. This may be clarified by upcoming data from BelleII [139] and high Q^2 theoretical predictions beyond the ERBL prediction will be especially useful in making the most out of the next generation of experimental data.

When choosing to evaluate the TFF for off-shell kinematics, we can completely avoid the poles in the quark propagator. In this case, the total momentum is chosen to be spacelike, $\Delta^2 = 4t > 0$, which means that no complex value is passed through the four-vector in the triangle and the condition for avoiding poles, Eq. (4.44), holds for all spacelike (Q^2, Q'^2) values. The left panel of Fig. 25 shows a sketch of the kinematic domain in the $Q^2 - Q'^2$ plane, indicating the symmetric and asymmetric limit and the location of the vector-meson poles in the timelike region. The parabola in shaded blue corresponds to values with off-shell and spacelike Δ.

Strictly speaking, the definition of transition matrix elements is in principle only meaningful on the mass shell. In fact, in the DSE approach, the meson bound-state amplitude is by definition an on-shell quantity. With this in mind, we chose to keep the on-shell Bethe-Salpeter scalar amplitudes f_i, even when evaluating the momenta in the triangle for off-shell

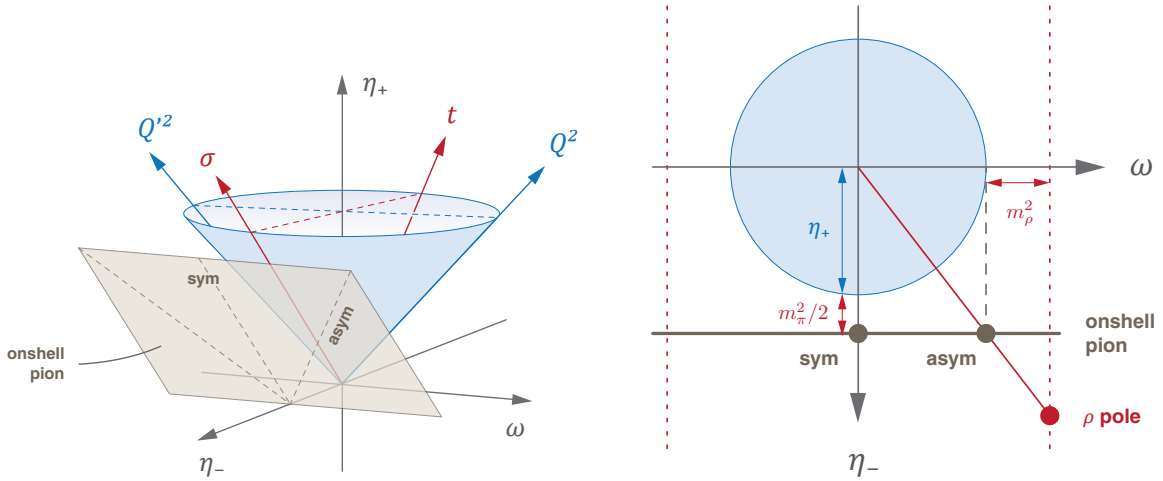

Figure 26: *Left*, kinematic domains in Q^2 and Q'^2 including the symmetric and asymmetric limits. The dotted lines indicate the vector-meson pole locations. The parabola is the spacelike region in the case of constant $t > 0$. *Right*, $\pi^0 \to \gamma\gamma$ transition matrix element.

kinematics. In this way, the off-shell effects only enter through the tensor part in the meson basis, Eq. (5.5).

When Δ is not fixed to the mass shell, the form factor depends on three variables and we can span the $\{Q^2, Q'^2, Q \cdot Q'\}$ space as shown on the left panel of Fig. 26. The cone corresponds to the equivalent parabola in the previous two-dimensional figure 25, and it once more corresponds to the region that is now evaluated in our calculation for $\Delta^2 > 0 \Rightarrow t > 0$. The shaded rectangle represents the on-shell pion plane where $\Delta^2 = 4t = -m_\pi^2$. The figure includes alternative axis in the other variables, which can be related by $\{Q^2, Q'^2, Q \cdot Q'\} = \{\eta_+ \pm \omega, \eta_-\} = \{\sigma + t \pm 2\sqrt{\sigma t}\, Z, \sigma - t\}$. Z is the angle between relative and total momentum $\Sigma \cdot \Delta = 2\sqrt{\sigma t}\, Z$ as previously defined below Eq. (4.46). We can calculate any value inside of the cone (left panel of Fig. 26) and the result for the TFF in this region can be seen in Fig. 25 on the right. The TFF for off-shell values turns out to be slightly smaller then for on-shell values. We will combine all these results to perform the extrapolation from the unphysical cone to large values in the singly-virtual plane.

The sketch in Fig. 26 on the right, gives an indication of how the extrapolation is performed and is a 2-d version of the figure on the left, showing the cone as a circle for a fixed η_+ value (visualized by cutting horizontally through the cone). The horizontal grey line on the right represents the physical on-shell plane and the dashed red line the location of the nearest vector-meson pole. The physical appearance of the vector-meson poles in the time-like regime is correctly incorporated in our quark-photon vertex and consequently in the TFF as well. We can use this as an additional constraint, such that we perform an interpolation between our data and this pole, rather than an extrapolation. At a fixed value for η_+ we consider the quantity

$$R(\eta_-^2 + \omega^2) = \frac{F_\pi(\eta_+, \eta_-, \omega)}{F_\pi(\eta_+, \eta_-, \omega = 0)}\,, \tag{5.15}$$

which runs along a radial line in the $\{\eta_-, \omega\}$-plane (indicated by dark red in Fig. 26 right). Here we divided by the values in the symmetric limit ($\omega = 0$) to minimize unphysical off-shell dependencies. At the vector meson pole, the TFF is singular, leading to $R(\text{“}\rho\text{-pole”}) = \infty$. As infinity is hard to quantify; we instead use the inverse value $R(\eta_-, \omega)^{-1}$ such that $R^{-1}(\text{“}\rho\text{-pole”}) = 0$. The interpolation then starts with all possible values on the inside of the cone, which are located along a radial line, connecting the origin ($R(0) = 1$) with the location of the ρ-meson pole. This line then coincides with the physical plane for asymmetric values,

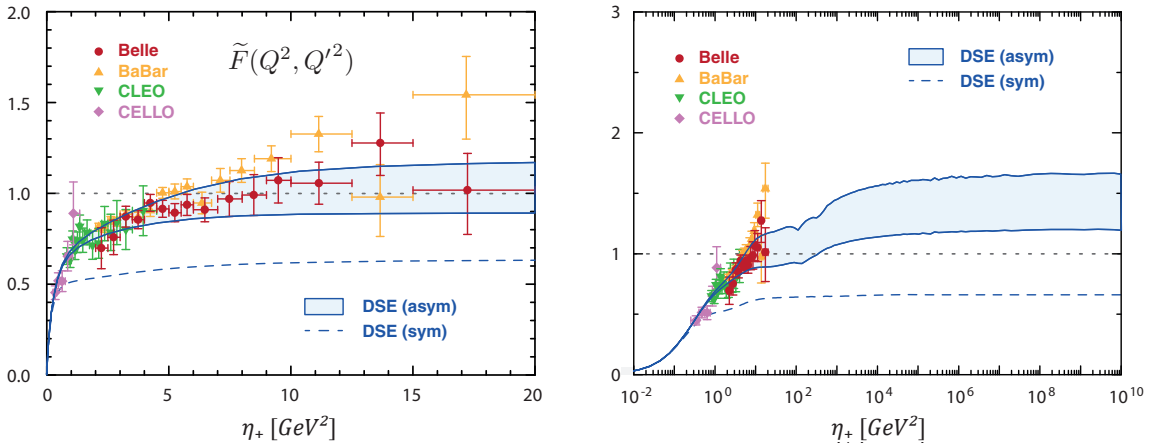

Figure 27: Weighted on shell transition form factor defined in Eq. (5.11) at large η_+. The band shows the result in the asymmetric limit which is compared to experimental data [123, 124, 134, 135], and the dashed line is the form factor in the symmetric limit. The former should asymptotically approach the value 1 (dotted line) whereas the latter converges towards 2/3. Note that $Q^2 = \eta_+$ and $Q^2 = 2\eta_+$ in the symmetric and asymmetric case, respectively.

which is the value of interest. To perform the interpolation we fit the data to a sum of polynomials with an explicit pole term. In the region where we could directly calculate the on-shell TFF ($Q^2 \lesssim 4\text{GeV}^2$) we checked that these fit results were in agreement with the direct calculation in the asymmetric limit.

The resulting form factor in the asymmetric limit is displayed in Fig. 27, where we compared our result with the experimental data from the Belle, BaBar, CLEO and CELLO collaborations [123, 124, 134, 135]. The results favor the Belle data but are also somewhat compatible with the data from BaBar. The form factor in the symmetric limit is shown as well, and it can be clearly seen that the asymptotic value of $\frac{2}{3}$ is reached early on. The asymmetric TFF, on the other hand, does not converge to its final asymptotic value until high Q^2 values. In this case, the TFF continuously rises up to $Q^2 \sim 10^2 - 10^3\text{GeV}^2$; after this, the pion amplitude settles into its asymptotic value, see Fig. 22 on the left, and an analogous behavior can be observed for the TFF, see Fig. 27 on the right. The error band is a combination of theoretical and numerical errors from the interpolation. The theoretical error is once more based on the variation of the η parameter in the MT interaction, Eq. (4.34). However, the dominating part comes from the interpolation. To gauge the impact of the physically motivated inclusion of the pole term, we compared the presented results to results from a pure extrapolation, only using the data points inside the cone. In this case we recover the ERBL limit, Eq. (5.12) $j(\pm\eta_+) = 1$. This leads us to the conclusion that the TFF, especially in the asymmetric limit, is sensitive to the effects from the vector-meson pole, even up to high scales and the correct inclusion of the pole, is crucial to obtain the proper asymptotic behavior. This also means that when one of the photons is close to its off-shell value the pole is relevant and tested at all scales of the other virtual momentum. This mechanism is independent of our approximations, as any reasonable model used for the truncation of the quark-gluon interaction should produce a vector-meson pole in the quark-photon vertex.

Thus it is conceivable, that any reaction with one of the photons close to the on-shell point and the other at large virtual momenta is affected by the vector-meson pole and leads to a correction to the suggested ERLB limit, independent of the method used to calculate the TFF.

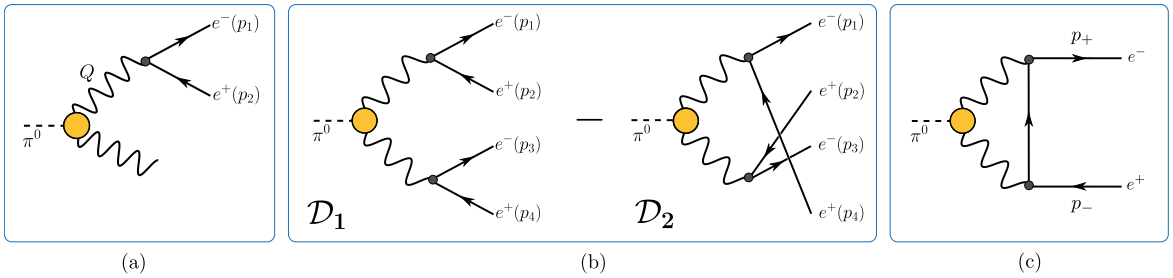

(a) (b) (c)

Figure 28: Electromagnetic decays of the neutral pion: a.) Dalitz decay $\pi^0 \to e^+e^-\gamma$. b.) Dalitz Decay $\pi^0 \to 2e^+2e^-$. c.) Rare decay $\pi^0 \to e^+e^-$ discussed in Sec. (5.3). All decays diagrams are leading-order in QED. The yellow circles indicates the pion's transition form factor $\mathcal{F}_\pi(Q^2, Q'^2)$, at an intermediate stage, which is the only non-perturbative input.

Beyond rainbow-ladder effects. At the end of this section, let us makes some brief remarks on the studies of Ref. [107], and the implication for the form factor calculation. As summarized in Sec. 4.4 we are facing the issue, that in the rainbow-ladder truncation resonances are not described properly. To explore to effects of a physically more accurate treatment, the authors in Ref. [107] performed a "beyond rainbow-ladder" calculation of the quark-photon vertex, incorporating the vector-meson in the timelike momentum region with a width.

In case of the TFF calculation for spacelike photon virtualities, the quark-photon vertices in the triangle diagram are also evaluates in the spacelike domain (the external photon momenta of the TFF are the total momenta in the vertex calculation (here referenced as Q)). The study showed that in particular the results of the vertex dressing functions remained unchanged in the spacelike domain. In this case, the impact of the proper incorporation of the rho-resonance has shown to be negligible and the finding reassures the choice of the RL truncation to be sufficient for TFF calculations in the light-meson sector.

5.2 Electromagnetic decays of the neutral pion

To probe the pion transition form factor in different kinematic domains, in this section, we present other electromagnetic decay processes of the neutral pion. Besides the leading decay into two photons, the neutral pion decays into various combinations of electrons and photons. The PDG [140] provides an overview of all decay channels observed in experiments, and the first six processes are quoted in Tab 5. The decay into two photons is by far the leading one. It is followed by the two Dalitz decays ($\pi^0 \to e^+e^-\gamma$) and ($\pi^0 \to 2e^+2e^-$) and ($\pi^0 \to e^+e^-$) with an even smaller branching ratio as the fifth likeliest decay mode. All these decays contain the TFF as an intermediate vertex. The Feynman diagrams for the decays

Mode		Fraction
Γ_1	2γ	(98.823 ± 0.034) %
Γ_2	$e^+e^-\gamma$	(1.174 ± 0.035) %
Γ_3	γ positronium	$(1.82 \pm 0.29) \times 10^{-9}$
Γ_4	$e^+e^+e^-e^-$	$(3.34 \pm 0.16) \times 10^{-5}$
Γ_5	e^+e^-	$(6.64 \pm 0.33) \times 10^{-8}$
Γ_6	4γ	$< 2 \times 10^{-8}$

Table 5: Decay channels of the neutral pion, according to Particle data group (PDG [140], 2019)

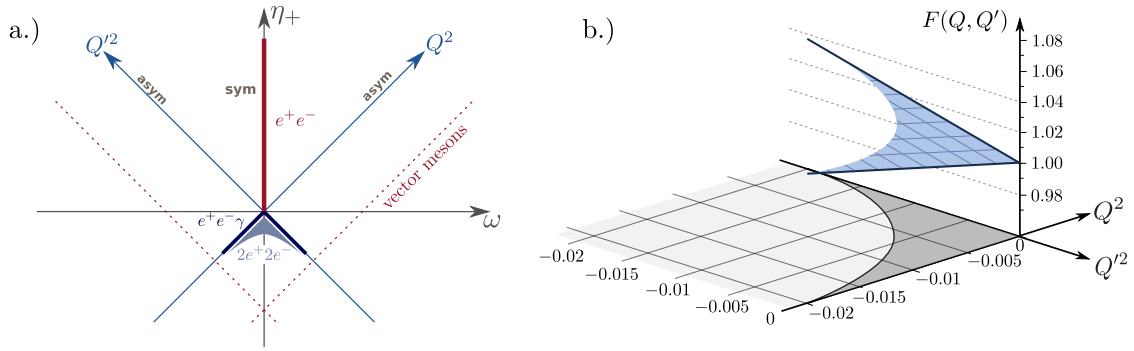

Figure 29: (a.) Relevant kinematic domains for the pion TFF, when applied in another decay process of the neutral pion. Represented in either $\{Q^2, Q'^2\}$ or $\{\eta_+, \omega\}$. (b.) Result for the pion TFF in the timelike domain used as an input for the Dalitz decays. The photon momenta, $\{Q^2, Q'^2\}$ are given in GeV^2 and $m_\pi^2 = 0.0188$.

can be seen in Fig. 28, and the yellow circles indicate the pion TFF. The photon-lepton vertex is a pure QED vertex ($\sim e\gamma^\mu$) that is well described perturbatively. Thus the only component containing effects of the strong force and therefore requiring a non-perturbative calculation is the TFF. The calculations for the decay rates are performed at leading-order QED, considering only the diagrams displayed in Fig. 28.

Fig. 29 (a.) shows an overview of Q^2 and Q'^2 values needed for each decay process. The figure furthermore indicates the symmetric ($Q^2 = Q'^2$) and asymmetric limit ($Q^2 \neq Q'^2, Q'^2 = 0$) and the location of vector-meson poles for guidance. The two Dalitz decays require a calculation of the TFF in the timelike region $Q^2 < 0,\ Q'^2 < 0$. In this sector, the calculation in the DSE approach is very limited, as we are exposed to multiple pole structures. Sampling timelike Q^2 and Q'^2 for the photons translates into complex values of momenta entering the quark-photon vertex. This can lead to the calculation encountering quark poles in the propagators as well as vector meson poles in the vertex. Fortunately, the small mass of the neutral pion ($m_\pi = 135$ MeV) sets the upper border of the phase-space integrals for the Dalitz decays, and thus, we only need timelike values up to $\{Q^2, Q'^2\} > -m_\pi^2$, which lies before the critical region. Details for the calculation of the two Dalitz decays will be explained in the next two sections.

The rare decay, $\pi^0 \to e^+e^-$, probes the form factor in a completely different domain: for spacelike momenta ($Q^2 > 0, Q'^2 > 0$) and in the symmetric limit ($Q^2 = Q'^2$) up to very large values. It is a particularly interesting case, as there is a significant discrepancy between current theoretical and experimental results, which will be discussed in section 5.3 below.

5.2.1 Dalitz Decay: $\pi^0 \to e^+e^-\gamma$

The Dalitz decay of the neutral pion into a photon and an electron-positron pair is the second decay channel with $B(\pi^0 \to e^+e^-\gamma) = (1.174 \pm 0.035)\%$ [141] . The corresponding Feynman diagram is shown in Fig. 28 (a.) and the decay rate to this channel evaluates to

$$\Gamma_{\pi^0\to e^+e^-\gamma} = \frac{e^6 m_\pi^3}{6(4\pi)^3} \int_{4m_e^2}^{m_\pi^2} \frac{dx}{x} \left| \frac{F_\pi(Q^2,0)}{4\pi^2 f_\pi} \right|^2 \sqrt{1-\frac{4m_e^2}{x}} \left(1+\frac{2m_e^2}{x}\right) \left(1-\frac{x}{m_\pi^2}\right)^3 , \quad (5.16)$$

where m_e is the electron mass and $x = -Q^2$. The pion TFF is evaluated in the asymmetric limit $F(Q^2, 0)$, because one of the photons is on-shell while the other carries timelike virtualities. The integrand in Eq. (5.16) is peaked in the the lower Q^2 region, such that the main contribution of the integral comes for values close to the anomaly value at $Q^2 = Q'^2 = 0$. The result for the TFF in his region is shown in Fig. 29 (b.) and, for this decay, only values

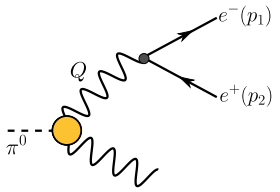

Collaboration	$\Gamma_{\pi^0\to e^+e^-\gamma}$ [10^{-11} GeV]
PDG [141]	9.06(18)
Experimental RC [143]	9.143(9)
Terschlüsen et al. [142]	9.26
Hoferichter et al. [83]	9.065
Our result	9.11(4)

Table 6: Comparison of results for the 3-body Dalitz decay rate for the π^0.

on the border of the region are sampled. Using the PDG [140] values for $m_e = 0.51099$ MeV and $\alpha_{\rm em}^{-1} = (4\pi)/e^2 = 137.035$ in Eq. (5.16), we obtained a final decay rate of

$$\Gamma_{\pi\to e^+e^-\gamma} = 9.11(4) \times 10^{-11}\ \text{GeV}\,. \tag{5.17}$$

The error bar comes entirely from the model dependence of m_π and f_π and is based on a variation of the η-parameter in the effective interaction.

Other theoretical evaluations. The decay rate has been calculated in other theoretical approaches [83, 142]. All calculations evaluate the decay at leading-order QED, leaving the TFF as the only non-trivial and non-perturbative input. Thus the differences in the results lie solely in how the calculation of the TFF is performed. Ref. [142] uses an effective theory. Effective theories are a low-energy description of the underlying physical theory using the appropriate degrees of freedom to describe physical phenomena at a chosen energy scale. The low-energy effective theory of QCD is χPT (Chiral perturbation theory). In χPT the degrees of freedom are not the fundamental particles (quarks and gluons) but composite particles, in this case, the lowest-lying bound-state, the pion. The authors of Ref. [142] use next-to-leading order χPT, including terms that couple the Goldstone bosons (pions) and external fields to vector mesons. Ref. [83] uses the dispersive framework to determine the form factor. In Sec. 5.1 we have sketched how the TFF is extracted in this data-driven framework, and Ref. [83] is one of the earlier calculation of the TFF in the dispersive set-up.

In Table 6 we show a comparison of our result with the experimental values and the results from other theoretical approaches [83, 142]. The experimental numbers quoted are the value from the Particle-Data-Group (PDG) [141] and a value from the reanalysis of Ref. [143], which improves the value from the PDG by two orders of magnitude, by including a set of next-to-leading-order radiative correction (RC) in the QED sector to perform the data-analysis. Within the quoted errors, all results are in good agreement. As the integrand in Eq. (5.16) is peaked in the lower momentum region, mostly values for the TFF close to the anomaly value contribute. Accordingly, it is to be expected that most theoretical predictions should be in close agreement, as any reasonable construction obeys the anomaly constraint. A pure QED calculation, without any non-perturbative form factor, yields a value which differs on the level of 0.2% ($\Gamma^{\rm QED}_{\pi^0\to e^+e^-\gamma} = 9.156 \times 10^{-11}$GeV). This leads to the conclusion that the impact of the TFF for the Dalitz decay is small, and efforts towards a higher precision on the level of the form factor determination will not lead to any new information in this decay channel.

5.2.2 Dalitz Decay: $\pi^0 \to 2e^+2e^-$

The four-body Dalitz decay also requires the pion TFF in the time like region, but for doubly virtual momenta, as the pion decays into two di-lepton pairs. It is the fourth most likely decay

mode with $B(\pi^0 \to e^+e^-e^+e^-) = (3.34 \pm 0.16) \times 10^{-5}$ [141]. The decay rate is given by

$$\Gamma_{\pi^0\to 2e^+2e^-} = \frac{1}{(2!)^2}\,\frac{1}{2m_\pi}\int d\Phi_4\,|\mathcal{M}|^2\,, \tag{5.18}$$

where $|\mathcal{M}|^2$ is the squared and spin-summed matrix element and the symmetry factor in front accounts for the two pairs of identical final-state particles. $d\Phi_4$ is the four-dimensional phase space measure (a detailed derivation is given in Appendix B).

Fig. 28 (b.) shows the corresponding Feynman diagrams and in this case there are two possible contributions at leading-order QED ($\mathcal{D}_1$ and $\mathcal{D}_2$), which differ by the combination of lepton anti-lepton pair. The exchange of two leptons introduces a relative minus sign between the two diagrams. Squaring the two contributions we obtain

$$|\mathcal{M}|^2 = |\mathcal{D}_1|^2 + |\mathcal{D}_2|^2 + 2\mathrm{Re}[\mathcal{D}_1\mathcal{D}_2^*]\,. \tag{5.19}$$

Applying the Feynman rules we express the two diagrams as

$$\mathcal{D}_1 = e^2\frac{\Lambda^{\mu\nu}(Q,Q')}{Q^2Q'^2}\,\bar u(p_1)\,\gamma^\mu\,v(p_2)\,\bar u(p_3)\,\gamma^\nu\,v(p_4)\,,\ \mathcal{D}_2 = e^2\frac{\Lambda^{\mu\nu}(Q,Q')}{Q^2Q'^2}\,\bar u(p_1)\,\gamma^\mu\,v(p_4)\,\bar u(p_3)\,\gamma^\nu\,v(p_2)\,, \tag{5.20}$$

where $\bar u$ and v are the spin projectors for the outgoing electron and positron and $\Lambda^{\mu\nu}(Q,Q')$ is the $(\pi^0\to\gamma\gamma)$ transition form factor defined in Eq. (5.1). As discussed in Refs. [142,144], the squared contributions are equal and can be combined. It follows that the decay rate can be decomposed into two parts

$$\Gamma_{\pi^0\to 2e^+2e^-} = \Gamma^{(\mathrm{direct})}_{\pi^0\to 2e^+2e^-} + \Gamma^{(\mathrm{indirect})}_{\pi^0\to 2e^+2e^-} =: \frac{1}{(2!)^2}\,\frac{1}{2m_\pi}\int d\Phi_4\left[\left(|\mathcal{D}_1|^2+|\mathcal{D}_2|^2\right)+2\mathrm{Re}[\mathcal{D}_1\mathcal{D}_2^*]\right]. \tag{5.21}$$

The first (direct) contribution corresponds to the two squared magnitudes and the second (indirect or interference) term to the cross-terms.

The squared amplitude for the direct contribution is then given by,

$$|\mathcal{D}_1|^2 + |\mathcal{D}_2|^2 = 2e^4\frac{\Lambda^{\mu\nu}(Q,Q')\,\Lambda^{\alpha\beta}(Q,Q')}{Q^4\,Q'^4}\,\mathrm{Tr}\,G_{34}^{\mu\alpha}\,\mathrm{Tr}\,G_{12}^{\nu\beta}\,,$$

where we used the abbreviation $G_{ij}^{\mu\nu} = (i\not{p}_i + m_e)\,\gamma^\mu\,(i\not{p}_j - m_e)\,\gamma^\nu$ and where the spin projector have been combined in the usual way ($\sum \bar u(p)u(p) = i\not{p}+m_e$). The twelve-dimensional phase-space integral reduces to five, as seven of integrals can be trivially performed and evaluate to a constant. In the direct case the integrand only depends on the pairwise sums $Q' = -(p_1+p_2)$ and $Q = p_3+p_4$ and the five integrals can be further reduced to two integrals. The decay rate for the direct contributions is given by

$$\Gamma^{(\mathrm{direct})}_{\pi^0\to 2e^+2e^-} = \frac{e^8}{36\,(2\pi)^5\,m_\pi^3}\int\limits_{4m_e^2}^{(m_\pi-2m_e)^2} dx \int\limits_{4m_e^2}^{(m_\pi-\sqrt{x})^2} dy\ \sqrt{x-4m_e^2}\sqrt{y-4m_e^2}\left[\frac{(x+y-m_\pi^2)^2}{4xy}-1\right]^{3/2} \times\left(1+\frac{2m_e^2}{x}\right)\left(1+\frac{2m_e^2}{y}\right)\left|\frac{F(Q^2,Q'^2)}{4\pi^2 f_\pi}\right|^2. \tag{5.22}$$

Here we introduced the shorthands $x = -Q^2$ and $y = -Q'^2$ for the two photon virtualities, where for values $x, y > 0$ we are using timelike momenta for the TFF and these are restricted by thresholds for the two two-body decays. Between direct and indirect contribution, the direct is the largest fraction of the final decay rate.

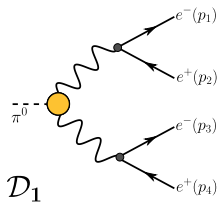

Collaboration	$\Gamma_{\pi^0\to 2e^+2e^-}$ [10^{-13} GeV]
PDG [141]	2.58(12)
Terschlüsen et al. [142]	2.68
Escribano et al. [144]	2.62
Our result	2.63(1)

Table 7: Comparison of result for the 4-body Dalitz decay rate for the π^0

The interference term, on the other hand, depends on all possible four-vector combinations of electron and positron pairs. Consequently, the phase-space integral cannot be further reduced and its integrand is given by

$$\mathrm{Re}[\mathcal{D}_1\mathcal{D}_2^*] = e^4\,\frac{\Lambda^{\mu\nu}(Q,Q')\,\Lambda^{\alpha\beta}(K,K')}{Q^2\,Q'^2\,K^2\,K'^2}\,\mathrm{Tr}\,G_{32}^{\mu\beta}\,G_{14}^{\nu\alpha}\,,$$

where $Q' = -(p_1+p_2)$, $Q = p_3+p_4$ and $K' = -(p_2+p_3)$, $K = p_1+p_4$ are the possible momenta of the virtual photons. To perform the five-dimensional integral, we used various methods, ranging from tensor-product quadrature with a combination of Gauss-Legendre and double exponential rules, to 5-dimensional adaptive cubature as well as standard Monte-Carlo methods [145]; all agreed perfectly.

For the direct and indirect contributions to the decay rate we obtain

$$\Gamma^{(\mathrm{direct})}_{\pi^0\to 2e^+2e^-} = \quad 2.66(1)\times 10^{-13}\,\mathrm{GeV}, \tag{5.23}$$
$$\Gamma^{(\mathrm{indirect})}_{\pi^0\to 2e^+2e^-} = -0.03\times 10^{-13}\,\mathrm{GeV}. \tag{5.24}$$

The final results is shown in Table 7 where we once more compare to other theoretical calculations and the value from experiment. The indirect part, Eq. (5.24), contributes less than 1% to the final result of the decay rate.

Comparison. The previously mentioned reference [142] performed the four-body Dalitz decay as well, delivering compatible results using chiral perturbation theory. Ref. [144] calculates the TFF in the data-driven Canterbury approach, applying rational polynomials to fit the form factor data. The authors therein applied fits for experimental data of the π^0, η and η' transition form factors in the spacelike region and use the fit to analytically continue the TFFs into to kinematic region relevant for the decay rate, which recall is timelike $(Q^2, Q'^2 < 0)$ with doubly virtual momenta. All results are compatible with experiment and consistent with each other within the quoted error. The phase-space restricts the virtual photons to timelike momenta between $4m_e^2$ and m_π^2 (kinematic domain in Fig. 29 (a.)) and entails that the sensitivity to the details of the TFF beyond the anomaly value is insignificant and deviates from its nominal value of 1 by no more than 3%.

To conclude, through exploring the Dalitz decays of the neutral pion, we could show that our TFF result fulfills the anomaly constraints and that the decay rates for these channels are correctly reproduced by the functional form of the TFF.

5.3 Rare decay: $\pi^0 \to e^+e^-$

The decay of the neutral pion into an electron-positron pair $\pi^0 \to e^+e^-$ poses an interesting puzzle: theoretical estimates show a discrepancy to the experimentally measured value from the KTeV E799-II experiment at Fermilab [131, 146–150] of similar magnitude as the discrepancy for the muonic $g-2$. The decay is called a "rare decay", as its branching ratio of

$B_{\text{PDG}}(\pi \to e^+e^-) = (6.46 \pm 0.33) \times 10^{-8}$ [141] is many orders of magnitude smaller than the leading decay modes, see Tab. 5. Compared to the pion decay into two photons, it is loop- and helicity-suppressed. This makes it potentially sensitive to new physics and the current discrepancy demands new insight from the theoretical as well as from the experimental side. However, the small branching ratio makes it very difficult to perform a precise measurement. It is the fifth most likely decay mode of the neutral pion and experimental processes including this decay are dominated by the Dalitz and photon decays. Using an elaborate reanalysis of the radiative corrections, the authors of [149, 150] were able to give an updated version of the experimental value of $B_{\text{exp}}(\pi^0 \to e^+e^-) = (6.87 \pm 0.36) \times 10^{-8}$. The current theoretical calculations range from $B_{\text{Theo}}(\pi^0 \to e^+e^-) = (6.21(3) - 6.23(9)) \times 10^{-8}$ and give a current discrepancy of order $\sim 2\sigma$. It remains to be seen if the tension is resolved or could be seen as an indication for physics beyond the Standard Model.

This chapter is structured as follows. We start the discussion by introducing the general equation for the theoretical calculation of the decay amplitude. Two strategies were pursued in this context and the different set-ups will be explained. We conclude with a discussion of the results, where our calculation is compared to other non-perturbative results and the experimental measurements, and we give an outlook on how the finding can be interpreted when moving forward.

At leading order in QED the process is described by the one-loop graph in Fig. 30 (a.), which includes the pion transition form factor $F_{\pi^0}(Q^2, Q'^2)$ as the only non-perturbative input. Compared to the previous Dalitz decays, in case of the rare decay, the TFF is probed for a larger range of space-like photon virtualities (formally for all values of spacelike Q^2, Q'^2), see kinematic comparison Fig. 29 (a.). Defining $t = \Delta^2/4$, where Δ is the momentum of the decaying pion, the corresponding normalized branching ratio is given by

$$R = \frac{B(\pi^0 \to e^+e^-)}{B(\pi^0 \to \gamma\gamma)} = 2\left(\frac{m_e\,\alpha_{\text{em}}}{\pi m_\pi}\right)^2 \beta(t_0)\;|\mathcal{A}^{\text{LO}}(t_0)|^2\,. \tag{5.25}$$

The factor $\beta(t) = \sqrt{1 + m_e^2/t}$ stems from the two-body phase-space integration and $B(\pi^0 \to \gamma\gamma) = (0.98823 \pm 0.00034)$, as quoted in the PDG [140]. The scalar amplitude $\mathcal{A}(t)$ can be viewed as the pseudo-scalar form factor of the electron, describing how the pion couples electromagnetically to it due to the underlying two-photon decay. For general calculations it is convenient to allow the pion momentum Δ to take arbitrary values such that t can differ from the on-shell value $t_0 = -m_\pi^2/4$. However, as a physical meaningful prediction, the amplitude has to be evaluated at the on-shell pion point. The decay rate is calculated at leading-order in QED (LO). Other SM contributions such as the weak interactions are negligible. With this in mind, we drop the "LO" superscript from now on.

In comparison to the previous Dalitz decays, this decay includes an additional integration over a photon-lepton-loop. Because the first part of the diagram, the pion transition to two photons, is itself a physically allowed decay, we encounter singularities as the photon in the loop can go on-shell. This makes it a more challenging task and as published in Ref. [81] we approached this problem with two different methods: (1) with a reformulation of the integral using the dispersive approach and (2) by deforming the integration path in the complex plane avoiding the pole structures. The two approaches will be described in detail in the following sections. Note that the section about the direct path deformation, Sec. 5.3.2, relies on definitions for the decay amplitude made in the dispersive introduction.

There is an on-going study at the NA62 experiment at CERN expecting new data in the upcoming year. It will perform the analysis including the radiative correction in the same manner as suggested by the authors of Ref. [150]. This will provide the first independent cross-check from the KTeV data and could help to clarify the significance of the discrepancy.

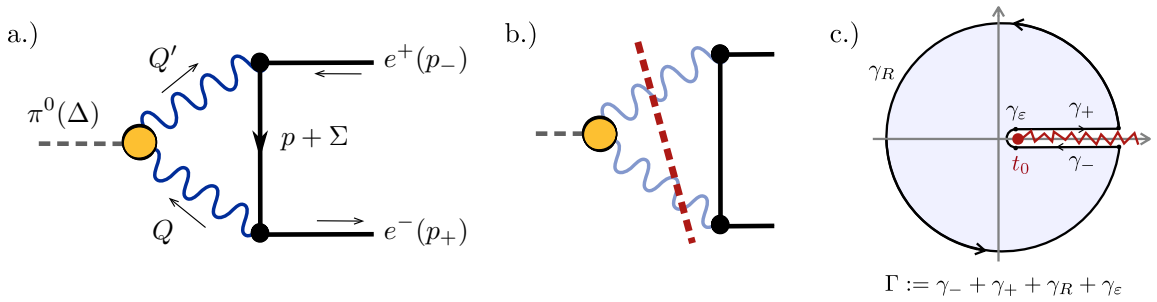

Figure 30: (a.) Feynman diagram for the $\pi^0 \to e^+e^-$ decay. The TFF is represented by the yellow circle. (b.) Cut structure for the Cutkoswky cutting rule to obtain the imaginary part of the diagram. The crossed propagators (photons) are put on-shell. (c.) Integration path in the complex $\mathcal{A}$(t) plane with a branch cut at $t = t_0$, in our case $t_0 = 0$. The path consists of four patches: $\Gamma := \gamma_+ + \gamma_- + \gamma_R + \gamma_-\varepsilon$.

5.3.1 Dispersive approach

The dispersive framework is derived using the unitarity of the S-matrix and will allow us to rephrase the integration over the singularity structures through path deformation. In the case of the direct path deformation discussed in Sec. (5.3.2) below, it is crucial to know the exact pole location. Here, by contrast, the dispersion relation is providing a more general framework to transform a certain type of pole structure.

The Feynman diagram for the rare decay, shown in Fig. 30 a.), corresponds to the amplitude defined by the matrix element

$$\langle e^+(p_+, s_+)e^-(p_-, s_-)|\pi^0(\Delta)\rangle = i(2\pi)^4\delta(\Delta + p_- - p_+)\,\mathcal{M}_{\pi^0\to e^+e^-}\,. \tag{5.26}$$

Following the usual Feynman rules, we find that the amplitude is given by

$$\begin{aligned}\mathcal{M}^{s_+s_-}_{\pi^0\to e^+e^-} &= \bar{u}_{s_+}(p_+)\mathbb{M}(p_+, p_-)v_{s_-}(-p_-) \\ &:= \bar{u}_{s_+}(p_+)\int\frac{d^4\Sigma}{(2\pi)^4}\,\gamma^\mu\,\mathbf{S}(p+\Sigma)\,\gamma^\nu\,\frac{\Lambda^{\mu\nu}(Q,Q')}{Q^2\,Q'^2}v_{s_-}(-p_-)\,,\end{aligned} \tag{5.27}$$

where $\mathbf{S}$ is the lepton propagator, $\bar{u}$ and v are the spin projectors for the outgoing electron and positron and $\Lambda^{\mu\nu}(Q, Q')$ is the $(\pi^0 \to \gamma\gamma)$ transition current from Eq. (5.1). The total decay rate is then determined by

$$\sum_{s_+,s_-}|\mathcal{M}^{s_+s_-}_{\pi^0\to e^+e^-}|^2 = \mathrm{Tr}[(i\not{p}_+ - m)\mathbb{M}(p_+, p_-)(i\not{p}_- - m)\mathbb{M}(p_+, p_-)]\,. \tag{5.28}$$

It is convenient to rewrite the previous equation in terms of an effective scalar amplitude $\mathcal{A}(t)$. It can be shown that the matrix element $\mathbb{M}(p_+, p_-)$ is equal to a scalar function multiplying a γ_5, as this is the only possible tensor structure for a pseudoscalar-lepton-lepton vertex. The total decay rate is then directly proportional to $|\mathcal{A}(t)|^2$. To do so we will use the positive-energy projector,

$$\Lambda(p_\pm) = \frac{1}{2}\left(\mathbb{1} + \not{p}_\pm/(im_e)\right). \tag{5.29}$$

For arbitrary pion virtuality $t = \Delta^2/4$, one can show that $\mathcal{A}(t)$ is defined as follows

$$\Lambda(p_+)\mathbb{M}(p_+, p_-)\Lambda(p_-) =: \frac{\mathcal{A}(t)}{(4\pi)^2}\,\frac{2im_e\,\alpha_{\mathrm{em}}}{\pi f_\pi}\,\Lambda(p_+)\,\gamma_5\,\Lambda(p_-)\,. \tag{5.30}$$

The only Dirac structure fulfilling all quantum numbers for the pseudo-scalar-lepton vertex is γ_5 and thus the matrix element can be decomposed as such, defining $\mathcal{A}(t)$ as the corresponding dressing function.

The momentum conventions follow those introduced for the pion TFF and are summarized for convenience in Appendix B. The relative photon momentum $\Sigma = (Q+Q')/2$ becomes the loop momentum in the additional photon-lepton loop. Since the integration is running over the full space-like domain, the photon virtualities Q^2 and Q'^2 are evaluated for complex momenta close to the symmetric limit ($Q^2 = Q'^2$). The evaluation of the physical decay rate has no free parameter left, as incoming and outgoing momenta are fixed by requiring that the particles are on their mass shells. The electron and positron momenta are thus fixed by $p_\pm^2 = (p \pm \Delta/2)^2 = -m_e^2$. The on-shell value for the pion is given by $t = t_0 (= -m_\pi^2/4)$. For the evaluation of the integral, however, we will keep the pion momentum arbitrary.

Taking traces and contracting the Lorenz indices yields the following expression for $\mathcal{A}(t)$:

$$\begin{aligned}\mathcal{A}(t) &= \frac{1}{2\pi^2}\int \mathrm{d}^4\Sigma\; \varepsilon^{\mu\nu\alpha\beta} Q'^{\alpha} Q^{\beta}\, \frac{\mathrm{Tr}\left[\gamma^\mu\; ((p+\Sigma)^\rho\, \gamma^\rho + m_e)\; \gamma^\nu\right]}{(p+\Sigma)^2 + m_e^2}\, \frac{F_{\pi^0}(Q^2, Q'^2)}{Q^2 Q'^2}\,, \\ &= \frac{1}{2\pi^2 t}\int \mathrm{d}^4\Sigma\, \frac{(\Sigma\cdot\Delta)^2 - \Sigma^2\Delta^2}{(p+\Sigma)^2 + m_e^2}\, \frac{F_{\pi^0}(Q^2, Q'^2)}{Q^2\, Q'^2}\,. \end{aligned} \tag{5.31}$$

Looking carefully at the denominator, we can already identify that the integrand has poles due to the intermediate particles going on-shell. Thus it cannot be naively integrated. One exception to this is given by the unphysical point $t = \Delta^2/4 = 0$, which is a removable singularity as numerator and denominator chancel perfectly, and where integral can thus be directly evaluated. The exact pole location will be discussed in more detail in the next section (5.3.2).

A standard way to circumvent the problem uses dispersive methods. Dispersion relations are an analytic tool that allows us to use knowledge of a correlation function in certain parts of the complex plane to obtain information in other regions of interest. In the particular case of the $\pi \to e^+e^-$ decay, it will help us to calculate the amplitude by combining knowledge of its imaginary part and the analytic structure in the complex plane. This includes multiple steps: (1) determining the imaginary part of the integral using cutting rules, (2) calculating the real part using a once-subtracted dispersion relation.

(1) Imaginary part of the amplitude: The Cutkosky cutting rules [151] are a set of relations used to calculate the imaginary part of a Feynman diagram by putting the intermediate particles on-shell. This is formally done by cutting the diagram, which mathematically means replacing the particles' propagators by delta functions. In the case of scalar particles the replacement rule is

$$\frac{i}{k^2 + m_i^2} \to (2\pi i)\, \Theta(k_0)\, \delta(k^2 + m_i^2)\,. \tag{5.32}$$

The triangle diagram can be cut in three different ways, cutting through two propagator lines at the time. Of the three cuts, it can be shown that only one is nonzero (cut seen on Fig. 30 b.)), due to kinematics and that the relation holds exactly in case of the pion as the

decay particle. [1] The amplitude in Eq. (5.31) transforms to

$$\begin{aligned} 2\,\mathrm{Im}\,\mathcal{A}(t) &= \frac{1}{2\pi^2 t}\int d^4\Sigma\,\frac{(\Sigma\cdot\Delta)^2-\Sigma^2\Delta^2}{(p+\Sigma)^2+m_e^2}\,F_{\pi^0}(Q^2,Q'^2)\,(2\pi i)^2\Theta(Q_0)\,\delta(Q^2)\,\Theta(Q_0')\,\delta(Q'^2)\,,\\ &= \frac{1}{4t\,E}\int d^3\mathbf{\Sigma}\,\frac{\left[\left((\Sigma\cdot\Delta)^2-\Sigma^2\Delta^2\right)\,F_{\pi^0}(Q^2,Q'^2)\right]_{Q=Q_0'=0}}{(\mathbf{p}+\mathbf{\Sigma})^2+m_e^2}\,\delta(|\mathbf{\Sigma}|-\sqrt{m_e^2+\mathbf{p}^2})\,, \end{aligned} \tag{5.33}$$

where $\mathbf{p}$ is the three momentum of the outgoing leptons. Since we are working in the pion rest frame the lepton momenta are equal in magnitude with opposite directions. Integrating out the three momentum and considering $t<0$, the imaginary part of the amplitude is given by

$$\mathrm{Im}\;\mathcal{A}(t) = \frac{\pi}{2\beta(t)}\;\ln\left[\gamma(t)\right]\;F_{\pi^0}(0,0)\,, \tag{5.34}$$

with $\gamma(t)=(1-\beta(t))/(1+\beta(t))$ and $\beta(t)=\sqrt{1+m_e^2/t}$. Due to cutting the photon line the pion TFF is solely evaluated at the on-shell point, which is known by the anomaly calculation as discussed in Sec. 3.1. Using the definition of the normalized TFF, as given in Eq. (5.1), we can replace $F(0,0)=1$ (neglecting corrections due to non-zero pion mass).

Before constraining the real part of $\mathcal{A}$ we give a brief aside about the unitary bound on the branching ratio. As the decay rate is proportional to $|\mathcal{A}|^2$ one can use the inequality $|\mathcal{A}(t_0)|^2 \geq |\mathrm{Im}\mathcal{A}(t_0)|^2$ at $t_0=-m_\pi^2/4$, which leads to the well-known unitary bound for the branching ratio

$$R=\frac{B(\pi^0\to e^+e^-)}{B(\pi^0\to\gamma\gamma)} \geq \left(\frac{m\alpha_{\mathrm{em}}}{m_\pi}\right)^2\frac{\ln^2\left[\gamma(t_0)\right]}{2\beta(t_0)} = 4.75\times10^{-8}\,.$$

This is a model-independent bound and it is more than 7σ below the experimentally measured value (KTeV), Ref. [146]. In the next step we will use a once-subtracted dispersion relation to obtain information for the real part of $\mathcal{A}(t)$ and in a final step combine this with the above-defined imaginary part to get a full prediction for the branching ratio.

(2) Dispersion relations: The general approach of dispersion theory is to reconstruct a function from information about its underlying analytic structure. This requires knowledge of residues at poles, discontinuities across cuts or subtraction constants (which are sometimes introduced to ensure that dispersive integrals are finite). This can, for example, help to analytically continue experimental data, which is measured in the time-like region, into the Euclidean space-like domain, where it is sometimes easier to make theoretical predictions. In our case, we will use a once-subtracted dispersion relation to avoid a direct calculation of the integral with pole structures. This relates the real part of the amplitude with a weighted integral of the imaginary part.

Recall Eq. (5.31), which is a analytic function of the incoming pion virtuality ($t=\Delta^2/4$) with a branch cut along the real t-axis, reaching from $t=0$ to ∞, see Fig. 30 (c.). To avoid the branch cut structure we can deform the integration path, as indicated in the figure and apply Cauchy's integral theorem. Here we introduce the parameter ε which describes the distance between the paths and the cut. Furthermore it can be shown that the only paths contributing are the two paths on both sides of the branch cut ($\gamma_+ + \gamma_-$). For ($\varepsilon\to 0$) the finite difference between the paths equals the imaginary part of the amplitude and we conclude that

$$\mathcal{A}(t) = \frac{1}{2\pi i}\oint_\Gamma \mathrm{d}t'\,\frac{\mathcal{A}(t')}{t'-t} = \frac{1}{\pi}\int_{t_0}^\infty \mathrm{d}t'\,\frac{\mathrm{Im}\,\mathcal{A}(t')}{t-t'}\,. \tag{5.35}$$

[1] When considering heavier particle decays such as eg. the $\eta\to\gamma\gamma$, contributions from higher order cuts need to be considered for the imaginary part of the diagram.

Notice that the dispersive integral is integrated over all t', such that the knowledge of $\mathrm{Im}(\mathcal{A})(t)$ is needed at all scales. Fortunately the cutting rules provide us with the required information, and the expression for the imaginary part Eq. (5.34) is inserted in Eq. (5.35) above. Looking carefully at the powers of t in the integrand, we observ a log-divergence. This is because $\mathrm{Im}(\mathcal{A})(t) \sim \log t$ for $t \to \infty$ and

$$\int_1^\Lambda dt' \frac{\log t'}{t'} \propto \log^2 \Lambda \,. \tag{5.36}$$

However we can use another tool of the dispersive approach and suppress the integrand by additional powers of t' to circumvent the divergence. This is achieved by multiplying with factors of $1/t'$ in the integrand and where each factor introduces a corresponding low-energy constant. The procedure is called subtraction and leads to the once-subtracted dispersion relation for $\mathcal{A}(t)$. The subtraction is performed using the identity

$$\frac{\mathcal{A}(t) - \mathcal{A}(0)}{t} = \frac{1}{\pi} \int_0^\infty \mathrm{d}t' \, \frac{1}{t' - t} \mathrm{Im} \left[\frac{\mathcal{A}(t') - \mathcal{A}(0)}{t'} \right] . \tag{5.37}$$

After reshuffling this leads to the final once-subtracted dispersion relation of

$$\mathcal{A}(t) = \mathcal{A}(0) + \frac{t}{\pi} \int_0^\infty \frac{dt'}{t'} \frac{\mathrm{Im}\, \mathcal{A}(t')}{(t' - t)} = \mathcal{A}(0) + \frac{1}{\beta(t)} \left[i \frac{\pi}{2} \ln \left[\gamma(t) \right] + \mathrm{Li}_2(-\gamma(t)) + \frac{\pi^2}{12} + \frac{1}{4} \ln^2 \gamma(t) \right] , \tag{5.38}$$

where $\mathrm{Li}_2(-\gamma(t))$ is the dilogarithm or Spence function. The expression for the imaginary part Eq. (5.34) was plugged in above. Since the imaginary part of the amplitude is already known trough the cutting rules, we can simply concentrate on the real part of the amplitude and conclude with the following relation,

$$\mathrm{Re}\ \mathcal{A}(t) = \mathcal{A}(0) + \frac{\ln^2 \gamma(t) + \frac{1}{3}\pi^2 + 4\,\mathrm{Li}_2(-\gamma(t))}{4\beta(t)} \,. \tag{5.39}$$

For the on-shell value this implies $\mathrm{Re}\ \mathcal{A}(t_0) = \mathcal{A}(0) + 31.92(2)$ so that the only unknown left is the subtraction constant $\mathcal{A}(0)$ which remarkably, is the only part that contains the non-perturbative effects from the transition form factor.

In fact, $t = 0$ is the only point where we can evaluate Eq. (5.31) directly, without singularities in the integrand and it breaks down to

$$\mathcal{A}(0) = \frac{4}{3} \int_0^\infty \mathrm{d}x \left[\frac{3}{2} - x + (x - 2) \sqrt{1 + \frac{1}{x}} \right] F(Q^2, Q^2) \,, \tag{5.40}$$

where the temporary abbreviation $x = Q^2/(4m_e^2)$ was used. In order to simplify Eq. (5.31) in this special case ($t = 0$), we needed to specify the four-vector such that we could evaluate their products. The form factor is evaluated in the symmetric limit like for $t = 0 : Q^2 = Q'^2 = \Sigma^2$. Thus both arguments of the TFF are the integration variables $F(Q^2, Q^2)$, such that $Q^2 \in \{0, \infty\}$. The evaluation of Eq. (5.40) is in particular convenient for the DSE approach as the calculation in the symmetric limit for the TFF does not face any kinematic limitations. The integrand in Eq. (5.40) is peaked in the low Q^2 region, which is already indicated through the scaled variable $x = Q^2/(4m_e^2)$. The highest weighted contributions are from Q^2 at the order of the electron mass (see Fig. 2 in Ref. [131] for a plot of the integral kernel, showing that the integrand is peaked in the lower momentum regime). Thus, the result for the subtraction constant is mostly dominated by the behavior of the form factor close to the anomaly value.

A similar formula as in Eq. (5.40) can be derived using a Mellin-Barnes representation [152]

$$\mathcal{A}(0) \approx -\frac{5}{4} + \frac{3}{2}\int_0^\infty \mathrm{d}x \ln(4x)\,\frac{d}{dx}F(Q^2,Q^2), \tag{5.41}$$

which is only valid to leading order in an expansion in the electron mass and thus is less precise then Eq. (5.40). However a cross-check with the data of our form factor showed no noticeable difference in the results evaluated with the different formulas.

Using the fit function Eq. (5.9) as the input for the TFF in the equation above, we obtain a final number for the subtraction constant of $\mathcal{A}(0) = -21.85(2)$. The error comes from varying the η parameter in the fit function. Now combining the result for the imaginary and real parts Eqs. (5.34–5.39), one arrives at the on-shell value $\mathcal{A}(t_0) = 10.07(4) - 17.45(1)\,i$, which corresponds to a branching ratio of

$$B(\pi \to e^+e^-) = 6.21(3) \times 10^{-8}\,. \tag{5.42}$$

5.3.2 Direct calculation by path deformation

Earlier calculations for the rare decay rate [131,147,148] used the dispersive formula explained in the previous section to evaluate the integral. In order to reform a completely independent calculation, we developed another strategy to directly solve the integral given in Eq. (5.31). This is done by carefully analyzing the singularity locations in the complex integration domain and performing a well-chosen path deformation to reach an equivalent integral that can be directly evaluated numerically.

Minkowski vs. Euclidean. Eq. (5.31) is defined in the Euclidean signature. This choice is motivated by limitations in the ranges of Q^2 and Q'^2 for which the TFF, $F_{\pi_0}(Q^2,Q'^2)$, is available, coming from the DSE calculation. The TFF itself was evaluated in Euclidean signature but with a complex value for the external pion momentum Δ, chosen to give the on shell result $\Delta^2 = -m_\pi^2$. As a result, slightly negative values of Q^2 and Q'^2 can be achieved but the full range of timelike momenta is not available. This is an important limitation for the present calculation because if we were to directly take the Minkowski version of Eq. (5.31), we would be required to integrate the TFF over both timelike and spacelike momenta.

However, the actual physical prediction comes from the Minkowski expression with real momenta. Thus we can use Eq. (5.31), only if we prove it is equivalent to the latter. This is an important general rule, nicely discussed in Ref. [43,44]: **A calculation in Euclidean space leads to the correct physical result, when the integral used corresponds to an analytic continuation of the original Minkowski integral that properly treats the singularities of the integrand.** As is illustrated in Figs. 4 and 5 of Ref. [44], the continuation requires deforming the integration contour so that branch cuts are never crossed. One can begin either with Minkowski or with real Euclidean momenta, but in the second case analytic continuation is necessary.

Example, to illustrate these ideas consider the function,

$$A(t) = \int dQ \frac{1}{[(Q-\sqrt{t})^2+1]^{3/2}}\,. \tag{5.43}$$

This function is reached by integrating $1/[(Q-\sqrt{t})^2 + k_x^2 + 1]^2$ over all values of k_x and can be thought of as an exemplary contribution to an amplitude in a toy 1+1 dimensional field

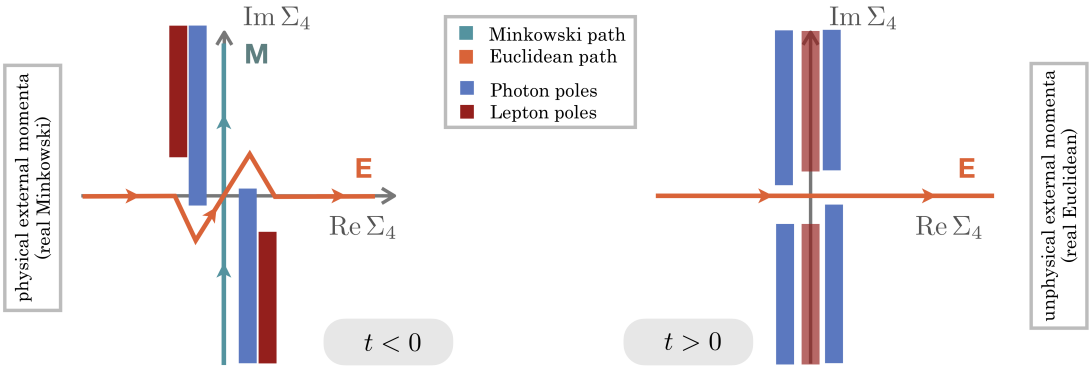

Figure 31: Sketch of the pole structure in the complex Σ_4 plane (red - lepton, blue - photon poles). *Left* shows the set-up when working with real Minkowski momenta and employing the $i\varepsilon$ prescription to shift the poles, such that we can perform the Minkowski integral without crossing singularities. *Right*, when choosing positive values for $t = \Delta^2/4$, which corresponds to real Euclidean values for the total momentum. Inspired by the plots in Ref. [44].

theory. Following the discussion above, we note that the integral is well defined for any real choice of $\sqrt{t}$. This corresponds to an amplitude with real external Euclidean momenta. To get to the physical prediction, we want to analytically continue to imaginary $\sqrt{t}$ meaning $t < 0$. As a specific example, suppose the physical result is given by $t_0 = -4$. If we naively evaluate the integrand at t_0 and integrate Q along the real axis then we reach a finite result of ≈ -0.309. Although the integral is well defined, the problem is that the Q contour intersects a branch cut, meaning that the value we reach is not equal to the analytic continuation of $A(t)$ and thus not the physical value. If we instead deform the contour (for example set $\mathrm{Im}Q = 2i$) to avoid the cut, then we reach the correct result $A(t_0) = -2$.

As explained in Ref. [44], this is a common issue in Euclidean bound-state calculations. From the reduced toy theory in that reference, the reader can learn a lot about how to reliably perform path deformations to connect to the Minkowski results. Contour deformation have been applied in different situation throughout the DSE community to calculate various two- and three-point Green functions, see Refs. [6, 107, 153–158]

Kinematic restrictions In Sec. 4.5 we have established that the TFF is subject to kinematic restrictions due to the quark poles, which were specified in Eq. (4.44). Following the same pattern, we can now identify a restricted area for the loop integral of the rare decay rate $\mathcal{A}(t)$, Eq. (5.31), which is restricted by the poles of the loop particles. The singularity condition on the involved momenta are then given by

$$\left(\mathrm{Im}\, Q^{(\prime)}\right)^2 < m_\gamma = 0 \quad \Rightarrow \quad \left(\mathrm{Im}\,\frac{\Delta}{2}\right)^2 < 0 \quad \text{and} \quad (\mathrm{Im}\, p)^2 < m_l^2\,, \tag{5.44}$$

where p denotes the relative momentum between the outgoing leptons. As the former relative momentum Σ becomes the loop momentum, $\Sigma \in \mathbb{R}$ and $Q = \Sigma \pm \Delta/2$. With these conditions we can again set up the four-vectors in a general frame, analogous to Eq.(4.45), and obtain

$$\Delta = \frac{1}{\mathcal{N}} \begin{bmatrix} 0 \\ 0 \\ -2i\sqrt{t}\sqrt{t+m_l^2} \\ 4\alpha t \end{bmatrix}, \; p = \frac{1}{\mathcal{N}} \begin{bmatrix} 0 \\ 0 \\ 2i\alpha\sqrt{t}\sqrt{t+m_l^2} \\ -(t+m_l^2) \end{bmatrix}, \tag{5.45}$$

with $\mathcal{N} = \sqrt{-(t+m_l^2)+4\alpha^2 t}$. With a specific choice for the frame parameter, the condition Eq. (5.44) then transforms to

$$t < 0 \quad \text{and} \quad (\operatorname{Im} t)^2 < 4m_l^2 \operatorname{Re}(-t)\,, \tag{5.46}$$

for the photon poles and the lepton pole, respectively . In case of the onshell value $t = -m_\pi^2/4 < 0$, the photon pole criteria is not fulfilled and prohibits a direct calculation. The lepton pole criterion on the other hand holds, $0 < m_l^2 m_\pi^2$ and this pole is in principle not located in the integration domain. However we have to be careful when the path is deformed in the complex plane to avoid crossing either pole structure.

Singularity structures. To perform the path deformation we need to carefully analyze Eq. (5.31) to determine the exact pole locations. Complex analysis tells us that we can solve an integral independent of its integration path, **if** start- and end-point is the same and **if** the path is transformed without crossing any singularities. The poles in Eq. (5.31) appear for vanishing denominators, which occurs when either of the loop particles goes on-shell (for the photons $\{Q^2, Q'^2\} = -m_\gamma^2 = 0$ and the electron $(p+\Sigma)^2 = -m_e^2$).

As defined in Eq. (5.31), we chose to keep the amplitude as a function of t, in order to explore this dependence. Recall that t is the rescaled pion momentum squared, $t = \Delta^2/4$. Any choice besides the on-shell value, $t_0 = -m_\pi^2/4$, is **unphysical** and has no implications outside this exploration. However, in the context of our approach is it interesting to investigate the behavior of the $\mathcal{A}(t)$ function and in particular the movement of the poles for different choices of t. For positive t-values ($t > 0$), the photons cannot go on-shell and the calculation of the integral requires no path deformation, as no singularities appear in the integrand. This corresponds to the case when working purely real Euclidean momenta only and the poles branch cut distribution are displayed in the right panel of Fig. 31. The figure shows the complex Σ_4 plane, as the outer most integral of the originally four-dimensional Eq. (5.31), and the branch-cuts, which correspond to the photon (blue) and lepton (red) cuts. Here we furthermore display the integration path for the Euclidean integral, and we see that in fact, the integral can be performed without crossing any singularities. However as the physical information is defined in the time-like region, an analytic continuation would be needed in that case.

The right panel of Fig. 31 shows the proper Minkowski version of the calculation, where the $i\varepsilon$ prescription is used to move the branch cuts from the y-axis into the complex plane and enable direct evaluation of the physical integral along the vertical path (turquoise). The Euclidean path follows from performing a Wick rotation. When we start with the Minkowski version of the integral, it is unambiguous which path one needs to choose for the deformed Euclidean path (orange), as the Wick rotation forces the path to be on the same side of the branch cuts.

An alternative approach is shown in the left panel of Fig. 31. Here $t > 0$ is an unphysical choice of kinematics, corresponding to real Euclidean momenta. This guarantees that no branch cuts will cross the horizontal axis so that the Euclidean integral has a clear definition. As discussed above, to reach the final result one must analytically continue in t. In doing so the branch cuts will move and the orange contour must be adjusted so that these are never crossed. In this way, the right panel is smoothly converted into the left, by continuing t.

Considering the integral for the decay amplitude, Eq. (5.31), we start the analysis of the poles by expressing the four-dimensional integral in terms of spherical coordinates,

$$\int d^4\Sigma = \int_0^\infty d\Sigma\, \Sigma^2 \int_0^\pi d\theta \sin^2\theta \int_0^\pi d\phi\, \sin\phi \int_0^{2\pi} d\psi = \frac{1}{2}\int_0^\infty d\sigma\sigma \int_{-1}^1 dZ\sqrt{1-Z^2}\int_{-1}^1 dY \int_0^{2\pi} d\psi\,. \tag{5.47}$$

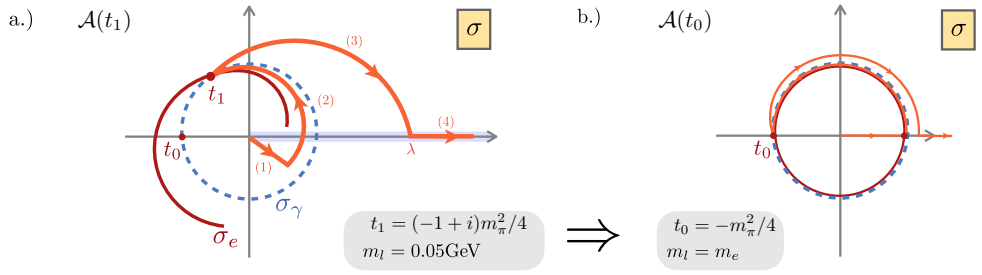

Figure 32: (a.) $\mathcal{A}(t_1)$: Sketch of the pole/branch cut structure in the complex σ-plane. The red (solid) curve corresponds to the electron cut σ_e and the blue (dasehed) to the poles introduced by the photons σ_γ. The deformed path is shown in orange. The naive path (shaded blue) connects the integration boundaries, $\sigma \in \{0, \infty\}$, via the positive real axis, crossing the photon poles. Here $t_1 = (-1+i)m_\pi^2/4$ and $m_l = 0.05\text{GeV}$ was chosen for graphical purpose, as the features of the paths can be seen in more detail. (b.) $\mathcal{A}(t_0)$: Shows cuts and path for the actual calculations at the on-shell point t_0. In this case the cuts are almost on top of another.

To identify the exact pole locations in terms of the spherical integration variables, we need to define the relevant four-vectors and their relations to the integration coordinates,

$$\sigma = \Sigma^2\,, \quad Z = \frac{\Sigma\cdot\Delta}{\sqrt{\Sigma^2\Delta^2}} = \frac{\Sigma\cdot\Delta}{2\sqrt{\sigma t}}\,, \quad Y = \frac{p\cdot\Sigma}{i\sqrt{\sigma}\sqrt{t+m_e^2}\sqrt{1-Z^2}}\,, \tag{5.48}$$

where once more Δ is the total momentum and Σ the relative momentum of the decaying pion but also the loop integration momentum. As discussed above, we always keep the Euclidean loop momentum real implying in this case that $\{\sigma, Z, Y\} \in \mathbb{R}$. For time-like t-values ($t < 0$) this implies $(\Sigma\cdot\Delta) \in \mathbb{C}$ in order to keep $Z \in \mathbb{R}$. In the pion rest-frame the four-vector are then given by,

$$\Delta = 2\sqrt{t}\begin{bmatrix}0\\0\\0\\1\end{bmatrix}\,, \quad p = i\sqrt{t+m_e^2}\begin{bmatrix}0\\0\\1\\0\end{bmatrix}\,, \quad \Sigma = \sqrt{\sigma}\begin{bmatrix}\sqrt{1-Z^2}\sqrt{1-Y^2}\sin\psi\\ \sqrt{1-Z^2}\sqrt{1-Y^2}\cos\psi\\ \sqrt{1-Z^2}\,Y\\ Z\end{bmatrix}\,. \tag{5.49}$$

The integration of the innermost angle is trivial, as the integrand does not depend on it, and evaluates to 2π. Using the scalar products for the four-vectors, the integral $\mathcal{A}(t)$, Eq. (5.31) takes the following form,

$$\mathcal{A}(t) = -\frac{2}{\pi^2}\frac{(2\pi)^4}{(2\pi)^3}\frac{1}{2}\int_0^\infty d\sigma\,\sigma^2 \int_{-1}^{1} dZ\,\frac{(1-Z)^{3/2}F(Q^2,Q'^2)}{(\sigma-t)^2+4t\sigma(1-Z)^2} \tag{5.50}$$
$$\times\int_{-1}^{1} dY\,\frac{1}{\sigma-t+2i\sqrt{\sigma}\sqrt{t+m_e^2}\sqrt{1-Z^2}Y}\,.$$

The denominator in the Z integral corresponds to the expression for the photons poles $Q^2Q'^2$ and likewise the denominator in the Y integral to the lepton pole contribution $((p+\Sigma)^2+m_e^2)$. The integration in Y can be performed analytically,

$$\int_{-1}^{1} dY\,\frac{1}{a+Y} = \ln\frac{a+1}{a-1}\,, \quad \text{with} \quad a := \frac{\sigma-t}{2i\sqrt{\sigma}\sqrt{t+m_e^2}\sqrt{1-Z^2}}\,, \tag{5.51}$$

for all $a \in \mathbb{C}$ except $-1 < a < 1$, in which case the logarithm develops a branch cut, which we refer to as the lepton cut, as it originates from that particle going onshell. For a general t we denote the values of the radial integration variable σ where the logarithm hits the lepton cut, by

$$\sigma_e^{\pm}(t,Z) = \left(\sqrt{tZ^2 - m_e^2(1-Z^2)} \pm i\sqrt{t+m_e^2}\sqrt{1-Z^2}\right)^2 . \tag{5.52}$$

This produces a cut in the complex σ-plane, see the red curve in Fig. 32 (b.), which can be obtained by varying Z in the integration region of $Z \in \{-1,1\}$. For $Z = \pm 1$ this corresponds to $\sigma_e^{\pm}(t,\pm 1) = t$ and for $Z = 0$ to the endpoints at $\sigma_e^{\pm}(t,0) = -(\sqrt{t+m_e^2} \pm m_e)^2$. As we can see in the figure, for the real integration contour $\sigma \in \{0,\infty\}$ and for any real value of t, the integral does not cross the lepton cut. However additional cuts, due to the photons, will force us to deform the contour into the complex plane. For this reason, it is important to be aware of, and navigate around, the lepton cut as well.

Turning now to the photons, these go onshell and produce a cut whenever

$$Q^2Q'^2 = 0 \quad \Rightarrow \quad \sigma_\gamma^{\pm}(t,Z) = t\left(Z \pm i\sqrt{1-Z^2}\right)^2 . \tag{5.53}$$

This describes a circle around the origin in the complex σ-plane with a radius of $|t|$ and an opening at $\sigma = t$, as at this point the numerator and the denominator in the Z integral cancel perfectly resulting in a removable singularity.

Path deformation. The combination of lepton and photon cut, Fig. 32 (b.) leave one possible path deformation. We are forced to separate the path into four pieces navigating through the narrow ridge between the cuts. The different paths are parameterized through,

$$\begin{aligned}
(1):\ & \gamma_1(t) = \frac{1}{2}\left(\sigma_\gamma^-(t,Z=0,) + \sigma_e(t,Z=0)\right)\alpha = -\sqrt{t+m_e^2}\,(\sqrt{t+m_e^2} - m)\alpha\,, \\
(2):\ & \gamma_2(t) = \frac{1}{2}\left(\sigma_\gamma^-(t,Z=\alpha) + \sigma_e(t,Z=\alpha)\right)\,, \\
(3):\ & \gamma_3(t) = (1+\alpha(\lambda-1))\,t^{1-\alpha}\,, \\
(4):\ & \gamma_4(t) = \lambda + \frac{\alpha^2}{[1-\alpha+1/\Lambda]}\,.
\end{aligned} \tag{5.54}$$

where $\alpha \in \{0,1\}$, λ is a point on the positive real axis far away from the cuts and $\Lambda \to \infty$ is the UV cutoff of the σ integral. To summarize, we were able to perform a direct calculation by (1) locating all cuts in the complex integration domain and (2) making use of Cauchy integral theorem, deforming the path into an integration contour connecting the original integration borders $\{0;\infty\}$ but without crossing any singularities.

The cut structure shown in Fig. 32 (b.) is displayed for $t_1 = (-1+i)m_\pi^2/4$ as this is better suited for explaining the path-deformation, however for the decay rate we need to evaluate $\mathcal{A}(t_0)$ at $t_0 = -m_\pi^2/4$, which is shown in Fig. 32 (c.). Due to the small lepton mass ($m_e \ll m_\pi$) the two cuts nearly overlap in this case. Fortunately, the cuts open up on opposite sides, such that a path-deformation as shown in the figure is still possible but numerically more difficult. The integrand in Z is highly peaked in this case and requires a high resolution in the angular grid. In the work presented in Ref. [81] an adaptive integration routine was used for this angular integration, distributing grid points as needed.

As mentioned above, t was left as a free parameter and the decay amplitude $\mathcal{A}(t)$ was calculated for all t values. The results published in Ref. [81] are shown in the right panel of Fig. 33. This shows very nicely that the amplitude develops a branch cut in the imaginary part for time-like t. The resulting on-shell value is given by

$$\mathcal{A}(t_0) = 10.10(3) + 17.45(1)i\,. \tag{5.55}$$

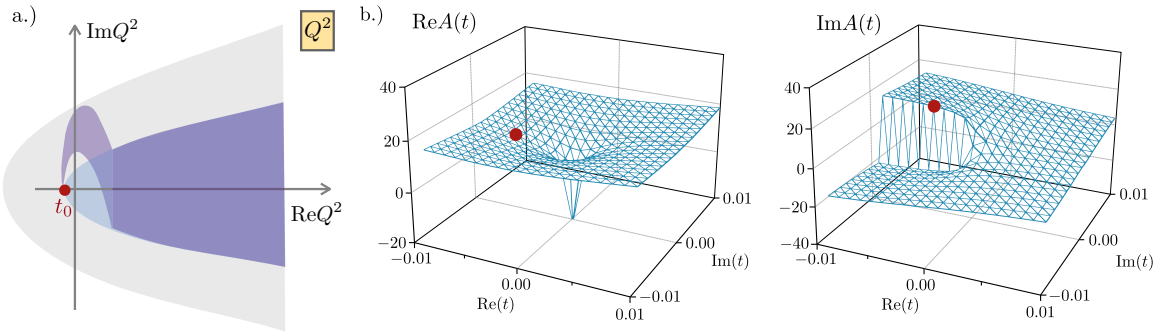

Figure 33: *Left*, values in the complex Q^2-plane for which we evaluate the TFF based on the integral boundaries. The shaded blue shows the original parabola around the real axis with apex at t_0. Due to the path-deformation the domain changes slightly (shaded violet) in the smaller Q^2 region. The Q'^2 regional plot covers the same plane and thus the total evaluation corresponds to a parabola in the complex $Q^2 - Q'^2$ plane. *Right*, result for decay-amplitude $\mathcal{A}(t)$ for complex t values. The unit for t is GeV^2 and $\mathcal{A}(t)$ is dimensionless. For the decay rate it was evaluated at $t_0 = -m_\pi^2/4 \approx -0.0005$ GeV^2 (red dot).

The error reflects the uncertainties associated with the form factor fit Eq.(5.8), reflected by the parameter $\xi = 1.0 \pm 0.1$.

Kinematic evaluation of the TFF. Applying the path deformation we are able to calculate the integral without crossing any singularities. In the course of the deformation, the TFF is now evaluated for slightly different values in the $\{Q^2, Q'^2\}$ plane compared to the original integration path. Recall the connection between the photon momenta and the integration variables in Eq. (5.50),

$$\{Q^2, Q'^2\} = \eta_+ \pm \omega = \Sigma^2 + \frac{\Delta^2}{4} \pm \Sigma \cdot \Delta = \sigma + t \pm 2\sqrt{\sigma\, t} Z \overset{\text{onshell}}{=} \sigma - \frac{m_\pi^2}{4} \pm i m_\pi \sqrt{\sigma} Z\,. \quad (5.56)$$

The original path runs over over $\sigma \in \{0, \infty\}$ and $Z \in \{-1, 1\}$, which leads to a parabola in the complex Q^2-plane with apex at zero, see right panel Fig. 33. With the path deformation, Eq. (5.54), the region slightly changes (light purple), such that overall the TFF is evaluated in a larger parabola in the complex Q^2 domain, indicated in light gray.

5.3.3 Summary and conclusion

To summarize, the calculation for the $\pi^0 \to e^+e^-$ decay rate was performed at leading-order in QED. In the previous sections, we present two different methods how to determine the decay rate, as singularities in the integrand complicate the evaluation of the loop-integral. Two different strategies were applied: (1) the use of a dispersion relation (DR), Eq. (5.38), and (2) solving the integral by deforming the integration path (direct), Eqs. (5.50) and (5.54). The first method was established by the authors in Ref. [147] and reduces the problem to an almost completely analytic integral, where the only non-perturbative input is the subtraction constant $\mathcal{A}(0)$. The constant relies on knowledge of the transition form factor in the symmetric limit ($Q^2 = Q'^2$ and $Q^2 \in \mathrm{R}$). Following along the lines of the references we used the results of our transition form factor calculation, given in Sec. 5.1, and obtained a value of $\mathcal{A}_{\mathrm{DR}}(t_0) = 10.07(4) - 17.45(1)i$.

In a second try, we worked out an independent way to transform the path in the complex plane, carefully avoiding the pole structures which arise in the integral. This required slightly different values for $\{Q^2, Q'^2\}$ in the complex momentum plane and led to a final value of

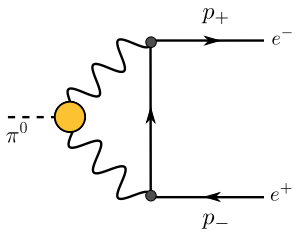

Collaboration	$\mathrm{B}(\pi^0 \to e^+e^-)\,[10^{-8}]$
Experiment [146, 149, 150]	6.87(36)
Dorokhov (2008) [147, 148]	6.2(1)
Masjuan (2015) [131]	6.23(5)
Our result (DR)	6.21(3)
Our result (direct)	6.22(3)

Table 8: Our result for the rare decay, obtained either with the dispersion relation (DR) or directly from the contour deformation, compared to other theoretical calculations and experiment.

$\mathcal{A}_{\mathrm{direct}}(t_0) = 10.10(3) + 17.45(1)i$, which is in agreement with the result from the dispersive formula within the error bars. The errors are once more based on the variation of the η parameter in the interaction model of our truncation, Eq. (4.34), and translate into the corresponding error, $\xi = 1.0 \pm 0.1$ in the TFF fit function, Eq. (5.9). The comparison between the two methods provides a valuable cross-check and supports previous results by other collaboration using the dispersive method, Refs. [131, 147, 148]. Even though the TFF is probed in different kinematic regions in both methods, the results are remarkably close, hinting that the impact of the TFF on the final result is small. Table 8 gives an overview of our final numbers and compares our calculation with results from other non-perturbative calculations and the experimental value measured at KTeV.

Other non-perturbative calculations. The authors in [131,147,148] used the dispersive relation explained in the previous section 5.3.1. In this case, the only non-perturbative input remaining is the subtraction constant $\mathcal{A}(0)$. The references use the Mellin-Barnes representation for the constant, Eq. (5.41), instead of the direct integral for $\mathcal{A}(0)$. However, this has shown to have a negligible effect on the final results and appears to be a fair approximation. Thus, the only difference between the two publications and our result lies in the input of the pion TFF to determine $\mathcal{A}(0)$.

In Refs. [147,148], $F_{\pi^0}(Q, Q')$ is obtained using a phenomenologically motivated parametrization of experimental data, which is based on the expected vector-meson-dominance of the TFF. The data is taken from the TFF measurement of the CLEO collaboration [124]. Due to the lack of data in the doubly-virtual sector, additional high-energy QCD constraints were applied to compensate for this deficit.

In the more recent Ref. [131], the authors use yet another data-driven reconstruction, but in this case, the fit uses rational polynomials. It is based on the theory of Padé approximants and is able to provide an error estimation combining the uncertainties from the experimental measurements and the error associated with the fitting procedure. For the doubly-virtual kinematics of the pion TFF, it is extended to Canterbury approximants. Since, in this case, the doubly-virtual experimental data are not available, the authors have to make assumptions motivated by the high energy behavior of the form factor to make a prediction. The fits are limited by the available experimental data of the pion TFF in the singly- and doubly-virtual regime.

Comparison of theoretical results. The comparison in Table. 8 shows that all results from non-perturbative calculations are in good agreement within their error bars. Since the same technique was applied, we conclude that the differences are based on the slightly different results for the pion transition form factor. Data-driven approaches such as [131, 147, 148] are limited to the available experimental measurements of $(\pi^0 \to \gamma\gamma)$, whereas our

approach delivers a top-down calculation of the TFF based on the gluon-quark interaction. On the other hand, it is suffering from an error that is not quantifiable due to the truncation performed at the level of these interactions. The data-driven approaches can provide a more rigorous error estimate due to error propagation of the error associated with the experimental measurements.

On the other hand, it appears that the decay rate is not overly sensitive to different representations for the TFF as long as QCD constraints, such as the anomaly value, are satisfied. Fig. 2 in Ref. [131] shows the contribution for the integral in Eq. (5.31) for different energy scales. It reveals that the integrand is peaked at very low energies and thus gives a large weight to the values close to the anomaly prediction. It furthermore shows that 99% of the integral contribution comes from the region below 1 GeV^2, such that the asymptotic behavior of the TFF at large momenta is basically irrelevant. In this context, it is not surprising that the final results are in good agreement, as any meaningful calculation for the pion TFF fulfills the anomaly constraints, and thus shows very similar behavior in the lower momentum regime.

Comparison to the experimental value. With the current theoretical results, the discrepancy of $2.0\,\sigma$ to the experimental measurement of KTeV remains. The tension could be resolved with a new and more precise measurement from the NA62 experiment at CERN. This is a kaon experiment with a decay-in-flight technique that is on the lookout for physics beyond the Standard Model in different kaon and pion decay processes, see Ref. [159, 160].

From the theoretical point of view one can choose to interpret the discrepancy in two directions, by either demanding more calculations based on the Standard Model (SM) or expecting that these effects are a strong indication for physics beyond the SM (BSM), which leads to different future plans:

- **SM physics**: Improvements on the calculations and experimental analyses based on the SM, demanding that all effects involved in this decay process are solely SM physics. In this case, the experimental analyses could be further improved by a reevaluation of the radiative corrections, which has previously already helped to reduce the uncertainties and discrepancies, Ref. [149, 150]. Furthermore, an investigation of the decay rates with other non-perturbative approaches, such as lattice QCD, could be beneficial.

- **BSM physics**: Studying new mechanisms beyond the Standard Model, see Ref. [161, 162].

5.4 η - η' transition form factor

The results of this section were presented in [77] and are summarized here to complete the story of meson pseudo-scalar form factors. As the numerical techniques, as well as available experimental data, evolves, more and more non-perturbative approaches can properly calculate the pion transition form factor and, consequently, using the dispersive formula, the pion-pole contribution to HLbL mesonic exchange. The lightest meson is undeniably the most important of these contributions, however, to achieve the desired accuracy in the case of the muon a_μ it is crucial to consider other meson exchange channels, such as the η, η'. The DSE approach is certainly not designed to achieve a high precision result (at least not in the RL truncation and with the unaccounted error), but we consider it a useful tool to give phenomenological guidance to other approaches (about asymptotic behavior and general form), as long as it remains to be numerically challenging or impossible to calculate this TFF in other non-perturbative methods. The additional difficulties associated with the $\eta - \eta'$ mixing, have lead few non-perturbative approaches to calculate this observable and thus we can certainly provide a useful result for cross-checking. The η, η' pole contribution

to a_μ follow along the same lines as in case of the pion, thus the η and η' TFF is needed, the details of this will be discussed in Sec. 5.6.1.

The $\eta - \eta'$ TFF have strangeness content, as their quark-field content is a linear combination of the three quark-antiquark pairs of up, down and strange and given by $\eta = 1/\sqrt{6}(\bar{u}u + \bar{d}d - 2\bar{s}s)$ and $\eta' = 1/\sqrt{3}(\bar{u}u + \bar{d}d + \bar{s}s)$. They are spin one particles and carry negative parity. In order to properly treat the combination including strange quarks we need to consider the effects of $\eta - \eta'$ mixing. It is easiest to start with *ideally mixed* states, these separate the flavor content between light and strange quark such that we divide between mesons with light ($n = \{u, d\}$) quark content only, $\pi^0 \sim (u\bar{u} - d\bar{d})/\sqrt{2}$ and $\eta_n \sim (u\bar{u} + d\bar{d})/\sqrt{2}$ respectively, and the strange $\eta_s \sim (s\bar{s})$ mesons. The same notation will be used for the according TFFs, with $F_{\pi\gamma\gamma}$, $F_{n\gamma\gamma}$ and $F_{s\gamma\gamma}$ and their decay constants denoted respectively by f_π, f_n and f_s. All TFF's in the DSE approach are calculated exactly like the pion TFF, by evaluation the triangle diagram, Fig. 19 (a.) and respectively Eq. (4.42). By changing the quark content of the decaying mesons, the mass of the loop particle changes accordingly and the flavor trace evaluates to a different factor. To account for this difference we define

$$\{F_{\pi\gamma\gamma},\, F_{n\gamma\gamma},\, F_{s\gamma\gamma}\} = \frac{1}{4\pi^2 f_\pi}\,\{\mathcal{F}_\pi,\, \tilde{c}_n\,\mathcal{F}_n,\, \tilde{c}_s\,\mathcal{F}_s\} \tag{5.57}$$

where $\tilde{c}_n = c_n\, f_\pi/f_n$, $\tilde{c}_s = c_s\, f_\pi/f_s$ and

$$c_n = \frac{q_u^2 + q_d^2}{q_u^2 - q_d^2} = \frac{5}{3}\,, \quad c_s = \frac{\sqrt{2}\,q_s^2}{q_u^2 - q_d^2} = \frac{\sqrt{2}}{3}\,, \tag{5.58}$$

so that the computation for the dimensionless $\mathcal{F}_{\pi,n,s}(Q^2, Q'^2)$ only differ by the quark-mass used for the loop particle. Since the quark content is the same for the light mesons, calculation wise one treats $\mathcal{F}_\pi(Q^2, Q'^2) = \mathcal{F}_n(Q^2, Q'^2)$.

For the calculation, we employed the same truncation and parameters, as in the case of the pion. Namely the Maris-Tandy model for the effective coupling $\alpha(k^2)$, Eq. (4.34), with parameters $\Lambda = 0.74$ GeV and $\eta = 1.85 \pm 0.2$. Recall that the scale parameter Λ is fixed by matching the experimental value for the mass and decay constant for the neutral pion. The η-parameter correspond to the shape of the interaction and, when varied in a small range, leaves the results for the pion mass unchanged. This is once more used as a rough estimate for the effects of the truncation. The mass of the strange quark is fixed at $m_s = 85$ MeV for the same renormalization point ($\mu = 19$ GeV) and we obtain a kaon mass of $m_K = 495.0(5)$ MeV. To summarize, by changing the current quark mass in the diagram to a strange quark, we can calculate results for $\mathcal{F}_{s\gamma\gamma}$. The anomaly demands that the on-shell form factor in the chiral limit is $\mathcal{F}(0,0) = 1$. For the light form factor, we previously obtained $\mathcal{F}_{\pi,n}(0,0) = 0.996$, correctly reproducing the anomaly. In the case of the strange TFF, we now obtain $\mathcal{F}_s(0,0) = 0.890$, which is slightly smaller as in the light quark case. The form factor was calculated in the directly accessible kinematic domain (see Fig. 21) and fitted. It turns out that the fit function used for the pion, Eq. (5.8), with adapted parameters, reproduced the $\mathcal{F}_s$ data correctly. The parameters for $\mathcal{F}_s$ can be seen in Tab. 9, where the result for the light TFF is restated for convenience. A comparison plot between the light and the strange pseudo-scalar TFF is given in Fig. 34.

The rainbow-ladder truncation does not produce the correct mixing behavior between $\eta - \eta'$, as the $U(1)$-anomaly term, that is responsible for the effect, is non-existing when working in this truncation. The AXWTI, as introduced in Eq. (2.64), only hold for flavor non-singlet vertices, whereas the η are exactly the singlets of the meson nonet. The full AXWTI with flavor indices is given in the Appendix, Eq. (B.17), and contains the term from the QCD anomaly. On the other hand, as the rainbow-ladder truncation performs very well in the light meson sector and fulfills the VWTI and the simplified AXWTI, thus guaranteeing charge conservation, we decided to stick to the truncation scheme and follow along the lines

$F_n(Q^2, Q'^2)$:

m_v	a_0	a_1	a_2	a_3	b_1	b_2	b_3
0.77 GeV	0.996	0.735	1.214	1.547	0.089	0.133	0.0002

c_1	c_2	d_1	d_2	e_1	e_2
0.384	0.430	2.010	0.024	1.540	0.00005

$F_s(Q^2, Q'^2)$:

m_v	a_0	a_1	a_2	a_3	b_1	b_2	b_3
1.02 GeV	0.890	1.016	1.181	1.493	1.140	0.043	0.00002

c_1	c_2	d_1	d_2	e_1	e_2
0.418	0.489	2.220	0.101	1.540	0.00005

Table 9: Parameters for the fit function Eq. (5.9) for the light transition form factor ($F_n(Q^2, Q'^2) = F_\pi(Q^2, Q'^2)$) re-quoted here for convenience from Tab.4) and the new result for the strange-quark TFF ($F_s(Q^2, Q'^2)$). The plotted form factors can be seen in Fig. 34.

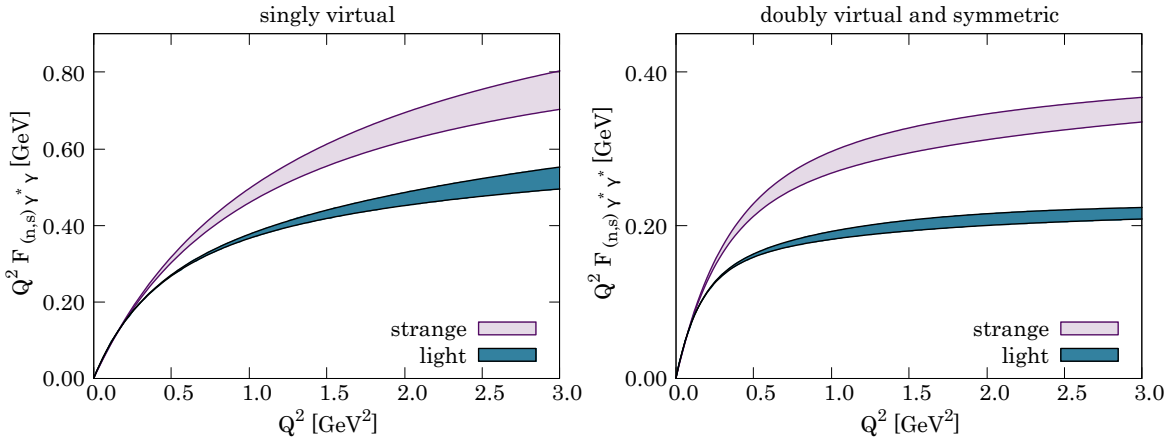

Figure 34: Transition form factor of ideally mixed pseudo-scalar meson states. *Left* in the singly virtual limit. *Right* for doubly virtual photon moment in the symmetric limit. The error-band in both cases stems from the error associated with the ξ parameter in the fit functions, Eq. (5.9) and parameters in Tab. 9.

of Ref. [163–166] to incorporate the mixing effects. This also ensures consistency between the calculation for the pion and the η-η' TFF.

The authors of Refs. [163–166] suggest a two-angle mixing scheme in the quark flavor basis in order to related the ideally mixed states (π^0, η_n, η_s) to the physical ones (η, η'). This can be done by multiplying with a mixing matrix $U(\phi)$ and reads,

$$\begin{pmatrix} \eta \\ \eta' \end{pmatrix} = U(\phi) \begin{pmatrix} \eta_n \\ \eta_s \end{pmatrix}, \quad \text{with} \quad U(\phi) = \begin{pmatrix} \cos\phi & -\sin\phi \\ \sin\phi & \cos\phi \end{pmatrix} \tag{5.59}$$

and where ϕ is the mixing angle. Following this scheme, the corresponding decay constants (to the different flavor bound-sates) can be written in a matrix notation and follow this pattern,

$$\begin{pmatrix} f_\eta^n & f_\eta^s \\ f_{\eta'}^n & f_{\eta'}^s \end{pmatrix} = U(\phi) \begin{pmatrix} f_n & 0 \\ 0 & f_s \end{pmatrix}. \tag{5.60}$$

In terms of flavour singlet and octet contributions to the decay constants of the physical

mesons the mixing pattern results in

$$\begin{pmatrix} f_\eta^8 & f_\eta^1 \\ f_{\eta'}^8 & f_{\eta'}^1 \end{pmatrix} = \begin{pmatrix} \cos\theta_8 & -\sin\theta_1 \\ \sin\theta_8 & \cos\theta_1 \end{pmatrix} \begin{pmatrix} f_8 & 0 \\ 0 & f_1 \end{pmatrix} \tag{5.61}$$

with two different angles θ_1 and θ_8. The different quantities are related to each other via [164]

$$\begin{aligned} f_8 &= \sqrt{(f_n^2 + 2f_s^2)/3}\,, \quad \theta_8 = \phi - \arctan\frac{\sqrt{2}f_s}{f_n}\,, \\ f_1 &= \sqrt{(2f_n^2 + f_s^2)/3}\,, \quad \theta_1 = \phi - \arctan\frac{\sqrt{2}f_n}{f_s}\,. \end{aligned} \tag{5.62}$$

The explicit values for f_n, f_s and the angle ϕ have been determined in a number of works, see e.g. Ref. [167] for an overview. For our calculations below we will use [165],

$$\frac{f_n}{f_\pi} = 1.07(2)\,, \quad \frac{f_s}{f_\pi} = 1.34(6)\,, \quad \phi = 39.3^\circ(1.0^\circ)\,. \tag{5.63}$$

Using the chiral anomaly predictions with $\mathcal{F}_n(0,0) = \mathcal{F}_s(0,0) = 1$ and assuming that the mixing in Eq. (5.59) is momentum independent one can find relations for the mixing of the TFFs in the chiral limit (see e.g. [168]). These are then generalized to physical quark masses and lead to

$$\begin{pmatrix} F_{\eta\gamma\gamma}(Q^2, Q'^2) \\ F_{\eta'\gamma\gamma}(Q^2, Q'^2) \end{pmatrix} = U(\phi) \begin{pmatrix} F_{n\gamma\gamma}(Q^2, Q'^2) \\ F_{s\gamma\gamma}(Q^2, Q'^2) \end{pmatrix}\,, \tag{5.64}$$

which we will use below to determine our results for the physical $\mathcal{F}_{\eta,\eta'}$.

In Ref. [169] a simplified mixing scheme ($\mathcal{F}_\pi = \mathcal{F}_n = \mathcal{F}_s$) was used to determine the η and η' TFFs. In this case, everything is described by the pion transition form factor, and no strange quarks are involved. In Ref. [77], we compared the TFFs using the mixing as suggested above, Eq. (5.64) and this simplified version to assess the relevance of the different dynamics of the strange quark, see therein for a discussion of the results.

To recap, for the final results of the η-η' transition form factor we thus follow Eq . (5.64), using the fit functions for the light and strange pseudo-scalar TFF (corresponding parameters in Tab. 9 and shown in Fig. 34) and multiplied with the mixing matrix, Eq. (5.59), and flavor factors, Eq. (5.4). In a last step we need to perform error propagation to provide the results plotted in Fig. 35 and Fig. 36 with the seen error-band.

Error propagation. As the result for the strange TFF ($\mathcal{F}_s$ in Tab. 9) was fitted with the same function, Eq. (5.9), it also contains the parameter ξ. This parameter reflects the combined theoretical uncertainty, including the error associated with the Maris-Tandy model and the error from the calculation of values in kinematically inaccessible regions (based on the extrapolation for larger Q^2). The choice $\xi = 1.0 \pm 0.1$ still holds in case of the strange TFF, as the value was a rather conservative estimate and the changes due to the strange mass are minimal, see Fig. 34 for comparison. Other numerical errors, such as the ones associated with the evaluation of the individual ingredients (meson amplitude, quark propagator and quark-photon vertex), are negligible compared to ξ. However we have to take into account the errors due to the approximate mixing scheme. These are represented by the uncertainties in the determination of the decay constants and mixing angle used therein, Eq. (5.63). We perform a proper error propagation and combine the uncertainties in quadrature, such that the error is given by,

$$\Delta\, F_{\eta(')\gamma\gamma}\left[\phi, (f_s/f_\pi), (f_n/f_\pi), \xi_n, \xi_s\right] = \sqrt{\left(\frac{\partial F_{\eta(')\gamma\gamma}}{\partial\phi}\,\Delta\phi\right)^2 + \left(\frac{\partial F_{\eta(')\gamma\gamma}}{\partial(f_s/f_\pi)}\,\Delta(f_s/f_\pi)\right)^2 + \ldots} \tag{5.65}$$

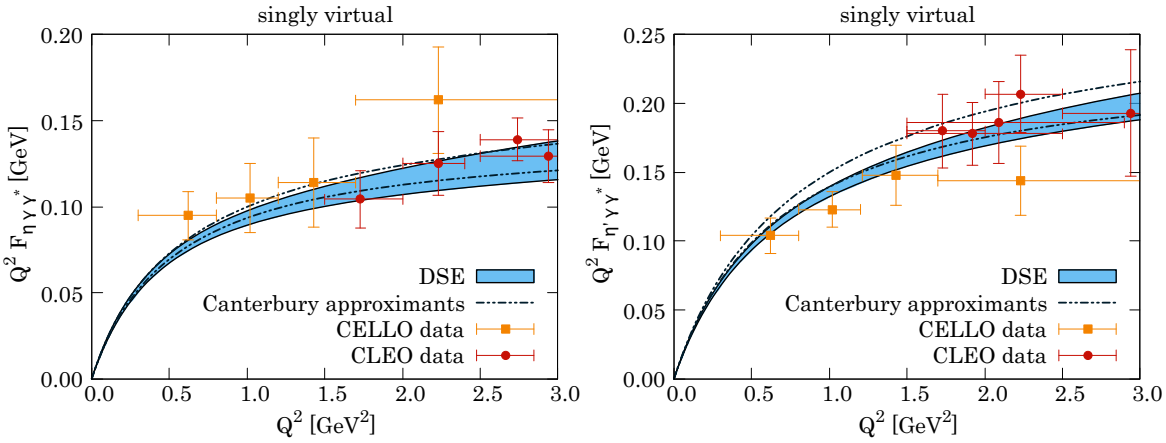

Figure 35: The transition form factors $F_{\eta\gamma\gamma}$ and $F_{\eta'\gamma\gamma}$ in the singly-virtual limit ($Q'^2 = 0$) (DSE [77]) compared to experimental results from CELLO [123] and CLEO [124] (results from different reactions averaged and error added in quadrature) and the results from a data based analysis using Canterbury approximants [85].

and added/subtracted from the central value to form the error-band. The form factor thus takes into account the dependencies on all the mixing parameters and the theoretical error in the fit ξ. Here we differentiate between ξ_n and ξ_s, as even though their absolute value is by coincident the same, the error itself corresponds to individual fit results, and each error has to be taken into account. The errors are: $\Delta\phi = 1.0°, \Delta(f_s/f_\pi) = 0.06, \Delta(f_n/f_\pi) = 0.02$ and $\Delta\xi_{n,s} = 0.1$. The main challenge for the DSE approach remains, however, a systematic error estimate. The error associated with the fit $\Delta\xi$ is only a rough guess and is not a measure for the total truncation error, but rather quantifies the model dependence. To do a more proper truncation estimate, one would have to include higher-order Green functions and evaluate the difference, meaning going beyond rainbow-ladder.

Our final results for the η and η' TFFs in the singly virtual case are shown in Fig. 35. We compare results with the experimental data from the CELLO [123], CLEO [124] and Babar [170] collaborations, and to the data-based analysis using Canterbury approximants [85].

Results in other approaches and comparison. The η and η' transition form factor has been calculated in other non-perturbative approaches as well as measured in several experiments, which allows for comparison and interpretation of our results. The authors of Refs. [133, 171] also work in the DSE framework, and their recent results followed along the lines of their previous publication on the pion TFF (Ref. [132]). Here we will briefly summarize the method therein and differences again to interpret the different results. In comparison to our study, Ref. [133] applies a modified truncation for the BSE kernel. The meson BSE is solved in the usual matter, but the authors refrain from solving the inhomogeneous BSE for the vertex. Instead, they work on the level of the unamputated vertex and approximate this quantity with Ansätze that are expressed in terms of the quark dressing functions (similar as in the case of the Ball-Chiu vertex). To obtain the correct anomaly value, additional parameters in these models are fixed accordingly. In order to ensure the correct mixing for the η and η' meson, they added an additional term to the interaction kernel in the BSE for the meson (references as "anomaly term" therein). In this way, the mixing of the η-states is naturally generated when solving the BSE. However, it introduces more parameters, which are then fixed by obtaining the correct masses and decay constants for η and η'. The additional term also breaks the AXWTI, Eq. (2.64), as the self-energy term in the quark DSE is not changed accordingly, which would generally mean that current conservation is not ensured. Such that in the end, incorporating the proper mixing scheme comes with some

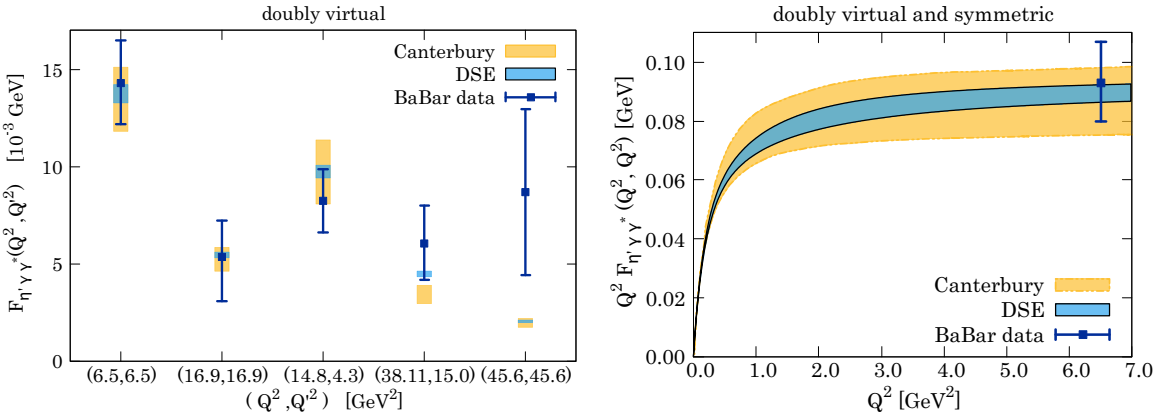

Figure 36: $F_{\eta'\gamma\gamma}$ for a set of point for doubly virtual photons. Compared to the experimental data from the BaBar Collaboration [170], which is plotted with a combination of statistical and systematic error, and the results from a data based analysis using Canterbury approximants [85].

subtleties which effects are hard to quantify. It conveniently provides us with the chance to directly compare the impact of these different truncation schemes within the DSE approach for physical observables and allows us to interpret the subtle differences, which is very useful for future studies in the DSE framework.

The Canterbury approximants avoid several complications that arise in other approaches (problems such as mixing or the heavier mass of the η_s), as they solely use different sets of experimental data, but apply the same form for fitting the data as in the case of the pion. This is a generalized Padé style fit function, Eq. (5.10). In case of the η/η' the approach is benefiting from the large set of available experimental data [123, 124, 170, 172–177], which is especially useful at lower energies where it allows to extract additional term in the fit expansion compared to the pion TFF. The Canterbury results pose as the currently most accurate theoretical prediction for the TFFs, as the data-driven nature provides an error estimate based on the performance of the fit and the error associated with the measured experiments. The currently largest error comes from the on-shell values of the TFF ($\mathcal{F}_{\eta-\eta'\gamma\gamma}(0,0)$). A reduction of the relative error related to this input parameter can substantially improve the total error of the fit. New experimental data concerning the η can be taken at the future *GlueX* experiment at JLab [178].

The singly-virtual domain was measured in the CLEO [124] and CELLO [123] experiment and is shown compared to our result and the Canterbury TFF in Fig. 35. For $F_{\eta\gamma\gamma^*}$, they are good agreement within another error-bar as well as with the experimental data from CLEO. In the case of the η', there are slight differences in the lower momentum region, however at lager momenta, the results seem to converge to the same asymptotic, and in the doubly virtual symmetric region it agrees within the error-bars, Fig. 36 rightmost. The first experimental measurement for doubly virtual photon momenta (momenta ranging from $2 < Q^2Q'^2 < 60\text{GeV}^2$) was performed by the Babar collaboration Ref. [170] and in Fig. 36 on the left, we compare our DSE results to the Canterbury calculation and experimental data for the $F_{\eta'\gamma\gamma}$ in the available sets of (Q^2, Q'^2) of the Babar measurement. The theoretical prediction and the Babar data agree fairly well besides for the data points at large values. In Ref. [170], the authors compared their results to model results from the VMD [179] (vector-meson dominance) model and a perturbative QCD [180] calculation and found that the data contradicts the VMD predictions and favor the pQCD.

The result for the η/η' transition form factor will be furthermore used to calculate the pseudo-scalar pole contribution to a_μ^{HLbL} in Sec. 5.6.1.

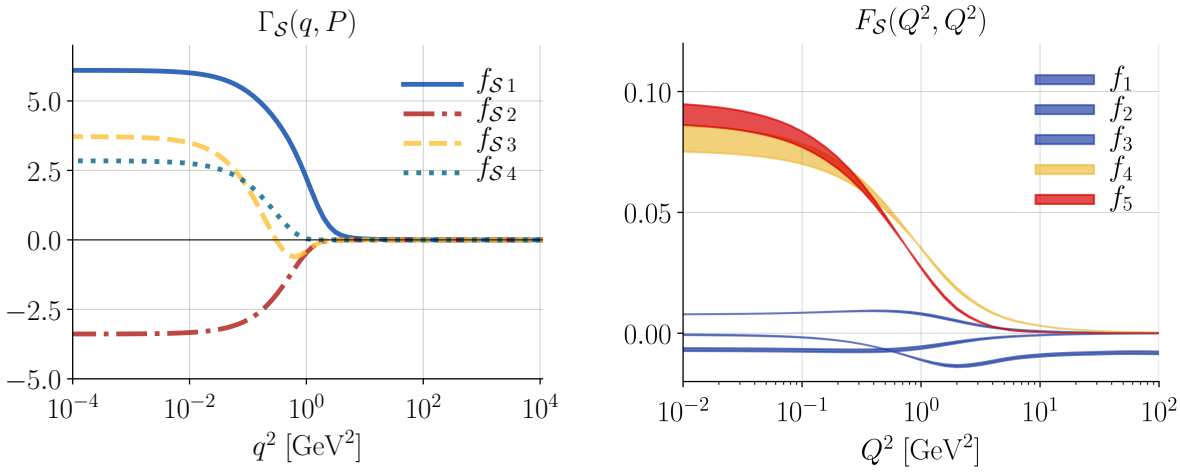

Figure 37: *Left*, dressing functions of the scalar Bethe-Salpeter amplitude $\Gamma_{\mathcal{S}}(q,P)$, with a bound-state mass of $m_{\mathcal{S}} = 675$ MeV. *Right*, preliminary results for the scalar TFF with the **Ball-Chui** vertex for the quark-photon vertex. The "gauge"-part of the dressing functions are plotted in blue, the yellow and red bands are the transverse scalar TFFs. The error-band is once more from the variation of the $\eta \in \{1.85, 2.06\}$

5.5 Scalar transition form factor

The matrix element for the scalar transition form factor, $\Lambda^{\mu\nu}_{\mathcal{S}}(Q,Q')$, can be decomposed as the product of tensor structures times scalar form factor amplitudes $F_{\mathcal{S}\,i}$ and is given by

$$\Lambda^{\mu\nu}_{\mathcal{S}}(Q,Q') = \sum_{i=0}^{5} \tau^{\mu\nu}_{\mathcal{S}\,i}(Q,Q')\, F_{\mathcal{S}\,i}(Q^2, Q'^2)\,, \tag{5.66}$$

where Q and Q' are the outgoing and incoming photon momenta and $\tau^{\mu\nu}_{\mathcal{S}\,i}$ the basis elements carrying two Lorentz indices. In the case of scalar quantum numbers ($J^{\mathsf{PC}} = 0^{++}$), the scalar-photon-photon vertex can be described by five possible tensor structures. Three of those can be associated with a "gauge" part and the remaining two are purely transverse. The gauge ones should have a value close to zero due to gauge-invariance. This poses as a good cross-check for the full determination of the TFFs.

To construct the basis for the scalar-photon-photon-vertex we proceed along the lines of Ref. [181] (see Eq. (13) therein) and obtain the following five basis elements,

$$\begin{aligned} \tau^{\mu\nu}_{\mathcal{S}\,1} &= \delta^{\mu\nu}\,, & \tau^{\mu\nu}_{\mathcal{S}\,2} &= Q^\mu Q'^\nu\,, & \tau^{\mu\nu}_{\mathcal{S}\,3} &= \left(Q^\mu Q^\nu + Q'^\mu Q'^\nu\right)\,, \\ \tau^{\mu\nu}_{\mathcal{S}\,4} &= t^{\mu\nu}_{QQ'}\,, & \tau^{\mu\nu}_{\mathcal{S}\,5} &= t^{\mu\alpha}_{QQ} t^{\alpha\nu}_{Q'Q'}\,, \end{aligned} \tag{5.67}$$

With the dimensionful transverse projector $t^{\mu\nu}_{ab} = (a\cdot b)\delta^{\mu\nu} - b^\mu a^\nu$. More details on how to construct a general basis for a current-vertex and the particular basis for the scalar-two-photon current can be found in [181] Sec. II. Recall the form factor integral as given by the triangle Feynman graph reads

$$\Lambda^{\mu\nu}_{\mathcal{S}}(Q,Q') = 2e^2\,\mathrm{Tr}\int\frac{d^4k}{(2\pi)^4}\, S(k_+)\,\mathbf{\Gamma}_{\mathcal{S}}(k,\Delta)\,S(k_-)\,\Gamma^\mu(r_-,-Q)\,S(k+\Sigma)\,\Gamma^\nu(r_+,Q')\,, \tag{5.68}$$

here with the scalar Bethe-Salpeter amplitude $\mathbf{\Gamma}_{\mathcal{S}}(k,\Delta)$ and the usual quark propagators $S(k_\pm)$ and quark-photon-vertices Γ^μ.

Scalar Bethe-Salpeter amplitude. A scalar meson carries quantum numbers $J^{\mathsf{PC}} = 0^{++}$ and the corresponding basis reads

$$\tau^i_{\mathcal{S}}(p,P) = \{\mathbb{1},\, i\not{P}\,(p\cdot P),\, i\not{p},\, [\not{p},\not{P}]\}\,, \quad \Rightarrow \quad \mathbf{\Gamma}^{AB\,ab}_{\mathcal{S}} = \sum_{i=0}^{4} f_i\, \tau^i_{\mathcal{S}}(p,P) \otimes \mathcal{C}^{AB}_{\mathcal{S}} \otimes \mathcal{F}^{ab}_{\mathcal{S}}\,. \tag{5.69}$$

In contrast to the pseudscalar meson, due the change in partiy $\mathsf{P} = +1$ the factor of γ_5 is no longer needed. To obtain the same properties under charge conjugation, the scalar product $(p\cdot P)$ is then multiplied to the second component such that $\bar{\mathbf{\Gamma}}_{\mathcal{S}}(p,P) = \mathbf{\Gamma}_{\mathcal{S}}(-p,P)$ (following the definition of charge conjugation in Eq. (5.6)). The matrix in color space is simply $\mathcal{C}^{AB} = \delta^{AB}$ and the flavor structure is the same as for the neutral pion, $\mathcal{F}^{ab} = \sigma^{ab}_3$.

The left panel of Fig. 37 shows a representative result of a scalar Bethe-Salpeter amplitude in the RL truncation. The effective interaction of the model was specified in Eq. (4.33) and the parameters therein chosen with $\Lambda = 0.74$ GeV and $\eta = 1.85$. As mentioned previously, the parameters are chosen to reproduce the physical pion mass and decay constant and the same set is used for all subsequent calculations, such as the scalar meson amplitude. Within the RL truncation we obtain a scalar meson mass of $m_{\mathcal{S}} = 675(3)$ MeV. In the calculation of scalar TFFs we will use the scalar dressing functions, as displayed in Fig. 37 left panel, but different masses (corresponding to various scalar states) for the total momentum in the triangle diagram ($\Delta^2 = -m_{\mathcal{S}\,\text{physical}}$). In this sense, the "off-shell" dependence of the scalar meson amplitude is only carried by the tensor part.

Scalar mesons decay electromagnetically into photons and leptons but also into lighter mesons (such as pions) through the strong force. Thus they are QCD resonances and carry a non-vanishing decay-width in comparison to the pions or kaons, which are true QCD bound-states. The functional form of the rainbow-ladder truncations does not allow for any intermediate decay channels, as this is not a part of the interaction kernel in a bound-state calculation. Thus it omits the proper treatment of these resonances but instead considers all BSAs as a QCD bound-states. The lightest scalar meson, the $\sigma/f_0(500)$, is a particularly broad resonance state. In fact, it is under debate if the underlying structure of the σ is really of quark-antiquark nature or if it could possibly be a four-quark-state (tetra-quark). This consideration are based on the unexpectedly large mass of the σ in comparison to the other scalar resonances in the nonet. This led to multiple investigations of this potential behavior in various non-pertubative approaches, see Refs. [182–184]. Recent studies of tetra-quark in DSE approach can be found in Refs. [8, 185, 186].

Bearing this in mind, we consider focusing on heavier scalar states, which could be considered as QCD bound-states in a narrow-width approximation. This, of course, comes with it's own set of problems, as large bound-state masses limit the kinematically accessible region, recall Fig. 21.

Kinematic domains. In Sec. 4.5 we explored the fact that the TFFs in our DSE calculation are objected to kinematic restriction due to the poles of the quark propagators. Due to the larger masses of the scalar mesons in comparison to the pion, the accessible range is reduced. The on-shell condition demands $\Delta = (0,0,0,-im_{\mathcal{S}})$, thus the mass of the decaying meson ultimately determines the complex momenta range evaluated in the triangle diagram. The kinematically accessible region for different values of the frame parameter α and different masses, with momentum choice as introduced in Eq. (4.45), is shown in Fig. 21. The overview revealed that for heavier masses the accessible domain continuously shrinks. The second row in this figure was chosen as a representative value for the scalar TFF with the DSE scalar meson mass of $m_{\mathcal{S}} = 675$MeV. For a meson mass > 1GeV the quark singularities completely omits a determination of the TFF. For slightly lighter scalar meson, where at least small region are accessible, we can consider a calculation using the technique applied in case of the pion TFF at large Q^2 values, see Sec. 5.1. In this case, we used an extrapolation with

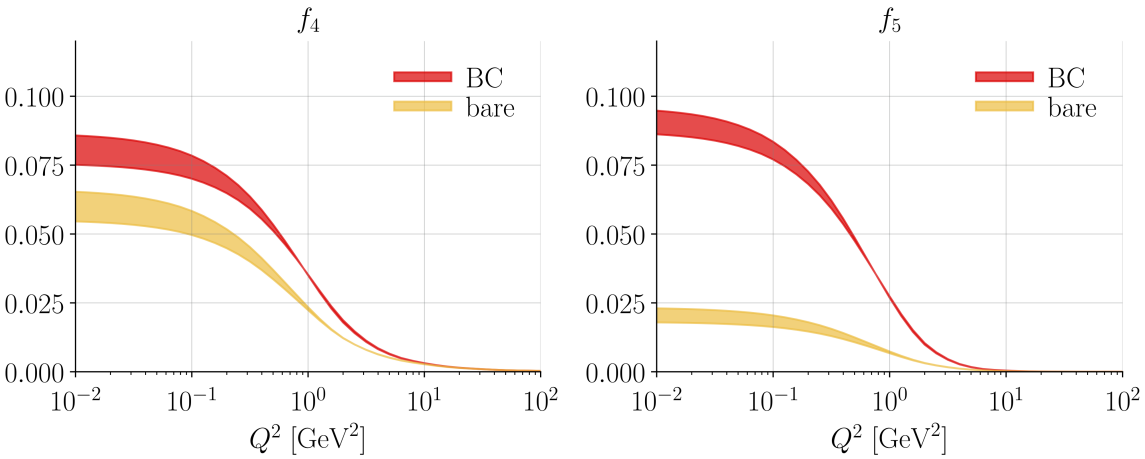

Figure 38: Scalar transition form factor dressing functions f_i in the symmetric limit ($Q^2 = Q'^2$): f_4 in the left and f_5 in the right panel. The two bands are obtained from using a bare quark-photon vertex or a Ball-Chiu vertex in the full Q^2 domain. The error-band corresponds to the variation of $\eta \in \{1.85, 2.06\}$

additional physical constraints. The DSE approach is more suited for lighter scalar states, and it seems feasible to calculate scalar TFF amplitudes ranging from the broad $\sigma/f_0(500)$ up till the $f_0(980)$ or the $a_0(980)$.

Besides the constraints from the quark poles, we face the additional difficulty that in the case of the scalar TFF the basis given in Eq. (5.67) degenerates in the symmetric limit. When $Q^2 = Q'^2$, the TFF depends on less independent variables, and the constructed basis, Eq. (5.67), breaks down. To obtain the value in the symmetric limit, we simply calculated values close to the limit and apply an interpolation. Another possibility would be to construct a reduced basis for this particular limit. At current status, further investigations are needed to explore the options and the numeric limitations.

Preliminary results and vertex dependence. The right panel in Fig. 37 shows results for all scalar TFF dressing functions f_i using the Ball-Chiu part for the quark-photon vertex, Eq (4.28) and in the symmetric limit ($Q^2 = Q'^2$). The first three amplitude are the gauge-part of the transition amplitude and gauge-invariance requires them to vanishes, and indeed we can observe that they are noticeably smaller then the transverse dressing functions: f_4, f_5. In Sec. 5.1 Fig. 23 right, we have shown, that only the full quark-photon vertex was able to produce the anomaly value and includes important physical effects, due the vector-meson poles, that propagate into the behavior of the TFFs. Consequently we expect a calculation with the full vertex to show a significant difference to the BC result, such that the first three unphysical amplitudes will complete converge to a value around zero.

Fig. 38 shows a close-up on the two transverse dressing function f_4, f_5, either calculated with a bare quark-photon vertex or using the Ball-Chiu part. The calculations with the full vertex are yet to be performed. Equally as in the case of the pion TFF, Fig. 23 on the right, we observe that applying the BC vertex rather than bare version enhances the value of the TFF amplitudes. Especially in case of the leading amplitude, f_5, we find a significant change.

Summary and Outlook. We have started the determination of the scalar transition form factor by performing a calculation employing a bare vertex or the Ball-Chiu part for the quark-photon vertex. These results already show general behavior of the form factors amplitude. In particular, we clearly observe the constraints by gauge-invariance, as the first three amplitudes are significantly smaller than the leading transverse amplitudes (f_4, f_5). As seen in the case of the pion TFF, we expect the full tensor structure of the quark-photon

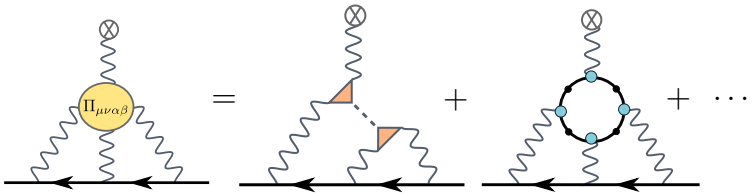

Figure 39: a_μ^{HLbL} involving the photon-four-point function $\Pi_{\mu\nu\alpha\beta}(q_1, q_2, q_3, Q)$. The right-hand side shows the leading contributions contributions: The *First* diagram is the meson-exchange part. *Second*, the quark-loop contribution further diagrams are negligible.

to be crucial for a complete description of electromagnetic transition form factors. Such that future studies are awaiting. When the final results with the full vertex are determined, the scalar TFF can be applied to give guidance on the importance of higher-meson-channel contributions to the Hadronic-Light-by-Light part in the muon $g-2$. An outlook on this topic will be given in Sec. 5.6.2.

5.6 Hadronic Light-by-Light contribution to a_μ

As introduced in Sec. 3.2, for the hadronic contribution to the muon's anomalous magnetic moment a_μ, one considers two main contributions: The leading hadronic-vacuum polarization (HVP) and the sub-leading hadronic-Light-by-Light (HLbL) part. In the following section, we will present our results for the HLbL contribution, as yet another application for transition form factors and compare to results from other non-perturbative approaches.

Contributions to HLbL from a dispersive view-point. The main part of the HLbL contribution, is the photon four-point function $\Pi_{\mu\nu\alpha\beta}$, as displayed in Fig. 39. This is defined as the Green function between four-vector currents (as defined in Eq. (2.53)), restated here for convenience,

$$\Pi^{\mu\nu\alpha\beta}(q_1, q_2, q_3, Q) = -i \int d^4x\, d^4y\, d^4z\, d^4w\, e^{i(q_1\cdot x + q_2\cdot y + q_3\cdot z + Q\cdot w)} \langle 0|\mathsf{T}\, j^\mu(x) j^\nu(y) j^\alpha(z) j^\beta(Q)\,|0\rangle\,. \tag{5.70}$$

As explained previously in Sec. 3.2, the photon four-point function can be expressed in terms of tensor elements times scalar dressing functions, where the particular form of the latter allows for the usage of dispersion relations [72–74,187]. This unitary relation offers an unique expansion of the photon four-point function in terms of diagrams involving one- or multiple-particle intermediate states. We identified a leading diagram in the HLbL part as the pion-pole contribution and the next sub-leading contribution as the pion-box term (which is part of the meson-loop topology), see Fig. 40. In this figure, the red lines indicate the on-shell nature of the intermediate particles, and we identified the vertices as form factor amplitudes (indicated by orange triangles), such that we require the knowledge of on-shell transition and electromagnetic meson form factors.

The pion-pole contribution is by far the leading part and thus has been considered in multiple determination of a_μ^{HLbL} over the past years. On the other hand, for the precision required to reduce the discrepancies in a_μ, the contributions of the remaining sub-leading channels become more and more relevant. Such channels are the pion- or kaon-box-diagram (left most diagram in the set of the meson-loop diagrams in Fig. 40), the scalar-pole contributions, or the η and the η'-pole contribution. The latter can be combined with the pion-pole to represent the pseudo-scalar-pole contributions.

The following sections contain results for the leading meson-pole contributions to a_μ^{HLbL}. Starting with the pion-pole and proceeding towards providing a complete pseudo-scalar contribution by incorporating the η and η' exchanges, as published in [77]. The section concludes

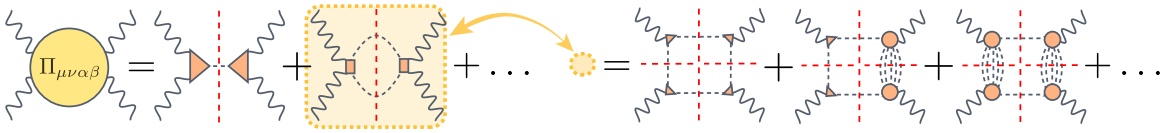

Figure 40: Dispersive expansion of a_μ^{HLbL}: *Left*, shows the decomposition of the photon four-point function $\Pi_{\mu\nu\alpha\beta}$ into pion(meson)-pole contribution and the two-pion cut. *Right*, shows the decomposition of the two-pion cut contribution, which can be furthermore split into the pion-box part and the two-pion rescattering diagrams. The double lines are suppose to denote heavy particle intermediate states (multi-pions states, heavier resonances).

with an outlook for new results in the scalar meson exchange channel, $a_\mu^{\mathcal{S}}$, in Sec. 5.6.2. For details on the pion-box contribution, I revise the reader to Ref. [77]. My collaborators have furthermore provided one of the first estimates for the sub-leading kaon-box, see Ref. [188] for details on this.

Expansion in fundamental degrees of freedom. Working directly in the space-like momentum domain that is characteristic for the LbL integral, the photon-four-point function could also be expanded in terms of quark and gluon degrees of freedom, see Fig. 41. This expansion and the subsequent resummation into hadronic degrees of freedom have been applied in previous DSE calculations and are discussed in detail in Ref. [63]. The expansion generally agrees with the standard treatments within effective models; see review Ref. [189] and references therein. The leading terms in this expansion are similar to the quark-loop and meson-exchange diagrams in the dispersive expansion (Fig. 40). However, different than in Fig. 40, where the intermediate mesons are on-shell propagators, the mesons appearing in this alternative expansion are of off-shell nature and represent a set of "resummed mesons", including higher-order channels (such as multi-particle exchanges). Considering the meson off-shell is a somewhat more complicated matter, as it requires a non-unique (but IR or UV-constrained) prescription for the off-shell meson propagators and likewise their transition form factors. This is principally achievable by treating the quark-Compton vertex, which appears in the expansion in Fig. 41 (light grey dot), along the lines of Refs. [13, 103]. In practice, however, this is currently not feasible due to unsolved problems with transversality and analyticity in the gauge dependent basis elements of the photon four-point function, see Ref. [181] for details.

DSE calculations for the HLbL contribution before 2017 used the expansion shown in Fig. 41. Due to the unresolved problems, the availability of new and improved form factor results, and the success of the dispersive expansion, we decided to change strategy. As the two calculations are based on completely different expansions, a comparison between the old and more recent results is meaningless, and the recent results do not supersede the old ones but represent a set of completely new and independent results. They will be compared to results applying the same dispersive expansion, such as the pure data-driven dispersive or Canterbury calculations.

Lattice calculation. By contrast, when calculating the HLbL contribution on the lattice, the four-point function, Eq. (5.70), does not need to be expanded into individual contributions. It can instead be directly calculated, implementing the full Green function. This brings the advantage of leaving no ambiguities of "higher-order" contributions that could possibly be missed. The approach simply and directly includes the full non-perturbative nature of the vector four-point function. The approach is numerically very challenging, and currently, only two lattice groups, the Mainz group and the RBC/UKQCD collaboration, have been working on formulating and carrying out the direct lattice calculation for a_μ^{HLbL}. This provides a

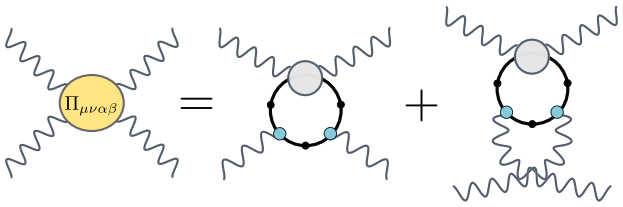

Figure 41: Alternative expansion for the photon-four-point function in terms of quark and gluon degrees of freedom, corresponding to an expansion in terms of the quark Compton vertex. This expansion was applied in [63, 64]. The fully dressed quark-loop is contained in the first diagram in this expansion.

first-principles evaluation, but results are not yet competitive in precision with the dispersive approach. Nonetheless, the lattice determinations today serve as an important consistency check and are expected to furthermore improve in the upcoming years.

5.6.1 Pseudo-scalar-pole contribution $a_\mu^{\mathbf{PS}}$

The meson-pole contribution (left most diagram in Fig. 40) are considered to be the leading terms in the dispersive expansion. For mesons with general parity and spin the HLbL part for the meson pole diagram is given by the permuted sum of two on-shell meson TFFs coupled with the corresponding meson propagator,

$$\Pi^{\mu\nu\alpha\beta}_{\text{meson-pole}}(q_1,q_2,q_3,Q) = \sum_M \mathcal{F}_M^{\mu\nu,\mathcal{I}}(q_1,q_2) D_M^{\mathcal{I}\mathcal{J}}(q_1+q_2) \mathcal{F}_M^{\alpha\beta,\mathcal{J}}(q_3,Q) + (\text{perms}). \tag{5.71}$$

Here, $\mathcal{F}_M^{\mu\nu,\mathcal{I}}(q_1,q_2)$ is the TFF for meson M and $D_M^{\mathcal{I}\mathcal{J}}(q_1+q_2)$ its free on-shell propagator, wich is given by

$$D_M^{\mathcal{I}\mathcal{J}}(Q) = \frac{1}{Q^2+m_M^2}\,, \tag{5.72}$$

where the superindices $\mathcal{I}$, $\mathcal{J}$ encode the total spin J of the intermediate state *viz.* $\mathcal{I} = \alpha_1 \dots \alpha_J$ and m_M denotes the mass. The sum in Eq. (5.71) runs over all possible meson exchanges M, where contribution by heavier mesons are suppressed as $D_M \propto m_M^{-2}$. As the class of pseudo-scalar ground-state mesons are the lightest in the spectrum, this is the leading contribution and it includes the exchange of the pion, the η, and the η' mesons. The permutation of diagrams corresponds to the s,t, and u-channel version for the propagator form factor combination above. In a next step we apply the projector in Eq. (3.18) on the full photon-four-point function to obtain the the Pauli-form factor $F_2(0)$ corresponding to a_μ. In a last step we then perform a Wick rotation of the expression and use the Gegenbauer technique to evaluate most of the angular integrals and reduce the total number of integral to three, one angular variable and two space-like momenta. The final expression for the meson-pole contribution is then given by,

$$a_\mu^{\text{HLbL; PS}} = \frac{-2\pi}{3}\left(\frac{\alpha}{\pi}\right)^3 \int_0^\infty dQ_1 dQ_2 \int_{-1}^{+1} dz \sqrt{1-z^2} Q_1^3 Q_2^3 \left[\frac{F_1 I_1(Q_1,Q_2,z)}{Q_2^2+m_M^2} + \frac{F_2 I_2(Q_1,Q_2,z)}{Q_3^2+m_M^2}\right]. \tag{5.73}$$

The expression contains the form factor amplitudes for the pseudo-scalar form factor defined in Eq. (5.1) through

$$F_1 = F_{\text{PS}}(Q_1^2,Q_3^2) F_{\text{PS}}(Q_2^2,0)\,, \quad F_2 = F_{\text{PS}}(Q_1^2,Q_2^2) F_{\text{PS}}(Q_3^2,0)\,, \tag{5.74}$$

where $Q_3 = (Q_1^2+Q_2^2+2Q_1Q_2z)$ and where the abbreviation for the numerator I_i is specified in appendix C.

Collaboration	$a_\mu^{\pi_0-\text{pole}}\,[10^{-11}]\,\text{GeV}$
Lattice (direct) [191]	72.0(39.8)(16.5)
Lattice + χPT: Gérardin et al. [25]	59.7 ± 3.6
Lattice + Exp: Gérardin et al. [25]	62.3 ± 2.3
Disperive: Hoferichter et al. [125]/ Update [47]	$62.6^{+3.0}_{-2.5}$ / $63.0^{+2.7}_{-2.1}$
Canterbury: Masjuan et al. [85]/ Update [47]	63.5(1.2)(2.3) / 63.6(2.7)
DSE: Raya et al. [133]	61.4 ± 2.1
DSE: **Our result** [77]	62.6(0.1)(1.3)

Table 10: Comparison of the **pion-pole** contribution to a_μ^{HLbL}. All quoted results using the dispersive expansion, Fig. 40, using their result for the pion TFF therein, besides the direct Lattice calculation [191], which directly evaluates the full photon four-point function.

Due to the integration in Eq. (5.73), the form factor is in principle needed in the full space-like domain, for both doubly-virtual and singly-virtual kinematics. However, when plotting the integrand, one discovers that it is peaked in the lower momentum region. Such that ultimately the contribution to a_μ is dominated by the form factor behavior at small $Q^2 \lesssim 1\text{GeV}^2$ (see Fig. 3 in Ref. [85] or Fig. 3 in Ref. [126] for a plot of the integrand).

To get an "exact" result for the meson-pole contribution to a_μ, one would have to include all possible meson exchange channels. Such that besides the leading pseudo-scalar, meson exchanges for scalar or axial-vector particles are taken into account too. However, as the contributions are suppressed with mass, the heavier channels become less and less important and irrelevant even in the light of high-level accuracy that g-2 requires. The contribution of an axial-vector exchange was calculated using quark models in Ref. [190].

Pion-pole contribution. As has been shown in [74], the special case of the pion pole contribution eventually reduces to a simple well-known formula that has been developed earlier [71] in the context of effective models. The pion-pole contribution can be attributed to the one-particle irreducible piece of the HLbL tensor, arising from a single pion propagator and is, as corresponding to the lightest particle, the leading contribution of all meson pole channels. For this reason, it is the most calculated contribution, and we can compare our results to many other non-perturbative calculations. We numerically solve the remaining three integrals in Eq. (5.73) and insert the fit for the pion TFF, presented in Eq. (5.8) with parameters of Tab. 4. This lead to the following result for the pion-pole contribution,

$$a_\mu^{\text{HLbL; }\pi^0\text{-pole}} = 62.6(0.1)(1.3) \times 10^{-11}. \tag{5.75}$$

The first error reflects the variation of the effective interaction parameter η, in Eq.(4.34), and translates into changing the associated parameter ($\xi = 1.0 \pm 0.1$) in the fit function. In the small momenta region, most relevant for a_μ, the impact on our form factor results are small, such that it has almost no effect on our final result. The second error lies around 2% and represents the numerical error accumulated by the calculation of each ingredient to the form factor (quark propagator, meson amplitude, and quark-photon vertex) and the form factor calculation itself. The numerical error associated with the final integral for a_μ, Eq. (5.73) is well under control and negligible.

Pion-pole in other non-perturbative frameworks and comparison. As the transition form factor is the only non-perturbative input required when using the dispersive expansion, any theoretical approach that is able to access this quantity (in the required kinematic

domain) can provide a result and comparison for the meson-pole contributions. In Sec. 5.1 Fig. 24, we compared our results for the transition form factor with other non-perturbative calculations and found that these agree with another within their error-bands.

The comparison in Tab. 10 quotes results from two data-driven approaches and the first-principle calculation obtained from Lattice QCD for the pion-pole contribution to a_μ^{HLbL}. The data-driven dispersive approach uses a set of dispersion relation to access the form factor; the Canterbury approach uses a fit based on rational polynomials. A comparison of the individual form factor has been discussed in Sec. 5.1.

In Lattice QCD, one can in principle calculate the full photon-four-point function and does not need to expand in individual components. However, given the current difficulties to evaluate the full four-point function and respectively the large error associated with recent results, the authors in Ref. [25] have also pursued a calculation in the dispersive context, Fig. 40, using their results of the pion transition form factor to calculate the pion-pole contribution. In this way, it is combining efforts from lattice and the dispersive approach to give a model and data-independent comparison for the pion-pole contribution. To use the transition form factor result for further calculation, e.g. as part of the muon's HLbL contribution, the lattice faces the issue that additional input is needed to fix the normalization of the TFF amplitude correctly. In the DSE approach, the correct normalization is ensured due to the canonical quantization condition, Eg. (4.12), which is applied to the meson amplitude used as an ingredient to the TFF calculation. Once the norm is fixed at the level of the meson, it ensures the correct charge for hadrons and consequently, the proper normalization for the form factor. The lattice calculation needs to use additional inputs to fix its scale. This can be done by either using experimental data or theoretical input from effective field theories. With data from the PrimEx measurement for $\pi^0 \to \gamma\gamma$ this lead to a lattice and data-driven value for the pion pole contribution of $a_\mu^{\text{HLbL; Lattice+Exp}} = (6.23 \pm 2.3) \times 10^{-11}$. The norm can also be fixed through chiral perturbation theory, as it depends on a low-energy constant that appears in the chiral Lagrangian for next-to-leading order calculation of the decay. This lead to the Lattice + χPT result of $a_\mu^{\text{HLbL; Lattice}} = (59.7 \pm 3.6) \times 10^{-11}$, which corresponds to a precision of 6%.

Since the TFFs are already in rather good agreement, it is no surprise that the values for the pion pole contribution are as well. More results of other non-perturbative methods and collaborations can be found in Refs. [34, 47] and references therein.

η and η'-pole contribution. The contribution for the η and η' exchange are calculated using Eq. (5.73) and replacing F_{PS} with the corresponding form factor as defined in Eq. (5.64) and with the Fit parameters in Tab. 9. This evaluated to the following result,

$$a_\mu^{\eta-\text{pole}} = 15.8\,(0.2)(0.3)(1.1) \times 10^{-11}\,, \tag{5.76}$$

$$a_\mu^{\eta'-\text{pole}} = 13.3\,(0.4)(0.3)(0.6) \times 10^{-11}\,. \tag{5.77}$$

The error follows the same conventions as in case of the pion TFF and consist of an error associated with the model component in the truncation and as a 2% numerical error. The additional third error reflects the uncertainties due to the mixing parameters, Eq. (5.63), applying error propagation as explained in Eq. (5.65). In case of the η and η' TFFs we are facing additional difficulties to properly describe the mixing effects between η and η' meson in the DSE approach. As explain in the Sec. 5.4, we employed an approximate mixing using the definition of a mixing matrix between a form factor with pseudo-scalar quantum numbers but only light-quark content and a form factor consistenting of a strange quark-antiquark pair.

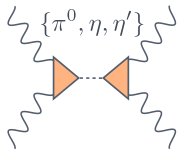

Collaboration	$a_\mu^{\text{PS-pole}}$ $[10^{-11}]$ GeV
Canterbury: Masjuan et al. [85]	94.3(5.3)
Dispersive π^0 + Canterbury $\eta^{(\prime)}$ [47]	$93.8^{+4.0}_{3.6}$
DSE: Raya et al. [133]	89.7 ± 4.8
DSE: **Our result** [77]	91.6(1.9)

Table 11: Comparison of the full **pseudo-scalar** pole contribution to a_μ^{HLbL}, including the exchanges for π^0, η and η' ($a_\mu^{\text{PS-pole}} = a_\mu^{\pi-\text{pole}} + a_\mu^{\eta/\eta'-\text{pole}}$).

The other DSE study for the η and η' transition form factor [133] has also applied the dispersive formula to evaluate the $(\eta - \eta')$-pole contributions, using their calculation for the form factors and they obtain a final result of $a_\mu^{\eta/\eta'-\text{pole}} = 14.7(1.9)/13.6(0.8) \times 10^{-11}$. This agrees with our result within the error-bars, but seems to show a slightly larger deviation in the result for η - exchange compared to ours.

In comparison to the integrand in the pion-pole contribution, the calculation for the ηs probes a larger momentum range, due to the larger mass of the mesons (for a plot of the integrand, see again Fig. 3 in [85] and equally [126]). In this sense, the details of the TFFs in higher Q^2 region are more relevant here and a deviation in the TFF has a bigger impact on the final results for a_μ^{HLbL}.

From the data-driven side, the contribution from the η-mesons has been calculated in the Canterbury approach [85]. The investigation in the pure dispersive approach is currently still facing some difficulties and relies heavily on data for the decays $\eta^{(\prime)} \to \pi^+\pi^-\gamma$, however, it is well on it's way and new results are expected soon (early 2020), as sketched in Refs. [130,192]. The Canterbury approximants avoid several complications that arise in other approaches (problems such as mixing or the heavier mass of the η_ss), as it solely uses different set of experimental data, but applies the same type of Padé fit function as in the case of the pion, Eq. (5.10). The result of the Canterbury (η/η')-TFFs are compared to our result in Fig. 35. These TFFs lead to the numbers from the Canterbury calculations of $a_\mu^{\eta-\text{pole}} = 16.3\,(1.0)(0.5)(0.9) \times 10^{-11} \to 16.3(1.4) \times 10^{-11}$ and $a_\mu^{\eta'-\text{pole}} = 14.5\,(0.7)(0.4)(1.7) \times 10^{-11} \to 14.5(1.9) \times 10^{-11}$, where the first error arises due to the fit of singly-virtual data, including normalization and slope. The second error reflects the uncertainties due to the fit of doubly-virtual data sets. In this regime, one of the fit parameters is fixed by the OPE limit, due to the lack of data. The third error reflects systematic uncertainties due to a truncation of the sequence in the fit functions. Once more, the results agree within the error-bars with our results. In the next paragraph, we will add the pion- and the η-pole contribution for the pseudo-scalar pole contribution.

Pseudo-scalar-pole contribution. Combining the results for π^0-pole and the η and η'-pole contribution we conclude in our total number for the pseudo-scalar channel,

$$a_\mu^{\text{PS-pole}} = 91.6\,(1.9) \times 10^{-11}\,, \tag{5.78}$$

where all errors are added in quadrature. An overview of the results for the pseudo-scalar pole-contribution is given in Tab. 11. Interestingly enough, the results achieved with different truncations in the DSE approach and from the purely data-driven Canterbury are consistent within another error bars, making a strong case for the size of this leading contribution. The g-2 white-paper [47] combines the results for the pion-pole from the dispersive calculation with the Canterbury result for the $\eta^{(\prime)}$-poles, providing the current estimate for a purely data-driven and systematic result. This number is situated within the error-bars of the other non-perturbative calculations, where the individual uncertainties of the dispersive pion form factor and Canterbury η and η' calculations have been combined linearly.

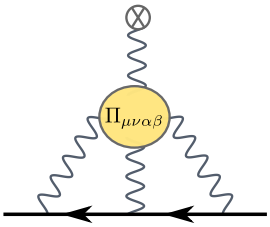

Contribution	$a_\mu^{\text{HLbL}}\ [10^{-11}]\,\text{GeV}$
pseudo-scalar poles	$93.8^{+4.0}_{3.6}$
π-Box	$-15.9(2)$
(SDC) Δa_μ	$\sim \pm(15)(10)$
$\pi\pi$	$-8(1)$
axial-vector poles	$\sim 6(5)$
scalar poles [193]	$\sim \left[(-5.35^{+3.27}_{-0.92}) - (-1.3^{+2.06}_{-0.91})\right]$
tensor pole [194]	$\sim 0.9(0.1)$
K-Box (VMD)	-0.5

Table 12: Contribution to a_μ^{HLbL} in the dispersive expansion, Fig. 39 or Fig. 40. The numbers quoted are results caculated in the disperive approach, or effective models for the higher channels, and are references from the current g-2 white paper. For details see Ref. [47] and references therein.

5.6.2 Outlook: Contribution of higher hadronic intermediate states

For the accuracy required to overrule the discrepancy in a_μ and with the updated results and improved precision from the experimental side, it has become more and more relevant to obtain results of high precision for both hadronic-contributions. The unitary relation used for separation into parts of the HLbL tensor generally involved the sum over all possible asymptotic states. However higher channels get topologically more difficult to calculate and contribute less, such that the main focus for a_μ^{HLbL} has been on the leading contribution, such as the pion pole contribution discussed in the previous section. The leading contributions are expected to come from lighter particles up to about 1.5GeV. Heavier particles $> \Lambda_{\text{QCD}}$ are expected to be suppressed, as indicated by effective field theory arguments. Following the dispersive expansion, Fig. 40, and considering channels from heavier particles we can divide a_μ^{HLbL} into the individual contributions, ordered by expected size,

$$a_\mu^{\text{HLbL}} = a_\mu^{\text{PS-pole}} + a_\mu^{\pi^0\text{-Box}} + a_\mu^{\pi\pi} + a_\mu^{\text{axial-vector-pole}} + a_\mu^{\text{scalar-pole}} + a_\mu^{\text{tensor-pole}} + a_\mu^{K\text{-Box}/KK} + \dots \tag{5.79}$$

Tab. 12 show an overview of the current estimates for these contributions. The numbers quoted are taken from the g-2 white paper [47] and summarize results from the dispersive approach as well as a combination of the dispersive expansion and a modeling component for the higher channels. The pseudo-scalar pole contribution is by far the leading one and has been calculated by multiple collaborations. Other meson exchange channels, in comparison, are harder to calculate and have not been as extensively studied, such that more work is needed in these channels to get reliable estimates of their contribution size.

On the other hand the estimated contributions in Tab. 12 show a clear demand for new insights considering the contribution from higher channels, such as the scalar-pole exchange, to a_μ^{HLbL}. In the DSE approach, the scalar transition form factor follows along the same lines as the pion TFF, as it is calculated using the same ingredients only exchanging the meson amplitude in the triangle diagram and the respective tensor basis, Eq. (5.67), as described in the previous Sec. 5.5.

Box topologies. The contribution from the pion-box topology was calculated by my collaborators in Ref. [77] and found to be of the size: $a_\mu^{\pi^0-\text{Box}} = -16.6(1)(7) \times 10^{-11}$. As in the DSE approach one is working in the isospin symmetric limit, in principle all pion (neutral and charged) carry the same mass of $m_{\pi^0} = 135.0(2)$MeV, which is what was used to obtain the first results for the box contribution. To gauge the effects of the iso-spin breaking we released an updated number in Ref. [188], which uses the experimental mass for the charged

pions $m_{\pi^\pm} = 139.57$MeV and changed the value to: $a_\mu^{\pi^\pm-\text{Box}} = -15.7(2)(3) \times 10^{-11}$. The kaon-box contribution was furthermore calculated and reported in Ref. [188], applying the same calculation as in the pion case, but using the electromagnetic form factor of the kaon instead. This lead to a value of, $a_\mu^{K-\text{Box}} = -0.65(3)(7) \times 10^{-11}$.

Quark-loop and short distance constraints. The dispersive expansion, summing over all intermediate one- or more-particle states (Fig. 40), can not reproduce all the QCD constraints unless we sum all contribution in the infinite series. As this is not feasible, additional constraints are needed to fix the short-distance behavior of the photon four-point function. The asymptotic behavior of form factors and other intermediate exchange channels is not expected to have a large contribution to the final values of a_μ^{HLbL}, however, it contains essential information for the error estimation. Thus short-distance constraints (SDC) are important and are used in different capacities throughout the determination of the HLbL tensor. The SDC come from different asymptotic limits of the photon four-point function, such as the case when all four-photon legs are highly virtual or the regime where on the of momenta is much smaller than the other two. In the case of the limit where all three virtualities are large, the main contribution is considered to be the quark-loop. In this sense, the quark-loop contribution $a_{\mu\,\text{SDC}}^{\text{quark-loop}}$ is not directly part of the dispersive expansion in terms of the unitarity relation (thus it is not added to the sum in Eq. (5.79)) but can be seen as a resummation of all these intermediate states. The perturbative quark-loop is the first term in an operator-product expansion (OPE), where soft photons are treated as background fields, see Ref. [195].

Opinions on the interpretation of this channel vary. In the recent white paper [47], the authors include the quark-loop into the short-distance-constraints (SDC) of a_μ^{HLbL}, as summarized above. In the context of previous studies in the DSE framework [65], the quark-loop directly appears in the expansion in terms of fundamental degrees of freedom, see Fig. 2 in Ref. [65]. In contrast to the perturbative treatment in the dispersive context, the quark-loop in the DSE expansion is fully dressed, incorporating non-perturbative effects to all orders. It should, however, reproduce the perturbative results in the asymptotic limits. As the dressed quark-loop contains diagrams that appear in different parts of the dispersive unitary relation, it is hard to gain any insights from a comparison between the methods. As already mentioned, the asymptotic behavior of the form factor and other exchange channels is not expected to give a large contribution HLbL tensor, however, they are important for estimating the errors. The number (SDC) quoted in Tab. 12, is understood as an error estimation $\Delta a_\mu^{\text{HLbL}}$ and it includes contributions from other SDC, not only the quark-loop.

Scalar-pole contribution. Strictly speaking, only true QCD bound-states can appear as single-particle poles in the dispersive expansion for a_μ^{HLbL}, Fig. 40. Pions and kaons are QCD bound-state, scalar mesons on the contrary, are resonances and decay into photons and light meson (eg. pions). The five lowest-lying resonances in the scalar channel (0^{++}) are the $\sigma/f_0(500)$, $a_0(980)$, $f_0(980)$, $f_0(1370)$, $a_0(1450)$ and $f_0(1500)$. A prober description of the resonances based on the unitary relation of the photon four-point function has not been derived due to the complicated topology for such a multi-particle intermediate state. In this sense, a different expansion, which could help to constrain these contributions, is needed to estimate their size. However, this expansion needs to work along the lines of the dispersion relations in order to avoid double counting. The partial-wave framework falls into this category, and the expansion into helicity partial waves can be generalized to include arbitrary intermediate states. On the other hand, the expansion suggests that, in particular, narrow resonances have a large contribution (in comparison to the other higher intermediate states). In these cases, we can apply a narrow-width approximation, and the spectral function of the partial wave becomes a δ-function, which reduces the dispersive integral to a simple

pole contribution, Eq. (5.71). This means that in this approximation, we use the same equation evaluated for the pion-pole contribution. Analogously the contributions of the scalar states are then expressed in terms of on-shell transition form factors and the scalar-meson propagators are treated as free propagators, as introduced in Eq. (5.72).

The narrow-resonance calculations can provide an estimate for the size of higher channel contributions and on their relevance for the full determination of a_μ^{HLbL}. The numbers quoted in Tab. 12 are narrow-resonance calculations, as this is currently the only estimate of these channels. A full dispersive treatment requires more work on the formalism (the expansion of the helicity partial wave needs to be extended to include odd ones, which would reflect multi-particle exchanges) as well as experimental data and has not yet been pursued. The current aim from the dispersive community lies in the reduction of the error associated with the leading contributions, as this has an overall larger effect on the precise determination of a_μ. However, this opens the possibility for model-dependent calculations to provide an estimate on the size of these contributions and whether they will be relevant if the discrepancy remains.

Applying the narrow-width approximation, the calculation of the scalar-pole contribution has been performed in Refs. [193, 194, 196–198]. All of the references use the dispersive expansion and differ by the choice of phenomenological motivated fit used to model the scalar transition form factor. In the DSE approach, this quantity is easily accessible, and the first results have been sketched in Sec. 5.5. To extend Eq. (5.71) for the scalar contribution, we need to include multiple form factor amplitudes, as the scalar TFF is decomposed into five tensor basis elements, Eq. (5.67). This splits into two transverse (f_4, f_5) and three longitudinal (f_1, f_2, f_3), where the latter ones can be omitted, due to the fact that in the region of small photon virtualities the transverse part dominates. This leads to more terms in the sum of the meson pole representation of $\Pi_{\mu\nu\alpha\beta}$, Eq (5.71). This can be divided into three contribution corresponding to the mixing of the two transverse TFF amplitudes, $a_\mu^{\mathcal{S}} = a_\mu^{\mathcal{S}\, f_4 f_4} + a_\mu^{\mathcal{S}\, f_4 f_5} + a_\mu^{\mathcal{S}\, f_5 f_5}$. The full expression for the individual part can be found in Eq. (3.9-3.11) of Ref. [193]. The scalar transition form factor in Sec. 5.5 was calculated for a scalar mass of $m_{\mathcal{S}} = 0.675\mathrm{GeV}$, which corresponds to the mass for the $f(500)/\sigma$ meson in the DSE approach. However, we can tune the mass of the decaying meson to calculate the contribution of other channels. In fact, the σ is a somewhat special case and should not be considered along the lines of the higher scalar channels.

Special case: $\sigma/f_0(500)$ Due to its broad width, the $f_0(500)$ can not be considered along with the other scalar contribution applying the narrow-width approximation. As its dominant decay channel is the decay into two pions, it is in fact, expected to be rather part of the two-pion-intermediate-state contribution, denoted earlier with $a_\mu^{\pi\pi}$. This corresponds to the last two diagrams in the expansion of the two-pion-cut contribution of the right side of Fig. 40, and follows a completely different determination. For details on this set-up, see Refs. [199, 200]. As noted in Sec. 5.5, it is currently under debate if the resonance should be even considered as a meson ($q\bar{q}$-state) or if it's unexpected structure can be interpreted as a tetra-quark candidate [182, 186]. In the context of the contribution to a_μ this might, however, be irrelevant, as we can clearly identify the dominant decay channel of $\pi\pi$, despite its underlying physical structure.

Previous calculations of the scalar contribution. In earlier evaluation of the scalar contribution, the form factors were treated with the extended Nambu-Jona-Lasinio model [196] and a later calculation [197] reconsidered the contribution using a similar model. These calculation also calculated the σ-pole contribution in the same approach, but due to the broad width result in this channel should be compared to the results of the S-wave $\pi\pi$-scattering contribution in the full dispersive treatment, eg. Ref. [199]. Another reference [198], uses the same underlying structure, however they use a VMD model for the representation

of the scalar form factor amplitudes and define an error estimation by varying the monopole mass between $(1-2)$GeV. They include the contribution from $a_0(980)$, $f_0(980)$ and $f_0(1370)$ and obtain a value of $a_\mu^{\mathcal{S}}\left[f_0(980), f_0', a_0\right] = [(3.1 \pm 0.8) - (-0.9 \pm 0.2)]$. In Ref. [193], the authors also use the VMD model and additionally consider the channel of the $f_0(1504)$ and even the σ-contribution (see Tab. 4 in Ref. [193]). In the latter case they apply an effective resonance model, to properly describe the physical nature of the σ, which is fitted to data from $\pi\pi \to \pi\pi$ and $\gamma\gamma \to \pi\pi$ scattering data. Within this model, they found that the σ contribution is the dominate one in the scalar channel, which seems to be a model independent finding. This is then analog to behavior the pseudo-scalar case, where the pion is also the largest contribution. It could be understood by the fact that the coupling of $\gamma\gamma$ to higher scalar states is much smaller than the one to the σ. The VMD representation used in the reference, includes a parameter which tries to account for the deviations from a true VMD dependence and represent their error estimate. This led to the final results for all scalar channel contribution between $a_\mu^{\mathcal{S}}\left[\text{all}\right] \sim \left[(-5.35^{+3.27}_{-0.92}) - (-1.3^{+2.06}_{-0.91})\right]$. In order to compare this to the previous calculation [198], we only consider all narrow-width channels (everything besides σ) and get a value of $a_\mu^{\mathcal{S}}\left[\text{without } \sigma\right] = \left[-(2.2^{+3.2}_{-0.7}), -(1.0^{+2.4}_{-0.4})\right] \times 10^{-11}$. The contribution of the σ carries about $(50\% \sim 98\%)$ of the complete scalar contribution and was determined with a value of $a_\mu^{\mathcal{S}}\left[\sigma/f_0(500)\right] = -(3.1^{+0.8}_{0.7} - 0.3^{+0.4}_{0.8}) \times 10^{-11}$.

Outlook in the Dyson-Schwinger framework. As far as applying the DSE result of the scalar transition form factor for contribution to a_μ^{HLbL}, this leaves us with two possible options:

1. To consider the contribution from higher scalar channels (> 1GeV) using the narrow width approximation with the corresponding masses for the decaying meson in the triangle diagram.

2. Perform a calculation of the σ-TFF and use the results in the calculation of the $\pi\pi$-scattering contribution [199, 200].

Looking back to the comparison in Tab. 12, we note that the value for the axial-vector channel is supposedly a slightly larger contribution to a_μ^{HLbL}. Following along the lines of the scalar TFF calculation, it would be straight forward to calculate the axial-vector transition form factor. This requires the (axial-vector)-vector-vector tensor basis and the axial-vector meson amplitudes, but otherwise, the same ingredients as the previous form factor calculations. Strictly speaking the production of an axial-vector into two real photons is forbidden by the Landau-Yang theorem (Refs. [201, 202]), the axial-vector meson can still produce virtual photons, which is what will be evaluated in the axial-pole contribution. Similar as in the case of the scalar TFF, there is little experimental data that can be used to apply a dispersive calculation and thus, so far, the contribution has only been calculated in model-dependent frameworks, see Refs. [198, 203] , which does not allow a systematic-error estimation.

Another meson exchange channel would be the tensor-pole contribution, which has been investigated in Refs. [194, 198]. The authors so far provide the only estimates on the tensor-pole contribution. Here, the latter references use updated data of the $f2(1270)$ TFF from the Belle Collaboration.

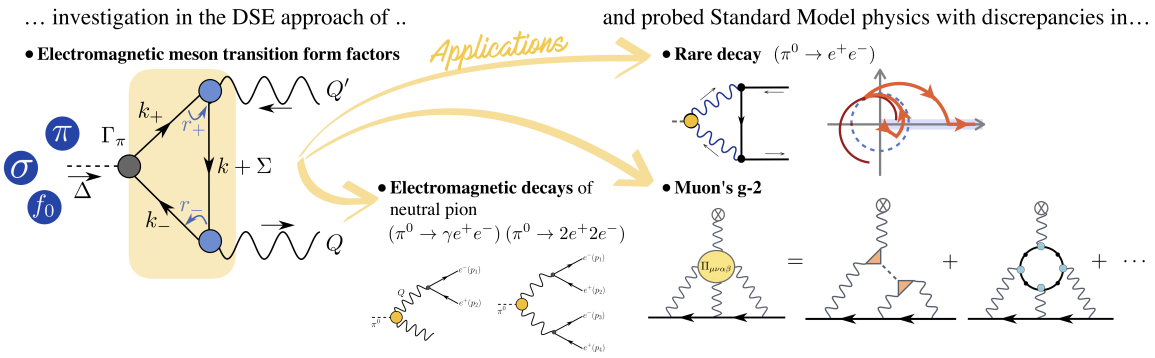

Figure 42: In this thesis, we performed an...

6 Summary & Outlook

Summary

In this thesis, we have presented the evaluation of electromagnetic transition matrix elements within the Dyson-Schwinger and Bethe-Salpeter framework. These were furthermore used to calculate observables that have the potential to challenge the formulation of the Standard Model. An overview chart of the objectives discussed in this context is given in Fig. 42.

The pion transition form factor (TFF) is one of the key elements in this context, and we calculated the form factor applying the rainbow-ladder truncation with the Maris-Tandy model consistently throughout the results presented in this thesis. The variation in the η parameter therein, Eq. 4.33, was used to quantify the error associated with the truncation and thus aimed to account for omitting higher-order Green functions. In this set-up, kinematic limitations come from poles in the calculation of the quark-propagator, and these determined the accessible kinematic values for the photon virtualities of the form factor, $F(Q^2, Q'^2)$. To investigate the scaling behavior of the TFF, we provided an update to previous DSE calculations by performing a calculation up to large Q^2 values in the singly-virtual limit. For this, we developed a strategy to perform an extrapolation beyond the accessible domain, which was constrained by the timelike vector-meson pole.

With the determination of the TFF in the full momentum range, we were able to define a fit function of our results, which helped us to furthermore apply the TFF as an intermediate vertex for calculations of other observables. In particular, we calculated the Dalitz decay rates of the pion ($\pi^0 \to e^+e^-\gamma$, $\pi^0 \to e^+e^-e^+e^-$). These decay channels are highly dominated by the anomaly value (value at the on-shell point for $\pi^0 \to \gamma\gamma$), and the results for the decay rates showed that our TFF result does properly produce this limit.

We also considered the very suppressed decay channel, $\pi^0 \to e^+e^-$, which provides a possible probe of new physics beyond the Standard Model (BSM physics). By performing a deformation of the Euclidean path-integral, we were able to provide the first independent results in comparison to previous theoretical studies. In this sense, we were able to give confidence to the number from the theoretical side, and with the current experimental value, the discrepancy remains. This leads to two possible strategies for the future: (1) the demand for further measurement and data-analysis from the experimental side, or (2) advances in the development of BSM physics that would describe the effects in this sector.

The anomalous moment of the muon is another potentially exciting source to look for BSM physics, and updates on the numbers from both theory and experiment are expected this year. In order to achieve a uniformly agreed number from the theoretical side, an initiative was founded, that aims to combine the effort of all non-perturbative calculations. Such high-precision observables require a reliable error estimation, and the currently most accurate

number is provided from the data-driven dispersive approach. The calculation for the muon's magnetic moment, a_μ, breaks down into multiple components, and as yet another application of the TFF, we look in particular at the Hadronic-Light-by-Light contribution to a_μ.

In this context, we extended our calculation of the pion TFF to other pseudo-scalar channels, namely the η and η' meson, and were able to provide a complete estimate for the pseudo-scalar exchange contribution to the HLbL part of a_μ. Furthermore, we provided an outlook on advances for the scalar transition form factor in the DSE approach, which could also be useful within the full determination of a_μ.

Outlook

In this thesis, we have explored the sector of electromagnetic meson decay processes within the Dyson-Schwinger and Bethe-Salpeter framework. In this context, the scalar transition form factor is a natural extension of the pion TFF, as it follows along the same line, only requiring a change of the underlying basis and the Bethe-Salpeter meson amplitude. Working in the rainbow-ladder truncation, the decay is described by the same triangle diagram and also needs quark propagator, quark-photon-vertex, and meson amplitude as input for the calculation. We have included an outline for the calculation of the scalar transition form factor, which presented the preliminary results using a reduced version for the quark-photon vertex, and a calculation with the full vertex is within reach.

The same story holds for axial-vector transition form factors. Following the construction principle for a meson-photon vertex basis, explained for the scalar mesons, we can easily set-up the equivalent axial-vector equation. The larger bound-state mass in this channel, will, however, lead to a smaller accessible kinematic domain, due to the quark-pole restrictions. This might be it harder to obtain reasonable data coverage to create a fit function for the full domain.

In the context of the Hadronic-Light-by-Light contribution to the muons $g-2$, this limitation is, however, not as relevant, as the integral evaluated for the meson-pole contribution takes most of its input for the lower momentum region. The channels for the scalar- axial-vector meson exchange are very sub-leading; nevertheless, towards a precise determination of the full HLbL contribution, an estimate of these contributions is highly relevant and can guide future calculations. Additionally, the limited experimental data in these channels makes it hard to calculate the TFFs from data-driven frameworks, given the DSE approach a unique selling-point to pursue calculation in this direction.

The limitations in the DSE calculation of these form factors are all based on particle poles appearing in the calculation of the individual components. On the one hand, these are the quark poles, which are based on the particular choice of the truncation and, in the case of this thesis, are dictated by rainbow-ladder. On the other hand, the poles of composite particles, such as the vector-meson poles, also play an important role. The development of a general method, similar to the path-deformation applied in case of the rare decay ($\pi^0 \to e^+e^-$), could improve the general reach of bound-state and form factor calculations in the Dyson-Schwinger approach. Moreover, it would help to incorporate a proper description of QCD resonances, including their nonzero widths, and advances in this direction have been discussed in Ref. [108].

A Appendix: Utilities

Euclidean and Minkowski conventions Throughout this thesis all equations are in the Euclidean signature, unless marked are explicitly with M for Minkowski as noted in Sec. 3.1, where we restated the textbook calculation of the axial anomaly using the mostly-minus metric. Another indication for the metric is the convention of the Lorenz indices, here we choose to write Euclidean indices both high and low, but typically all at the same height in a given expression

$$Q_\alpha Q'_\beta \varepsilon_{\alpha\beta\mu\nu} = Q^\alpha Q'^\beta \varepsilon^{\alpha\beta\mu\nu} \,. \tag{A.1}$$

Minkowski indices, on the other hand, must always be contracted with one high and one low and must always match on the two sides of the equation, for example

$$p_\mu = g_{\mu\nu}\, p^\nu \,. \tag{A.2}$$

When Minkowski is used in this work, it is always defined with the **mostly minus metric**

$$g_{\mu\nu} = \begin{pmatrix} 1 & & & \\ & -1 & & \\ & & -1 & \\ & & & -1 \end{pmatrix} , \tag{A.3}$$

This also means $k_M^2 = (k^0)^2 - \vec{k}^2$. The euclidean four-vector is defined by $k_E^2 = (k^0)^2 + \vec{k}^2$. The gamma matrices are also affected by Euclidean versus Minkowski. In case of Minkowski matrices the identity holds such that $\{\gamma_\mu^M, \gamma_\nu^M\} = 2g_{\mu\nu}$. By contrast, the Euclidean conventions are given by,

$$\{\gamma_E^\mu, \gamma_E^\nu\} = 2\delta^{\mu\nu} \,, \qquad \gamma_E^\mu = \left(\gamma_E^\mu\right)^\dagger \,, \qquad \not{p} = p^\mu \gamma_E^\mu \,, \qquad p^2 = p^\mu\, p^\mu \,, \qquad p \cdot q = \sum_{k=1}^{4} p_k\, q_k \,. \tag{A.4}$$

Here the dot product is defined with a sum over 1 to 4 and, in the main text, we use both k_4 and k_0 to indicate the time component, depending on the specific context. It is also useful to define the additional matrices:

$$\sigma^{\mu\nu} = -\frac{i}{2}\left[\gamma^\mu, \gamma^\nu\right] \,, \qquad \gamma^5 = -\gamma^1\gamma^2\gamma^3\gamma^4 = -\frac{1}{24}\varepsilon^{\mu\nu\alpha\beta}\gamma^\mu\gamma^\nu\gamma^\alpha\gamma^\beta \,. \tag{A.5}$$

Finally, the charge conjugation matrix is expressed through,

$$\mathcal{C} = \gamma^4\gamma^2 \,, \qquad \mathcal{C}^{\mathrm{T}} = \mathcal{C}^\dagger = \mathcal{C}^{-1} = -\mathcal{C} \,, \tag{A.6}$$

as used to define the charge conjugation properties of the Bethe-Salpeter meson amplitude in Eq. (5.6). Using Euclidean vectors, we then define ($p^2 > 0$) to be spacelike and ($p^2 < 0$) timelike, where the latter can only be reached if the Euclidean four-vector has non-zero imaginary components ($\mathrm{Im}\, p \neq 0$), as extensively discussed in Sec. 5.3.2 and Sec. 4.5.

To completely define the decay constant as introduced in Eq. (2.58), restated here for convience,

$$\langle 0|\, j_{5\,a}^\mu(x)\, |\lambda_b\rangle = -i\delta^{ab}\, P^\mu f_\lambda e^{-ix\cdot P} \,, \tag{A.7}$$

we need to define our conventions in three respects: **(1)** the normalization of the bound-state $|\lambda_b\rangle$, **(2)** the current $j_a^{[\mu]}$ and **(3)** the normalization of the vaccuum $\langle 0|$.

- (1) The normalization of the bound-state in the BSE-DSE framework is defined by the normalization condition in Eq. (2.50). This follows from the standard normalization condition for a single-particle state

$$\langle \mathbf{p}, a|\mathbf{p}', b\rangle = [\delta_{ab}] \times 2\omega_p (2\pi)^3 \delta^3(\mathbf{p} - \mathbf{p}') \,, \tag{A.8}$$

  where $\omega_p = \sqrt{\mathbf{p}^2 + m^2}$.

- (2) To complete the definition of the currents, introduced in Eq. (2.53), we need to fix our conventions for the generators of the underlying flavor symmetry group t_a. The convention for t_a is defined by

$$[t_a, t_b] = f_{abc}\, t_c\,, \qquad \mathrm{Tr}[t_a^2] = \frac{1}{2}\,. \tag{A.9}$$

  To fix the conventions we now set $a = 1$ and get

$$t_1 = \frac{1}{2}\begin{pmatrix} 0 & 1 & 0 \\ 1 & 0 & 0 \\ 0 & 0 & 0 \end{pmatrix}\,. \tag{A.10}$$

  The definition of Eq. (2.53) holds in the Euclidean metric j_μ^E. The Euclidean and Minkowski versions can differ by a factor of i.

- (3) One final convention for exact definition of f_π, is the normalization of the vacuum state

$$\langle 0|0\rangle = 1\,. \tag{A.11}$$

With all conventions fixed this completely defines, Eq. (A.7) as used in Eq. (2.53), such that

$$\langle 0|j^\mu_{5a=1}|\pi^-, \mathbf{p}\rangle = \frac{1}{2}\langle 0|\overline{\mathcal{U}}(x)\gamma_5\gamma^\mu\mathcal{D}(x)|\pi^-, \mathbf{p}\rangle = -\frac{1}{2}ip^\mu\sqrt{2}f_\pi\,, \tag{A.12}$$

where $f_\pi \approx 92$MeV is the pion decay constant.

It is also convenient to express this using the isospin basis for the pions. For example we have

$$\langle 0|\left[\frac{j^\mu_{5a=1} + ij^\mu_{5a=2}}{2}\right]\frac{1}{\sqrt{2}}\left[|\pi_1, \mathbf{p}\rangle - i|\pi_2, \mathbf{p}\rangle\right] = -\frac{1}{\sqrt{2}}ip^\mu f_\pi = \frac{1}{\sqrt{2}}\langle 0|j^\mu_{5a=1}|\pi_1, \mathbf{p}\rangle\,, \tag{A.13}$$

implying

$$\langle 0|j^\mu_{5a}|\pi, \mathbf{p}, b\rangle = -ip^\mu\delta_{ab}f_\pi\,. \tag{A.14}$$

Math tools. The Feynman parameters and Schwinger parameter were used in Sec. 3.1 in the calculation of the anomaly prediction, perturbatively evaluating the triangle diagram:

- **Feynman parameters**

$$\begin{aligned}\frac{1}{ABC} &= \int_0^1 dx\, dy\, dz\ \delta(1-x-y-z)\,\frac{1}{[Ax+By+Cz]^3} \\ &= 2\int_0^1 dx\int_0^{1-x} dy\,\frac{1}{[x(A-C)+y(B-C)+C]^3}\,.\end{aligned} \tag{A.15}$$

- **Schwinger parameter**

$$\frac{2}{D^3} = \int_0^\infty d\alpha\,\alpha^2\, e^{-\alpha D}\,. \tag{A.16}$$

B Appendix: Calculation related details

Kinematic set-up for form factors

The purpose of this appendix is to provide an overview chart of all possible choices for the kinematic variables in the calculation of the transition form factor, see Fig. 43. The form factor $(\Lambda^{\mu\nu}(Q^2, Q'^2, Q\cdot Q'))$ generally depends on three scalar variables. As physical process this is evaluated at the physical on-shell point of the decaying meson and virtual photons, such that after fixing the total momentum $\Delta^2 = -M^2$, two variables remain.

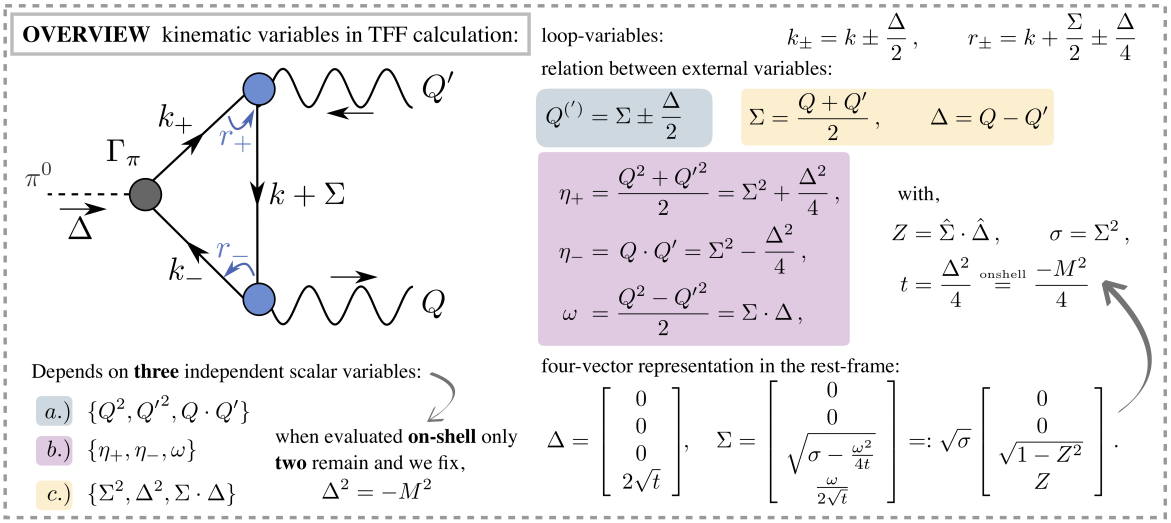

Figure 43: Lookup table for all possible kinematic variables used in the context of the transition form factor calculation.

Quark-photon-vertex

The fermion-photon vertex is a vector-current vertex, Eq. (2.52), with quantum numbers $J^{\mathsf{PC}} = 1^{--}$ and depends on two independent four-vector (often chosen as the relative momentum between the quarks q and the total momentum of the photon P). The underlying basis structure is a combination of the following Dirac and Lorenz structures

$$\{\gamma^\mu, P^\mu, q^\mu\} \quad \times \quad \{\mathbb{1}, \not{q}, \not{P}, [\not{q}, \not{P}]\}\,. \tag{B.1}$$

To constructs the final basis we follow the principle explained in the previous section for the meson-photon vertex, which is based on Ref. [103] where the authors thoroughly explained the concept in case of the Nucleon-Compton scattering and connected properties. In this sense one starts by writing down all possible basis elements, as a combination from Eq. (B.1), and aims to construct a basis where the elements are kinematic independent.

This leads to one possible choice for the full basis of the quark-photon vertex, as also used in Refs. [95, 103],

$$\begin{aligned}
&\tau_1^\mu = i\gamma^\mu\,, && \tau_2^\mu = iq^\mu \not{q}\,, && \tau_3^\mu = q^\mu\,, && \tau_4^\mu = q^\mu\,[\not{q}, \not{P}]\,, \\
&\tau_5^\mu = t_{PP}^{\mu\nu}\gamma^\nu\,, && \tau_6^\mu = \frac{i}{2}(q.P)\,[\gamma^\nu, \not{q}]\,, && \tau_7^\mu = \frac{i}{2}\,[\gamma^\nu, \not{P}]\,, && \tau_8^\mu = \frac{1}{6}\,[\gamma^\mu, \not{q}, \not{P}]\,, \\
&\tau_9^\mu = it_{PP}^{\mu\nu}q^\nu\,, && \tau_{10}^\mu = t_{PP}^{\mu\nu}q^\nu \not{q}\,, && \tau_{11}^\mu = t_{Pq}^{\mu\nu}(q.P)\,\gamma^\mu\,, && \tau_{12}^\mu = \frac{i}{2}\,t_{Pq}^{\mu\nu}\,[\gamma^\nu, \not{q}]\,,
\end{aligned} \tag{B.2}$$

where $t_{ab}^\mu = (a \cdot b)\delta_{\mu\nu} - b^\mu a^\nu$ is a transverse projector. Note that in this definition the tensor carries units of energy squared, whereas in previous section the dimensionless transverse tensor was often used, by dividing with the squared momenta. The full quark-photon vertex is then given by,

$$\Gamma^\mu(q,P) = \sum_{i=0}^{12} f_i(q,P)\,\tau_i^\mu(q,P) \tag{B.3}$$

with the scalar dressing functions f_i. As introduced in Sec. 2.4.3 and Sec. 4, to calculate the scalar dressing functions we need to solve the inhomogeneous Bethe-Salpeter equation,

$$\Gamma_a^\mu(q,P) = \Gamma_{0\,a}^\mu + \mathbf{K}\;\Gamma_a^\mu = Z_2 i\gamma^\mu t_a + \int_l \mathbf{K}_{ab}(l,q,P)\;\Gamma_b^\mu(l,P)\,. \tag{B.4}$$

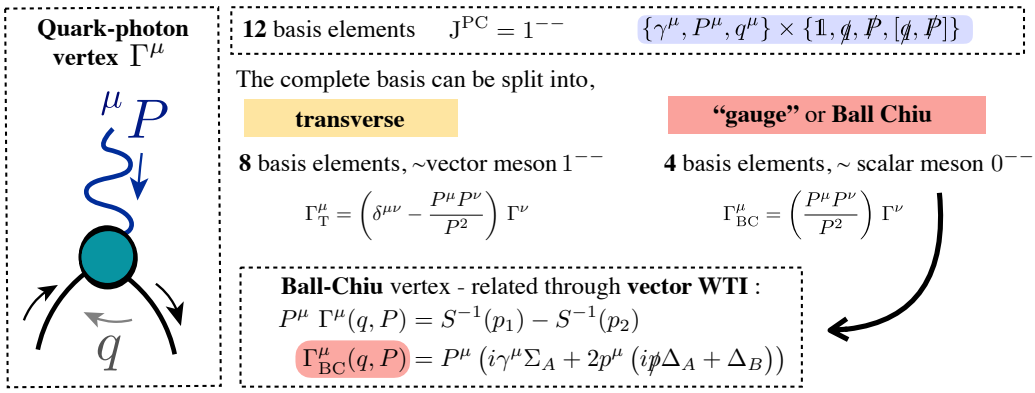

Figure 44: Float-chart for the quark-photon-vertex. Vertex can be broken up into transverse and longitudinal part. Longitudinal part is constrained by the vector WTI.

Z_2 correspond to the renormalization constant form the quark propagator.

Within the basis elements, Eq. (B.2), we can identify a set of purely transverse structures, which are eight $\{\tau_5^\mu : \tau_{12}^\mu\}$,

$$\Gamma^\mu_{\rm T} := T^{\mu\nu}(P,P)\,\Gamma^\mu = \left(\delta^{\mu\nu} - \frac{P^\mu P^\nu}{P^2}\right)\,\Gamma^\mu\,. \tag{B.5}$$

The same set of basis structured would be used for for a vector meson amplitude and it corresponds to solving the homogeneous version of the vertex BSE in the proximity of the ρ-meson pole. The remaining four components, $\{\tau_1^\mu : \tau_4^\mu\}$ contain transverse and longitudinal parts. This is what will call the "gauge" part of the vertex (in previous section also indicated as the Ball-Chiu vertex), as it is constrained by gauge invariance and is related to the quark propagator through the vector Ward-Takahashi identity, Eq. (2.63),

$$\Gamma_{\rm BC} := P^\mu\,\Gamma^\mu(q,P)\,, \quad T^{\mu\nu}(P,P)\,\Gamma^\mu_{\rm BC} \neq 0\,. \tag{B.6}$$

Applying the VWTI, this part is then complete determined by the dressing functions of the quark propagator. To emphasize the connection we restate the VWTI and the corresponding BC vertex. The VWTI is given by,

$$P^\mu\,\Gamma^\mu(p,P) = S^{-1}(p_1) - S^{-1}(p_2) = P^\mu\left(i\gamma^\mu\Sigma_A + 2p^\mu\left(i\not{p}\Delta_A + \Delta_B\right)\right)\,, \tag{B.7}$$

which follows the form of the Ball-Chiu vertex as,

$$\Gamma^\mu_{\rm BC} = i\gamma^\mu\,\Sigma_A(q,P) + 2p^\mu\,\left(i\not{p}\Delta_A(q,P) + \Delta_B(q,P)\right)\,, \tag{B.8}$$

with the definitions for the dressing function as,

$$\Sigma_A = \frac{A(p_+^2) + A(p_-^2)}{2}\,, \quad \Delta_A = \frac{A(p_+^2) - A(p_-^2)}{p_+^2 - p_-^2}\,, \quad \Delta_B = \frac{B(p_+^2) - B(p_-^2)}{p_+^2 - p_-^2}\,, \tag{B.9}$$

with the momentum convention, $p_\pm = p \pm P/2$. The contracted gauge part ($P^\mu\,\Gamma^\mu_{\rm BC} \sim \Gamma_{\mathcal{S}}$), carries the same quantum numbers and thus basis structures as a scalar meson, Eq. 5.69, such that the dressing functions of the BC part can also be obtained by solving a homogeneous BSE for a scalar meson. On the other hand, this means that the scalar meson is also directly connected to the dressing functions of the quark propagator and we principally do not need to solve the BSE for the meson amplitude when using the VWTI.

Fig. 44, show as float-chart of the quark-photon vertex and the separation into transverse- and gauge-part as described in this paragraph. Since transverse and gauge part decouple we

can solve two separate BSE, instead of the full equation with twelve tensor structures. This saves computation time and when using the VWTI we in fact only need to solve the transverse part of the equation.

Connecting the underlying structures and relation, we can identify **three** scenarios of how to calculate the vertex,

1. Solving the full inhomogeneous vertex equation for all twelve tensor structures.

2. Using the fact that the equation decouples and separately calculating the transverse and the gauge part. The transverse part can then be obtained by either,

   a.) solving the inhomogeneous BSE for the transverse part ($\{\tau_5^\mu : \tau_{12}^\mu\}$). or

   b.) calculating a homogeneous BSE for a vector meson, which can require a transformation of the dressing functions afterward, if the definition of the basis for the vector meson and the transverse parts in the vertex basis vary by momentum dependent prefactors.

   The gauge part is then obtained by either,

   a.) calculating the dressing function of a scalar meson with a homogeneous BSE, or

   b.) applying the VWTI and expressing it in terms of quark dressing functions, Eq. (B.8).

Method 2. a.) + b.) can be identified as least numerical effort and is thus what is applied in most calculations. However, pursuing the other path carries educational benefits and can be useful when searching for possible bugs in the calculation. It can also help problems associated with the numerical evaluation in difficult momentum regions, as eg. solving a homogeneous BSE shows much better convergence. The evaluation of the vertex, as straight forward as it seems, contains many numerical subtleties. Especially in the limit when one quark legs carry a large momentum transverse and the other almost none. The integrand in the BSE becomes peaked at the corners of the angular integral and requires an appropriate distribution in the angular grid in order to obtain a grid-point-independent and numerically-stable result.

The quark-photon vertex has been calculated from multiple DSE collaborations, see Refs. [63, 96–100], and poses as one of the key Green function in our approach. It naturally incorporates the effects from the vector-meson pole in the form factor calculation, as discussed in Sec. 4.5. The most recent publication, Ref. [106], compares results from a gauge-fixed lattice calculation with the ones in the DSE approach.

Deriviation of the Ward-Takahashi identities.

The symmetry considered to derive the axial-vector vertex Ward-Takahashi identity (AXWTI) is a global $U_A(N_f) \simeq U_A(1) \times SU_A(N_f)$ transformation. In the case of three-flavor physics, this is generated in the fundamental representation by the eight Gell-Mann Matrices plus the three-dimensional identity matrix. The generators of the group are thus given through $t^a = \lambda^a/2$, with the Gell-Mann Matrices λ^a. In addition, the generator of the $U_A(1)$ is included in the first generator as t^0. The transformation in the fundamental representation of $U_A(N_f)$ is given by:

$$g(\theta) = e^{i\theta^a t^a \gamma_5}\,, \tag{B.10}$$

where θ^a is the parameter of the transformation and is thought to be infinitesimal. The quark fields transform according to

$$\psi' = e^{i\theta^a t^a \gamma_5}\ \psi \quad , \quad \bar{\psi}' = \bar{\psi}\ e^{i\theta^a t^a \gamma_5}\,. \tag{B.11}$$

In order to derive the AXWTI we once more use the invariance of the path integral under field redefinitions. Consider the expectation value of a general operator, $\mathcal{O}$, which stays invariant under the redefinition of the fields $\psi \to \psi'$:

$$\begin{aligned}\langle \mathcal{O} \rangle &= \frac{1}{Z[0]} \int \mathcal{D}\bar{\psi}\mathcal{D}\psi \; e^{-S} \; \mathcal{O} \stackrel{!}{=} \frac{1}{Z[0]} \int \mathcal{D}\bar{\psi}\mathcal{D}\psi \; (\mathcal{J}) \; e^{-S'} \; \mathcal{O}' \,, \\ &= \frac{1}{Z[0]} \int \mathcal{D}\bar{\psi}\mathcal{D}\psi \; (e^{\log \mathcal{J}[\theta]}) \; e^{-(S+\delta S[\theta])} \; (\mathcal{O} + \delta\mathcal{O}[\theta]) \,, \end{aligned} \tag{B.12}$$

where the change in the measure is noted by introducing a Jacobian $\mathcal{J}$. As Eq. (B.12) holds, the differences introduced by the transformation have to be equal to zero. The transformation changes the expectation values in three parts: the integral measure ($\mathcal{J}[\theta]$), the operator itself ($\delta\mathcal{O}[\theta]$) and in the action ($\delta S[\theta]$). We now carry out a **local** transformation, such that $\theta(z)^a$ depends on a space-time point. If we further take this to be infinitesimal, then we can expand the exponentials in Eq.(B.12) through their Taylor series, $e^{f[\theta]} = (1 + f[\theta] + O(\theta^2))$, and keep only the leading term. By comparison of the right- and left-hand side we then find the following relation:

$$\begin{aligned} 0 &\stackrel{!}{=} \frac{1}{Z[0]} \int \mathcal{D}\psi\mathcal{D}\bar{\psi} \; (\log \mathcal{J}[\theta] - \delta S[\theta] + \delta\mathcal{O}[\theta]) \\ &= \langle \log \mathcal{J} - \delta S + \delta\mathcal{O} \rangle \,. \end{aligned} \tag{B.13}$$

In the next step we are going to specify the variations that occur through the transformation. Let's start by looking at the measure change. Chapter 30 of [1] offers a thorough explanation about the details of the so called axial anomaly, here however I will first only quote the result:

$$\mathcal{J} = \exp \left[i \int_z \theta^a(z) \frac{e^2}{16\pi^2} \mathrm{Tr}[t^a Q^2] \; \epsilon_{\alpha\beta\mu\nu} F_{\alpha\beta} F_{\mu\nu} + i \int_z \theta^a(z) \frac{g^2 N_f}{32\pi^2} \mathrm{Tr}[t^a t^i t^j] \; \epsilon_{\alpha\beta\mu\nu} F^i_{\alpha\beta} F^j_{\mu\nu} \right] , \tag{B.14}$$

where t^i are once more the Gell-Mann matrices, as generators of the $SU(3)$ gauge group, $Q = \mathrm{diag}(2/3, -1/3, -1/3)$ is the quark charge matrix, e and g are the electromagnetic and strong coupling constants, N_f is the number of flavors in the theory, $F_{\mu\nu}$ represents the Abelian photon field-strength tensor and $F^a_{\mu\nu}$ the non-Abelian gluon fields. The traces are defined in color and flavor space. For different values of a there will either be a contribution or else the trace may evaluate to zero. In order to calculate this one can proceed with a method first used by Fujikawa [1]. Here one expands the functional determinant into eigenfunctions of the Dirac operator. Since the Jacobian introduced by the measure change is divergent, one has to use a cutoff with a regulator mass for ensuring the renormalization of the integral. The mass is taken to infinity at the last step and we obtain the terms introduces in Eq. (B.14). One can show that the result is independent of the choice of regularization.

The second change due to this infinitesimal local variation, is the change of the action, $\delta S = S[\bar{\psi}, \psi] - S[\bar{\psi}', \psi']$:

$$\delta S = -i \int_z \theta^a(z) \partial^\mu (\bar{\psi}\gamma^\mu\gamma_5 t^a \psi) + i \int_z \theta(z) \; \bar{\psi}\gamma_5 \{M, t^a\} \psi \,, \tag{B.15}$$

where M is the quark mass matrix. The partial derivative is acting on the full expression in bracket, which is denoted as the axial-vector current $j^\mu_{5\,a} = \bar{\psi}\,\gamma^\mu\gamma_5\,t^a\psi$.

Last we consider the variation of the operator $\delta\mathcal{O}$. For deriving the AXWTI of interest in the DSE approach, we choose the operator to be the quark bilinear: $\mathcal{O} = \psi(x)\bar{\psi}(y)$. Different choices for the operator will lead to other relations between n-point Green functions. Thus, in principle, one can derive infinitely many different relations by varying the choice of $\mathcal{O}$.

Of course, one then has to identify whether these are useful in the context of a specific calculation. The local variation of the quark bilinear gives

$$\frac{\delta\mathcal{O}}{\delta\theta^a(z)} = i\ \gamma_5 t^a\ \delta(z-x)\ \psi(x)\bar{\psi}(y) + i\ \psi(x)\bar{\psi}(y)\ \delta(y-z)\ \gamma_5 t^a\,. \tag{B.16}$$

Finally we can substitute all changes into Eq. B.13, and write down the full AXWTI as

$$\begin{aligned}\langle\partial_\mu j^\mu_{5\,a}\ \psi(x)\bar{\psi}(y)\rangle &= \gamma_5\, t^a\,\delta_{xz}\,\psi(x)\langle\psi(x)\bar{\psi}(y)\rangle + \langle\psi(x)\bar{\psi}(y)\rangle\ \delta_{yz}\gamma_5 t^a + \langle j^a_5\psi(x)\bar{\psi}(y)\rangle \\ &+ \frac{e^2}{16\pi^2}\mathrm{Tr}[t^a Q^2]\ \epsilon_{\alpha\beta\mu\nu}\langle(F_{\alpha\beta}F_{\mu\nu})_z\psi(x)\bar{\psi}(y)\rangle \\ &+ \frac{g^2 N_f}{32\pi^2}\mathrm{Tr}[t^a t^i t^j]\ \epsilon_{\alpha\beta\mu\nu}\langle(F^i_{\alpha\beta}F^j_{\mu\nu})_z\psi(x)\bar{\psi}(y)\rangle\,,\end{aligned} \tag{B.17}$$

with the abbreviation $\delta_{xz} = \delta(x-z)$. Note that $\langle\psi(x)\bar{\psi(y)}\rangle$ can be identified all the fully dressed quark propagator. The final step in the derivation is to Fourier transform both sides of Eq. (B.17). This then leads to Eq. (2.64) of the main text.

Alternative method: Another way to derive the AXWTI is by using the canonical description of the Greens functions. Thereby one also starts with a generic n-point Greens function, considers the divergence of it and uses the current algebra to replace and relate appearing current-field commutators. The current algebra incorporates the underlying symmetry relation in this case.

Four-body phase space

In this appendix we work out the four-body phase-space integral $d\Phi_4$ that enters in the $\pi^0 \to e^+e^-e^+e^-$ decay of Eq. (5.18). The decay width of a particle with momentum P and mass M decaying into n daughter particles with momenta p_i and masses m_i is given by

$$\Gamma(P \to p_i) = \frac{1}{S}\frac{1}{2M}\int d\Phi_n\,|\mathcal{M}|^2\,, \tag{B.18}$$

with S the symmetry factor, $|\mathcal{M}|^2$ the spin summed and squared matrix element, and $d\Phi_n$ the phase-space integral for an n-particle final state given by

$$d\Phi_n = (2\pi)^4\delta^4\left(P - \sum_{i=1}^n p_i\right)\prod_{i=1}^n \frac{d^3\mathbf{p}_i}{(2\pi)^3\,2E_i}\,. \tag{B.19}$$

Following Ref. [204], we rewrite the integration in terms of invariant mass variables. For $n = 4$ one obtains

$$d\Phi_4 = \frac{1}{(2\pi)^8}\frac{\pi^2}{32M^2}\,\frac{ds_{12}\,ds_{34}\,ds_{124}\,ds_{134}\,ds_{14}}{\sqrt{-\Delta_{(4)}}} \tag{B.20}$$

where, for degenerate decay products with $m_i = m$, the two- and three-particle Mandelstam variables read

$$\begin{aligned} s_{ij} &= -(p_i+p_j)^2 = 2m^2 - 2p_i\cdot p_j\,, \\ s_{ijk} &= -(p_i+p_j+p_k)^2 = s_{ij}+s_{ik}+s_{jk}-3m^2 \end{aligned} \tag{B.21}$$

and the four-dimensional Gram determinant $\Delta_{(4)}$ contains all possible dot products of four-vectors:

$$\Delta_{(4)} = \det\begin{bmatrix} -m^2 & p_1\cdot p_2 & p_1\cdot p_3 & p_1\cdot p_4 \\ p_1\cdot p_2 & -m^2 & p_2\cdot p_3 & p_2\cdot p_4 \\ p_1\cdot p_3 & p_2\cdot p_3 & -m^2 & p_3\cdot p_4 \\ p_1\cdot p_4 & p_2\cdot p_4 & p_3\cdot p_4 & -m^2 \end{bmatrix}. \tag{B.22}$$

In contrast to [144, 204, 205] we employ a Euclidean signature, however with s_{ij} and s_{ijk} defined such that they have the same meaning in Minkowski and Euclidean conventions. To work with the invariant mass variables of Eq. (B.20), one replaces the $p_i \cdot p_j$ in the Gram determinant according to Eq. (B.21) together with

$$\sum_{i<j} s_{ij} = -(M^2 + 8m^2)\,. \tag{B.23}$$

The physical region of integration is bounded by the surface $\Delta_{(4)} = 0$. Following the derivation of Refs. [144,205,206], we impose this relation on the invariant mass variables and begin by solving $\Delta_{(4)} = 0$ for s_{14}. It yields

$$s_{14}^{\pm} = \frac{b \pm 2\sqrt{G(s_{124}, s_{34}, s_{12})\, G(s_{134}, s_{12}, s_{34})}}{\lambda(s_{12}, s_{34}, M^2)}\,, \tag{B.24}$$

where $\lambda(u, v, w) = u^2 + v^2 + w^2 - 2uv - 2uw - 2vw$ is the Källen function, the G functions are given by

$$\begin{aligned} G(u, v, w) &= m^2(w - M^2)^2 \\ &+ v\left[(u - m^2)^2 - (u + m^2)(w + M^2) + wM^2 + uv\right], \end{aligned}$$

and b is the coefficient of $-8\Delta_{(4)}$ linear in s_{14}:

$$\begin{aligned} b &= G(s_{124}, s_{34}, s_{12}) + G(s_{134}, s_{12}, s_{34}) \\ &+ M^2 cd - (c + d)(s_{12}\, d + s_{34}\, c) \end{aligned}$$

with $c = s_{124} - m^2$ and $d = s_{134} - m^2$.

The regions of the s_{124} and s_{134} integrations are bounded by the surfaces satisfying $s_{14}^{+} = s_{14}^{-}$, which is fulfilled when either of the G functions in Eq. (B.24) vanishes $G(s_{124}, s_{34}, s_{12}) = 0$ or $G(s_{134}, s_{12}, s_{34}) = 0$. Solving $G(u, v, w) = 0$ for u yields

$$s_{14}^{\pm} = \frac{w - v + M^2 + 2m^2}{2} \pm \frac{\sqrt{v - 4m^2}\sqrt{\lambda(v, w, M^2)}}{2\sqrt{v}}$$

and thus determines the integration boundaries $s_{124}^{\pm}$ and $s_{134}^{\pm}$ as functions of the two dilepton invariant masses s_{12} and s_{34}.

Finally, s_{34} and s_{12} range from the threshold at $4m^2$ to $(M - \sqrt{s_{12}})^2$ and $(M - 2m)^2$, respectively; here the ordering is arbitrary and could also be exchanged.

A valuable check when rewriting the phase space integral in different coordinates is the massless limit. For massless daughter particles the n-body phase space is given by

$$\Phi_n = \frac{1}{2\,(4\pi)^{2n-3}} \frac{M^{2n-4}}{\Gamma(n)\,\Gamma(n-1)}\,. \tag{B.25}$$

Integrating over the phase space volume only, as given in Eq. (B.20) with the borders as suggested for $m = 0$, reproduces the limit exactly as it should.

The final decay rate for the decay of the neutral pion ($M = m_\pi$) into two dileptons ($m = m_e$) is then given by

$$\Gamma_{\pi^0 \to 2e^+ 2e^-} = \frac{1}{2^{16}\,\pi^6\, m_\pi^3} \int_{4m_e^2}^{(m_\pi - 2m_e)^2} ds_{12} \int_{4m_e^2}^{(m_\pi - \sqrt{s_{12}})^2} ds_{34} \int_{s_{124}^{-}}^{s_{124}^{+}} ds_{124} \int_{s_{134}^{-}}^{s_{134}^{+}} ds_{134} \int_{s_{14}^{-}}^{s_{14}^{+}} ds_{14}\, \frac{|\mathcal{M}|^2}{\sqrt{-\Delta_{(4)}}}\,. \tag{B.26}$$

C Appendix: Dispersion relation

As introduced in Sec. 2.3, the dispersion relation is a non-perturbative data-driven method, which makes use of two fundamental properties of our QFT, namely the unitarity of the S-matrix and causality. With the equations, we are able to relate the imaginary part of scattering amplitudes to cross-section data from experimental measurements. By doing so one is able to calculate and even predict new physical observables through the experimental data of related processes. This section briefly summarized the general concept of the dispersion relations as reviewed e.g in Ref. [29].

Scattering amplitudes and vertex functions will, in general, contain both, a real and an imaginary part. The imaginary part comes from the resonances that are associated with intermediate particle states. Causality implies that the momentum representation of a scattering amplitude is an analytic function in the upper complex half-plane. In the upper half-plane, as along the real axis the function contains the physical branch-cuts, that run along the real axis, starting from the two-particle threshold continuing up to infinity. Any such function can be described dispersively, and the dispersion relation is based on a deforming of the path with the usual $i\varepsilon$ prescription and applying Cauchy integral theorem, this leads to the following expression

$$\mathrm{Re}\, f(s) = \frac{1}{\pi} \int_0^\infty ds' \, \frac{\mathrm{Im}\, f(s')}{s' - s - i\varepsilon} \,. \tag{C.1}$$

The dispersive integral runs over all s', which means that in order to know the real part of the function at small length-scales, we need to know how the imaginary part of the amplitude behaves at all momentum scales. As the information in the large momentum regime is often hard to obtain in particle physics measurements or calculations, we can use a trick to suppress the dependence of the higher energy regions. By subtracting a low-energy constant we will reduce the powers of energy in the integrand, suppressing the high energy contributions. This means the integrand in Eq. (C.1) gets additional factors of $1/s$, such that higher s' values will be weighted less, while the integral will still run over the full range in s'. The subtracted relation is then given by,

$$\frac{f(s) - f(0))}{s} = \frac{1}{\pi} \int \frac{ds'}{s' - s - i\varepsilon} \mathrm{Im} \left[\frac{f(s') - f(0)}{s'} \right] = \frac{1}{\pi} \int \frac{ds'}{s'} \, \frac{\mathrm{Im}\, f(s')}{s' - s - i\varepsilon} \,, \tag{C.2}$$

where the last step followed from $\mathrm{Im}\, f(0) = 0$. In this sense we were able to reduce the impact of $\mathrm{Im}\, f(s')$ at higher energies by introducing the unknown subtraction constant $f(0)$. This shifts our problem from calculating an amplitude in a high energy region, to the determination of a single number. The subtraction constant are often equivalent to the parameters in effective Lagrangians.

The unitarity of the S-matrix implies the optical theorem, which helps us to relate the imaginary part of the scattering amplitude to physically measurable cross-sections. This means that most of the time, one will identify the lowest-lying singularity structures of the unitary relation, and starts by including all important sub-processes. In some cases the imaginary part is directly measured in experiments, however, in most cases, additional theoretical methods, such as a partial wave expansion or additional theoretical constraints through Roy-Steinert equations are needed to relate the scattering amplitude to processes that are measured in experiments.

In Sec. 5.1 we give a brief discourse about the dispersive calculation of the pion transition form factor and which experimental data-sets are relevant in this case.

Details on the dispersive equations for $a_\mu^{\mathbf{HLbL}}$ We follow along the lines of Refs. [85, 199] to define the details of the dispersive equations for a_μ^{HLbL}. In Sec. 5.6.1 we have presented the results for the pseudo-scalar pole contribution to a_μ^{HLbL}. To calculate this meson-pole

contribution, we evaluate the following expression (restated from Eq. (5.73) for convenience),

$$a_\mu^{\text{HLbL; PS}} = \frac{-2\pi}{3}\left(\frac{\alpha}{\pi}\right)^3 \int_0^\infty dQ_1 dQ_2 \int_{-1}^{+1} dz \sqrt{1-z^2} Q_1^3 Q_2^3 \left[\frac{F_1 I_1(Q_1,Q_2,z)}{Q_2^2+m_M^2} + \frac{F_2 I_2(Q_1,Q_2,z)}{Q_3^2+m_M^2}\right], \tag{C.3}$$

which contains the pseudo-scalar transition form factor amplitudes F_{PS}, as defined in case of the pion in Eq. (5.1), through

$$F_1 = F_{\text{PS}}(Q_1^2,Q_3^2)F_{\text{PS}}(Q_2^2,0)\,, \quad F_2 = F_{\text{PS}}(Q_1^2,Q_2^2)F_{\text{PS}}(Q_3^2,0)\,, \tag{C.4}$$

where $Q_3 = (Q_1^2+Q_2^2+2Q_1Q_2z)$. The numerators I_i are specified by,

$$\begin{aligned} I_1(Q_1,Q_2,z) = \frac{-1}{m_\mu^2 Q_3^2}\,[\,&\frac{4m_\mu^2 z}{Q_1Q_2} + (1-R_{m_1})\left(\frac{2Q_1 z}{Q_2}4(1-z^2)\right) - (1-R_{m_1})^2\frac{Q_1 z}{Q_2} \\ &- 8X(Q_1,Q_2,z)(Q_2^2-2m_\mu^2)(1-t^2)\,]\,, \end{aligned}$$

and

$$\begin{aligned} I_2(Q_1,Q_2,z) = \frac{-1}{m_\mu^2 Q_3^2}\,[\,&2(1-R_{m_1})\left(\frac{Q_1 z}{Q_2}+1\right) + 2(1-R_{m_2})\left(\frac{Q_2 z}{Q_1}+1\right) \\ &+ 4X(Q_1,Q_2,z)(Q_3^2+2m_\mu^2)(1-z^2)\,, \end{aligned} \tag{C.5}$$

in which the following functions have been employed,

$$X(Q_1,Q_2,z) = \frac{1}{\sqrt{1-z^2}Q_1Q_2}\arctan\left(\frac{b\sqrt{(1-z^2)}}{1-bz}\right), \tag{C.6}$$

$$b = \frac{Q_1Q_2}{4m_\mu^2}(1-R_{m_1}(1-R_{m_2}))\,, \tag{C.7}$$

$$R_{m_i} = \sqrt{1+4m_\mu^2/Q_i^2}\,. \tag{C.8}$$

D Bibliography

[1] M. D. Schwartz, *Quantum Field Theory and the Standard Model*. Cambridge University Press, 2014.

[2] M. Srednicki, *Quantum field theory*. Cambridge University Press, 2007.

[3] M. E. Peskin and D. V. Schroeder, *An Introduction to quantum field theory*. Addison-Wesley, Reading, USA, 1995.

[4] R. A. Briceno, J. J. Dudek and R. D. Young, *Scattering processes and resonances from lattice QCD*, *Rev. Mod. Phys.* **90** (2018) 025001 [1706.06223].

[5] G. Eichmann, H. Sanchis-Alepuz, R. Williams, R. Alkofer and C. S. Fischer, *Baryons as relativistic three-quark bound states*, *Prog. Part. Nucl. Phys.* **91** (2016) 1 [1606.09602].

[6] R. Williams, *Vector mesons as dynamical resonances in the Bethe-Salpeter framework*, 1804.11161.

[7] P.-L. Yin, C. Chen, G. Krein, C. D. Roberts, J. Segovia and S.-S. Xu, *Masses of ground-state mesons and baryons, including those with heavy quarks*, *Phys. Rev.* **D100** (2019) 034008 [1903.00160].

[8] P. C. Wallbott, G. Eichmann and C. S. Fischer, $X(3872)$ *as a four-quark state in a Dyson-Schwinger/Bethe-Salpeter approach*, *Phys. Rev.* **D100** (2019) 014033 [1905.02615].

[9] S.-S. Xu, Z.-F. Cui, L. Chang, J. Papavassiliou, C. D. Roberts and H.-S. Zong, *New perspective on hybrid mesons*, *Eur. Phys. J.* **A55** (2019) 113 [1805.06430].

[10] H. Sanchis-Alepuz, C. S. Fischer, C. Kellermann and L. von Smekal, *Glueballs from the Bethe-Salpeter equation*, *Phys. Rev.* **D92** (2015) 034001 [1503.06051].

[11] L. P. Kaptari, B. Kaempfer and P. Zhang, *Analytical properties of the gluon propagator from truncated Dyson-Schwinger equation in complex Euclidean space*, 1811.01479.

[12] G. Eichmann, *Progress in the calculation of nucleon transition form factors*, 2016, 1602.03462.

[13] G. Eichmann and G. Ramalho, *Nucleon resonances in Compton scattering*, *Phys. Rev.* **D98** (2018) 093007 [1806.04579].

[14] K. Aoki, *Introduction to the nonperturbative renormalization group and its recent applications*, *Int. J. Mod. Phys.* **B14** (2000) 1249.

[15] C. Bagnuls and C. Bervillier, *Exact renormalization group equations. An Introductory review*, *Phys. Rept.* **348** (2001) 91 [hep-th/0002034].

[16] J. M. Pawlowski, *Aspects of the functional renormalisation group*, *Annals Phys.* **322** (2007) 2831 [hep-th/0512261].

[17] B.-J. Schaefer and J. Wambach, *Renormalization group approach towards the QCD phase diagram*, *Phys. Part. Nucl.* **39** (2008) 1025 [hep-ph/0611191].

[18] H. Gies, *Introduction to the functional RG and applications to gauge theories*, *Lect. Notes Phys.* **852** (2012) 287 [hep-ph/0611146].

[19] R. Alkofer, A. Maas, W. A. Mian, M. Mitter, J. Paris-Lopez, J. M. Pawlowski et al., *Bound state properties from the functional renormalization group*, *Phys. Rev.* **D99** (2019) 054029 [1810.07955].

[20] M. Lüscher, *Volume Dependence of the Energy Spectrum in Massive Quantum Field Theories. 2. Scattering States*, *Commun. Math. Phys.* **105** (1986) 153.

[21] H.-W. Lin et al., *Parton distributions and lattice QCD calculations: a community white paper*, *Prog. Part. Nucl. Phys.* **100** (2018) 107 [1711.07916].

[22] M. T. Hansen and S. R. Sharpe, *Lattice QCD and three-particle decays of resonances*, *Annual Review of Nuclear and Particle Science* **69** (2019) 65 [1901.00483].

[23] M. Bruno et al., *Simulation of QCD with $N_f = 2 + 1$ flavors of non-perturbatively improved Wilson fermions*, *JHEP* **02** (2015) 043 [1411.3982].

[24] M. Bruno, T. Korzec and S. Schaefer, *Setting the scale for the CLS $2 + 1$ flavor ensembles*, *Phys. Rev.* **D95** (2017) 074504 [1608.08900].

[25] A. Gérardin, H. B. Meyer and A. Nyffeler, *Lattice calculation of the pion transition form factor with $N_f = 2 + 1$ Wilson quarks*, *Phys. Rev.* **D100** (2019) 034520 [1903.09471].

[26] I. Montvay and G. Münster, *Quantum fields on a lattice*, Cambridge Monographs on Mathematical Physics. Cambridge University Press, 1997, 10.1017/CBO9780511470783.

[27] C. Gattringer and C. B. Lang, *Quantum chromodynamics on the lattice*, *Lect. Notes Phys.* **788** (2010) 1.

[28] T. DeGrand and C. DeTar, *Lattice Methods for Quantum Chromodynamics*. World Scientific, 2006.

[29] J. F. Donoghue, *Dispersion relations and effective field theory*, in *Advanced School on Effective Theories Almunecar, Spain, June 25-July 1, 1995*, 1996, hep-ph/9607351.

[30] A. Anisovich, V. Anisovich, M. Matveev, V. Nikonov, J. Nyiri and A. Sarantsev., *Three-particle physics and dispersion relation theory*. World Scientific, Hackensack, USA, 2013.

[31] B. Ananthanarayan, I. Caprini and B. Kubis, *Constraints on the $\omega\pi$ form factor from analyticity and unitarity*, *Int.J.Mod.Phys.* **31** (2016) 1630020.

[32] J. A. Oller, *A Brief Introduction to Dispersion Relations*, SpringerBriefs in Physics. Springer, 2019, 10.1007/978-3-030-13582-9.

[33] B. Pasquini and M. Vanderhaeghen, *Dispersion theory in electromagnetic interactions*, *Ann.Rev.Nucl.Part.Sci.* **68** (2018) 75 [1805.10482].

[34] I. Danilkin, C. F. Redmer and M. Vanderhaeghen, *The hadronic light-by-light contribution to the muon?s anomalous magnetic moment*, *Prog.Part.Nucl.Phys.* **107** (2019) 20 [1901.10346].

[35] R. Alkofer and L. von Smekal, *The infrared behaviour of qcd green's functions: Confinement, dynamical symmetry breaking, and hadrons as relativistic bound states*, *Physics Reports* **353** (2001) 281 .

[36] C. D. Roberts and A. G. Williams, *Dyson-schwinger equations and their application to hadronic physics*, *Progress in Particle and Nuclear Physics* **33** (1994) 477 .

[37] G. Eichmann, "Introduction to hadron physics -lecture notes." http://cftp.tecnico.ulisboa.pt/~gernot.eichmann/ws2014, Winter term, 2014/15.

[38] Y. Takahashi, *On the generalized ward identity*, *Il Nuovo Cimento (1955-1965)* **6** (1957) 371.

[39] J. C. Ward, *An identity in quantum electrodynamics*, *Phys. Rev.* **78** (1950) 182.

[40] T. Göcke, *Hadronic contributions to the anomalous magnetic moment of the muon*, Ph.D. thesis, Giessen U., 2012.

[41] S. L. Adler, *Axial vector vertex in spinor electrodynamics*, *Phys. Rev.* **177** (1969) 2426.

[42] J. S. Bell and R. Jackiw, *A PCAC puzzle: $\pi^0 \to \gamma\gamma$ in the σ model*, *Nuovo Cim.* **A60** (1969) 47.

[43] R. A. Briceno, M. T. Hansen and C. J. Monahan, *Role of the Euclidean signature in lattice calculations of quasidistributions and other nonlocal matrix elements*, *Phys. Rev.* **D96** (2017) 014502 [1703.06072].

[44] G. Eichmann, P. Duarte, M. T. Peña and A. Stadler, *Scattering amplitudes and contour deformations*, 1907.05402.

[45] Muon g-2 collaboration, G. W. Bennett et al., *Final Report of the Muon E821 Anomalous Magnetic Moment Measurement at BNL*, *Phys. Rev.* **D73** (2006) 072003 [hep-ex/0602035].

[46] D. W. Hertzog, *Next Generation Muon g-2 Experiments*, *EPJ Web Conf.* **118** (2016) 01015 [1512.00928].

[47] C. Gilberto, D. Michel, E. Simon, E.-K. Aida, L. Christoph, M. Tsutomu et al., *$g-2$ Theory white-paper - to appear*, .

[48] D. Hanneke, S. F. Hoogerheide and G. Gabrielse, *Cavity Control of a Single-Electron Quantum Cyclotron: Measuring the Electron Magnetic Moment*, *Phys. Rev.* **A83** (2011) 052122 [1009.4831].

[49] S. Laporta, *High-precision calculation of the 4-loop contribution to the electron g-2 in QED*, *Phys. Lett.* **B772** (2017) 232 [1704.06996].

[50] B. L. Roberts, *Status of the Fermilab Muon $(g-2)$ Experiment*, *Chin. Phys.* **C34** (2010) 741 [1001.2898].

[51] Fermilab E989 collaboration, G. Venanzoni, *The New Muon g-2 experiment at Fermilab*, *Nucl. Part. Phys. Proc.* **273-275** (2016) 584 [1411.2555].

[52] E34 collaboration, M. Otani, *Status of the Muon g-2/EDM Experiment at J-PARC (E34)*, *JPS Conf. Proc.* **8** (2015) 025008.

[53] A. Crivellin, M. Hoferichter and P. Schmidt-Wellenburg, *Combined explanations of $(g-2)_{\mu,e}$ and implications for a large muon EDM*, *Phys. Rev.* **D98** (2018) 113002 [1807.11484].

[54] D. Stockinger, *The Muon Magnetic Moment and Supersymmetry*, *J. Phys.* **G34** (2007) R45 [hep-ph/0609168].

[55] F. Jegerlehner, *The Anomalous Magnetic Moment of the Muon*, *Springer Tracts Mod. Phys.* **274** (2017) pp.1.

[56] M. Davier, A. Hoecker, B. Malaescu and Z. Zhang, *A new evaluation of the hadronic vacuum polarisation contributions to the muon anomalous magnetic moment and to* $\boldsymbol{\alpha(m_Z^2)}$, 1908.00921.

[57] A. Keshavarzi, D. Nomura and T. Teubner, *The* $g-2$ *of charged leptons,* $\alpha(M_Z^2)$ *and the hyperfine splitting of muonium*, 1911.00367.

[58] M. Benayoun, L. Delbuono and F. Jegerlehner, *BHLS*$_2$*, a New Breaking of the HLS Model and its Phenomenology*, 1903.11034.

[59] B. Chakraborty, C. T. H. Davies, P. G. de Oliviera, J. Koponen, G. P. Lepage and R. S. Van de Water, *The hadronic vacuum polarization contribution to* a_μ *from full lattice QCD*, *Phys. Rev.* **D96** (2017) 034516 [1601.03071].

[60] Budapest-Marseille-Wuppertal collaboration, S. Borsanyi et al., *Hadronic vacuum polarization contribution to the anomalous magnetic moments of leptons from first principles*, *Phys. Rev. Lett.* **121** (2018) 022002 [1711.04980].

[61] RBC, UKQCD collaboration, T. Blum, P. A. Boyle, V. Gülpers, T. Izubuchi, L. Jin, C. Jung et al., *Calculation of the hadronic vacuum polarization contribution to the muon anomalous magnetic moment*, *Phys. Rev. Lett.* **121** (2018) 022003 [1801.07224].

[62] A. Gérardin, M. Cé, G. von Hippel, B. Hörz, H. B. Meyer, D. Mohler et al., *The leading hadronic contribution to* $(g-2)_\mu$ *from lattice QCD with* $N_{\rm f} = 2+1$ *flavours of O(a) improved Wilson quarks*, *Phys. Rev.* **D100** (2019) 014510 [1904.03120].

[63] T. Goecke, C. S. Fischer and R. Williams, *Hadronic light-by-light scattering in the muon g-2: a Dyson-Schwinger equation approach*, *Phys. Rev.* **D83** (2011) 094006 [1012.3886].

[64] T. Goecke, C. S. Fischer and R. Williams, *Leading-order calculation of hadronic contributions to the muon* $g-2$ *using the Dyson-Schwinger approach*, *Phys. Lett.* **B704** (2011) 211 [1107.2588].

[65] G. Eichmann, C. S. Fischer, W. Heupel and R. Williams, *The muon g-2: Dyson-Schwinger status on hadronic light-by-light scattering*, *AIP Conf. Proc.* **1701** (2016) 040004 [1411.7876].

[66] W. A. Bardeen and W. K. Tung, *Invariant amplitudes for photon processes*, *Phys. Rev.* **173** (1968) 1423.

[67] R. Tarrach, *Invariant Amplitudes for Virtual Compton Scattering Off Polarized Nucleons Free from Kinematical Singularities, Zeros and Constraints*, *Nuovo Cim.* **A28** (1975) 409.

[68] M. Procura, G. Colangelo, M. Hoferichter and P. Stoffer, *Dispersion relations for hadronic light-by-light scattering and the muon g–2*, *EPJ Web Conf.* **166** (2018) 00014.

[69] J. Aldins, S. J. Brodsky, A. J. Dufner and T. Kinoshita, *Photon-photon scattering contribution to the sixth-order magnetic moments of the muon and electron*, *Phys. Rev. D* **1** (1970) 2378.

[70] R. Barbieri and E. Remiddi, *Electron and muon 12(g?2) from vacuum polarization insertions*, *Nuclear Physics B* **90** (1975) 233 .

[71] M. Knecht and A. Nyffeler, *Hadronic light by light corrections to the muon g-2: The Pion pole contribution*, *Phys. Rev.* **D65** (2002) 073034 [hep-ph/0111058].

[72] G. Colangelo, M. Hoferichter, M. Procura and P. Stoffer, *Dispersive approach to hadronic light-by-light scattering*, *JHEP* **09** (2014) 091 [1402.7081].

[73] V. Pauk and M. Vanderhaeghen, *Anomalous magnetic moment of the muon in a dispersive approach*, *Phys. Rev.* **D90** (2014) 113012 [1409.0819].

[74] G. Colangelo, M. Hoferichter, M. Procura and P. Stoffer, *Dispersion relation for hadronic light-by-light scattering: theoretical foundations*, *JHEP* **09** (2015) 074 [1506.01386].

[75] S. Mandelstam, *Determination of the pion - nucleon scattering amplitude from dispersion relations and unitarity. General theory*, *Phys. Rev.* **112** (1958) 1344.

[76] J. Prades, E. de Rafael and A. Vainshtein, *The Hadronic Light-by-Light Scattering Contribution to the Muon and Electron Anomalous Magnetic Moments*, *Adv. Ser. Direct. High Energy Phys.* **20** (2009) 303 [0901.0306].

[77] G. Eichmann, C. S. Fischer, E. Weil and R. Williams, *Single pseudoscalar meson pole and pion box contributions to the anomalous magnetic moment of the muon*, 1903.10844.

[78] g-2 collaboration, C. Gabbaninion, *The g - 2 experiment*, *Nuovo Cim.* **C42** (2019) 146.

[79] Muon g-2 collaboration, I. Logashenko et al., *The Measurement of the Anomalous Magnetic Moment of the Muon at Fermilab*, *J. Phys. Chem. Ref. Data* **44** (2015) 031211.

[80] T. P. Gorringe and D. W. Hertzog, *Precision Muon Physics*, *Prog. Part. Nucl. Phys.* **84** (2015) 73 [1506.01465].

[81] E. Weil, G. Eichmann, C. S. Fischer and R. Williams, *Electromagnetic decays of the neutral pion*, *Phys. Rev.* **D96** (2017) 014021 [1704.06046].

[82] G. Eichmann, C. S. Fischer, E. Weil and R. Williams, *On the large-Q^2 behavior of the pion transition form factor*, *Phys. Lett.* **B774** (2017) 425 [1704.05774].

[83] M. Hoferichter, B. Kubis, S. Leupold, F. Niecknig and S. P. Schneider, *Dispersive analysis of the pion transition form factor*, *Eur. Phys. J.* **C74** (2014) 3180 [1410.4691].

[84] K. Raya, L. Chang, A. Bashir, J. J. Cobos-Martinez, L. X. Gutiérrez-Guerrero, C. D. Roberts et al., *Structure of the neutral pion and its electromagnetic transition form factor*, *Phys. Rev.* **D93** (2016) 074017 [1510.02799].

[85] P. Masjuan and P. Sanchez-Puertas, *Pseudoscalar-pole contribution to the $(g_\mu - 2)$: a rational approach*, *Phys. Rev.* **D95** (2017) 054026 [1701.05829].

[86] C. Ayala, S. V. Mikhailov, A. V. Pimikov and N. G. Stefanis, *Form factor $\pi^0\gamma^*\gamma$ in lightcone sum rules combined with renormalization-group summation vs experimental data*, *EPJ Web Conf.* **222** (2019) 03017 [1911.02845].

[87] J. Leutgeb, J. Mager and A. Rebhan, *Pseudoscalar transition form factors and the hadronic light-by-light contribution to the anomalous magnetic moment of the muon from holographic QCD*, *Phys. Rev.* **D100** (2019) 094038 [1906.11795].

[88] N. G. Stefanis, *Pion-photon transition form factor in QCD. Theoretical predictions and topology-based data analysis*, 1904.02631.

[89] C. D. Roberts, M. S. Bhagwat, A. Holl and S. V. Wright, *Aspects of hadron physics*, *Eur. Phys. J. ST* **140** (2007) 53 [0802.0217].

[90] R. Alkofer, W. Detmold, C. S. Fischer and P. Maris, *Analytic properties of the Landau gauge gluon and quark propagators*, *Phys. Rev.* **D70** (2004) 014014 [hep-ph/0309077].

[91] A. Windisch, *Analytic properties of the quark propagator from an effective infrared interaction model*, *Phys. Rev.* **C95** (2017) 045204 [1612.06002].

[92] A. Bender, D. Blaschke, Y. Kalinovsky and C. D. Roberts, *Continuum study of deconfinement at finite temperature*, *Phys. Rev. Lett.* **77** (1996) 3724 [nucl-th/9606006].

[93] M. S. Bhagwat, M. A. Pichowsky, C. D. Roberts and P. C. Tandy, *Analysis of a quenched lattice QCD dressed quark propagator*, *Phys. Rev.* **C68** (2003) 015203 [nucl-th/0304003].

[94] M. Oettel, L. von Smekal and R. Alkofer, *Relativistic three-quark bound states in separable two-quark approximation*, *Computer Physics Communications* **144** (2002) 63 .

[95] H. Sanchis-Alepuz and R. Williams, *Recent developments in bound-state calculations using the Dyson-Schwinger and Bethe-Salpeter equations*, *Comput. Phys. Commun.* **232** (2018) 1 [1710.04903].

[96] P. Maris and P. C. Tandy, *The Quark photon vertex and the pion charge radius*, *Phys. Rev.* **C61** (2000) 045202 [nucl-th/9910033].

[97] P. Maris and P. C. Tandy, *The quark photon vertex and meson electromagnetic form-factors*, *Nucl. Phys.* **A663** (2000) 401 [nucl-th/9908045].

[98] P. Maris and P. C. Tandy, *Electromagnetic transition form-factors of light mesons*, *Phys. Rev.* **C65** (2002) 045211 [nucl-th/0201017].

[99] M. S. Bhagwat and P. Maris, *Vector meson form factors and their quark-mass dependence*, *Phys. Rev.* **C77** (2008) 025203 [nucl-th/0612069].

[100] G. Eichmann, *Nucleon electromagnetic form factors from the covariant Faddeev equation*, *Phys. Rev.* **D84** (2011) 014014 [1104.4505].

[101] J. S. Ball and T.-W. Chiu, *Analytic Properties of the Vertex Function in Gauge Theories. 1.*, *Phys. Rev.* **D22** (1980) 2542.

[102] T. Goecke, C. S. Fischer and R. Williams, *Role of momentum dependent dressing functions and vector meson dominance in hadronic light-by-light contributions to the muon $g-2$*, *Phys. Rev.* **D87** (2013) 034013 [1210.1759].

[103] G. Eichmann and C. S. Fischer, *Nucleon Compton scattering in the Dyson-Schwinger approach*, *Phys.Rev.* **D87** (2013) 036006 [1212.1761].

[104] G. Eichmann, *Probing nucleons with photons at the quark level*, *Acta Phys. Polon. Supp.* **7** (2014) 597 [1404.4149].

[105] C. Tang, F. Gao and Y.-X. Liu, *Practical scheme from QCD to phenomena via Dyson-Schwinger equations*, *Phys. Rev.* **D100** (2019) 056001 [1902.01679].

[106] A. Sternbeck, M. Leutnant and G. Eichmann, *Towards lattice-assisted hadron physics calculations based on QCD n-point functions*, *PoS* **LATTICE2018** (2019) 068 [1904.10705].

[107] A. S. Miramontes and H. Sanchis-Alepuz, *On the effect of resonances in the quark-photon vertex*, *Eur. Phys. J.* **A55** (2019) 170 [1906.06227].

[108] G. Eichmann, *Towards resonance properties in the Dyson-Schwinger approach*, 2019, 1912.08873.

[109] M. Q. Huber, *Gluon and ghost propagators in linear covariant gauges*, *Phys. Rev.* **D91** (2015) 085018 [1502.04057].

[110] M. Q. Huber, *Gluonic vertices and the gluon propagator in Landau gauge Yang-Mills theory*, *Acta Phys. Polon. Supp.* **13** (2020) 133 [1909.10867].

[111] A. G. Williams, F. D. R. Bonnet, P. O. Bowman, D. B. Leinweber, J. I. Skullerud and J. M. Zanotti, *Gluons, quarks, and the transition from nonperturbative to perturbative QCD*, in *Proceedings, Workshop on Lepton Scattering, Hadrons and QCD: Adelaide, Australia, March 26-April 6, 2001*, pp. 138–145, 2001, hep-ph/0107029, DOI.

[112] A. Windisch, M. Hopfer and R. Alkofer, *Towards a self-consistent solution of the Landau gauge quark-gluon vertex Dyson-Schwinger equation*, 1210.8428.

[113] E. Rojas, J. P. B. C. de Melo, B. El-Bennich, O. Oliveira and T. Frederico, *On the Quark-Gluon Vertex and Quark-Ghost Kernel: combining Lattice Simulations with Dyson-Schwinger equations*, *JHEP* **10** (2013) 193 [1306.3022].

[114] R. Williams, C. S. Fischer and W. Heupel, *Light mesons in QCD and unquenching effects from the 3PI effective action*, *Phys. Rev.* **D93** (2016) 034026 [1512.00455].

[115] A. L. Blum, R. Alkofer, M. Q. Huber and A. Windisch, *Three-point vertex functions in Yang-Mills Theory and QCD in Landau gauge*, *EPJ Web Conf.* **137** (2017) 03001 [1611.04827].

[116] H. Sanchis-Alepuz and R. Williams, *Hadronic Observables from Dyson-Schwinger and Bethe-Salpeter equations*, *J. Phys. Conf. Ser.* **631** (2015) 012064 [1503.05896].

[117] P. Isserstedt, M. Buballa, C. S. Fischer and P. J. Gunkel, *Baryon number fluctuations in the QCD phase diagram from Dyson-Schwinger equations*, *Phys. Rev.* **D100** (2019) 074011 [1906.11644].

[118] P. J. Gunkel, C. S. Fischer and P. Isserstedt, *Quarks and light (pseudo-)scalar mesons at finite chemical potential*, *Eur. Phys. J.* **A55** (2019) 169 [1907.08110].

[119] P. Maris and P. C. Tandy, *Bethe-Salpeter study of vector meson masses and decay constants*, *Phys. Rev.* **C60** (1999) 055214 [nucl-th/9905056].

[120] R. Alkofer, P. Watson and H. Weigel, *Mesons in a Poincare covariant Bethe-Salpeter approach*, *Phys. Rev.* **D65** (2002) 094026 [hep-ph/0202053].

[121] M. Q. Huber, *Nonperturbative properties of Yang-Mills theories*, habilitation, Graz U., 2018. 1808.05227.

[122] G. Eichmann and C. S. Fischer, *Unified description of hadron-photon and hadron-meson scattering in the Dyson-Schwinger approach*, *Phys. Rev.* **D85** (2012) 034015 [1111.0197].

[123] CELLO collaboration, H. J. Behrend et al., *A Measurement of the pi0, eta and eta-prime electromagnetic form-factors*, *Z. Phys.* **C49** (1991) 401.

[124] CLEO collaboration, J. Gronberg et al., *Measurements of the meson - photon transition form-factors of light pseudoscalar mesons at large momentum transfer*, *Phys. Rev.* **D57** (1998) 33 [hep-ex/9707031].

[125] M. Hoferichter, B.-L. Hoid, B. Kubis, S. Leupold and S. P. Schneider, *Pion-pole contribution to hadronic light-by-light scattering in the anomalous magnetic moment of the muon*, *Phys. Rev. Lett.* **121** (2018) 112002 [1805.01471].

[126] M. Hoferichter, B.-L. Hoid, B. Kubis, S. Leupold and S. P. Schneider, *Dispersion relation for hadronic light-by-light scattering: pion pole*, *JHEP* **10** (2018) 141 [1808.04823].

[127] A. Nyffeler, *Precision of a data-driven estimate of hadronic light-by-light scattering in the muon $g-2$: Pseudoscalar-pole contribution*, *Phys. Rev.* **D94** (2016) 053006 [1602.03398].

[128] M. Knecht and A. Nyffeler, *Resonance estimates of O(p**6) low-energy constants and QCD short distance constraints*, *Eur. Phys. J.* **C21** (2001) 659 [hep-ph/0106034].

[129] A. Gerardin, H. B. Meyer and A. Nyffeler, *Lattice calculation of the pion transition form factor $\pi^0 \to \gamma^*\gamma^*$*, *Phys. Rev.* **D94** (2016) 074507 [1607.08174].

[130] B. Kubis, *Dispersive analysis of light-meson transition form factors*, *EPJ Web Conf.* **218** (2019) 03001.

[131] P. Masjuan and P. Sanchez-Puertas, *Phenomenology of bivariate approximants: the pi0 to e+e- case and its impact on the electron and muon g-2*, 1504.07001.

[132] K. Raya, M. Ding, A. Bashir, L. Chang and C. D. Roberts, *Partonic structure of neutral pseudoscalars via two photon transition form factors*, *Phys. Rev.* **D95** (2017) 074014 [1610.06575].

[133] K. Raya, A. Bashir and P. Roig, *Contribution of neutral pseudoscalar mesons to a_μ^{HLbL} within a Schwinger-Dyson equations approach to QCD*, 1910.05960.

[134] BaBar collaboration, B. Aubert et al., *Measurement of the gamma gamma* —> pi0 transition form factor*, *Phys. Rev.* **D80** (2009) 052002 [0905.4778].

[135] Belle collaboration, S. Uehara et al., *Measurement of $\gamma\gamma^* \to \pi^0$ transition form factor at Belle*, *Phys. Rev.* **D86** (2012) 092007 [1205.3249].

[136] A. Gerardin, H. B. Meyer and A. Nyffeler, *Lattice calculation of the pion transition form factor $\pi^0 \to \gamma^*\gamma^*$*, *PoS* **LATTICE2016** (2016) 175 [1611.02190].

[137] G. P. Lepage and S. J. Brodsky, *Exclusive Processes in Perturbative Quantum Chromodynamics*, *Phys. Rev.* **D22** (1980) 2157.

[138] A. V. Efremov and A. V. Radyushkin, *Factorization and Asymptotical Behavior of Pion Form-Factor in QCD*, *Phys. Lett.* **94B** (1980) 245.

[139] Belle-II collaboration, T. Abe et al., *Belle II Technical Design Report*, 1011.0352.

[140] Particle Data Group collaboration, M. Tanabashi, K. Hagiwara, K. Hikasa, K. Nakamura, Y. Sumino, F. Takahashi et al., *Review of particle physics*, *Phys. Rev. D* **98** (2018) 030001.

[141] C. Patrignani et al.*Chin. Phys. C, 40, 100001* (2016) .

[142] C. Terschlüsen, B. Strandberg, S. Leupold and F. Eichstädt, *Reactions with pions and vector mesons in the sector of odd intrinsic parity*, *Eur. Phys. J.* **A49** (2013) 116 [1305.1181].

[143] T. Husek, E. Goudzovski and K. Kampf, *Precise determination of the branching ratio of the neutral-pion Dalitz decay*, *Phys. Rev. Lett.* **122** (2019) 022003 [1809.01153].

[144] R. Escribano and S. Gonzalez-Solis, *A data-driven model-independent approach to π^0, η and η' single and double Dalitz decays*, 1511.04916.

[145] T. Hahn, *CUBA: A Library for multidimensional numerical integration*, *Comput. Phys. Commun.* **168** (2005) 78 [hep-ph/0404043].

[146] KTeV collaboration, E. Abouzaid et al., *Measurement of the rare decay pi0 —> e+ e-*, *Phys. Rev.* **D75** (2007) 012004 [hep-ex/0610072].

[147] A. E. Dorokhov and M. A. Ivanov, *Rare decay pi0 —> e+ e-: Theory confronts KTeV data*, *Phys. Rev.* **D75** (2007) 114007 [0704.3498].

[148] A. E. Dorokhov, *How the recent BABAR data for P —> gamma gamma* affect the Standard Model predictions for the rare decays P —> l+ l-*, *JETP Lett.* **91** (2010) 163 [0912.5278].

[149] P. Vasko and J. Novotny, *Two-loop QED radiative corrections to the decay pi0 -> e+ e- : The virtual corrections and soft-photon bremsstrahlung*, *JHEP* **10** (2011) 122 [1106.5956].

[150] T. Husek, K. Kampf and J. Novotny, *Rare decay $\pi^0 \to e^+e^-$: on corrections beyond the leading order*, *Eur. Phys. J.* **C74** (2014) 3010 [1405.6927].

[151] R. E. Cutkosky, *Singularities and discontinuities of Feynman amplitudes*, *J. Math. Phys.* **1** (1960) 429.

[152] H. Ghaderi Master's thesis, Uppsala University, 2013.

[153] P. Maris, *Confinement and complex singularities in QED in three-dimensions*, *Phys. Rev.* **D52** (1995) 6087 [hep-ph/9508323].

[154] G. Eichmann, *Hadron Properties from QCD Bound-State Equations*, Ph.D. thesis, Graz U., 2009. 0909.0703.

[155] S. Strauss, C. S. Fischer and C. Kellermann, *Analytic structure of the Landau gauge gluon propagator*, *Phys. Rev. Lett.* **109** (2012) 252001 [1208.6239].

[156] A. Windisch, R. Alkofer, G. Haase and M. Liebmann, *Examining the Analytic Structure of Green's Functions: Massive Parallel Complex Integration using GPUs*, *Comput. Phys. Commun.* **184** (2013) 109 [1205.0752].

[157] A. Windisch, M. Q. Huber and R. Alkofer, *On the analytic structure of scalar glueball operators at the Born level*, *Phys. Rev.* **D87** (2013) 065005 [1212.2175].

[158] J. M. Pawlowski, N. Strodthoff and N. Wink, *Finite temperature spectral functions in the O(N)-model*, *Phys. Rev.* **D98** (2018) 074008 [1711.07444].

[159] NA48/2 collaboration, E. Goudzovski, *Search for the dark photon in π^0 decays by the NA48/2 experiment at CERN*, *EPJ Web Conf.* **96** (2015) 01017 [1412.8053].

[160] NA62 collaboration, R. Volpe, *Physics beyond SM with kaons from NA62*, in *Meeting of the Division of Particles and Fields of the American Physical Society (DPF2019) Boston, Massachusetts, July 29-August 2, 2019*, 2019, 1910.09422.

[161] Y. Kahn, M. Schmitt and T. M. P. Tait, *Enhanced rare pion decays from a model of MeV dark matter*, *Phys. Rev.* **D78** (2008) 115002 [0712.0007].

[162] Q. Chang and Y.-D. Yang, *Rare decay pi0 —¿ e+ e- as a sensitive probe of light CP-odd Higgs in NMSSM*, *Phys. Lett.* **B676** (2009) 88 [0808.2933].

[163] J. Schechter, A. Subbaraman and H. Weigel, *Effective hadron dynamics: From meson masses to the proton spin puzzle*, *Phys. Rev.* **D48** (1993) 339 [hep-ph/9211239].

[164] T. Feldmann, P. Kroll and B. Stech, *Mixing and decay constants of pseudoscalar mesons: The Sequel*, *Phys. Lett.* **B449** (1999) 339 [hep-ph/9812269].

[165] T. Feldmann, P. Kroll and B. Stech, *Mixing and decay constants of pseudoscalar mesons*, *Phys. Rev.* **D58** (1998) 114006 [hep-ph/9802409].

[166] T. Feldmann, *Quark structure of pseudoscalar mesons*, *Int. J. Mod. Phys.* **A15** (2000) 159 [hep-ph/9907491].

[167] R. Escribano, S. Gonzalez-Solis, P. Masjuan and P. Sanchez-Puertas, *η' transition form factor from space- and timelike experimental data*, *Phys. Rev.* **D94** (2016) 054033 [1512.07520].

[168] R. Escribano, P. Masjuan and P. Sanchez-Puertas, *The η transition form factor from space- and time-like experimental data*, *Eur. Phys. J.* **C75** (2015) 414 [1504.07742].

[169] P. Roig, A. Guevara and G. Lopez Castro, *$VV'P$ form factors in resonance chiral theory and the $\pi - \eta - \eta'$ light-by-light contribution to the muon $g-2$*, *Phys. Rev.* **D89** (2014) 073016 [1401.4099].

[170] BaBar collaboration, J. P. Lees et al., *Measurement of the $\gamma^\star\gamma^\star \to \eta'$ transition form factor*, *Phys. Rev.* **D98** (2018) 112002 [1808.08038].

[171] M. Ding, K. Raya, A. Bashir, D. Binosi, L. Chang, M. Chen et al., *$\gamma^*\gamma \to \eta, \eta'$ transition form factors*, *Phys. Rev.* **D99** (2019) 014014 [1810.12313].

[172] BaBar collaboration, P. del Amo Sanchez et al., *Measurement of the $\gamma\gamma^* - - > \eta$ and $\gamma\gamma * - - > \eta'$ transition form factors*, *Phys. Rev.* **D84** (2011) 052001 [1101.1142].

[173] NA60 collaboration, R. Arnaldi et al., *Precision study of the $\eta \to \mu^+\mu^-\gamma$ and $\omega \to \mu^+\mu^-\pi^0$ electromagnetic transition form-factors and of the $\rho \to \mu^+\mu^-$ line shape in NA60*, *Phys. Lett.* **B757** (2016) 437 [1608.07898].

[174] NA60 collaboration, R. Arnaldi et al., *Study of the electromagnetic transition form-factors in eta —¿ mu+ mu- gamma and omega —¿ mu+ mu- pi0 decays with NA60*, *Phys. Lett.* **B677** (2009) 260 [0902.2547].

[175] P. Adlarson et al., *Measurement of the $\omega \to \pi^0 e^+ e^-$ and $\eta \to e^+ e^- \gamma$ Dalitz decays with the A2 setup at MAMI*, *Phys. Rev.* **C95** (2017) 035208 [1609.04503].

[176] BESIII collaboration, M. Ablikim et al., *Observation of the Dalitz Decay $\eta' \to \gamma e^+ e^-$*, *Phys. Rev.* **D92** (2015) 012001 [1504.06016].

[177] P. Aguar-Bartolomé, J. R. M. Annand, H. J. Arends, K. Bantawa, R. Beck, V. Bekrenev et al., *New determination of the η transition form factor in the Dalitz decay $\eta \to e^+ e^- \gamma$ with the Crystal Ball/TAPS detectors at the Mainz Microtron*, *Physical Review C* **89** (2014) .

[178] J. Dudek et al., *Physics Opportunities with the 12 GeV Upgrade at Jefferson Lab*, *Eur. Phys. J.* **A48** (2012) 187 [1208.1244].

[179] L. G. Landsberg, *Electromagnetic Decays of Light Mesons*, *Phys. Rept.* **128** (1985) 301.

[180] E. Braaten, *QCD CORRECTIONS TO MESON - PHOTON TRANSITION FORM-FACTORS*, *Phys. Rev.* **D28** (1983) 524.

[181] G. Eichmann, C. S. Fischer and W. Heupel, *Four-point functions and the permutation group S4*, *Phys. Rev.* **D92** (2015) 056006 [1505.06336].

[182] J. R. Pelaez, *From controversy to precision on the sigma meson: a review on the status of the non-ordinary $f_0(500)$ resonance*, *Phys. Rept.* **658** (2016) 1 [1510.00653].

[183] A. Francis, R. J. Hudspith, R. Lewis and K. Maltman, *Lattice predictions for bound heavy tetraquarks*, *PoS* **ICHEP2018** (2019) 257.

[184] D. Darvish, R. Brett, J. Bulava, J. Fallica, A. Hanlon, B. Hörz et al., *Including Tetraquark Operators in the Low-Lying Scalar Meson Sectors in Lattice QCD*, in *15th International Conference on Meson-Nucleon Physics and the Structure of the Nucleon (MENU 2019) Pittsburgh, Pennsylvania, USA, June 2-7, 2019*, 2019, 1909.07747.

[185] G. Eichmann, C. S. Fischer and W. Heupel, *The light scalar mesons as tetraquarks*, *Phys. Lett.* **B753** (2016) 282 [1508.07178].

[186] P. C. Wallbott, G. Eichmann and C. S. Fischer, *Towards Heavy–Light Axialvector Tetraquarks in a Dyson–Schwinger/Bethe–Salpeter Approach*, *Acta Phys. Polon. Supp.* **13** (2020) 139.

[187] G. Colangelo, M. Hoferichter, B. Kubis, M. Procura and P. Stoffer, *Towards a data-driven analysis of hadronic light-by-light scattering*, *Phys. Lett.* **B738** (2014) 6 [1408.2517].

[188] G. Eichmann, C. S. Fischer and R. Williams, *Kaon-box contribution to the anomalous magnetic moment of the muon*, 1910.06795.

[189] F. Jegerlehner and A. Nyffeler, *The Muon g-2*, *Phys. Rept.* **477** (2009) 1 [0902.3360].

[190] A. E. Dorokhov, A. P. Martynenko, F. A. Martynenko, A. E. Radzhabov and A. S. Zhevlakov, *The LbL contribution to the muon g-2 from the axial-vector mesons exchanges within the nonlocal quark model*, *EPJ Web Conf.* **212** (2019) 05001 [1910.07815].

[191] T. Blum, N. Christ, M. Hayakawa, T. Izubuchi, L. Jin, C. Jung et al., *The hadronic light-by-light scattering contribution to the muon anomalous magnetic moment from lattice QCD*, 1911.08123.

[192] B. Kubis, *Towards a dispersive determination of the η and η' transition form factors*, *EPJ Web Conf.* **166** (2018) 00012.

[193] M. Knecht, S. Narison, A. Rabemananjara and D. Rabetiarivony, *Scalar meson contributions to a_μ from hadronic light-by-light scattering*, *Phys. Lett.* **B787** (2018) 111 [1808.03848].

[194] I. Danilkin and M. Vanderhaeghen, *Light-by-light scattering sum rules in light of new data*, *Phys. Rev.* **D95** (2017) 014019 [1611.04646].

[195] J. Bijnens, N. Hermansson-Truedsson and A. Rodriguez-Sanchez, *Short-distance constraints for the HLbL contribution to the muon anomalous magnetic moment*, *Phys. Lett.* **B798** (2019) 134994 [1908.03331].

[196] J. Bijnens, E. Pallante and J. Prades, *Analysis of the hadronic light by light contributions to the muon g-2*, *Nucl. Phys.* **B474** (1996) 379 [hep-ph/9511388].

[197] E. Bartos, A. Z. Dubnickova, S. Dubnicka, E. A. Kuraev and E. Zemlyanaya, *Scalar and pseudoscalar meson pole terms in the hadronic light by light contributions to a**had(mu)*, *Nucl. Phys.* **B632** (2002) 330 [hep-ph/0106084].

[198] V. Pauk and M. Vanderhaeghen, *Single meson contributions to the muon's anomalous magnetic moment*, *Eur. Phys. J.* **C74** (2014) 3008 [1401.0832].

[199] G. Colangelo, M. Hoferichter, M. Procura and P. Stoffer, *Dispersion relation for hadronic light-by-light scattering: two-pion contributions*, *JHEP* **04** (2017) 161 [1702.07347].

[200] G. Colangelo, M. Hoferichter, M. Procura and P. Stoffer, *Hadronic light-by-light contribution to $(g-2)_\mu$: a dispersive approach*, *EPJ Web Conf.* **175** (2018) 01025 [1711.00281].

[201] L. D. Landau, *On the angular momentum of a system of two photons*, *Dokl. Akad. Nauk SSSR* **60** (1948) 207.

[202] C.-N. Yang, *Selection Rules for the Dematerialization of a Particle Into Two Photons*, *Phys. Rev.* **77** (1950) 242.

[203] P. Roig and P. Sanchez-Puertas, *Axial-vector exchange contribution to the hadronic light-by-light piece of the muon anomalous magnetic moment*, 1910.02881.

[204] E. Byckling and K. Kajantie, *Particle Kinematics*. University of Jyvaskyla, Finland, 1971.

[205] P. Nyborg, H. S. Song, W. Kernan and R. H. Good, *Phase-Space Considerations for Four-Particle Final States*, *Phys. Rev.* **140** (1965) B914.

[206] N. Byers and C. N. Yang, *Physical Regions in Invariant Variables for n Particles and the Phase-Space Volume Element*, *Reviews of Modern Physics* **36** (1964) 595.

Acknowledgments

To begin, I would like to thank my advisor Christian Fischer, for supervision and collaboration over the past six years. When I started my studies, I would have never believed that I would leave the JLU with a Phd in physics. His excitement and curiosity in this field are contagious, and he always had an open door whenever I was stuck with the project or wanted to discuss details.

A special thanks goes to Richard Williams, who has always been at my side with advice and support over the past few years and has spared no effort to explore various aspects of my work together with me. Through conversations over cake and tea, I was able to benefit from his breadth of knowledge, which lead to work presented in this thesis.

In this spirit, I would also like to thank Gernot Eichmann for the collaboration throughout this Phd. For the incredibly detailed explanations whenever I was lost and the inspiration to approach topics from a different angle and not to give up.

This work was funded partly by the Phd scholarship of the Justus-Liebig University Giessen and partly by the doctoral scholarships within the cooperative agreement between the JLU and GSI Darmstadt. I would like to thank the HGS-Hire Graduate school for sponsorship and the opportunities to take part in international conferences, schools, seminars, and research stay abroad throughout my Phd. I highly benefited from the broad program offered through the school. In this context, I would also like to thank Anthony Francis for his supervision during my research stay at CERN.

A special thanks for the thorough feedback and corrections that highly improved this thesis towards its final form goes to Christian Fischer, Gernot Eichmann, and Maxwell Hansen.

Thanks to the members at the theoretical Institute at the JLU Giessen, our secretaries, and everyone else who created a pleasant research environment. In particular, the members of the Fischer workgroup (Pascal, Phillip, Nico, Christian W., Christian S., Markus, and many others) who shared many lunches and great discussions with me in the past years. In particular, thanks to Paul, for being there throughout the Phd, both in the office and away from it.

Zuletzt möchte ich mich bei meiner ganzen Familie bedanken, für all die Unterstützung und Hilfe in den letzten Jahren. Vielen Dank an meine Eltern, an Robin, in Gedenken meinen Opa, und insbesondere an Max.

Selbstständigkeitserklärung

Ich erkläre:

Ich habe die vorgelegte Dissertation selbstständig und ohne unerlaubte fremde Hilfe und nur mit den Hilfen angefertigt, die ich in der Dissertation angegeben habe. Alle Textstellen, die wörtlich oder sinngemäß aus veröffentlichten Schriften entnommen sind, und alle Angaben, die auf mündlichen Auskünften beruhen, sind als solche kenntlich gemacht. Ich stimme einer evtl. Überprüfung meiner Dissertation durch eine Antiplagiat-Software zu. Bei den von mir durchgeführten und in der Dissertation erwähnten Untersuchungen habe ich die Grundsätze guter wissenschaftlicher Praxis, wie sie in der „Satzung der Justus-Liebig-Universität Gießen zur Sicherung guter wissenschaftlicher Praxis“ niedergelegt sind, eingehalten.

Ort, Datum	Unterschrift